

POLITECNICO DI TORINO

Department of Mechanical and Aerospace Engineering

Master's degree in Aerospace Engineering

Master's degree Thesis

Preliminary design of a Lunar Nano Drone for a mission of exploration of lava tubes on the Moon: study of the Mission Flight Profile and identification of the most suitable Energy Storage System



THESIS ADVISORS

Prof. Paolo Maggiore

Ing. Piero Messidoro

Gen. Roberto Vittori

CANDIDATE

Stefano Pescaglia

December 2020



Abstract

On September 25th, 2020, Hon. Riccardo Fraccaro, Undersecretary of State at the Presidency of the Italian Council of Ministers and NASA Administrator Jim Bridenstine signed a joint statement of intent for cooperation in the Artemis Program. This new chapter in NASA's lunar exploration has the task of not just going to the Moon, to create a long-term human presence on and around it, but also to prepare for ever-more-complex human missions to Mars.

The United States and Italy have a long history of successful cooperation in science and exploration of outer space for peaceful uses. It all began in 1962, the year of the cooperation agreement that allowed two years later to launch the San Marco satellite from the USA, the first Italian object in orbit. More recently, the Italy-United States agreement on the supply of pressurised modules for the Space Shuttle and the International Space Station (ISS) has given Italy privileged access (for astronauts and experiments) to the orbiting outpost.

This new declaration of intent focuses on Italy's possible contribution to habitat modules, telecommunications and enabling technologies, all in relation to future activities on the lunar surface. This work concentrates specifically on these enabling technologies. In particular, this study aims to achieve the preliminary design of a spacecraft, called “LuNaDrone” (Lunar Nano Drone) and its mission definition, whose purpose is to explore lunar caves. The concept of a LuNaDrone is based on the strategic idea already experienced with Cubesat: small spacecraft, low mass, low cost, standardised, affordable by Academies and SME's and easy to deliver in Space.

As mentioned before, NASA's goal is to create a long-term human presence on the Moon. In this regard, NASA, ESA and other agencies have been exploring for many years the possibility of stable lava tubes as a potential site. In 2009, data provided by the Terrain Camera aboard JAXA's SELENE spacecraft indicated the presence of three huge pits on the surface of the Moon. These pits were of particular interest since they were seen as possible openings (or skylights) to subsurface lava channels. The Marius Hills region, where they were found, is likely to be the site of future lunar missions and could even be the site of a future lunar habitat. Consequently, these are the reasons why the LuNaDrone's mission objective is to explore the inside of one of these lunar caves.

Considering the context in which this study is developed, many design choices will inevitably be influenced by the need to adopt, where possible, Italian technologies in order to fulfill the mission in a reasonable time and cost. In addition to a preliminary study on the general characteristics of the mission, this thesis will address two specific issues: the identification of the most suitable energy storage system, and the development of a physical model able to simulate the propellant consumption associated with the various flight phases that LuNaDrone will have to perform. Finally, this model will not only be crucial in the design and sizing of the individual spacecraft subsystems, but will also make it possible to assess the feasibility of the mission itself.



Acknowledgment

I would like to thank my thesis supervisors, Professor Paolo Maggiore, Engineer Piero Messidoro and Astronaut Roberto Vittori, for the invaluable opportunity they gave me. It is hard to even describe the feeling of working on a project like this, with the support of an astronaut, of someone who is part of that group of truly exceptional people who have the burden, and honour, of representing humanity on the most extreme exploration and scientific missions. I would therefore like to express my deepest thanks to General Roberto Vittori for letting me participate in this project. I also owe special thanks to Professor Paolo Maggiore, not only for giving me the opportunity to work on this important study, but also for the teachings I had the pleasure of receiving from him during my studies at Politecnico di Torino. Regardless of the subject, I always knew I could take my questions to him and get solid advice. I would also like to thank Engineer Nicolas Bellomo, CTO of T4i, and Engineer Devis Paulon, for helping me and my colleagues during these months and for always being very willing to answer our many questions. It has been truly instructive and motivating to meet people who are as passionate about their field of study as they are.

Finally, if I have achieved this first important accomplishment, I owe it to my family, my parents, my sister and you, grandpa, who taught me so much, ... lessons that I will always carry with me. Last but not least, I thank my friends and my girlfriend who have always supported me during these years and without whom life would lose a lot of its meaning.



Contents

Figures	V
Tables	IX
Nomenclature	X
1 Context and objectives of the study	1
1.1 Mission statement and objectives	1
1.2 Observational evidence and characteristics of lunar lava tubes	1
1.3 State-of-the-art of mission concepts	4
1.4 Challenges	4
1.5 Summary.....	5
1.6 Possible supporting missions.....	5
2 LuNaDrone mission design	7
2.1 Mission overview	7
2.2 Spacecraft overview	10
3 Flight Profile	16
3.1 General assumptions.....	16
3.2 Vertical ascent	20
3.2.1 Vertical ascent without braking thrust.....	20
3.2.2 Vertical ascent without braking thrust – Results and conclusions.....	28
3.2.3 Vertical ascent with braking thrust.....	31
3.2.4 Vertical ascent with braking thrust – Case 1: $T/m = \text{cost}$	35
3.2.5 Vertical ascent with braking thrust – Case 2: $T = \text{cost}$, $m \neq \text{cost}$	38
3.2.6 Vertical ascent with braking thrust – Results and conclusions.....	44
3.3 Horizontal translation	46
3.3.1 Horizontal translation with auxiliary thrusters – Case 1: $T_X = \text{cost}$, $m = \text{cost}$	49
3.3.2 Horizontal translation with auxiliary thrusters – Case 2: $T_X = \text{cost}$, $m \neq \text{cost}$	52
3.3.3 Horizontal translation without auxiliary thrusters	57
3.3.4 Horizontal translation – Results and conclusions.....	58
3.4 Vertical Descent	62
3.4.1 Vertical Descent – Results and conclusions	69
3.5 Hovering.....	72
3.6 Thrust control techniques	74
3.7 Conclusions and Recommendations.....	79
4 EPS.....	92
4.1 Introduction	92
4.2 Prime power sources – Solar Arrays	94
4.3 Prime power sources – Nuclear Systems.....	96
4.4 Energy storage systems	98
4.5 Primary Batteries (SOP).....	98
4.5.1 Silver-Zinc ($\text{Zn-Ag}_2\text{O}$) Batteries	98
4.5.2 Lithium-Sulfur Dioxide (Li-SO_2) Batteries	100
4.5.3 Lithium-Thionyl Chloride (Li-SOCl_2) Batteries.....	101
4.6 Advanced Primary Batteries.....	102

4.7	Rechargeable batteries (SOP)	104
4.8	Capacitors	104
4.9	Fuel Cells.....	105
4.10	Conclusions	107
5	Annex 01 - Analysis of vertical ascent without braking thrust	111
6	Annex 02 – Vertical ascent ($T_B \neq 0$, $m \approx \text{cost}$) parametric sweep of m_0	127
7	Annex 03 – Vertical ascent ($T_B \neq 0$, $m \approx \text{cost}$) parametric sweep of h_1	132
8	Annex 04 – Vertical ascent ($T_B \neq 0$, $m \approx \text{cost}$) parametric sweep of I_{sp}	137
9	Annex 05 – Vertical ascent, comparison between Case 1 and Case 2	141
10	Annex 06 – Horizontal translation	148
11	References	153

Figures

Figure 1.1 – Potential entrance outcomes from observed pits and rilles	2
Figure 1.2 – Mare Tranquillitatis Pit [9]	3
Figure 1.3 – The known mare pits and highland pits [10]	3
Figure 2.1 – Illustration of the flight segments	7
Figure 2.2 – Brainstorming on the possible scenarios of the mission.....	9
Figure 2.3 – Side view #1 of the current configuration of LuNaDrone.....	12
Figure 2.4 – Side view #2 of the current configuration of LuNaDrone.....	13
Figure 2.5 – Top view of the current configuration of LuNaDrone	14
Figure 2.6 – Bottom view of the current configuration of LuNaDrone	15
Figure 3.1 – Coordinate systems to describe the two-dimensional spacecraft motion [19].....	17
Figure 3.2 – Forces acting on the spacecraft.....	18
Figure 3.3 – The outline of the vertical ascent manoeuvre	22
Figure 3.4 – Main system of the vertical ascent model (without braking thrust).....	24
Figure 3.5 – Thrust Control System of the vertical ascent model (without braking thrust)	25
Figure 3.6 – Hovering subsystem of the vertical ascent model (without braking thrust).....	26
Figure 3.7 – Model output example [vertical ascent model (without braking thrust)]	27
Figure 3.8 – Vertical ascent w. and w/o. braking thrust (right and left respectively).....	31
Figure 3.9 – Acceleration and velocity as a function of time for case A (left) and B (right).	33
Figure 3.10 – Relation between TB, h1 and mp with: $T_{0B} = 50N$, $m = 15\text{ kg}$, $I_{sp} = 150\text{ s}$	37
Figure 3.11 – Relation between TB and mp varying h1 with: $T_{0B} = 50N$, $m = 15\text{ kg}$, $I_{sp} = 150\text{ s}$	37
Figure 3.12 – Main sytem of the vertical ascent model (with braking thrust)	40
Figure 3.13 – Thrust Control System of the vertical ascent model (with braking thrust)	42
Figure 3.14 – Model output example [vertical ascent model (with braking thrust)]	43
Figure 3.15 – Thrust components in the horizontal translation	46
Figure 3.16 – One auxiliary thruster configuration (left), two auxiliary thrusters configuration (right).....	49
Figure 3.17 – Propellant mass varying T_x/m and d_{12} in the case of $T_x/m = \text{cost}$ and $t_{V12max} = t_I$	51
Figure 3.18 – Main system of the horizontal translation model (with auxiliary thrusters)	53
Figure 3.19 – Thrust Control System of the horizontal translation model (with auxiliary thrusters).....	54
Figure 3.20 – Model output example [horizontal translation model (with auxiliary thrusters)]	56
Figure 3.21 – Main system of the horizontal translation model (without auxiliary thrusters)	57
Figure 3.22 – Horiz. transl. (Case 2), assuming $t_I \equiv t_{V12max}$: $m_{prop} = fT_{12}, d_{12}$	58
Figure 3.23 – Horiz. transl. w/o auxiliary thrusters, $m=\text{cost}$ case	60
Figure 3.24 – Horizontal translation w/o auxiliary thrusters: $m_1 = 15\text{ kg}$ $I_{sp} = 150\text{ s}$ $d_{12} = 150\text{ m}$	61
Figure 3.25 – Vertical descent manoeuvre.....	62
Figure 3.26 – Main system of the vertical descent model	66
Figure 3.27 – Thrust Control System of the vertical descent model.....	67
Figure 3.28 – Model output example (Vertical descent model)	68
Figure 3.29 – Vertical descent, $m_{prop}T_{23}, V_{23max} - d_{12} = 10\text{ m}$	69
Figure 3.30 – Vertical descent, $m_{prop}T_{23}, V_{23max} - d_{12} = 100\text{ m}$	70
Figure 3.31 – Vertical descent, $m_{prop}T_{23}, V_{23max} - d_{12} = 500\text{ m}$	71
Figure 3.32 – Propellant mass consumed during a hovering manoeuvre (minutes).....	72
Figure 3.33 – Propellant mass consumed during a hovering manoeuvre (seconds)	73
Figure 3.34 – Solenoid shut-off valve.....	74
Figure 3.35 – PWM-Thrust block (integration with the main model)	76
Figure 3.36 – PWM-Thrust subsystem	76

Figure 3.37 – PWM Generator.....	77
Figure 3.38 – Output example of vertical ascent model with bang-bang control	78
Figure 3.39 – dz/dt as a function of time, zoom of Figure 3.38.....	78
Figure 3.40 – Effect of V_{max} and T_{max} on propellant consumption of the vertical ascent manoeuvre	79
Figure 3.41 – Effect of V_{max} and T_{Xmax} on prop. consumption of the horiz. translation manoeuvre.....	81
Figure 3.42 – Effect of V_{max} and T_{max} on prop. consumption of the vertical descent manoeuvre.....	82
Figure 3.43 – Navigation system requirement	83
Figure 3.44 – Propellant consumption caused by navigation system requirement.....	84
Figure 3.45 – Propellant consumption of the Hor. Translation varying T_{12}	84
Figure 3.46 – Propellant consumption varying T_{12}	85
Figure 3.47 – Mass of the thruster as a function of the thrust magnitude.....	86
Figure 3.48 – Prop. consumption of ver. ascent and descent manoeuvres ($m_i = 15\text{ kg}$, $I_{sp} = 150\text{ s}$).....	87
Figure 3.49 – Mass of propellant and propulsion system as a function of thrust	88
Figure 3.50 – Illustration of the nominal trajectory of the LuNaDrone.....	89
Figure 3.51 – Flight profile simulation of the trajectory depicted in Figure 3.50.....	91
Figure 4.1 – Elements of the Electrical Power System	92
Figure 4.2 – Options for various mission power needs and duration.....	92
Figure 4.3 – Schematic of typical spacecraft power system block elements [22]	94
Figure 4.4 – Performance of Li-CFx D-cell at different discharge currents [26].....	102
Figure 4.5 – Performance of Li/CFX-MnO ₂ D-type cell at different temperatures [26].....	103
Figure 4.6 – Schematic of a hydrogen/oxygen fuel cell.....	105
Figure 4.7 – Functional Breakdown for the Spacecraft's Power Subsystem [32].....	107
Figure 4.8 – Specific energy at varying discharge current and operating temperature	109
Figure 4.9 – Li/CFX-MnO ₂ Primary Electrochemistry Rate-Optimized, High Energy Pouch Cell [33].....	110
Figure 5.1 – $h_1 = 50\text{ m}$, $I_{sp} = 150\text{ s}$, $m_0 = 15\text{ kg}$	111
Figure 5.2 – $h_1 = 50\text{ m}$, $I_{sp} = 150\text{ s}$, $m_0 = 15\text{ kg}$	112
Figure 5.3 – $h_1 = 50\text{ m}$, $I_{sp} = 150\text{ s}$, $m_0 = 15\text{ kg}$	112
Figure 5.4 – $h_1 = 50\text{ m}$, $I_{sp} = 150\text{ s}$, $m_0 = 15\text{ kg}$	113
Figure 5.5 – $h_1 = 50\text{ m}$, $I_{sp} = 150\text{ s}$, $m_0 = 15\text{ kg}$	113
Figure 5.6 – $h_1 = 50\text{ m}$, $I_{sp} = 150\text{ s}$, $m_0 = 15\text{ kg}$	114
Figure 5.7 – $h_1 = 50\text{ m}$, $I_{sp} = 150\text{ s}$, $m_0 = 15\text{ kg}$	114
Figure 5.8 – $h_1 = 100\text{ m}$, $I_{sp} = 150\text{ s}$, $m_0 = 15\text{ kg}$	115
Figure 5.9 – $h_1 = 100\text{ m}$, $I_{sp} = 150\text{ s}$, $m_0 = 15\text{ kg}$	116
Figure 5.10 – $h_1 = 500\text{ m}$, $I_{sp} = 150\text{ s}$, $m_0 = 15\text{ kg}$	116
Figure 5.11 – $h_1 = 500\text{ m}$, $I_{sp} = 150\text{ s}$, $m_0 = 15\text{ kg}$	117
Figure 5.12 – $h_1 = 1000\text{ m}$, $I_{sp} = 150\text{ s}$, $m_0 = 15\text{ kg}$	117
Figure 5.13 – $h_1 = 1000\text{ m}$, $I_{sp} = 150\text{ s}$, $m_0 = 15\text{ kg}$	118
Figure 5.14 – $h_1 = 50\text{ m}$, $I_{sp} = 150\text{ s}$, $m_0 = 10\text{ kg}$	118
Figure 5.15 – $h_1 = 50\text{ m}$, $I_{sp} = 150\text{ s}$, $m_0 = 10\text{ kg}$	119
Figure 5.16 – $h_1 = 100\text{ m}$, $I_{sp} = 150\text{ s}$, $m_0 = 10\text{ kg}$	119
Figure 5.17 – $h_1 = 100\text{ m}$, $I_{sp} = 150\text{ s}$, $m_0 = 10\text{ kg}$	120
Figure 5.18 – $h_1 = 500\text{ m}$, $I_{sp} = 150\text{ s}$, $m_0 = 10\text{ kg}$	120
Figure 5.19 – $h_1 = 500\text{ m}$, $I_{sp} = 150\text{ s}$, $m_0 = 10\text{ kg}$	121
Figure 5.20 – $h_1 = 1000\text{ m}$, $I_{sp} = 150\text{ s}$, $m_0 = 10\text{ kg}$	121
Figure 5.21 – $h_1 = 1000\text{ m}$, $I_{sp} = 150\text{ s}$, $m_0 = 10\text{ kg}$	122
Figure 5.22 – $h_1 = 50\text{ m}$, $I_{sp} = 150\text{ s}$, $m_0 = 20\text{ kg}$	122
Figure 5.23 – $h_1 = 50\text{ m}$, $I_{sp} = 150\text{ s}$, $m_0 = 20\text{ kg}$	123

Figure 5.24 – $h1 = 100\text{ m}$, $Isp = 150\text{ s}$, $m0 = 20\text{ kg}$	123
Figure 5.25 – $h1 = 100\text{ m}$, $Isp = 150\text{ s}$, $m0 = 20\text{ kg}$	124
Figure 5.26 – $h1 = 500\text{ m}$, $Isp = 150\text{ s}$, $m0 = 20\text{ kg}$	124
Figure 5.27 – $h1 = 500\text{ m}$, $Isp = 150\text{ s}$, $m0 = 20\text{ kg}$	125
Figure 5.28 – $h1 = 1000\text{ m}$, $Isp = 150\text{ s}$, $m0 = 20\text{ kg}$	125
Figure 5.29 – $h1 = 1000\text{ m}$, $Isp = 150\text{ s}$, $m0 = 20\text{ kg}$	126
Figure 6.1 – $h1 = 50\text{ m}$, $Isp = 150\text{ s}$, $m0 = 5\text{ kg}$	127
Figure 6.2 – $h1 = 50\text{ m}$, $Isp = 150\text{ s}$, $m0 = 10\text{ kg}$	128
Figure 6.3 – $h1 = 50\text{ m}$, $Isp = 150\text{ s}$, $m0 = 15\text{ kg}$	128
Figure 6.4 – $h1 = 50\text{ m}$, $Isp = 150\text{ s}$, $m0 = 20\text{ kg}$	129
Figure 6.5 – $h1 = 50\text{ m}$, $Isp = 150\text{ s}$, $m0 = 25\text{ kg}$	129
Figure 6.6 – $h1 = 50\text{ m}$, $Isp = 150\text{ s}$, $m0 = 30\text{ kg}$	130
Figure 6.7 – $h1 = 50\text{ m}$, $Isp = 150\text{ s}$, $m0 = 60\text{ kg}$	130
Figure 6.8 – $h1 = 50\text{ m}$, $Isp = 150\text{ s}$, $m0 = 120\text{ kg}$	131
Figure 7.1 – $h1 = 1\text{ m}$, $Isp = 150\text{ s}$, $m0 = 15\text{ kg}$	132
Figure 7.2 – $h1 = 10\text{ m}$, $Isp = 150\text{ s}$, $m0 = 15\text{ kg}$	133
Figure 7.3 – $h1 = 20\text{ m}$, $Isp = 150\text{ s}$, $m0 = 15\text{ kg}$	133
Figure 7.4 – $h1 = 50\text{ m}$, $Isp = 150\text{ s}$, $m0 = 15\text{ kg}$	134
Figure 7.5 – $h1 = 80\text{ m}$, $Isp = 150\text{ s}$, $m0 = 15\text{ kg}$	134
Figure 7.6 – $h1 = 500\text{ m}$, $Isp = 150\text{ s}$, $m0 = 15\text{ kg}$	135
Figure 7.7 – $h1 = 1000\text{ m}$, $Isp = 150\text{ s}$, $m0 = 15\text{ kg}$	135
Figure 7.8 – $h1 = 2000\text{ m}$, $Isp = 150\text{ s}$, $m0 = 15\text{ kg}$	136
Figure 8.1 – $h1 = 50\text{ m}$, $Isp = 2\text{ s}$, $m0 = 15\text{ kg}$	137
Figure 8.2 – $h1 = 50\text{ m}$, $Isp = 10\text{ s}$, $m0 = 15\text{ kg}$	138
Figure 8.3 – $h1 = 50\text{ m}$, $Isp = 50\text{ s}$, $m0 = 15\text{ kg}$	138
Figure 8.4 – $h1 = 50\text{ m}$, $Isp = 250\text{ s}$, $m0 = 15\text{ kg}$	139
Figure 8.5 – $h1 = 50\text{ m}$, $Isp = 150\text{ s}$, $m0 = 15\text{ kg}$	139
Figure 8.6 – $h1 = 50\text{ m}$, $Isp = 500\text{ s}$, $m0 = 15\text{ kg}$	140
Figure 9.1 – $h1 = 100\text{ m}$, $Isp = 150\text{ s}$, $m0 = 15\text{ kg}$ black · $m \neq cost$ mag. · $m = cost$	141
Figure 9.2 – $h1 = 100\text{ m}$, $Isp = 150\text{ s}$, $m0 = 15\text{ kg}$ black · $m \neq cost$ mag. · $m = cost$	142
Figure 9.3 – $h1 = 100\text{ m}$, $Isp = 150\text{ s}$, $m0 = 15\text{ kg}$ black · $m \neq cost$ mag. · $m = cost$	142
Figure 9.4 – $h1 = 100\text{ m}$, $Isp = 10\text{ s}$, $m0 = 5\text{ kg}$ black · $m \neq cost$ mag. · $m = cost$	143
Figure 9.5 – $h1 = 100\text{ m}$, $Isp = 10\text{ s}$, $m0 = 5\text{ kg}$ black · $m \neq cost$ mag. · $m = cost$	143
Figure 9.6 – $h1 = 100\text{ m}$, $Isp = 10\text{ s}$, $m0 = 5\text{ kg}$ black · $m \neq cost$ mag. · $m = cost$	144
Figure 9.7 – $h1 = 100\text{ m}$, $Isp = 10\text{ s}$, $m0 = 5\text{ kg}$ black · $m \neq cost$ mag. · $m = cost$	144
Figure 9.8 – $h1 = 100\text{ m}$, $Isp = 10\text{ s}$, $m0 = 5\text{ kg}$ black · $m \neq cost$ mag. · $m = cost$	145
Figure 9.9 – $h1 = 100\text{ m}$, $Isp = 10\text{ s}$, $m0 = 1\text{ kg}$ black · $m \neq cost$ mag. · $m = cost$	145
Figure 9.10 – $h1 = 100\text{ m}$, $Isp = 10\text{ s}$, $m0 = 5\text{ kg}$ black · $m \neq cost$ mag. · $m = cost$	146
Figure 9.11 – y-axis: a x-axis: t $T0B = 50\text{ N}$, $TB = 60\text{ N}$, $m0 = 5\text{ kg}$, $Isp = 10\text{ s}$, $h1 = 100\text{ m}$	146
Figure 9.12 – y-axis: a x-axis: t $T0B = 50\text{ N}$, $TB = 60\text{ N}$, $m0 = 15\text{ kg}$, $Isp = 150\text{ s}$, $h1 = 100\text{ m}$	147
Figure 9.13 – y-axis: a x-axis: t $T0B = 25\text{ N}$, $TB = 10\text{ N}$, $m0 = 15\text{ kg}$, $Isp = 150\text{ s}$, $h1 = 100\text{ m}$	147
Figure 10.1 – Horizontal translation: $mprop = fT12, V12max$ with $d12 = 1\text{ m}$	148
Figure 10.2 – Horizontal translation: $mprop = fT12, V12max$ with $d12 = 1\text{ m}$	149
Figure 10.3 – Horizontal translation: $mprop = fT12, V12max$ with $d12 = 50\text{ m}$	149
Figure 10.4 – Horizontal translation: $mprop = fT12, V12max$ with $d12 = 50\text{ m}$	150
Figure 10.5 – Horizontal translation: $mprop = fT12, V12max$ with $d12 = 150\text{ m}$	150
Figure 10.6 – Horizontal translation: $mprop = fT12, V12max$ with $d12 = 150\text{ m}$	151

Figures

<i>Figure 10.7 – Horizontal translation: $m_{prop} = f_{T12, V12max}$ with $d_{12} = 300m$</i>	<i>151</i>
<i>Figure 10.8 – Horizontal translation: $m_{prop} = f_{T12, V12max}$ with $d_{12} = 300m$</i>	<i>152</i>

Tables

<i>Table 1.1 – High resolution imaging confirms existence of cavernous lunar sub-surfaces [8]</i>	2
<i>Table 2.1 – Mission requirements</i>	8
<i>Table 2.2 – Mission contingencies</i>	10
<i>Table 2.3 – Main characteristics of the current configuration of the spacecraft</i>	10
<i>Table 2.4 – Part numbers</i>	11
<i>Table 3.1 – Summary of vertical ascent manoeuvre (without braking thrust)</i>	21
<i>Table 3.2 – Summary of the values obtained in Annex 01 for the “full throttle” cases</i>	29
<i>Table 3.3 – Summary of the vertical ascent manoeuvre (with braking thrust)</i>	32
<i>Table 3.4 – Summary of horizontal translation manoeuvre</i>	48
<i>Table 3.5 – Summary of vertical descent manoeuvre</i>	63
<i>Table 3.6 – Coordinates of the points shown in Figure 3.50 with respect to the inertial reference frame</i>	89
<i>Table 3.7 – Propellant masses and manoeuvre times of the flight profile presented in Figure 3.51</i>	90
<i>Table 3.8 – Percentages of propellant consumption and manoeuvring time</i>	90
<i>Table 4.1 – RTG system performance</i>	97
<i>Table 4.2 – Primary Cells Used in Shuttle Missions [21]</i>	99
<i>Table 4.3 – Zinc Anode Primary Cell Characteristics [21]</i>	99
<i>Table 4.4 – State of Practice of Primary Batteries [27]</i>	100
<i>Table 4.5 – Characteristics of SOP Primary Batteries Used in PSD Missions [29]</i>	101
<i>Table 4.6 – Battery level performance of Lithium Primary Batteries [29]</i>	103
<i>Table 4.7 – Performance summary of fuel cells for space use [22]</i>	105
<i>Table 4.8 – Summary of primary cells for space applications</i>	108
<i>Table 4.9 – Technical characteristics of the navigation system components</i>	109

Nomenclature

a	Acceleration of the spacecraft with respect to the inertial reference frame
A_t	Throat area of the nozzle
c	Effective exhaust velocity
C_F	Thrust coefficient
d_{12}	Distance between point 1 and point 2
g_0	Standard sea level Earth gravitational acceleration
g	Moon's gravitational field strength
h_1	Altitude of point 1
I_{sp}	Specific impulse
m	Spacecraft total mass
m_p	Propellant mass
\dot{m}_p	Propellant mass flow
p_c	Chamber pressure
t	Time
t_f	Final time
t_i	Initial time
T	Thrust
T_{avg}	Average thrust
T_{max}	Maximum continuous thrust
T_{nom}	Nominal thrust value
V	Velocity of the spacecraft with respect to the inertial reference frame
V_{avg}	Average velocity
X, Y, Z	Axis of the inertial reference frame
x, y, z	Axis of the vehicle reference frame
α	Angle between T and V
φ	Angle between V and X -axis
θ	Pitch angle
Δt_h	Time frame of the hovering manoeuvre
ΔV	Velocity increment of the spacecraft
$\Delta V_{gravity}$	Velocity increment induced by gravity
ΔV_{prop}	Ideal velocity increment
CLPS	Commercial Lunar Payload Services
ConOps	Concept of Operations
DC	Duty Cycle
EPS	Electrical Power System
ESA	European Space Agency
FOV	Field of View
GN&C	Guidance Navigation and Control
GRAIL	Gravity Recovery and Interior Laboratory
JAXA	Japan Aerospace Exploration Agency

LOS	Line of Sight
LRO	Lunar Reconnaissance Orbiter
LuNaDrone	Lunar Nano Drone
NASA	National Aeronautics and Space Administration
PWM	Pulse Width Modulation
SELENE	Selenological and Engineering Explorer
SLIM	Smart Lander for Investigating Moon
SME	Small and Medium Enterprises
SOP	State of Practice
T4i	Technology for propulsion and innovation S.P.A.
TCS	Thermal Control System
TBC	To be Confirmed
TBD	To be Defined
TMC	Thrust Magnitude Control
VIPER	Volatiles Investigating Polar Exploration Rover

1 Context and objectives of the study

1.1 Mission statement and objectives

Mission statement:

“To design a flying drone able to autonomously hover inside a lava tube entering a skylight, taking photos and mapping the internal surface. The concept of the drone is based on the strategic idea already experienced with Cubesats: small spacecraft, low mass and cost, standardised, affordable by Academies and SME’s and easy to deliver in Space”

The primary and secondary objectives of the mission have been deduced from the mission statement and are:

Primary objectives:

- To design an autonomously flying drone
- To explore and photograph lava tubes

Secondary objectives:

- To map the interior of lava tubes
- To develop a low cost and low mass drone concept to be standardised

1.2 Observational evidence and characteristics of lunar lava tubes

The chance for the actual existence of lunar lava tubes was postulated during the early 1960's. In 1971, a study concerning the possible presence of lava tubes in the Marius Hills region was published, with the evidence of rilles on the surface [1].

In 2009, the 10 m–resolution images taken by the Terrain Camera (TC) aboard SELENE (nicknamed Kaguya) showed three huge vertical holes in the lunar Marius Hills, Mare Tranquillitatis and Mare Ingenii. The holes have aperture diameters and depths of several tens of metres to one hundred metres [2]. Haruyama et al. (2009) [3] hypothesised that they are possible “skylights” opened on subsurface caverns such as lava tubes.

In 2010, NASA’s Lunar Reconnaissance Orbiter (LRO) photographed the skylight in the Marius Hills in more detail, showing both the 65-metre-wide pit and the floor of the pit about 36 metres below [4]. The LRO has also imaged over 200 pits that show the signature of being skylights into subsurface voids or caverns, ranging in diameter from about 5 m (16 ft) to more than 900 m (3,000 ft), although some of these are likely to be post-flow features rather than volcanic skylights [5]. Figure 1.3 shows some examples.

In 2011, NASA launched GRAIL, whose purpose was to evaluate the gravity field of the Moon in order to detect its internal structure. It also made it possible to confirm the presence of lava tubes underneath the surface. To this purpose, a skylight of 65 metres in diameter and 80-85 metres deep, with a roof thickness of 20-25 metres has been proven to exist. It is located in the Marius Hills region and occurs in a shallow rille-like trough about 400 metres wide and 300-400 metres deep. It is expected to hide a large cavern beneath the visible surface that extends about 60 km to the west of the skylight, where the cavern itself is approximately 30 km in length [6].

Again in 2011, a study conducted on Chandrayaan-1's observations, an Indian lunar spacecraft, showed a buried, un-collapsed and near horizontal lava tube in the vicinity of Rima Galilaei [7].

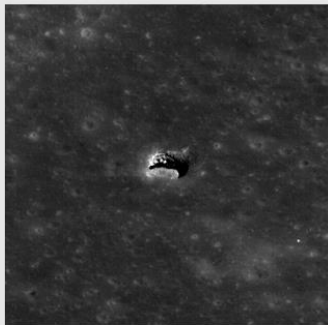
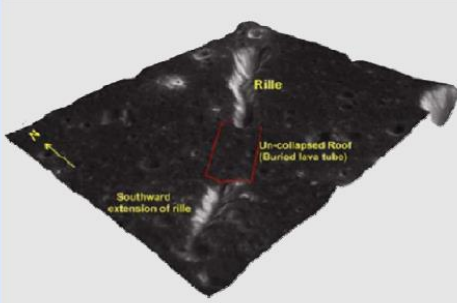
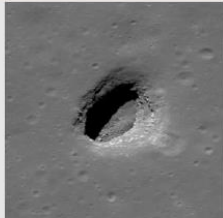

Recently Discovered Lunar Pits and Tubes	
 <p>Marius Hills Skylight</p> <ul style="list-style-type: none"> • 14.09 deg. N. 303.31 deg. E. • 45 m deep • 48 m to 57 m diameter 	 <p>Chandrayaan-1 Lava Tube</p> <ul style="list-style-type: none"> • North of Rima Galilaie, region of Oceanus Procellarum • 1.72 km length (un-collapsed section) • Tube diameter estimated at 120 m (Rille depth is ~85 m)
 <p>Mare Ingenii Pit</p> <ul style="list-style-type: none"> • 35.95 deg. S. 166.06 deg. E. (Far Side) • 101 m x 66 m wide with a depth of ~60 m • SSE side of pit wall slopes ~45 deg. 	 <p>Mare Tranquillitatis Pit</p> <ul style="list-style-type: none"> • 8.34 deg. N. 33.22 deg. E. • 84 m to 99 m diameter • 107 m deep

Table 1.1 – High resolution imaging confirms existence of cavernous lunar sub-surfaces [8]

A remnant of the volcanic tube, whose roof has capsized and created a valley is named a “rille”. It may happen that the roofs of such tubes do not collapse and remain intact, with a hollow interior in most cases. A skylight is a lava tube ceiling collapse potentially providing a means of entrance into the tunnel. Figure 1.1 illustrates typical entrance possibilities which may be encountered for the pits and tubes identified in Table 1.1. More details about Mare Tranquillitatis Pit are reported in Figure 1.2.

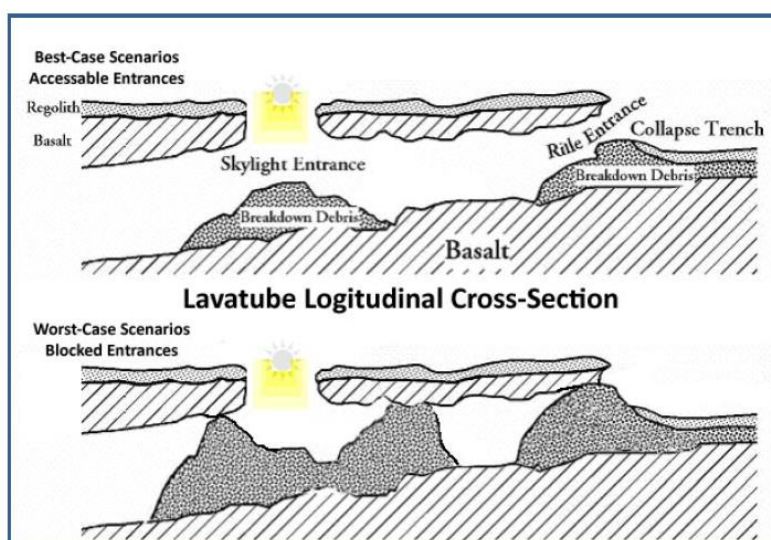


Figure 1.1 – Potential entrance outcomes from observed pits and rilles

Scientifically speaking, to map the distribution and age of bedrock at the surface, investigations for understanding the geological processes associated with ancient lunar basaltic lava flows are needed.

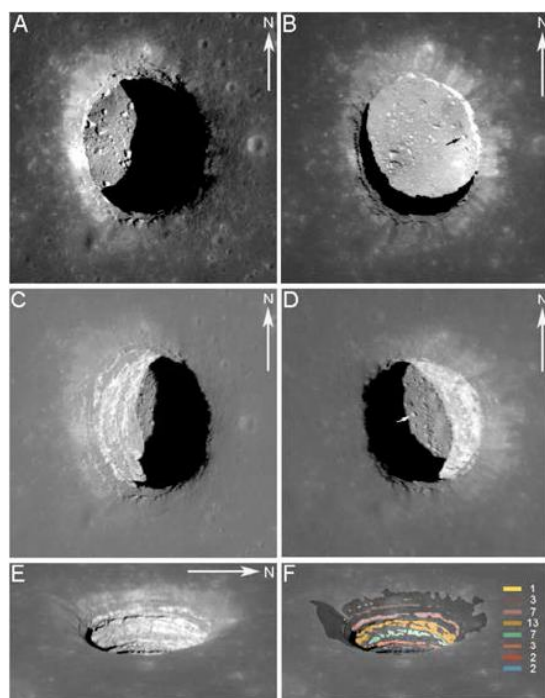


Figure 1.2 – Mare Tranquillitatis Pit [9]

Figure 1.2: (A, B) Mare Tranquillitatis Pit in two near nadir images with opposite Sun azimuth angles, both images are approximately 175 m wide. Oblique views: (C) layering in west wall and a portion of pit floor beneath overhanging mare (29° ema); (D) A significant portion of the illuminated area is beneath the eastern overhanging mare in this image (26° ema), white arrow indicates same boulder marked with black arrow in B. Detailed layering is revealed in (E) and (F). Outcropping bedrock layer thickness estimates are presented in (F) in metres, $\pm 1\text{m}$

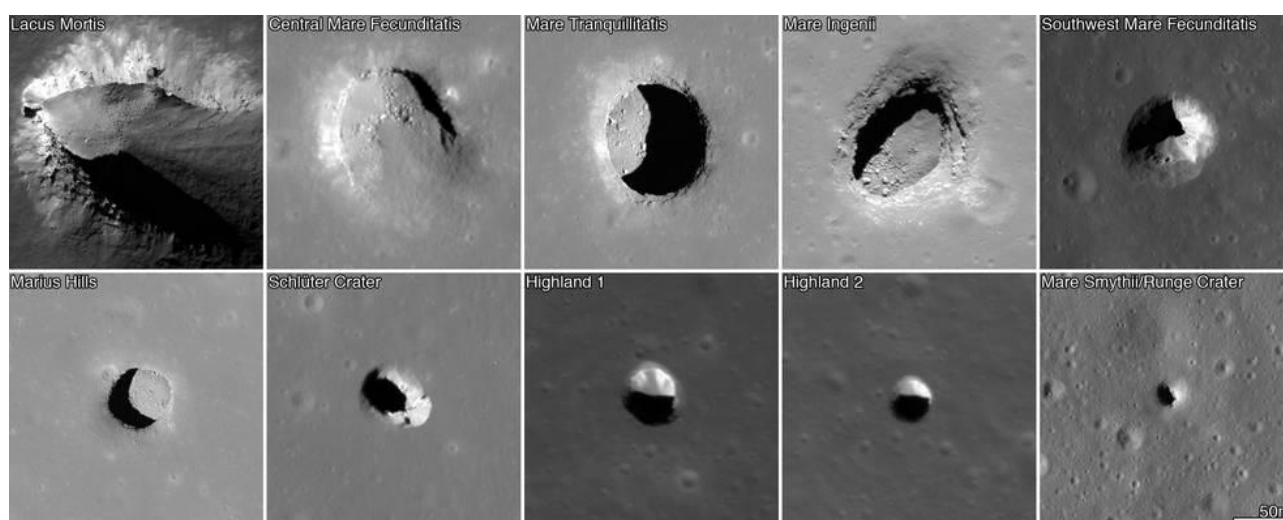


Figure 1.3 – The known mare pits and highland pits [10]

Figure 1.3: these images from NASA's LRO spacecraft show all of the known mare pits and highland pits. Each image is 222 metres wide.

Lava tubes tend to have smooth floors, with possible “soda straws” stalactites formed by lava dipping from the ceiling. Due to the lesser gravity, lava tubes on the Moon may be much larger in diameter than those found on Earth [11]. These caverns would be suitable for human habitation, because they could provide safety from hazardous radiations, micro-meteoritic impacts, extreme temperatures and dust. However, polar regions are interesting as well, because they appear to have abundant ice water. According to a new discovery presented at NASA’s Lunar Science for Landed Missions Workshop, it appears that there is a location on the Moon that merges both aspects: a possible lava tube that is located in the northern polar region (Philolaus Crater) [12].

For what concerns radiation protection, the thickness of the roof of the caves is expected to be tens of metres [7], that would certainly be advantageous, but, on the other hand, it would represent an obstacle for the design of a communication system between the inside of these caves and the surface.

On the surface of the Moon the fluctuations of the temperature are extremely wide, whereas the interior of the caves is expected to maintain an almost constant temperature around -20°C . As a result, this aspect would greatly ease the design of the thermal control system of all those devices that would operate in this environment.

1.3 State-of-the-art of mission concepts

Mission architecture usually includes the number of robotic entities and their roles (i.e. probes, landers...), their approximate mass (which has implications on the traditional space mission architecture components of launch vehicle and trajectory), the methods of communication, the power strategies employed, and the concept of operations. Multi-mission architectures are also possibilities for skylight and cave exploration. One such multi-mission architecture would be broken into three phases, the first phase being the flyover and surface investigation of a skylight and deployment of a sensor package to a skylight entrance. The second phase could send mobile robots in to explore lava tubes or cave network. The third phase could include deliver of habitats, robots and personnel with specialized scientific instruments. A reference set of mission goals can be defined in order to compare mission architectures. Those goals are to enter a lava tube cave via skylight, to explore it and to send data [11].

1.4 Challenges

From several tests on Earth, it is known that ground penetrating radar often fails to detect lava tubes especially if the lava was deposited in multiple flows. This is because of the partial reflection of the radar at interfaces between layers of material, caused by repeated lava flows.

From a scientific perspective, in many cases it may be sufficient to get beyond the “twilight zone” (the transition between areas illuminated for some period during the day and areas of constant darkness) to define the distance to be travelled inside a cave. This region is likely to be indicative of the variation of different significative parametres, such as potential to support life, volatile contents and geological features, impacted by sunlight, temperature variations or rock fall during skylight formation.

Moreover, some scientists believe that using propulsive vehicles may lead to possible problems, such as the contamination of volatiles trapped at the bottom of a skylight or even the death of living organisms inside a cave. Additionally, there may be the possibility of contaminating scientifically important sites with that strategy.

The main issues to cope for planetary cave exploration are:

- access to the cave
- in-cave mobility
- data collection and processing
- power sources
- communication

Spacecraft configuration has a large impact on how these issues have to be managed. As an example, the lack of solar power underground may put large limitations on how the spacecraft could move. Energetically, it does not make sense to carry the propulsion system required for landing along for further cave explorations activities. Tethered solutions may also be considered.

Note that modelling in lava tubes requires active sensing and due to the expected larger size of lava tubes on the Moon, sensors in this environment must have long range, which requires increased power. To this purpose, technologies like active sensing could provide a physical barrier to miniaturization [11].

1.5 Summary

Hybrid propulsive configurations may be considered. External tethered lighting or power source systems may also be considered. Wireless power and data transmission within line of sight of the tethered communication node would eliminate the need for exploration robot to physically reach it, which is critical in unpredictable environments. Combination of active sensing (good for shadowed regions but lower resolution and range limited by power) and cameras (higher resolution but unable to determine 3D scale) required to build sufficiently detailed models for science and robot operations. Commercial magneto-inductive communications system indicates an achievable data rate of 2412bps through rock. Magneto-inductive comm requires a large and heavy antenna. While it is a great technology for later use in cave operations, it may not be feasible for the first, lightweight robotic explorers [11].

For what concerns power and communication, extended periods without access to solar power, limited accessibility to communication and operating exclusively in a dark environment have to be taken into account. High energy density batteries would enable longer cave excursions with low battery masses [11].

Limited data link through rock can be achieved with very low-frequency radio or magneto-inductive comm. These technologies are under development terrestrially for cave and mining communication and rescue and have undergone significant advances in mass and power requirements over the past few years [11].

1.6 Possible supporting missions

Moon exploration will gain more and more interest in the next few years. To this purpose, many different companies are developing new landers and rovers to be launched. The study in this document is based on the idea that LuNaDrone will have to be carried to the proximity of an above-mentioned skylight by one of them. For instance, JAXA's lander named SLIM (Smart Lander for Investigating Moon), whose departure is planned for January 2022, will land in the vicinity of Marius Hills Hole, with an accuracy of about 100 metres, next to a lava tube [13].

It would also be reasonable to take into consideration NASA's CLPS (Commercial Lunar Payload Services), an initiative which allows rapid acquisition of lunar delivery services from American companies for payloads that advance capabilities for science, exploration or commercial development of the Moon. Investigations and demonstrations launched on commercial Moon flights will help the agency study Earth's nearest neighbour under the Artemis program. Moreover, NASA has identified agencies and external science payloads that will fly on future CLPS missions, including the Volatiles Investigating Polar Exploration Rover (VIPER). Future payloads could include other rovers, power sources, and science experiments, including the technology demonstrations to be infused into the Artemis program [14]. NASA has chosen Astrobotic, Intuitive Machine and Masten to take part to CLPS programme.

Finally, Hakuto-R is the program name for iSpace's first two lunar missions, a commercial initiative with the purpose to demonstrate the capability to softly land and release a rover. It will lead to various subsequent high-frequency, cost-effective missions to establish a payload delivery system to the Moon [15].

2 LuNaDrone mission design

2.1 Mission overview

The mission concept is based on the assumption that a lander and/or a rover would deploy LuNaDrone in the proximity of a selected skylight, at a maximum distance of TBD metres from the waypoint from which the vertical descent phase will start. That distance shall be later in subsequent iterations decided according to the physical dimensions of the crater to be explored and the performances/architecture of the spacecraft.

After the deployment, LuNaDrone shall be able to conduct at least one autonomous flight. It consists of different phases: take off, climb, hover, horizontally translate to reach the skylight, descend into the lunar pit and come back to the initial point following the same trajectory.

Because landing hazard avoidance was not prioritized, the flight will start and end within an area to be pre-inspected and determined to be safe in terms of obstacles and ground slope.

While hovering, LuNaDrone has to be able to deal with disturbance of the flight and maintain its stability. In addition, a plan about when and how to implement the acquisition of the images has to be carefully developed. During the acquisition, LuNaDrone would need to enlighten the subject.

LuNaDrone has to be able to either store and/or forward the images to the rover/lander.

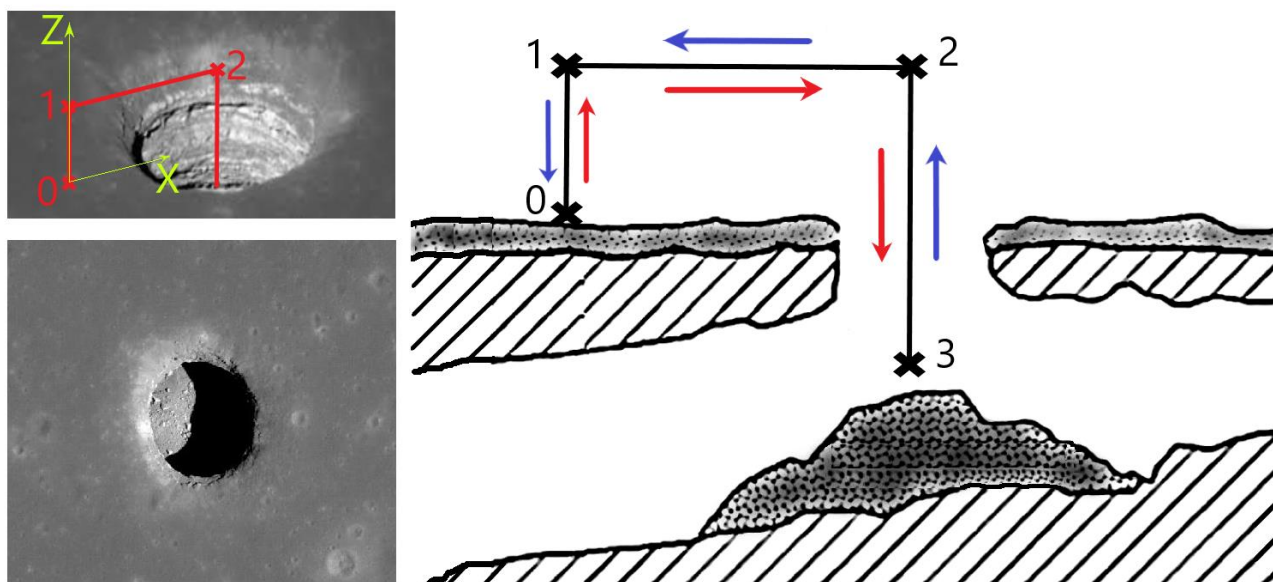


Figure 2.1 – Illustration of the flight segments

A possible flight of LuNaDrone might be the one shown in Figure 2.1. The first step, identified by the numbers 0-1, refers to a vertical ascent manoeuvre in which the spacecraft rises from the lunar surface and reaches a predetermined altitude. It will then follow the horizontal translation manoeuvre, where the spacecraft will cover a certain distance along the X-axis without changing its altitude. The last manoeuvre, identified by the

numbers 2-3, refers to the descent segment where the spacecraft will decrease its altitude until it stops at point 3. It is assumed that LuNaDrone will reach points 1, 2 and 3 with zero residual velocity and, if required, it will have to hover at these points for a predetermined time frame before moving on to the next flight segment. After acquiring the photos of the inside of the lunar pit, LuNaDrone will have to come back to the initial point, following the same trajectory.

Code	Functional and Performance Requirements
R1	The LuNaDrone shall be able to autonomously depart from the surface of a rover, hover, enter in a target Lunar Cave and exit at the end of the mission returning to the rover (TBC)
R2	The LuNaDrone shall be equipped with a propulsion system able to support the entire mission
R3	The LuNaDrone shall be able to withstand a travel time of at least TBC min
R4	The LuNaDrone shall be able to withstand a travel distance of at least TBC Km
R5	The LuNaDrone shall be able to take images of the Cave, store them on-board and transmit them to the Rover and/or Lander at the end of the mission or as soon as possible (TBC)
R6	The LuNaDrone wet mass shall be less than 15 Kg (TBC)
R7	The volume of the LuNaDrone shall be less than 30 X 20 X 20 (TBC) cm while in stowage in the ROVER
	Interface Requirements
R8	The LuNaDrone vehicle shall be able to autonomously depart from the surface of a rover, hover and return to its base on top of the rover.
	Environmental Requirements
R9	The LuNaDrone shall be able to withstand environment (day/night) of the Moon site and Moon Cave (TBC)
R10	The LuNaDrone shall be able to withstand the launch and transport to the Moon environment in stowed conditions (TBC)
	Operational Requirements
R11	The LuNaDrone shall be able to take pictures in visual wavelengths (TBC).
R12	The LuNaDrone shall be able to fly autonomously by means of a pre-programmed flight sequence
	Implementation requirements
R13	The LuNaDrone shall make use of non-toxic propellants that are safe to handle on ground
R14	The LuNaDrone functional simulator shall be able to show the vehicle functional architecture and simulate the mission
R15	The LuNaDrone 3D-printed scaled model shall be able to show the vehicle physical architecture and the technology critical components

Table 2.1 – Mission requirements

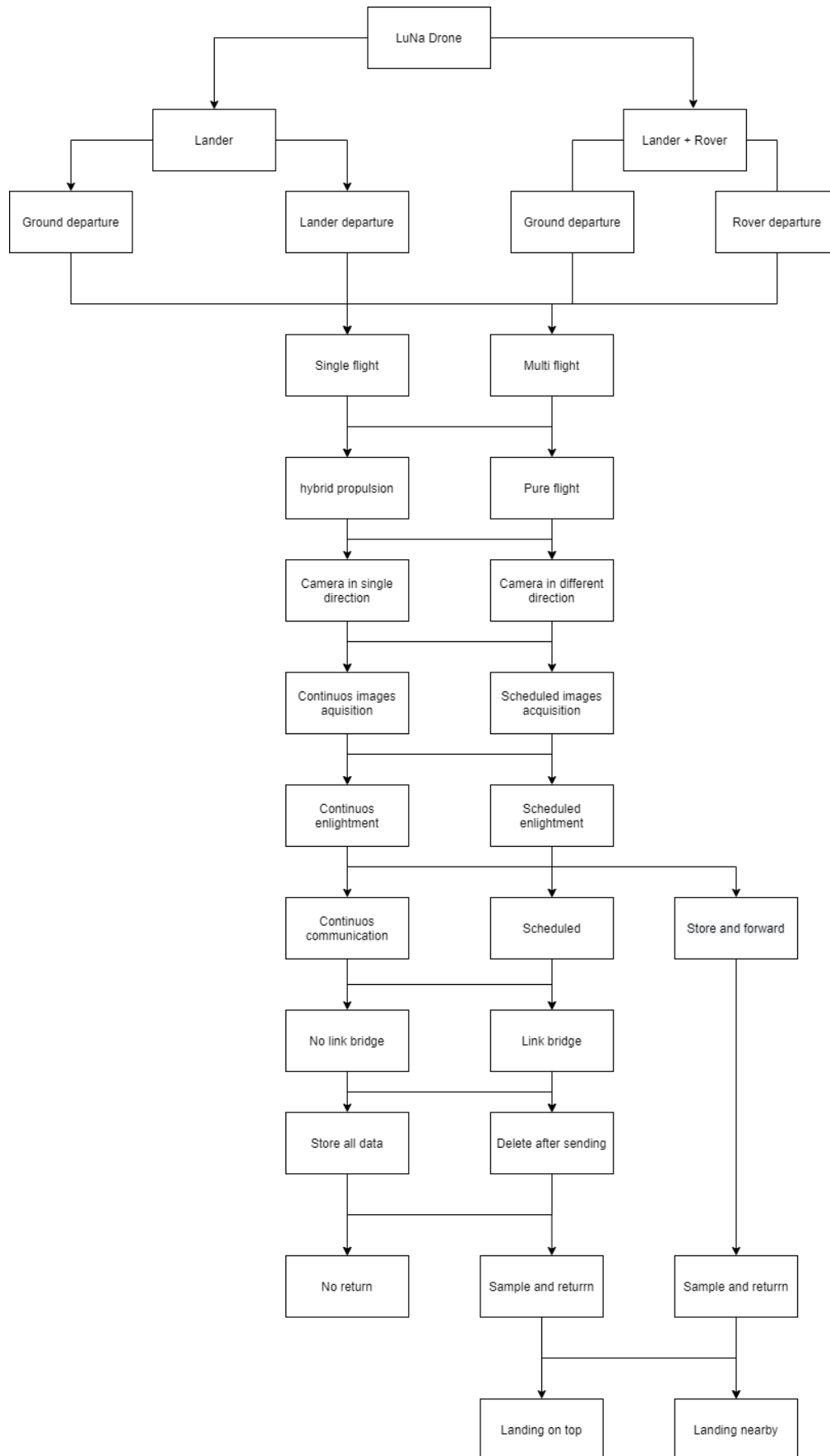


Figure 2.2 – Brainstorming on the possible scenarios of the mission

ID	Subject	Mission contingencies
MC-001	Lander	The lander must land no more than TBD meters from the skylight.
	Lander + rover	The rover must be able to approach at least TBD meters from the skylight.
MC-002	Ground departure	The LuNaDrone will first be released to the lunar surface and then take off.
	Rover/Lander departure	The LuNaDrone will take off directly from the lander/rover
MC-003	Continuous communication	The LuNaDrone must be able to communicate continuously.
	Scheduled communication	The LuNaDrone has to communicate only when necessary
MC-004	Store and forward	The LuNaDrone will communicate mission data once it emerges from the lava tube.
	Sample and return	The LuNaDrone will be able to return to the lander/rover.
MC-005	No return	The LuNaDrone will not necessarily be able to return to the lander/rover.
	Flight	The LuNaDrone must be able to explore the hole by flying.
MC-006	Hybrid propulsion	In addition to flying, the LuNaDrone must be able to move on the surface with a more efficient propulsion.
	Landing on top of the lander/rover	The LuNaDrone must be able to land on top of the lander/rover.
MC-007	Landing nearby	The LuNaDrone must be able to land at a maximum distance of TBD meters from the lander/rover.
	NO link bridge	The LuNaDrone shall be able to communicate without LOS through the rocks
MC-008	Link bridge TBD	The LuNaDrone shall be able to communicate in LOS with a TBD link bridge
	Camera/cameras in single direction	The LuNaDrone shall be able to take images only towards its movement
MC-009	Camera/cameras in different directions	The LuNaDrone shall be able to take images in all/different directions
	Single flight approach	The LuNaDrone shall depart only once, do its operations and land only once.
MC-010	Multi-phase flight approach	The LuNaDrone shall depart and land TBD times, with scheduled and programmed acquisition plan.
	Store all data	The LuNaDrone shall be equipped with sufficient memory to save all the mission data
MC-011	Delete stored data after sending	The LuNaDrone shall not preserve data after sending
	Continuous images acquisition	The LuNaDrone shall continuously use cameras
MC-012	Scheduled images acquisition	The LuNaDrone shall use cameras following a predicted plan
	Continuous enlightenment	The LuNaDrone shall continuously enlight its way for the cameras
	Scheduled enlightenment	The LuNaDrone shall enlight following cameras needs

Table 2.2 – Mission contingencies

2.2 Spacecraft overview

The main objective of the mission is to acquire images of the inside of lava tubes on the Moon. At this purpose, the system of cameras which will be designed and utilized is of fundamental importance. In particular, the number of cameras, their resolution and their positioning will have to be discussed in order to find the best solution in terms of mass, volume and compatibility with the other subsystems. The propulsion system includes one hydrogen peroxide monopropellant rocket as main engine and at least other eight for the ACS. The spacecraft will obtain its necessary electrical power from lithium primary batteries. The above-mentioned subsystems are strongly linked to the flight profile development, which can state how efficient a manoeuvre is and the angle of inclination of the spacecraft for its movements, which in turn gives information again to the navigation and propulsion systems design.

Subsystem/component	Type
Navigation	IMU+Visual Navigation, IMU+LiDARs
Image acquisition	One 12 Mpx camera, 120° FOV, 15 fps
Propulsion	Hydrogen peroxide 92% wt monopropellant rockets
Electrical power source	Lithium primary batteries
CommSys	X-band 8 GHz, 40-50 Mbit/s

Table 2.3 –Main characteristics of the current configuration of the spacecraft

The drafting of Chapter 1 and Chapter 2 was carried out in collaboration with two colleagues from Politecnico di Torino: Gabriele Podestà [16] and Gael Latiro [17], who were respectively responsible for developing the propulsion and navigation system of the spacecraft.

Here below some images of the current configuration are presented. They do not represent a complete spacecraft and no detailed analysis for the compatibility of the subsystems have been carried out. The purpose of these images is to give a rough idea of how the room inside the spacecraft may be utilised, considering the requirements of the different components (e.g. the necessity of the LiDARs to have nothing to hinder their view).

Number	Component
1	LiDAR – 360° horizontal plane
2	Propellant tank
3	IMU
4	Lithium primary D-cells
5	OBC
6	LiDAR – vertical plane
7	LED + optics
8	Camera + optics
9	ACS thrusters
10	Pressurant tank
11	Engine

Table 2.4 – Part numbers

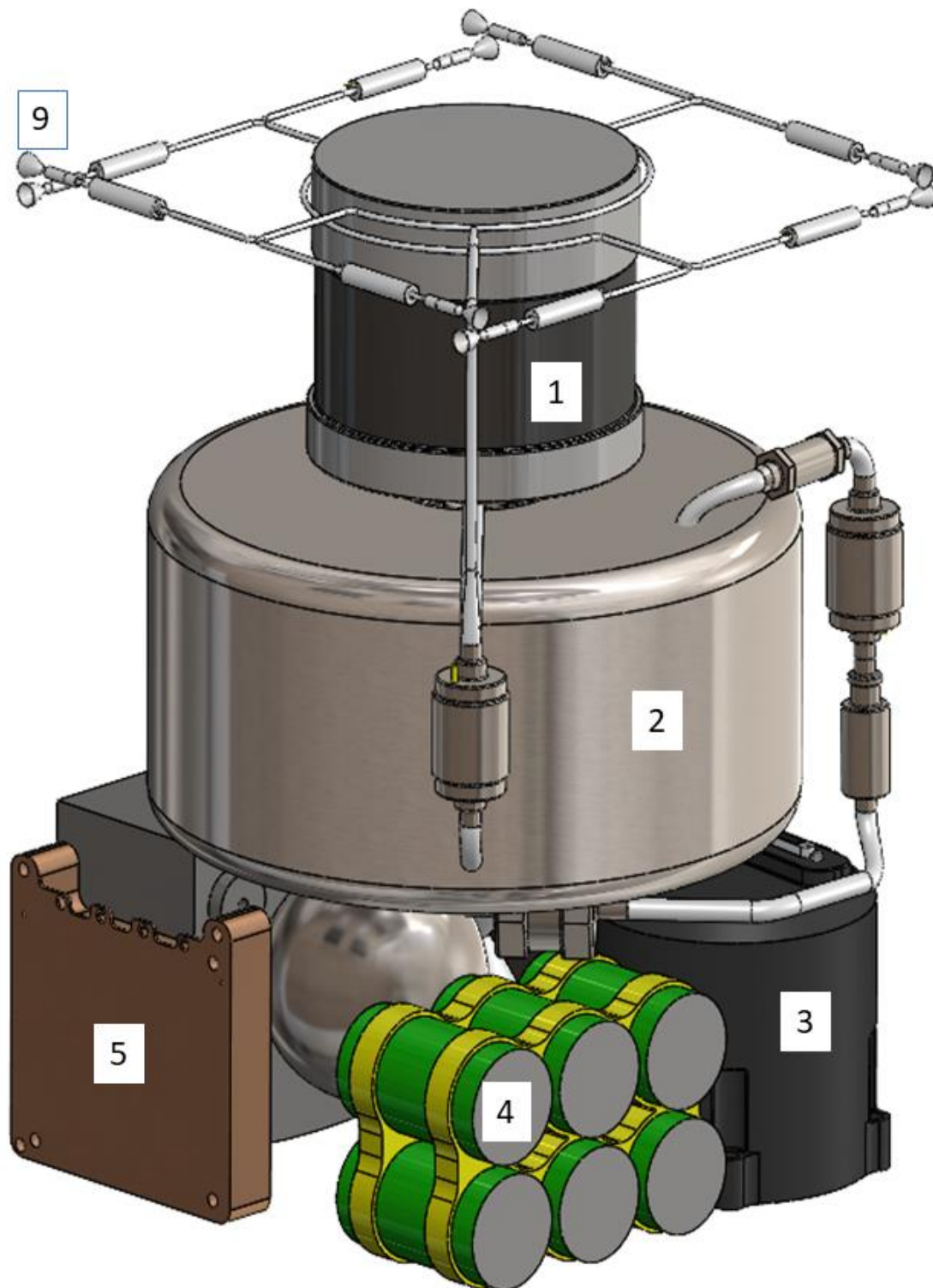


Figure 2.3 – Side view #1 of the current configuration of LuNaDrone

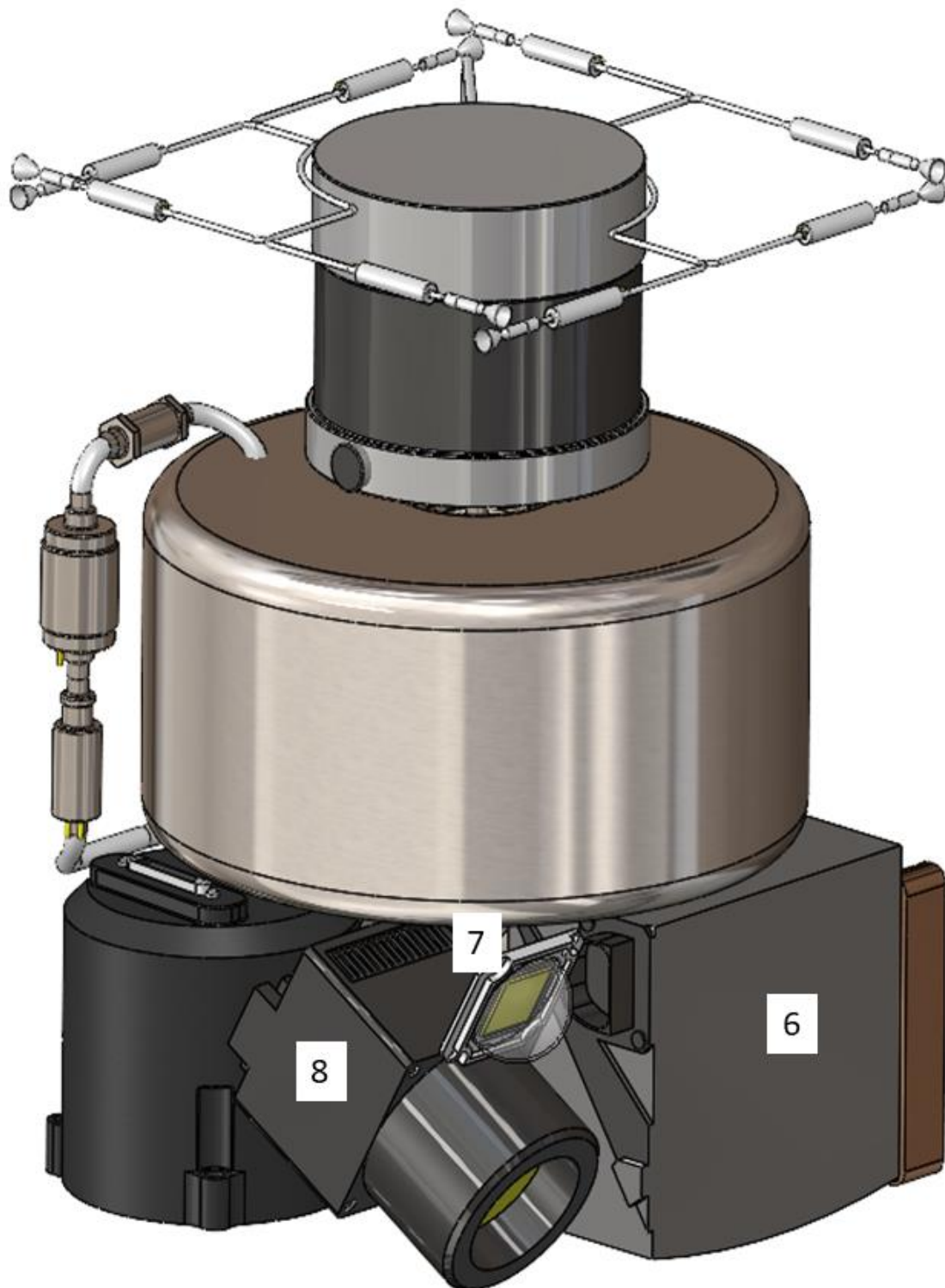


Figure 2.4 – Side view #2 of the current configuration of LuNaDrone

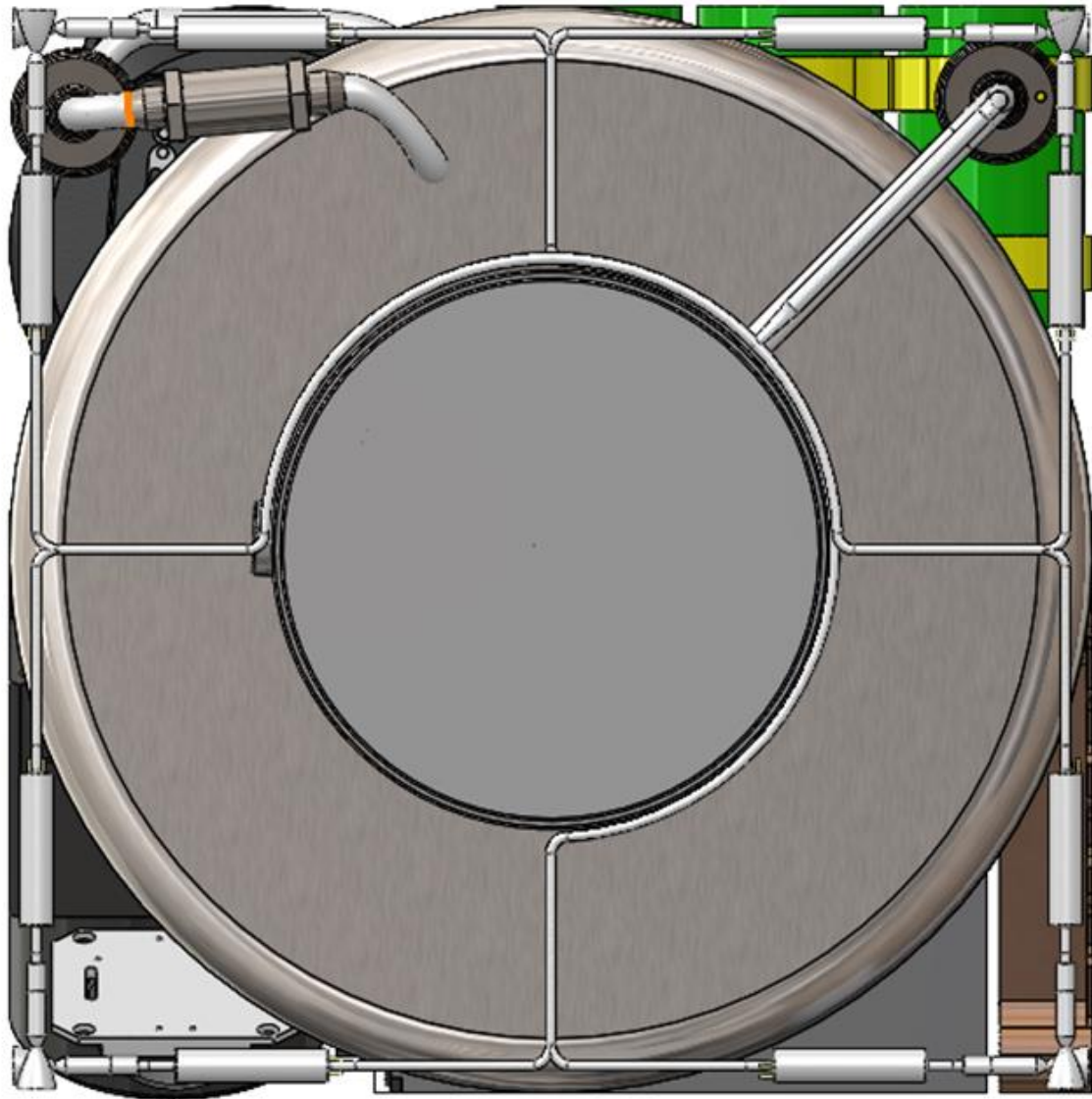


Figure 2.5 – Top view of the current configuration of LuNaDrone

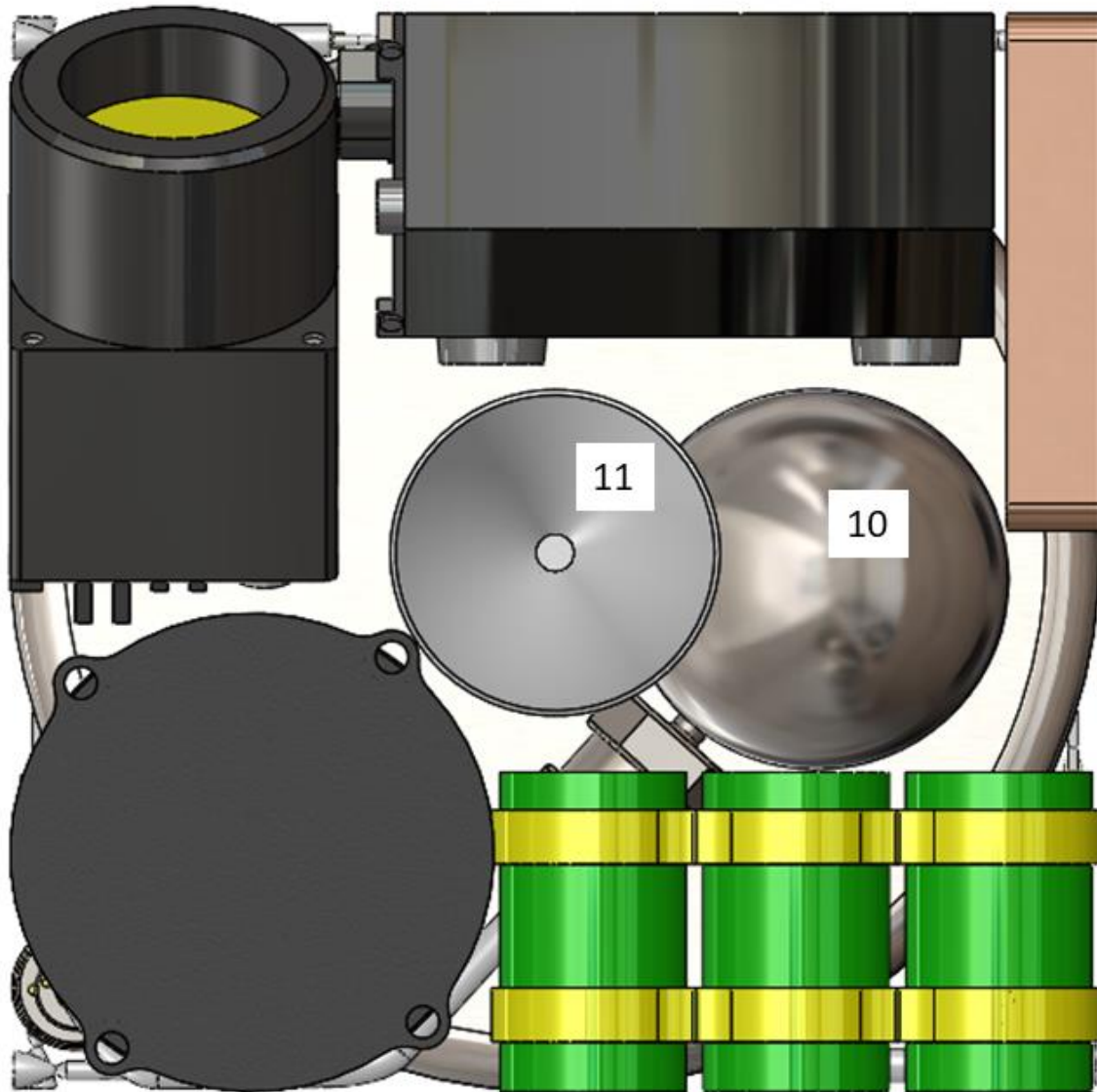


Figure 2.6 – Bottom view of the current configuration of LuNaDrone

3 Flight Profile

The main goal of this section is to develop a physical model (using the MATLAB/Simulink environment) to simulate the most significant phases of the flight that LuNaDrone will have to perform during its mission. Before I explain the structure of such a model, I would like to specify why this study was necessary and what usefulness it may bring.

One of the main purposes of this model is to provide useful information for the proper design of all spacecraft subsystems. In particular, this study shall provide quantitative analyses which relate flight performance (e.g. flight range) to the design choices and figures of merit of the various subsystems.

In addition to guiding most of the project choices, this study has the critical task of assessing the feasibility of the mission itself. In essence, this model represents a fundamental tool to verify whether the mission requirements can be met, while ensuring the success of the mission.

The flight profile analysed in this chapter is designed for simplicity. It will consist of elementary flight segments similar to those designed for NASA's Mars Helicopter [18]. In particular, each flight will be composed of a succession of the following manoeuvres: vertical ascent, horizontal translation, vertical descent and hovering (see Figure 2.1).

As mentioned before, the main purpose of this study is to guide the design and sizing of the individual subsystems by converting some of their figures of merit into other parameters (such as flight range), and, in general, to highlight their impact on propellant consumption and therefore on the feasibility of the mission itself. In order to do this, it is necessary to identify, for each individual manoeuvre, the thrust program that leads to the lowest propellant consumption. For this reason, in the following chapters an optimisation analysis will always be carried out in order to identify the most efficient propulsion strategy.

3.1 General assumptions

The assumptions and relations presented in this chapter will then be applied to all the following flight segments: vertical ascent, horizontal translation, vertical descent and hovering.

Homogeneous gravitational field

In a homogeneous gravitational field the field strength, g , is constant. If we consider the Moon locally as being flat, the local gravitational field may be considered homogeneous. Therefore, as long as the altitude and range are small relative to the mean Moon's radius (1731 km), the Moon may be considered flat and the field strength can be approximated very well by a constant [19]. Considering our mission objectives, we can reasonably assume that the distance covered during the flight, and the maximum altitude reached by the spacecraft, will remain relatively small, compared to the Moon's radius, and hence the hypothesis of homogeneous gravitational field holds.

2D motion and nominal trajectories

As the assumption of a pure two-dimensional motion will greatly simplify the treatment of the spacecraft motion, we will assume that the complete trajectory of the centre of mass of the vehicle lies in a single plane. In this case, there are only three degrees of freedom: two for the position of the centre of mass and one for the

orientation of the LuNaDrone. In practice, pure 2D motion does not occur because of the presence of forces perpendicular to the instantaneous plane of motion, such as gravitational forces or components of the thrust (since the drone will operate on the Moon, there will be no aerodynamic forces). Thrust misalignments, navigation system errors, unexpected mass distribution (e.g. due to propellant sloshing), etc., cause the real trajectory to deviate from the nominal one. Although these factors play a key role in the spacecraft design, only the nominal trajectories will be discussed in this section.

To describe the motion of the spacecraft we need the following reference frames (the same used in [19]):

- *Inertial frame OXYZ*. This frame is chosen such that the trajectory of the centre of mass of the LuNaDrone lies in the XZ-plane. In particular, assuming to operate in a homogeneous gravitational field, we choose the X-axis of the inertial system to coincide with the flat Moon surface and the Z-axis vertical, (then $g_X = 0$ and $g_Z = -g \approx -1.62 \text{ m/s}^2$).
- *Vehicle reference frame oxyz*. The origin of this frame is the centre of mass of the drone. The x-axis coincides with the longitudinal axis of the spacecraft and is positive forwards. The y- and z-axes are chosen such that they form an orthogonal right-handed Cartesian frame, the xz-plane coinciding with the XZ-plane. The position of the spacecraft is determined by the X- and Z-coordinates of its centre of mass, while the orientation is determined by the angle between the x-axis and the X-axis: the pitch angle θ .

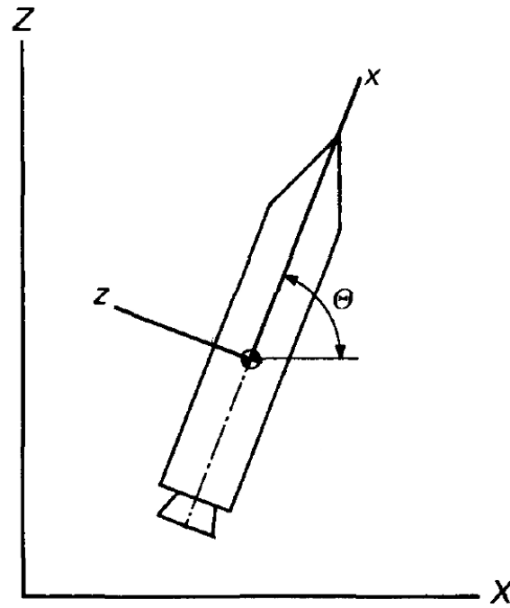


Figure 3.1 – Coordinate systems to describe the two-dimensional spacecraft motion [19]

With the exception of the case of the horizontal translation manoeuvre, we will assume that the thrust acts along the x-axis, i.e. $T_y = T_z = 0$. Then, the equations of translational motion are:

$$\begin{cases} (X) & m \frac{dV_X}{dt} = T \cos \theta \\ (Z) & m \frac{dV_Z}{dt} = T \sin \theta - mg \end{cases} \quad \left[\frac{dX}{dt} = V_X, \quad \frac{dZ}{dt} = V_Z, \quad \frac{dm}{dt} = -\dot{m}_p, \quad T = \dot{m}_p c = \dot{m}_p g_0 I_{sp} \right] \quad (3.1)$$

Where: T is the thrust, \dot{m}_p is the propellant mass flow, c is the effective exhaust velocity, I_{sp} is the specific impulse of the propulsion system, g_0 is the standard Earth's gravity ($g_0 \approx 9,81 \text{ m/s}^2$), g is the Moon's gravitational field strength ($g \approx 1,62 \text{ m/s}^2$), m is the spacecraft total mass and θ is the pitch angle.

In some of the following analyses, a constant total mass of the spacecraft will be assumed. For this approximation to be acceptable, it is necessary that the mass of propellant consumed during the manoeuvre is not an important fraction of the total mass of the spacecraft. Nonetheless, it is quite easy to express the total mass of the spacecraft as a function of time using the following equation (which basically describes the conservation of linear momentum):

$$T = \dot{m}_p c \quad \rightarrow \quad m = m_i - \int_{t_i}^t \dot{m}_p dt = m_i - \underbrace{\int_{t_i}^t \frac{T}{c} dt}_{m_p} \quad (3.2)$$

Where m_i is the initial total mass of the LuNaDrone.

Propellant consumption is related to the ideal ΔV (hereinafter referred to as ΔV_{prop}) according to the Tsiolkovsky rocket equation:

$$\Delta V_{prop} = \int_{t_i}^{t_f} \frac{T}{m} dt = I_{sp} g_0 \ln \frac{m_i}{m_f} = c \ln \frac{m_i}{m_i - m_p} \quad (3.3)$$

It should be noted that this ΔV_{prop} does not correspond to the actual ΔV that the spacecraft will undergo during the manoeuvre. In fact, the two changes in velocity would be the same only if no other forces (such as gravity) act on the spacecraft and if the thrust vector has no misalignment with the velocity vector. Since we are looking for the most efficient manoeuvre, we will have to find the thrust program that leads to the lowest m_p , and thus, for fixed I_{sp} and m_i , the lowest ΔV_{prop} .

By integrating the equation of motion (3.4) it is possible to highlight the dependence of ΔV_{prop} on gravity and misalignment losses as well as on the actual change in velocity of the spacecraft ΔV (which we can see as a sort of boundary condition imposed by the objective of the manoeuvre).

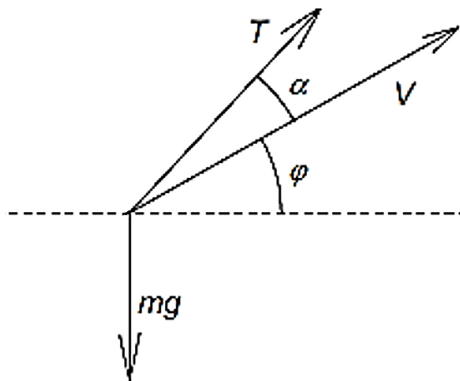


Figure 3.2 – Forces acting on the spacecraft

$$\frac{dV}{dt} = \frac{T}{m} \cos(\alpha) - g \sin(\varphi) \quad (3.4)$$

$$\frac{dV}{dt} = \frac{T}{m} - \frac{T}{m} (1 - \cos(\alpha)) - g \sin \varphi \quad (3.5)$$

$$\Delta V = \underbrace{\int_{t_i}^{t_f} \frac{T}{m} dt}_{\Delta V_{prop}} - \int_{t_i}^{t_f} \frac{T}{m} (1 - \cos(\alpha)) dt - \int_{t_i}^{t_f} g \sin(\varphi) dt \quad (3.6)$$

$$\Delta V_{prop} = \Delta V + \underbrace{\int_{t_i}^{t_f} \frac{T}{m} (1 - \cos(\alpha)) dt}_{\text{misalignment losses}} + \underbrace{\int_{t_i}^{t_f} g \sin(\varphi) dt}_{\text{gravity losses}} \quad (3.7)$$

Hence, when in the following chapters we will have to analyse the efficiency of a certain manoeuvre, we can use these two equations:

$$\begin{aligned} 1) \quad \Delta V_{prop} &= \int_{t_i}^{t_f} \frac{T}{m} dt & 2) \quad \Delta V_{prop} &= \Delta V + \underbrace{\int_{t_i}^{t_f} \frac{T}{m} (1 - \cos(\alpha)) dt}_{\text{misalignment losses}} + \underbrace{\int_{t_i}^{t_f} g \sin(\varphi) dt}_{\text{gravity losses}} \end{aligned} \quad (3.8)$$

3.2 Vertical ascent

The vertical ascent manoeuvre allows the spacecraft to increase its altitude without gaining or losing vertical velocity. In particular, it will be assumed that both the initial and final velocity of the spacecraft are equal to zero. This is the general objective of the manoeuvre and, as we will see in the following chapters, there are countless ways to meet this goal. Our task is to identify the thrust program that leads to the lowest possible propellant consumption and quantify the effect of parameter variations on propellant consumption.

3.2.1 Vertical ascent without braking thrust

Since the objective of this manoeuvre is to increase the altitude of the spacecraft, let's suppose that during the whole flight $\theta = 90^\circ$ (see Figure 3.1). If we have zero initial horizontal velocity the trajectory will be a straight line parallel to the Z-axis and V_Z will be equal to the total velocity of the spacecraft: V .

Thus, the equations of motion (3.1) simplify to:

$$\frac{d^2 Z}{dt^2} = \frac{dV}{dt} = \frac{T}{m} - g \quad (3.9)$$

In this chapter we will make the following assumptions (the angles α and φ are depicted in Figure 3.2):

1. $\varphi = 90^\circ \forall t$,
2. $\alpha = 0^\circ \forall t$ ($\theta = \alpha + \varphi = 90^\circ \forall t$),
3. $V_i = V_f = 0 \rightarrow \Delta V = 0$.

By substituting these relations into Equation (3.7), we find:

$$\Delta V_{prop} = \Delta V + \int_{t_i}^{t_f} \frac{T}{m} (1 - \cos(\alpha)) dt + \int_{t_i}^{t_f} g \sin(\varphi) dt \rightarrow \Delta V_{prop} = \int_{t_i}^{t_f} g dt = g(t_f - t_i) \quad (3.10)$$

Thus, according to this equation, if we want to reduce the ΔV_{prop} , and hence the propellant consumption, we just need to minimise gravity losses.

$$\Delta V_{prop} = \int_{t_i}^{t_f} g dt = \int_{t_i}^{t_f} \frac{g}{V} V dt = \int_{t_i}^{t_f} \frac{g}{V} \frac{dZ}{dt} dt = \left(\frac{g}{V}\right)_{avg} (Z_f - Z_i) \quad (3.11)$$

Since $Z_f - Z_i$ corresponds to the change in altitude, i.e. the objective of the manoeuvre itself, the only parameter we can vary is the average ascent velocity. In particular, the higher the average velocity, the more efficient the manoeuvre.

In order to obtain the highest V_{avg} , the overall manoeuvre time $t_f - t_i$ must be as short as possible. Since we have made the hypothesis of $V_i = V_f = 0$, the manoeuvre will inevitably be divided into an acceleration and deceleration phase. In order to reach the highest V_{avg} , the average acceleration and deceleration values must be as high as possible.

Since we have assumed $\alpha = 0^\circ$ and $\varphi = 90^\circ$, it is not possible to exert any braking thrust (in this case we would have $\alpha = 180^\circ$). Thus, the maximum average deceleration will be equal to g which is simply the case

when the propulsion system does not exert any thrust during the whole deceleration phase, and hence it is the lunar gravity alone that is slowing down the ascent of the spacecraft.

As far as the acceleration phase is concerned, assuming that the propulsion system is able to provide a maximum continuous thrust of T_{max} , the maximum average acceleration, for a given spacecraft initial mass, will be obtained by constantly exerting a thrust equal to T_{max} throughout the acceleration phase.

Consequently, taking into account the assumptions made so far, the most efficient manoeuvre (depicted in Figure 2.1 as a vertical line between points 0 and 1) will have the characteristics summarised in Table 3.1.

	$t = t_0$	$t_0 < t < t_S$		$t = t_S$	$t_S < t < t_1$	$t = t_1$
$Z [m]$	0	$0 < Z < Z_S$		$Z = Z_S$	$Z_S < Z < Z_1$	$Z = Z_1$
$V \left[\frac{m}{s} \right]$	0	$0 < V < V_{01max}$	$V = V_{01max}$	$0 < V \leq V_{01max}$	$0 < V < V_{01max}$	0
$a \left[\frac{m}{s^2} \right]$	$\frac{T_{0S}}{m_0} - g$	$\frac{T_{0S}}{m(t)} - g$	0	$-g$	$-g$	0
$m [kg]$	m_0	$0 < m < m_0$	$0 < m < m_0$	$0 < m < m_0$	$0 < m < m_0$	$0 < m < m_0$
$T [N]$	T_{0S}	T_{0S}	$m(t)g$	0	0	$m(t)g$

Table 3.1 – Summary of vertical ascent manoeuvre (without braking thrust)

$t = t_0$

At time t_0 the propulsion system will exert the maximum continuous thrust of the vertical ascent manoeuvre: T_{0S} , which, assuming it is greater than the weight of the spacecraft, and that the thrust vector has no misalignment ($\alpha = 0^\circ$ and $\varphi = 90^\circ$), will produce a positive vertical acceleration (according to the positive direction of the Z-axis).

$t_0 < t < t_S$

Since we are looking for the most efficient trajectory, there is no reason to consider a non-constant thrust program (which would also have the disadvantage of a more difficult implementation from a technological point of view). Consequently, as mentioned before, the optimal thrust program (for the acceleration phase 0-S) consists in constantly exerting a thrust equal to T_{0S} . However, due to various reasons (e.g. related to the performance of the GN&C system) the spacecraft may have to operate under a certain maximum ascent velocity: V_{01max} . Therefore, when $V = V_{01max}$, the propulsion system will have to exert a thrust equal to the weight of the spacecraft in order to not exceed the maximum vertical velocity, but at the same time maintaining the average acceleration as high as possible.

$t = t_S$

Once the spacecraft has reached a certain speed and altitude, the propulsion system will no longer have to exert any thrust, so that the deceleration phase can begin. In order to determine whether the spacecraft has reached point S we can use Equation (3.12). This equation also shows that there is no dependence with the altitude and velocity-time history but only with their instantaneous values.

$t_S < t < t_1$

The S-1 section identifies the deceleration phase. As mentioned before, the optimum condition is that the average deceleration is as high as possible. Consequently, during this phase the propulsion system will not exert any thrust in order not to decrease the braking action of gravity.

$t = t_1$

Once the spacecraft reaches point 1, the model must be able to simulate a stationary hover lasting Δt_{h1} seconds. Obviously, the most efficient condition will be the one in which $\Delta t_{h1} = 0$ s.

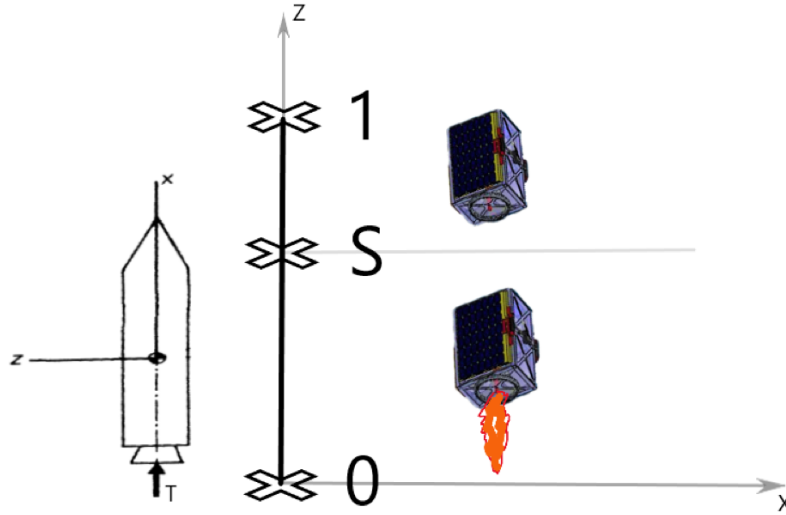


Figure 3.3 – The outline of the vertical ascent manoeuvre

During a private consultation with T4i, I was advised to consider $1g_0$ as guideline value for the maximum acceleration of the spacecraft. In order to correctly estimate this value it would be necessary to have all the details concerning the structure of the spacecraft, the type of instruments installed on board, and also the performance limits of certain subsystems such as the GN&C system. Considering that the LuNaDrone will have to be designed to withstand launch loads, which are often the sizing requirements for the structure and other parts of the spacecrafts, it is actually fairly reasonable to consider a guideline value of $1g_0$ as the maximum continuous vertical acceleration. There are two ways to ensure that the LuNaDrone does not exceed this value. The first one is to ensure that the maximum thrust that can be delivered by the propulsion system, compared to the dry mass of the spacecraft, does not induce an acceleration greater than $1g_0$. The second approach is to assume that the GN&C system will limit the thrust exerted by the propulsion system in order not to exceeding the maximum sustainable acceleration. The following models will be developed following the first approach. This would mean that assuming a spacecraft mass of about 15kg, the thrust should not exceed approximately 150N. However, only to give a better picture of the relation between propellant consumption and thrust magnitude, in some simulations will be considered thrusts up to 250N.

The parameters that define the vertical ascent manoeuvre (with no braking thrust) are:

- m_0 = LuNaDrone total mass at t_0
- T_{0S} = maximum continuous accelerating thrust
- c = effective exhaust velocity
- V_{01max} = maximum velocity
- h_1 = altitude of point 1 ($h_1 = Z_1$ assuming $Z_0 = 0$ m)
- Δt_{h1} = time frame of the hovering manoeuvre at point 1

Please note that point S is not an input data as it is uniquely determined by the parameters listed above (except for Δt_{h1}). During the vertical ascent, the model should therefore be able to determine whether or not the spacecraft has reached this point. But then the question is: how will the model recognise when, during the ascent, the propulsion system must stop thrusting? In other words, what is the trigger event that indicates that the spacecraft have to start the deceleration phase? During the deceleration phase (S-1) the spacecraft will have a constant deceleration of g , and thus, we can apply the following kinematical equations:

$$V_1 = V_S - g(t_1 - t_S) = 0 \quad \rightarrow \quad g(t_1 - t_S) = V_S$$

$$Z_1 - Z_S = V_S(t_1 - t_S) - \frac{1}{2}g(t_1 - t_S)^2 = \frac{V_S^2}{g} - \frac{1}{2}g \frac{V_S^2}{g^2} = \frac{V_S^2}{2g} \quad \rightarrow \quad Z_1 - Z_S = \frac{V_S^2}{2g}$$

At each integration step the model evaluates both the instantaneous altitude Z and the instantaneous velocity V . Knowing the altitude of the spacecraft, it is possible to estimate, at each integration step, the distance between the LuNaDrone and point 1 which is: $h_1 - Z$. Consequently, the propulsion system will have to stop thrusting when the following equation is verified:

$$h_1 - Z = \frac{V^2}{2g} \quad (3.12)$$

Let's see the operating principles of the model, developed with MATLAB-Simulink, of the vertical ascent manoeuvre.

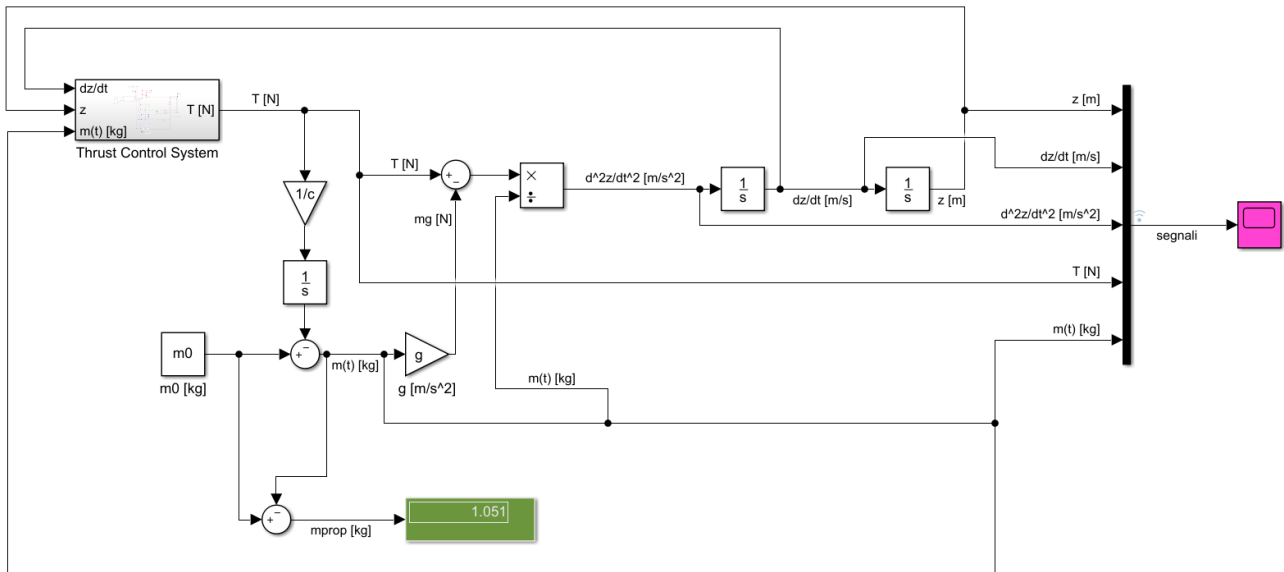


Figure 3.4 – Main system of the vertical ascent model (without braking thrust)

The main system is simply the "elementary" blocks representation of the following two differential and integral equations:

$$\frac{T(t) - m(t)g}{m(t)} = \frac{d^2Z}{dt^2} \quad (3.13)$$

$$m(t) = m_0 - \int_0^t \frac{T(t)}{c} dt \quad (3.14)$$

In order to solve these equations it is necessary to know the instantaneous thrust value which in turn depends on the instantaneous values of mass, velocity and altitude. The "Thrust Control System" has the task of providing the correct thrust value by receiving the 3 above-mentioned values as inputs.

cond1

if $h_1 - Z = \frac{v^2}{2g}$, then cond1 will go from 0 to 1 and will remain equal to 1 until the end of the simulation. This approach was chosen because in this way the condition not only acts as a trigger event (the propulsion system stops thrusting when cond1 goes from 0 to 1) but also gives continuous information about the spacecraft phase (if 0: acceleration phase or intermediate phase ($V = V_{01_{max}}$), if 1: deceleration phase).

cond2

if $\frac{|h_1 - Z|}{h_1} \leq tol2$, then cond2 is equal to 1, else it is equal to 0. Cond2 is not an essential condition for the functioning of this model but is useful to figure out if the spacecraft is close to point 1. If only this condition were used to switch to the hovering mode, the model would have a strong dependence on both the tol2 value and the type of solver and its integration step. In particular, if tol2 is too small with respect to the integration step, once the spacecraft gets close to point 1, instead of switching to the hovering mode, it slows down until it reverses its motion falling back towards point 0. On the contrary, if tol2 is too big, the spacecraft switches to the hovering mode when it is still too far from point 1, and we will therefore obtain results that are not consistent with the input parameters ($h_{1_{model}} < h_{1_{input}}$). Since we're going to execute parametric sweeps,

using only this condition to switch to the hovering mode, and hence stop the ascent of the spacecraft, would mean that we would have to carefully choose the integration step and tol2 value for each set of input parameters, and this would obviously take too much time.

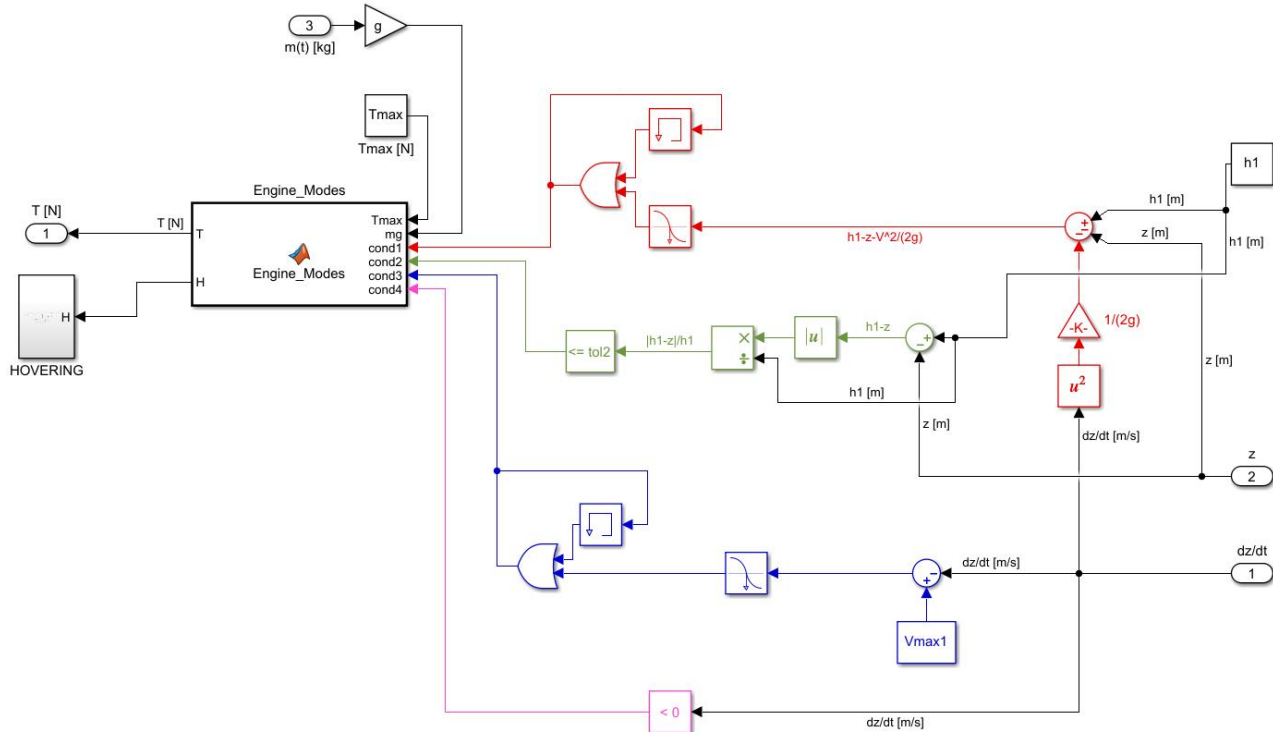


Figure 3.5 – Thrust Control System of the vertical ascent model (without braking thrust)

cond4

if $V < 0$, then cond4 is equal to 1, else, it is equal to 0. This condition is used to switch to the hovering mode. The velocity remains greater than or equal to zero during the entire manoeuvre except when the spacecraft reaches the highest point of its trajectory (point 1) where it begins to reverse its motion. Using this condition, instead of cond2, we can reduce the difference between $h_{1,model}$ and $h_{1,input}$ by simply acting on the integration step and solver type. Taking as an example the ode1(Euler) solver, the smaller the integration step the more precise the cond1 will be, and then the spacecraft will start the deceleration phase with better timing thus reversing its motion at a point closer to point 1 (input parameter).

cond3

When $V_{01,max} - V(t)$ goes from a positive to a negative value, cond3 goes from 0 to 1 and will remain 1 until the end of the simulation. This condition is used to limit the maximum speed by lowering the thrust from T_{0S} to $m(t)g$ during the acceleration phase.

The logic used in the "Engine_Modes" block is well summarised by the following code.

```
H=0;
if cond1==0 && cond3==0
    T = Tmax;
elseif cond1==0 && cond3==1
    T = mg;
elseif cond1==1 && cond4==1 && cond2==1
    T = mg;
```

```

H = 1;
elseif cond1==1 && ~(cond2==1 && cond4==1)
    T = 0;

```

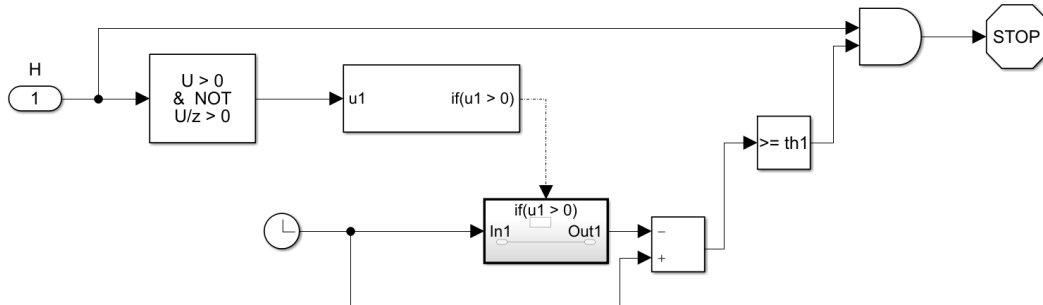


Figure 3.6 – Hovering subsystem of the vertical ascent model (without braking thrust)

As regards the “HOVERING” subsystem, when the H signal goes from 0 to 1, it starts counting time and stops the simulation once Δt_{h_1} seconds has passed.

The input parameters used to obtain the results depicted in Figure 3.7 are:

$T_{0S} = 50 \text{ N}$	$h_1 = 100 \text{ m}$	$tol2 = 0.1$
$V_{01max} = 5 \text{ m/s}$	$I_{sp} = 150 \text{ s}$	Solver: ode1(Euler)
$m_0 = 15 \text{ kg}$	$\Delta t_{h_1} = 2 \text{ s}$	$DT = 1 \text{ ms}$

Where DT is the integration step.

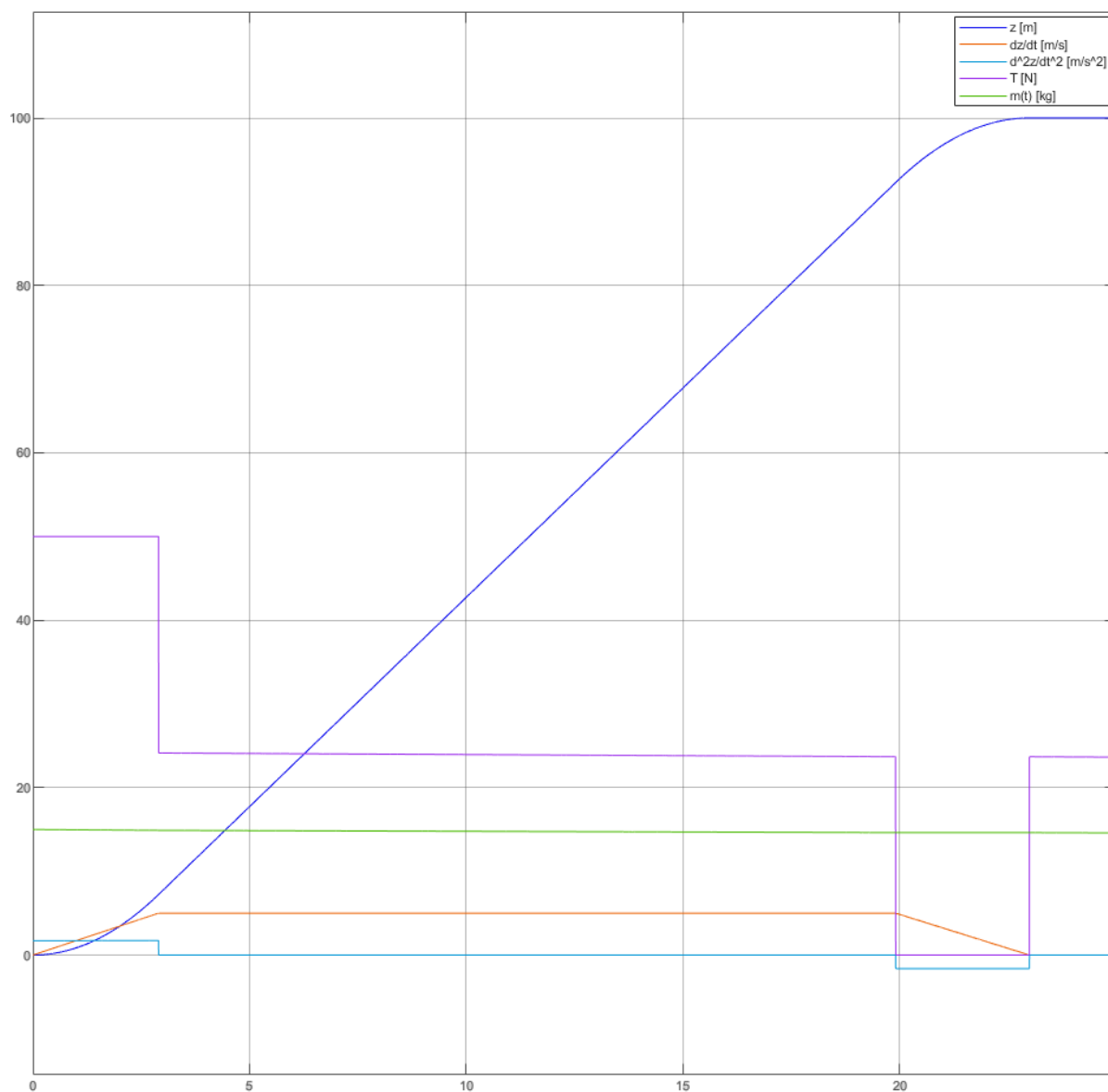


Figure 3.7 – Model output example [vertical ascent model (without braking thrust)]

3.2.2 Vertical ascent without braking thrust – Results and conclusions

Chapter 5 Annex 01 shows the results of a parametric sweep analysis that was carried out taking into account the following considerations.

I_{sp}

At the present time, the main propulsion system, which is expected to be installed on the LuNaDrone, is a hydrogen peroxide monopropellant thruster designed and produced by the Italian company T4i. During a private consultation with T4i, I was advised to use an indicative value of 150s as specific impulse.

m_0 and m_p

One of the main mission requirements is that the LuNaDrone shall not exceed a total mass of 15kg. Another mission requirement sets the maximum volume of the spacecraft at 12U. Taking into account current analyses of the propulsion system [16], in order to comply with the maximum volume constraint of 12U, it seems to be quite tricky to install more than 3kg of propellant. Anyway, in order to analyse a wide range of cases, we will consider three different initial masses: 20kg, 15kg and 10kg.

Δt_{h_1} and T_{0s}

Since we will discuss the hovering manoeuvre in Chapter 3.5, in these analyses we will only consider vertical ascent manoeuvres with $\Delta t_{h_1} = 0$. As far as the maximum thrust is concerned, it was decided not to consider thrusts higher than 250N for the same reasons described on page 22.

V_{01max}

As mentioned before, the maximum velocity can be imposed by a number of factors. Among these, the most important is probably the performance of the navigation system. For example, in the case of NASA's Mars Helicopter, the visual-inertial navigation system limits the nominal horizontal translational velocity up to 2 m/s, which is chosen to keep features on the ground from disappearing too quickly from the field of view [18]. In case obstacle avoidance techniques are adopted, the maximum velocity could also be influenced by the maximum distance at which an obstacle can be perceived, the responsiveness of the GN&C system in elaborating the appropriate actuation command and the performance of the propulsion system and attitude control system. Regardless of the reasons for which it is imposed, in these analyses we will consider very low maximum velocities (0.5-1 m/s) up to values large enough to simulate a complete manoeuvre without any reduction in thrust ($V < V_{01max}$ throughout the vertical ascent).

The propellant mass: $m_p = f(V_{01max}, T_{0s})$, and the time of the manoeuvre: $t_1 = f(V_{01max}, T_{0s})$, are depicted in Figure 5.1 and Figure 5.5 respectively. Both figures show a similar pattern because even if the m_p in Figure 5.1 has been calculated according to Equation (3.2), the same parameter can also be calculated by algebraically manipulating Equation (3.3) and thus obtaining:

$$m_{p_{t1}} = m_0 \left(1 - e^{-\frac{gt_1}{\Delta V_{prop}}} \right) \quad (3.15)$$

Where ΔV_{prop} , according to Equation 3.10, is equal to gt_1 , and this explains why Figure 5.1 and Figure 5.5 have a very similar shape. As further evidence of this, Figure 5.6 and Figure 5.7 show the propellant mass as

a function of T_{0S} and V_{01max} calculated according to Equation 3.15 (where t_1 is determined by the model, while c and m_0 are input parameters).

According to the results reported in Chapter 5, we can say that, as we deduced by analysing Equation (3.11), the greater the thrust, the lower the propellant consumption. However, if the propulsion system has to exert a greater thrust, the thruster and other hardware components (pipes, valves, etc.) could become larger and heavier. For example, as far as pipes are concerned, the speed of the propellant flowing inside them must not exceed a certain maximum value in order to avoid severe vibrations and excessive pressure losses. However, according to Equation (3.2), in order to achieve a higher thrust, given the specific impulse of the propulsion system, one can only increase the propellant flow rate. Consequently, as the thrust increases, the flow rate will also increase and in order not to exceed a certain maximum velocity inside the tubes, it is necessary to increase the section of the pipes, thus increasing their mass and size. So, to what extent should the thrust be increased ? At a certain point, the saved propellant mass will no longer justify the increase in weight and size of the propulsion system components. Thanks to this model it will be possible to quantitatively identify the optimal configuration, allowing us to compare the saved propellant mass with the mass and size increase induced by the higher thrust required.

If we want to observe the effects of the thrust, without having the influence of the maximum speed, we can analyse the cases at high V_{01max} , i.e. those cases where, during the acceleration phase, V remains always lower than V_{01max} . Looking at the results reported in Table 3.2 we can see a substantial gap between the propellant mass of case $T_{01} = 25 \text{ N}$ and the one of case $T_{01} = 50 \text{ N}$, while there is a much smaller difference between case $T_{01} = 50 \text{ N}$ and case $T_{01} = 250 \text{ N}$. Thus, from these results, and from the those reported in Chapter 5, we can reasonably affirm that, from the point of view of propellant consumption, it would be appropriate for the propulsion system to exert thrusts equal to or greater than 50 N (this value is not mandatory, it acts more as a reference value).

m0 [kg]	h1 [m]	T [N]	mprop [kg]	%	m0 [kg]	h1 [m]	T [N]	mprop [kg]	%	m0 [kg]	h1 [m]	T [N]	mprop [kg]	%
15	50	25	0,6229	358,4%	10	50	18	0,26	191,7%	20	50	35	0,59	219,4%
		51,39	0,1773	30,5%			50	0,1046	17,4%			50	0,2882	56,0%
		250	0,1359	-			250	0,08912	-			250	0,1847	-
	100	25	0,83	332,3%		100	18	0,3606	186,9%		100	35	0,8127	212,0%
		51,39	0,25	30,2%			50	0,1475	17,3%			50	0,4057	55,7%
		250	0,192	-			250	0,1257	-			250	0,2605	-
	500	25	1,555	265,4%		500	18	0,7504	169,0%		500	35	1,654	186,4%
		51,39	0,5516	29,6%			50	0,3264	17,0%			50	0,8892	54,0%
		250	0,4256	-			250	0,279	-			250	0,5775	-
	1000	25	2,003	234,9%		1000	18	1,013	158,4%		1000	35	1,013	158,4%
		51,39	0,7725	29,2%			50	0,458	16,8%			50	0,458	16,8%
		250	0,598	-			250	0,392	-			250	0,392	-

Table 3.2 – Summary of the values obtained in Annex 01 for the “full throttle” cases

As in the case of thrust, the higher the maximum velocity, the lower the propellant consumption. It should be noted that in the y-axes of the figures in Chapter 5, “VMAX” refers to the maximum sustainable velocity and not the maximum speed actually reached during the manoeuvre. In order to determine whether there is a difference between these two velocities, we can look at the respective “% full throttle” graphs. If the manoeuvre has a value of 100% it means that, while constantly exerting a thrust equal to T_{0S} during the acceleration phase, the spacecraft has never reached the maximum sustainable velocity V_{01max} , thus the maximum velocity reached during the manoeuvre is lower than the one indicated by the y-axis. In all other cases, the two velocities

are just the same. In fact, the value indicated in the figures depicting the “throttle” of the manoeuvre is simply: $(t_{v_{max}}/t_S) \cdot 100$, where $t_{v_{max}}$ identifies the time when the actual maximum velocity was reached and t_S is the time when the spacecraft start the deceleration phase.

3.2.3 Vertical ascent with braking thrust

In this chapter we will consider a manoeuvre similar to the one presented in Chapter 3.2.1 with the difference that this time the spacecraft will be able to exert a constant braking thrust during the deceleration phase (B-1).

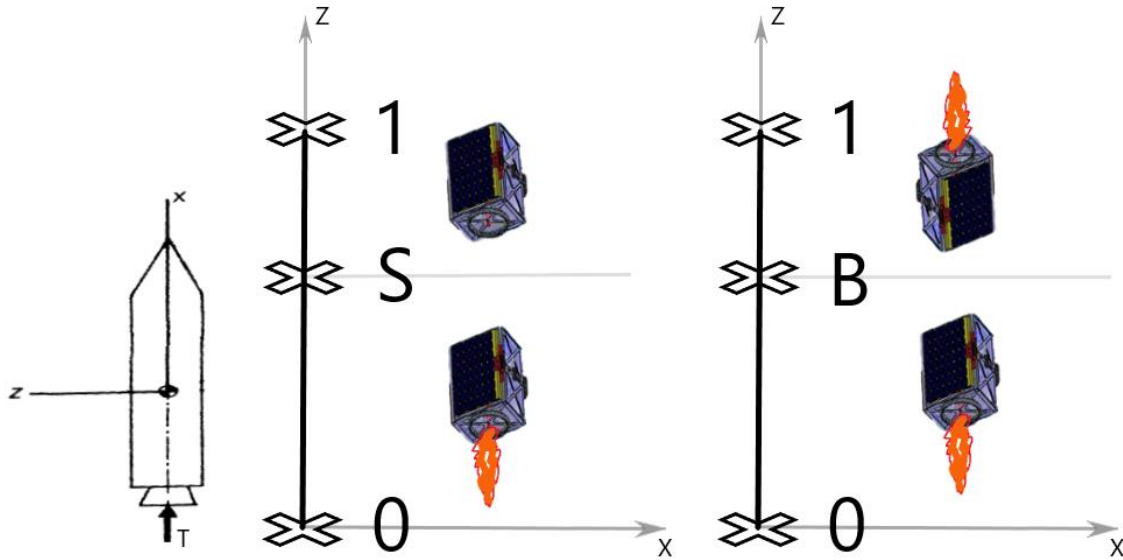


Figure 3.8 – Vertical ascent w. and w/o. braking thrust (right and left respectively)

As we will demonstrate below, exerting any braking thrust (i.e. a thrust acting along the negative Z-axis direction) always leads to higher propellant consumption compared to the case where it is only the lunar gravity that slows down the ascent of the spacecraft. As a result, the characteristics of this manoeuvre, well summarised in Table 3.3, are not dictated by any optimisation needs, and hence, they have been chosen to make the development of the model as simple as possible.

$t = t_0$

At time t_0 the propulsion system will exert a thrust equal to T_{0B} which, assuming it is greater than the weight of the spacecraft, and that the thrust vector has no misalignment ($\alpha = 0^\circ$ and $\varphi = 90^\circ$), will produce a positive vertical acceleration (according to the positive direction of the Z-axis).

$t_0 < t < t_B$

During the acceleration phase the propulsion system will constantly exert a thrust equal to T_{0B} . However, due to various reasons (e.g. related to the performance of the GN&C system) the spacecraft may have to always operate under a certain maximum ascent velocity: $V_{01_{max}}$. Thus, if the velocity of the spacecraft reaches this value, the propulsion system will exert a thrust equal to the weight of the spacecraft so as not to increase its velocity and at the same time do not start the deceleration phase (which would happen if it stopped thrusting).

$t = t_B$

Once the spacecraft has reached a certain speed, mass, and altitude, the propulsion system will exert a constant braking thrust equal to T_B (pointing the negative direction of the Z-axis). In order to determine whether the spacecraft has reached point B we can use Equation (3.38). This equation also shows that there is no dependence with the altitude, spacecraft mass and velocity time history but only with their instantaneous values.

$$t_B < t < t_1$$

The B-1 section identifies the deceleration phase where the propulsion system will constantly exert a braking thrust equal to T_B .

$$t = t_1$$

Once the spacecraft reaches point 1, the model must be able to simulate a stationary hover lasting Δt_{h1} seconds. Obviously, the most efficient condition will be the one in which $\Delta t_{h1} = 0$ s.

	$t = t_0$	$t_0 < t < t_B$		$t = t_B$	$t_B < t < t_1$	$t = t_1$
z [m]	0	$0 < Z < Z_B$		$Z = Z_B$	$Z_B < Z < Z_1$	$Z = Z_1$
V [$\frac{m}{s}$]	0	$0 < V < V_{01max}$	$V = V_{01max}$	$0 < V \leq V_{01max}$	$0 < V < V_{01max}$	0
a [$\frac{m}{s^2}$]	$\frac{T_{0B}}{m_0} - g$	$\frac{T_{0B}}{m(t)} - g$	0	$-\frac{T_B}{m(t)} - g$	$-\frac{T_B}{m(t)} - g$	0
m [kg]	m_0	$0 < m < m_0$	$0 < m < m_0$	$0 < m < m_0$	$0 < m < m_0$	$0 < m < m_0$
T [N]	T_{0B}	T_{0B}	$m(t)g$	T_B	T_B	$m(t)g$

Table 3.3 – Summary of the vertical ascent manoeuvre (with braking thrust)

In Chapter 3.2.1, in order to determine the optimal thrust program, considerations were made on Equation (3.10). By developing the term for gravity losses, it was seen that the higher the average speed, the lower the propellant consumption. So, the question arises: can it be convenient, from the point of view of propellant consumption, to exert a thrust along the negative direction of the Z-axis which helps gravity to brake the spacecraft during the deceleration phase? In fact, thanks to this braking thrust it would be possible to reach higher deceleration values during the deceleration phase, thus being able to accelerate more during the accelerating phase, having the overall effect of increasing the V_{avg} of the manoeuvre, and thus reducing gravity losses. It follows that less propellant will be spent due to gravity losses, but exerting that braking thrust leads to misalignment losses which were absent in the case presented in Chapter 3.2.1, and hence it is not clear whether or not this manoeuvre would lead to propellant savings.

Let's suppose we want to compare the two cases (vertical ascent with and without the braking thrust, hereinafter referred to as case B and case A respectively) considering for both the same accelerating thrust. As in case B the spacecraft is able to brake more intensively during the braking phase, the accelerating phase can last longer as the braking capabilities are such that the spacecraft can be stopped in a shorter distance ($Z_B > Z_S$) and with a higher initial speed ($V_B > V_S$) than in case A. In short, being able to brake more means that the acceleration phase will last longer. Since propellant consumption is equal to the integral over time of the ratio between thrust and effective exhaust velocity (see Equation (3.2)), for a fixed accelerating thrust, the longer the acceleration phase the more propellant is consumed. Therefore, in case B we would have a more expensive acceleration phase, from the point of view of propellant consumption, and we would also have the “cost” of the braking manoeuvre, which was absent in case A. So in the end the only advantage of case B would be to complete the manoeuvre in less time ($t_1 \downarrow$) but with higher propellant consumption ($m_p \uparrow$) and with the problem of installing an additional thruster capable of providing that braking thrust (although, in theory, we could use only one main thruster to exert both the accelerating and braking thrust and simply turn the spacecraft upside-down between the two phases, assuming that this is compatible with all the spacecraft systems).

For the case *A* we have demonstrated that the optimum thrust program, for the acceleration phase, was to constantly exert the maximum continuous thrust that the propulsion system is able to exert. However, if we suppose to compare the two cases assuming for both the same propulsion system, and hence the same maximum continuous thrust, it is not necessarily true that the optimal thrust program of case *B* would be the same as the one of case *A*. In fact, the optimal thrust program for the case *A* has been obtained starting from Equation (3.7) and assuming $\alpha = 0^\circ \forall t$, whereas, in case *B*, $\alpha = 0^\circ$ during the acceleration phase but $\alpha = 180^\circ$ during the deceleration phase. Consequently, in case *B* misalignment losses are not zero as they were for the case *A*, and it is therefore no longer necessarily true that, the lowest propellant consumption is obtained by exerting the maximum continuous thrust during the acceleration phase (in fact, the results will show that this is definitely not the case).

Assuming we consider the same input parameters for both cases, fixed a certain T_B , there will be an accelerating thrust T_{0B} that leads to the lowest propellant consumption for case *B*. Let's suppose we use the same accelerating thrust for the case *A* ($T_{0S} = T_{0B}$). According to what we said before, if we compare the two cases assuming the same accelerating thrust for both, the most efficient case will always be case *A*. Therefore, not only does case *B* leads to higher propellant consumption than case *A*, but if the accelerating thrust that we selected (which led to the lowest propellant consumption for case *B*) was not the maximum continuous thrust that can be delivered by the propulsion system, case *A* would have led to even lower propellant consumption if we had considered a higher accelerating thrust. In conclusion, exerting a braking thrust always leads to higher propellant consumption than if this thrust is not exerted at all, and this is true for any thrust programs as we will try to demonstrate below.

$$\begin{cases} T(t) = \dot{m}_p(t) c \\ m(t) = m_0 - m_p(t) \\ m_p(t) = \int_{t_0}^t \frac{|T|}{c} dt = \frac{1}{c} \int_{t_0}^t |T| dt \end{cases} \quad a(t) = \frac{T(t)}{m(t)} - g \quad V(t) = \int_{t_0}^t a(t) dt + V_0 \quad Z(t) = \int_{t_0}^t V(t) dt + Z_0$$

Note: we are assuming $V_0 = Z_0 = t_0 = 0$.

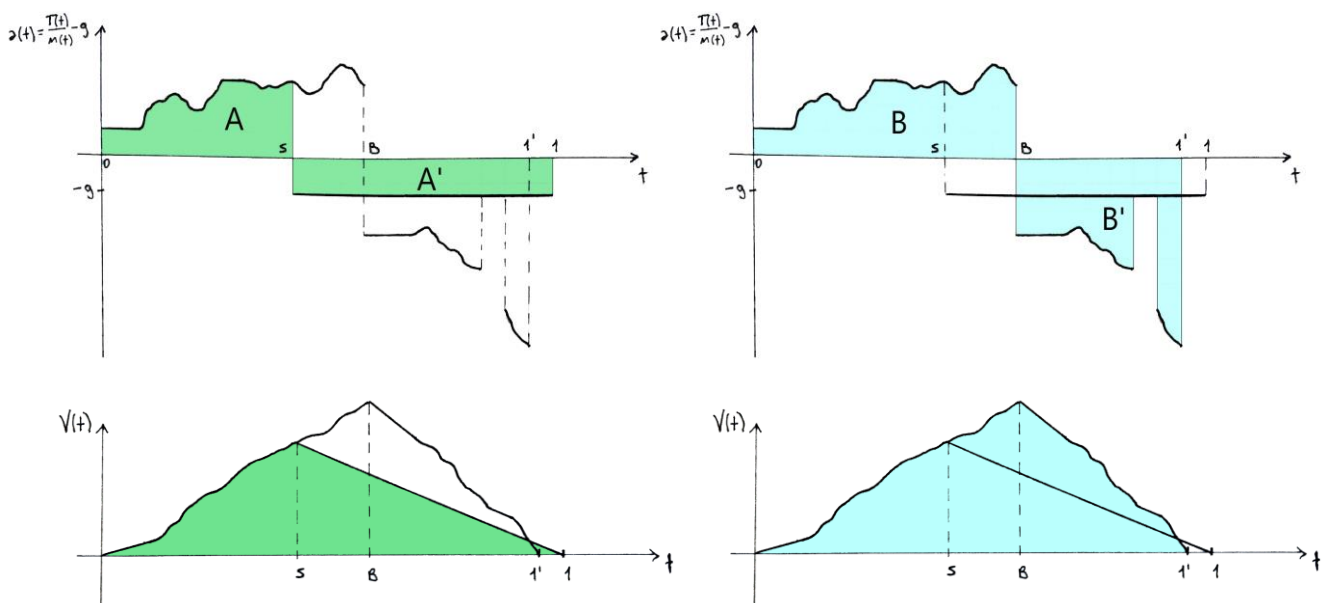


Figure 3.9 – Acceleration and velocity as a function of time for case *A* (left) and *B* (right).

Figure 3.9 shows acceleration and velocity as a function of time. The acceleration is directly related to the thrust as:

$$T(t) = a(t)m(t) + m(t)g = m(t)(g + a(t)) \quad m(t) = m_0 - \frac{1}{c} \int_{t_0}^t |T(t)| dt \quad (3.16)$$

According to Equation (3.16), if we assume to use the same thrust program, in the 0-S section, for both cases, the acceleration curves will inevitably be the same in that section. Since we assumed that $V_0 = V_1 = 0$, the acceleration time integral between t_0 and t_1 has to be zero, hence, area “A” will be equal to area “A'” and, in the same way, $B=B'$. Moreover, since we are comparing case A and case B assuming for both the same Z_1 , it follows that the velocity time integral, between t_0 and t_1 , has to be the same for the two cases (i.e., the green area of case A has to be equal to the blue area of case B).

Since in the 0-S section the acceleration curves of the two cases are identical, it follows that the speed curves will also be the same in that section. After point S, the velocity of case A will decrease with a constant slope (because the deceleration is constant and equal to g), while the one of case B will continue to rise as the acceleration phase lasts longer ($t_B > t_S$). After t_B , the absolute value of the acceleration of case B will be greater or equal to that of case A. It follows that the slope of the speed curve will also be greater or equal to that of case A and this, combined with the facts that $t_B > t_S$, $V_B > V_S$ and that the two areas must be equal, means that $t_{1'}$ will inevitably be smaller than t_1 .

Since both cases have the same thrust program for the 0-S stretch, and since the initial conditions are the same, the propellant consumption, up to point S, will be completely identical. For the rest of the manoeuvre, case B will consume some propellant for both the acceleration section S-B and the braking section B-1', while case A will consume no other propellant. This leads to the conclusion that the most efficient manoeuvre will always be the vertical ascent manoeuvre without braking thrust regardless the thrust program of the acceleration and braking phases.

Although we have found that the vertical ascent manoeuvre with the braking thrust is never more efficient than the one without the braking thrust, it may still be useful to quantify the propellant consumption of this manoeuvre. Therefore, a model similar to the one presented in Chapter 3.2.1 will be developed.

We will make the following assumptions (the angles α and φ are depicted in Figure 3.2):

1. $\varphi = 90^\circ \forall t$,
2. $\alpha = 0^\circ$ when: $t_0 \leq t < t_B$
3. $\alpha = 180^\circ$ when: $t_B \leq t \leq t_1$
4. $V_0 = V_1 = 0 \rightarrow \Delta V = 0$
5. $T_{0B} = \text{cost}$
6. $T_B = \text{cost}$

Where T_{0B} and T_B are the accelerating and braking thrust respectively.

By substituting these relations into Equation (3.7), we find:

$$\Delta V_{prop} = \overbrace{\Delta \vec{V}}^{=0} + \overbrace{\int_{t_0}^{t_B} \frac{T}{m} (1 - \cos(0^\circ)) dt}^{=0} + \int_{t_B}^{t_1} \frac{T}{m} \overbrace{(1 - \cos(180^\circ))}^{=2} dt + \int_{t_0}^{t_1} g \sin(90^\circ) dt$$

$$\Delta V_{prop} = \int_{t_B}^{t_1} 2 \frac{T_B}{m} dt + g(t_1 - t_0) = 2\Delta V_B + g \frac{1}{V_{avg}} (Z_1 - Z_0) = 2\Delta V_B + \Delta V_{gravity} \quad (3.17)$$

Note that $t_B \neq t_0$ corresponds to the time at which the propulsion system exerts the braking thrust T_B (i.e. "B" refers to the time at which the braking phase begins). It should also be noted that ΔV_B is intended as the change in velocity imposed by the sole thrust T_B without taking into account the decelerating effect of gravity and should not be confused with the actual change in velocity that the spacecraft will undergo during this phase. The relation between these two velocity changes is expressed by the following equation:

$$\Delta V_{B1eff} = \Delta V_B + g(t_1 - t_B) \quad (3.18)$$

3.2.4 Vertical ascent with braking thrust – Case 1: $T/m = \text{cost}$

In addition to the hypotheses made before, in this chapter we will also make the following simplifying assumption: $T/m \approx \text{cost}$. This means that if we assume $T \approx \text{cost}$, then also $m \approx \text{cost}$ which is acceptable only when the propellant mass ejected throughout the manoeuvre is not a significant fraction of the initial mass of the spacecraft. Anyway, under these assumptions the deceleration of the spacecraft during the deceleration phase will be equal to:

$$a_{Bg} = a_B + g \quad (3.19)$$

Where $a_B = T_B/m$ is deceleration induced by the braking thrust and $g \approx 1,62 \text{ m/s}^2$ is the gravitational acceleration. Assuming that the spacecraft does not reach the maximum velocity throughout the acceleration phase, the following relations hold:

$$0B: \begin{cases} a_{0B} = \frac{T_{0B}}{m} - g \\ V = a_{0B}t \\ Z = \frac{1}{2} a_{0B}t^2 \end{cases} \quad (3.20)$$

Where m is the spacecraft mass.

$$B1: \begin{cases} a_{Bg} = \frac{T_B}{m} + g \\ V = V_B - a_{Bg}(t - t_B) \\ Z = Z_B + V_B(t - t_B) - \frac{1}{2} a_{Bg}(t - t_B)^2 \end{cases} \quad (3.21)$$

Note that according to Equation (3.21): $V_1 = V_B - \overbrace{a_{Bg}(t_1 - t_B)}^{\Delta V_{B1eff}} = 0$.

By using Equations (3.20) and (3.21) it can be derived that:

$$\begin{cases} V_B = a_{0B}t_B = a_{Bg}(t_1 - t_B) \rightarrow t_1 = \left(\frac{a_{0B}}{a_{Bg}} + 1 \right) t_B \\ h_1 = Z_B + (Z_1 - Z_B) = \frac{1}{2} a_{0B}t_B^2 + V_B(t_1 - t_B) - \frac{1}{2} a_{Bg}(t_1 - t_B)^2 \end{cases} \quad (3.22)$$

With Equation (3.22), we find after some algebraic manipulations:

$$h_1 = \frac{1}{2}a_{0B}t_B^2 + \frac{1}{2}a_{Bg}(t_1 - t_B)^2 = \frac{1}{2}a_{0B}t_B^2 + \frac{1}{2}a_{Bg}\frac{a_{0B}^2}{a_{Bg}^2}t_B^2 = \frac{1}{2}\left(a_{0B} + \frac{a_{0B}^2}{a_{Bg}}\right)t_B^2 \quad (3.23)$$

thus:

$$t_B = \sqrt{\frac{2h_1}{a_{0B} + \frac{a_{0B}^2}{a_{Bg}}}} \quad (3.24)$$

$$t_1 = \left(\frac{a_{0B}}{a_{Bg}} + 1\right) \sqrt{\frac{2h_1}{a_{0B} + \frac{a_{0B}^2}{a_{Bg}}}} = \left(\frac{a_{0B}}{a_{Bg}} + 1\right)t_B \quad (3.25)$$

Considering Equation (3.17) and assuming that $t_0 = 0$, if we want to evaluate the propellant mass consumed during the manoeuvre we can simply use the Tsiolkovsky 's equation:

$$m_p = m_0 \left(1 - e^{-\frac{\Delta V_{prop}}{c}}\right)$$

$$\Delta V_{prop} = 2\Delta V_B + \Delta V_{gravity} = 2(a_{Bg} - g)(t_1 - t_B) + gt_1$$

$$m_p = f(a_{0B}, a_B, g, h_1, c, m_0) = m_0 \left(1 - e^{-\frac{2(a_{Bg}-g)(t_1-t_B)+gt_1}{c}}\right) \quad (3.26)$$

To allow for an easier interpretation of the results, although Equation (3.26) is valid for the case $T/m = cost$, we will refer to the more restrictive case: $T_{0B} = cost$, $m = cost$, and $T_B = cost$. Thanks to the assumptions made throughout this chapter, it is possible to estimate the propellant consumption using a simple algebraic equation (Eq. 3.26). Consequently, parametric sweep studies were conducted using a MATLAB script that implemented equations 3.26, 3.24 and 3.25.

The results of these analyses are shown in Figure 3.10 and Figure 3.11. According to these results, the most efficient condition is the one in which the braking thrust is zero ($T_B = 0$), which is in line with what we have demonstrated in Chapter 3.2.3. Since the computational cost of this MATLAB script is considerably lower than the Simulink models developed for the vertical ascent manoeuvre with and without the braking thrust, it has been decided to carry out several parametric sweep studies, reported in the Annexes 02, 03 and 04.

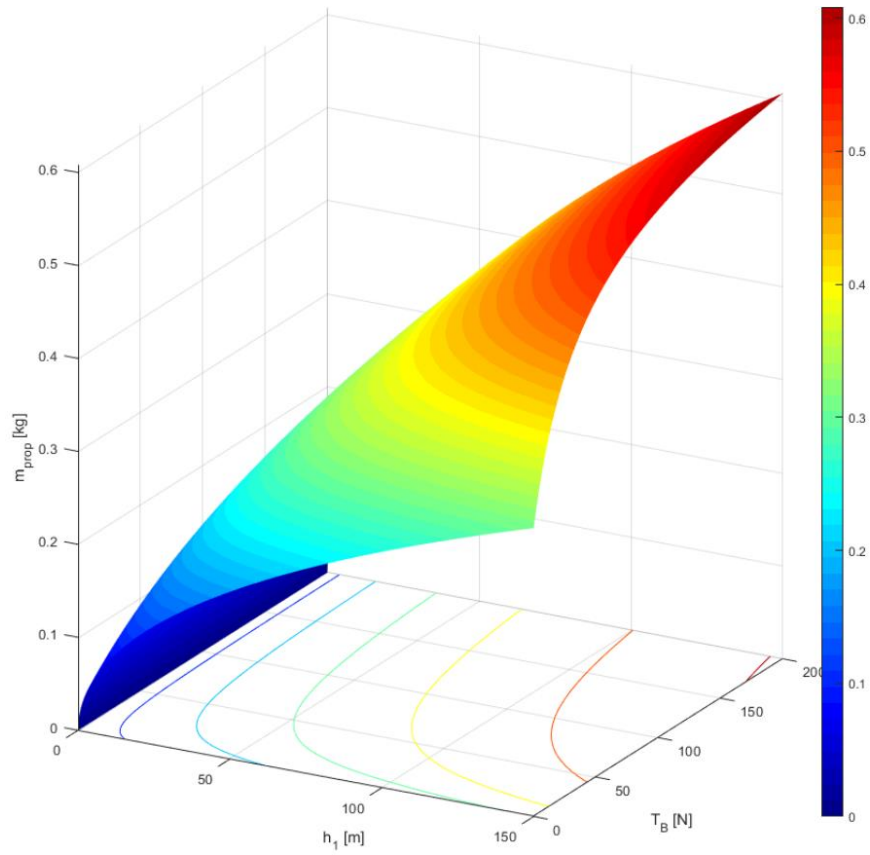


Figure 3.10 – Relation between T_B , h_1 and m_p with: $T_{0B} = 50N$, $m = 15\text{ kg}$, $I_{sp} = 150\text{ s}$

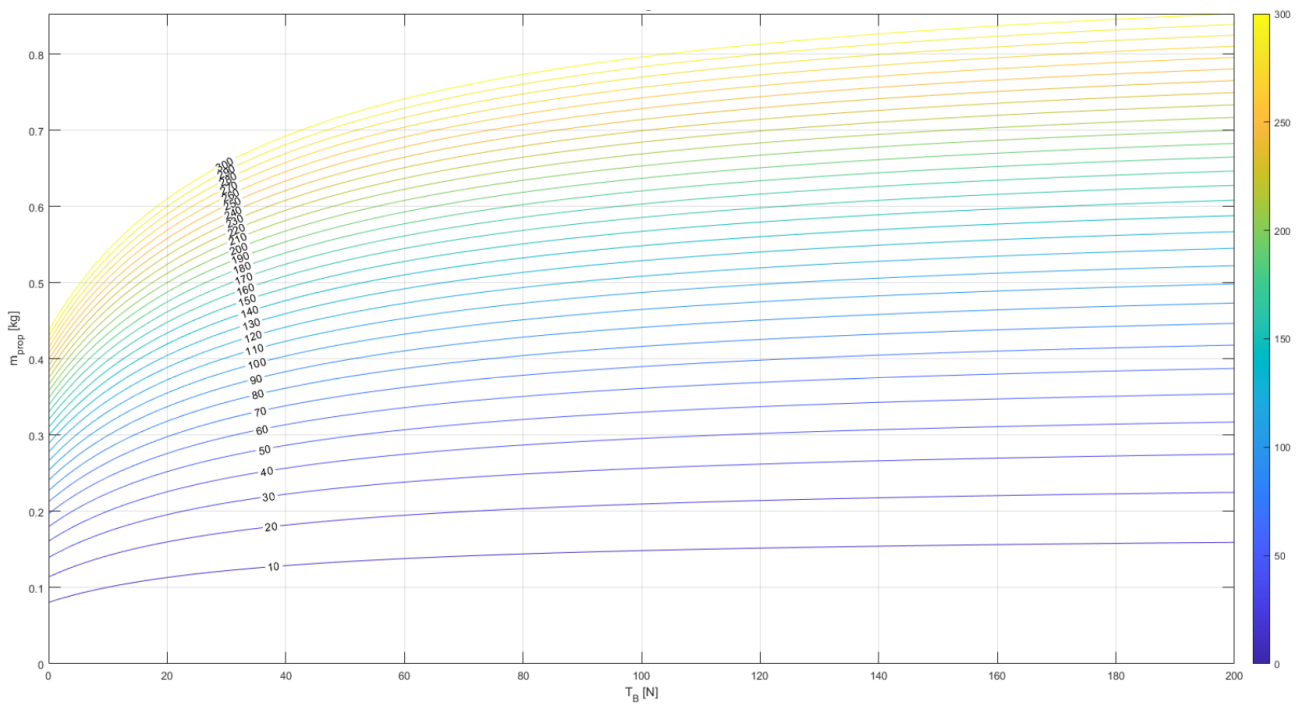


Figure 3.11 – Relation between T_B and m_p varying h_1 with: $T_{0B} = 50N$, $m = 15\text{ kg}$, $I_{sp} = 150\text{ s}$

3.2.5 Vertical ascent with braking thrust – Case 2: $T = \text{cost}$, $m \neq \text{cost}$

In the case we are going to analyse, T_{0B} and T_B will still be constant while the mass of the spacecraft will vary according to propellant consumption.

In Chapter 3.2.1, the condition which, if verified, made it possible to determine when the deceleration phase should begin, was expressed by Equation (3.12). This condition was derived for the case of constant deceleration (g). On the contrary, in this case, having assumed a constant braking thrust and a spacecraft variable mass, the deceleration will certainly not be constant. We therefore need to find a condition similar to that expressed by Equation (3.12), capable of taking into account the progressive lightening of the spacecraft induced by the consumption of propellant, which in turn is caused by the braking thrust.

$$\frac{dm}{dt} = \frac{T}{c} \xrightarrow{T, c = \text{cost}} m(t) = m_0 - \frac{T}{c} t \quad (3.27)$$

$$a_{B1}(t) = -\frac{T_B}{m} - g = -\frac{T_B}{m_B - \frac{T_B}{c} t} - g = -\frac{c}{\frac{m_B c}{T_B} - t} - g \quad (T_B, m_B, c, g > 0) \quad (3.28)$$

$$V_{B1}(t) = V_B + \int_0^t \left(-\frac{c}{\frac{m_B c}{T_B} - t} - g \right) dt = V_B + c \ln \left(\frac{m_B c}{T_B} - t \right) - gt - c \ln \left(\frac{m_B c}{T_B} \right) \quad (3.29)$$

where: $0 \leq t \leq t_1 - t_B$

$$\begin{aligned} Z_{B1}(t) &= Z_B + \int_0^t \left[V_B + c \ln \left(\frac{m_B c}{T_B} - t \right) - gt - c \ln \left(\frac{m_B c}{T_B} \right) \right] dt = \\ &= Z_B + V_B t + c \left[\left(t - \frac{m_B c}{T_B} \right) \ln \left(\frac{m_B c}{T_B} - t \right) - t \right] - \frac{1}{2} g t^2 - c \ln \left(\frac{m_B c}{T_B} \right) t + c \left(\frac{m_B c}{T_B} \right) \ln \left(\frac{m_B c}{T_B} \right) \end{aligned} \quad (3.30)$$

For the sake of simplicity, in these equations it was considered that $t_B = 0$, therefore when $t = 0 \rightarrow Z = Z_B$, $V = V_B$ and when $t = t_1 - t_B \rightarrow Z = Z_1 = h_1$, $V = 0$. By substituting these last relations in equations 3.29 and 3.30 we obtain

$$0 = V_B + c \ln \left(\frac{m_B c}{T_B} - (t_1 - t_B) \right) - g(t_1 - t_B) - c \ln \left(\frac{m_B c}{T_B} \right) \quad (3.31)$$

and:

$$\begin{aligned} h_1 - Z_B &= V_B (t_1 - t_B) + c \left[\left((t_1 - t_B) - \frac{m_B c}{T_B} \right) \ln \left(\frac{m_B c}{T_B} - (t_1 - t_B) \right) - (t_1 - t_B) \right] - \frac{1}{2} g (t_1 - t_B)^2 + \\ &\quad - c \ln \left(\frac{m_B c}{T_B} \right) (t_1 - t_B) + c \left(\frac{m_B c}{T_B} \right) \ln \left(\frac{m_B c}{T_B} \right) \end{aligned} \quad (3.32)$$

From Equation (3.31) we obtain:

$$c \ln \left(\frac{m_B c}{T_B} - (t_1 - t_B) \right) = g(t_1 - t_B) + c \ln \left(\frac{m_B c}{T_B} \right) - V_B \quad (3.33)$$

Substitution of Equation (3.33) into Equation (3.32) yields:

$$h_1 - Z_B = V_B (t_1 - t_B) + \left[-\frac{m_B c}{T_B} + (t_1 - t_B) \right] \left[g(t_1 - t_B) + c \ln \left(\frac{m_B c}{T_B} \right) - V_B \right] + \\ -c(t_1 - t_B) - \frac{1}{2} g(t_1 - t_B)^2 - c \ln \left(\frac{m_B c}{T_B} \right) (t_1 - t_B) + c \left(\frac{m_B c}{T_B} \right) \ln \left(\frac{m_B c}{T_B} \right) \quad (3.34)$$

$$h_1 - Z_B = V_B (t_1 - t_B) - \frac{m_B c}{T_B} g(t_1 - t_B) - \frac{m_B c}{T_B} c \ln \left(\frac{m_B c}{T_B} \right) + \frac{m_B c}{T_B} V_B + g(t_1 - t_B)^2 + c \ln \left(\frac{m_B c}{T_B} \right) (t_1 - t_B) \\ - V_B (t_1 - t_B) - c(t_1 - t_B) - \frac{1}{2} g(t_1 - t_B)^2 - c \ln \left(\frac{m_B c}{T_B} \right) (t_1 - t_B) + c \left(\frac{m_B c}{T_B} \right) \ln \left(\frac{m_B c}{T_B} \right) \quad (3.35)$$

$$h_1 - Z_B = -\frac{m_B c}{T_B} g(t_1 - t_B) + \frac{m_B c}{T_B} V_B + \frac{1}{2} g(t_1 - t_B)^2 - c(t_1 - t_B) = (t_1 - t_B) \left[-\frac{m_B c}{T_B} g - c \right] + \\ + \frac{1}{2} g(t_1 - t_B)^2 + \frac{m_B c}{T_B} V_B \quad (3.36)$$

By setting $t_1 - t_B = x$, we can see Equation (3.36) as a standard quadratic equation.

$$\underbrace{\frac{1}{2} g (t_1 - t_B)^2}_{a \quad x^2} + \underbrace{\left[-\frac{m_B c}{T_B} g - c \right] (t_1 - t_B)}_{b \quad x} + \underbrace{Z_B + \frac{m_B c}{T_B} V_B - h_1}_{d} = 0 \quad \rightarrow \quad x = \frac{-b \pm \sqrt{b^2 - 4ad}}{2a}$$

$$a = \frac{1}{2} g > 0$$

$$b = -\frac{m_B c}{T_B} g - c < 0$$

$$d = \underbrace{(Z_B - h_1)}_{<0} + \underbrace{\frac{m_B c}{T_B} V_B}_{>0} = \underbrace{\frac{m_B c}{T_B} V_B}_{>(h_1 - Z_B)} - (h_1 - Z_B) > 0$$

From Equation (3.27) we have that $\frac{m_B c}{T_B}$ corresponds to the time instant in which the spacecraft mass goes to zero ($m_p = m_0$). Thus, since we are only interested in physically meaningful results, we know for sure that $t_1 - t_B < \frac{m_B c}{T_B}$. During the deceleration phase, the velocity will always be lower than V_B , so if we consider the distance that the spacecraft would ideally cover if it travelled at V_B for a time longer than the actual duration of the braking phase ($\frac{m_B c}{T_B} > t_1 - t_B$), will certainly be greater than the actual distance covered by the spacecraft: $\frac{m_B c}{T_B} V_B > h_1 - Z_B$.

Thus:

$$x = \frac{-b \pm \sqrt{b^2 - \overbrace{(\dots > 0)}^{<|b|}}}{2a}$$

Although there are two mathematically acceptable results, the equation root we are interested in is:

$$t_1 - t_B = \frac{\frac{m_B c}{T_B} g + c - \sqrt{\left(\frac{m_B c}{T_B} g + c\right)^2 - 2g \left(\frac{m_B c}{T_B} V_B - (h_1 - Z_B)\right)}}{g} \quad (3.37)$$

By substituting this relation into Equation (3.31), we finally obtain the condition to be verified at each integration step of the model in order to determine when the deceleration phase begins (the parameters m, V, z are those that vary over time).

$$0 = V + c \ln \left(\frac{mc}{T_B} - \left[\frac{\frac{mc}{T_B} g + c - \sqrt{\left(\frac{mc}{T_B} g + c\right)^2 - 2g \left(\frac{mc}{T_B} V - (h_1 - Z)\right)}}{g} \right] \right) +$$

$$-g \left[\frac{\frac{mc}{T_B} g + c - \sqrt{\left(\frac{mc}{T_B} g + c\right)^2 - 2g \left(\frac{mc}{T_B} V - (h_1 - Z)\right)}}{g} \right] - c \ln \left(\frac{mc}{T_B} \right) \quad (3.38)$$

Let us now see the main differences with the MATLAB-Simulink model presented in Chapter 3.2.1.

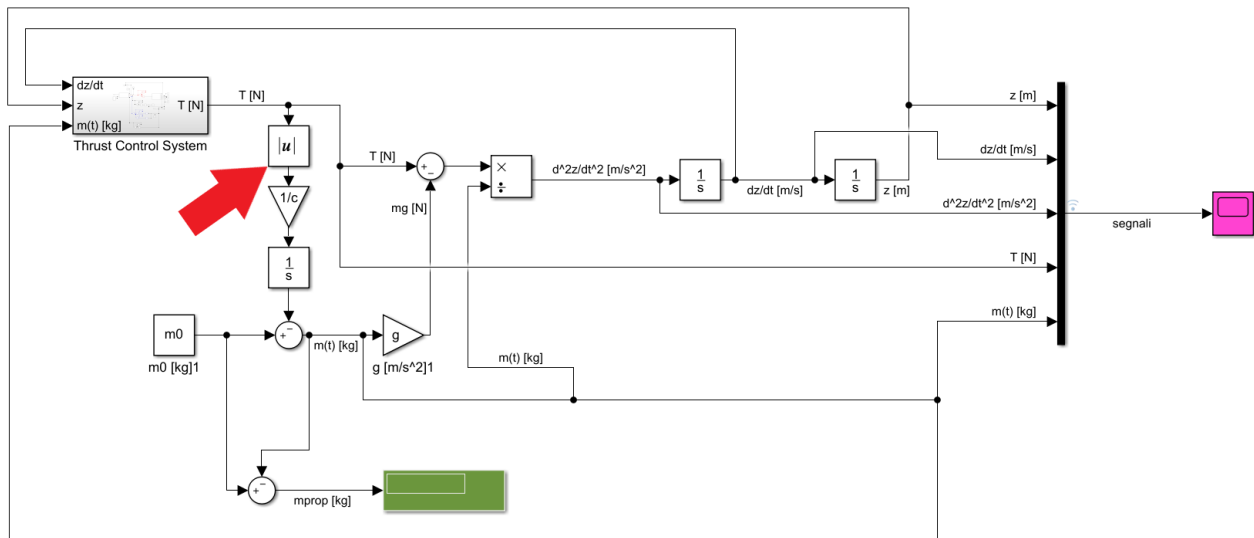


Figure 3.12 – Main sytem of the vertical ascent model (with braking thrust)

The main system is very similar to that of the vertical ascent without the braking thrust. In fact, both systems have the same task of computing Equation (3.13), which is obviously still valid for this case. The only

difference, well highlighted by the red arrow in Figure 3.12, is that the thrust, in this case, can assume negative values, so when calculating the instantaneous mass of the spacecraft it is necessary to use the absolute value of the thrust. Therefore, Equation (3.14), which is computed by the Main system of the model, becomes:

$$m(t) = m_0 - \int_0^t \frac{|T(t)|}{c} dt \quad (3.39)$$

As for the model presented in Chapter 3.2.1, in order to solve these equations (3.13 and 3.39) it is necessary to know the instantaneous value of the thrust which in turn depends on the instantaneous values of mass, velocity and altitude. The "Thrust Control System" depicted in Figure 3.13 has to provide the correct thrust by receiving the 3 above-mentioned values as inputs.

cond1

If Equation (3.38) is satisfied, then cond1 goes from 0 to 1 and will remain equal to 1 until the end of the simulation, else, until the equation is not satisfied, cond1 remains equal to 0. This approach was chosen because in this way the condition not only acts as a trigger (the propulsion system will exert a braking thrust equal to T_B when cond1 goes from 0 to 1) but also gives information about the phase in which the spacecraft is operating (if 0: acceleration phase or intermediate phase ($V = V_{01_{max}}$), if 1: deceleration phase).

cond2

if $\frac{|h_1 - Z|}{h_1} \leq tol2$, then cond2 is equal to 1, else it is equal to 0.

This condition has remained unchanged compared to that of the model presented in Chapter 3.2.1. Thus, for the role played by this condition, please refer to page 25.

cond4

if $V < 0$, then cond4 is equal to 1, else, it is equal to 0.

This condition has remained unchanged compared to that of the model presented in Chapter 3.2.1. Thus, for the role played by this condition, please refer to page 25.

cond3

When $V_{01_{max}} - V(t)$ goes from a positive to a negative value, cond3 goes from 0 to 1 and will remain 1 until the end of the simulation.. This condition is used to limit the maximum speed by lowering the thrust from T_{0B} to $m(t)g$ during the acceleration phase.

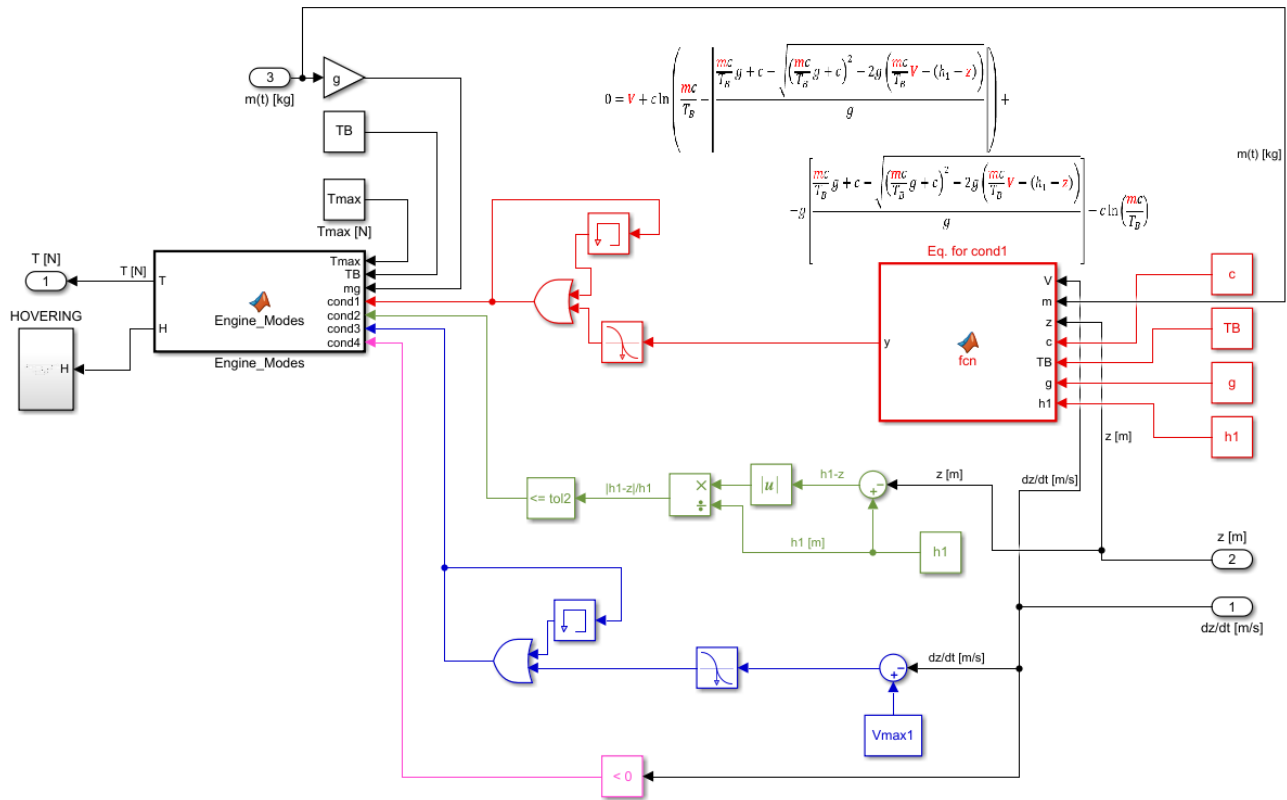


Figure 3.13 – Thrust Control System of the vertical ascent model (with braking thrust)

The logic behind the "Engine_Modes" block is well summarised by the following code.

```
H=0;
if cond1==0 && cond3==0
    T = T0B;
elseif cond1==0 && cond3==1
    T = mg;
elseif cond1==1 && cond4==1 && cond2==1
    T = mg;
    H = 1;
elseif cond1==1 && ~(cond2==1 && cond4==1)
    T = -TB;
```

Finally, as far as the “HOVERING” subsystem is concerned, it is identical to that of the model without the braking thrust (shown in Figure 3.6).

The input parameters used to obtain the results in Figure 3.14 are:

$T_{0B} = 50 \text{ N}$	$h_1 = 100 \text{ m}$	$tol2 = 0.1$
$T_B = 20 \text{ N}$	$I_{sp} = 150 \text{ s}$	Solver: ode1(Euler)
$V_{01_{max}} = 10 \text{ m/s}$	$\Delta t_{h_1} = 5 \text{ s}$	$DT = 1 \text{ ms}$
$m_0 = 15 \text{ kg}$		

Where DT is the integration step.

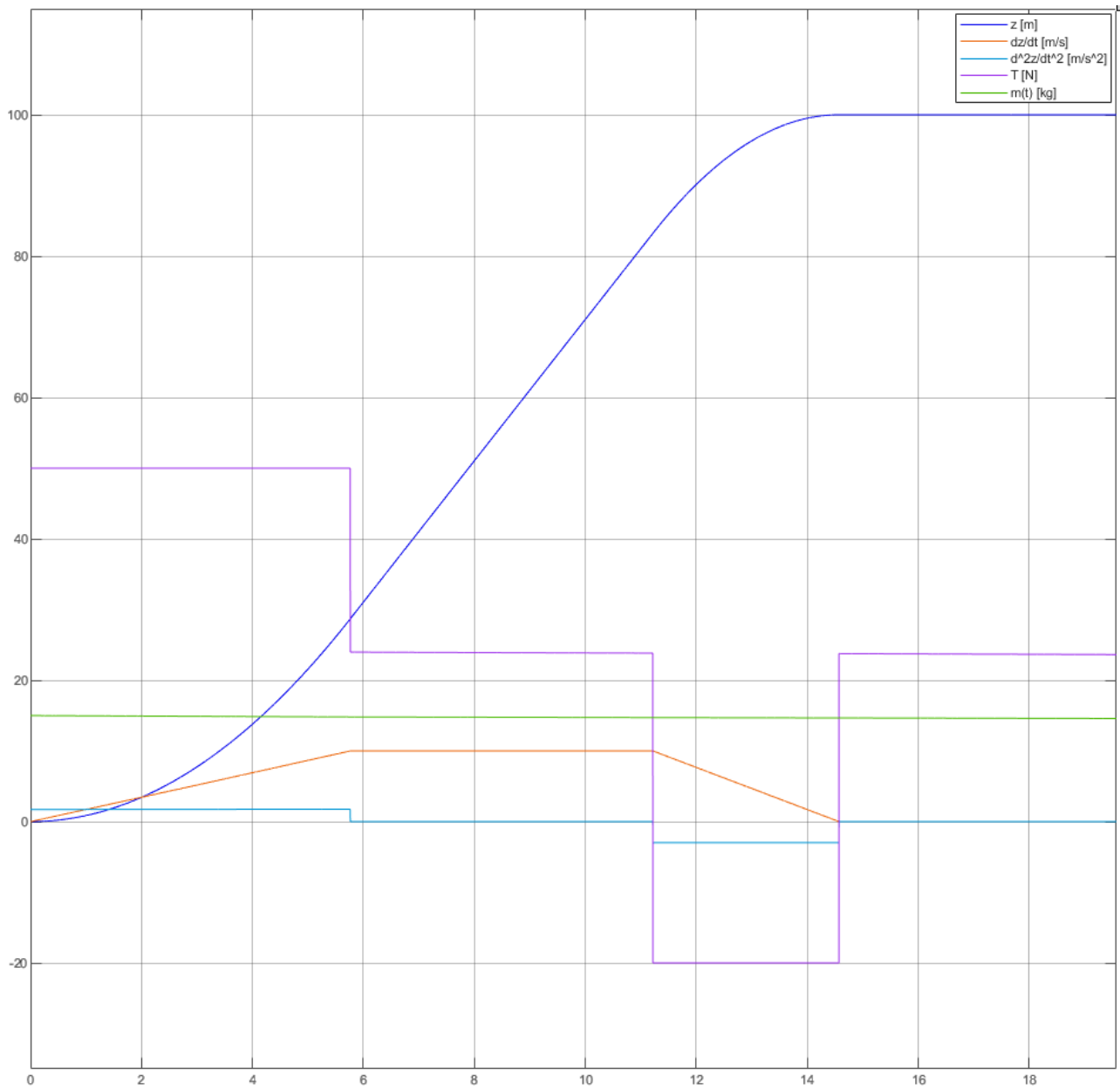


Figure 3.14 – Model output example [vertical ascent model (with braking thrust)]

3.2.6 Vertical ascent with braking thrust – Results and conclusions

Chapter 9 - Annex 04 shows the results of the comparison between Case 1 and Case 2 which was carried out considering two scenarios, one realistic and one exaggerated.

The aim of the exaggerated scenario is to make the differences between the two cases as evident as possible. The constitutive equations of Case 1 are based on the simplifying hypothesis: $T/m = cost$, i.e. constant acceleration. In both cases we have chosen to consider constant thrusts, the main difference between the two models is therefore that Case 1, unlike Case 2, does not take into account the variation in the mass of the spacecraft induced by propellant consumption. Therefore, Case 1, even in the case of substantial propellant consumption, will continue to consider $T/m = cost$, while Case 2 will in fact operate with a variable acceleration over time. Therefore, we expect substantial differences between the two models when the variation in the acceleration during the manoeuvre is no longer negligible; which happens, in the case of constant thrusts, when the variation in the spacecraft mass, induced by the expulsion of the propellant, becomes relevant. This can be determined directly from the time acceleration graphs, or indirectly through the values of t_B and t_1 (if the acceleration and deceleration of the spacecraft remain approximately constant during the respective phases, these values will be almost equal between the two cases).

As far as the "exaggerated" scenario is concerned, the following input parameters were considered: $m_0 = 5kg$, $h_1 = 100m$ and $I_{sp} = 10s$. The black dots shown in Figure 9.4, 9.5, 9.6, 9.7, 9.8, 9.9, and 9.10 represent the results of Case 2 calculated considering the following thrust values: $T_{B0} = 50, 40, 30, 20, 12, 8.5 N$ and $T_B = 60, 50, 40, 30, 20, 10, 5, 3, 1, 0 N$. The magenta points refer instead to the results of Case 1 obtained considering the same values of T_{B0} and T_B .

From Figure 9.11, it is clear that the "exaggerated" case actually leads to a non-constant acceleration and this justifies the substantial differences between the results of Case 1 and Case 2 for this scenario.

The results related to the "realistic" scenario, obtained considering the following input parameters: $m_0 = 15 kg$ and $I_{sp} = 150s$, are shown in Figure 9.1, 9.2 and 9.3. In this scenario the differences between the two cases are clearly less evident, except for the results having $T_{0B} = 25N$. A comparison between Figure 9.12 and Figure 9.13 explains the reason for this exception. Both figures refer to Case 2 with two different values of T_{0B} . It is evident how in Figure 9.13 the acceleration, during the acceleration phase, varies in a not negligible way (in Case 1 it remains constant by hypothesis). In particular, due to the lightening of the spacecraft caused by the expulsion of the propellant mass during the manoeuvre, the average acceleration will inevitably be greater than in Case 1 and this suggests why Case 2 gives lower m_p values for the results relative to $T_{0B} = 25N$. Conversely, as shown in Figure 9.12, for accelerating thrusts greater than $T_{0B} = 25N$, the acceleration assumes approximately constant values, and therefore the results of Case 2 relating to these thrust levels are similar to those of Case 1. The same thing can be deduced by observing the values of t_B and t_1 . Considering the case: $T_{0B} = 25 N$, $T_B = 60 N$, $m_0 = 15 kg$, $I_{sp} = 150 s$, and $h_1 = 100 m$; for Case 2 the following values were obtained: $t_B = 49.84 s$ and $t_1 = 50.66 s$, while Case 1 gave the following results: $t_B = 65.20 s$ and $t_1 = 65.74 s$. As mentioned before, for higher values of T_{0B} (let's consider for example the same case as before but with $T_{0B} = 40N$ and $T_B = 20N$), there is no longer so much difference between the two values (Case 2: $t_B = 11.73 s$ and $t_1 = 15.96 s$ vs Case 1: $t_B = 11.88 s$ and $t_1 = 16.09 s$).

Since the results of Case 1 were obtained by means of a MATLAB script that simply had to implement Equation (3.26), the computational cost of this model is much lower than the one of Case 2. If a large number of simulations were to be carried out, for example in the case of parametric sweep analyses, it would be

important to understand whether a lower computational cost instrument, such as Case 1, can be used compared to a less performing tool, such as the Case 2 model. The results reported in Chapter 9 - Annex 04 allow us to assess when it is appropriate to use one tool rather than the other. Furthermore, these results have shown once again how the most efficient thrust program, for the vertical ascent, is the one in which $T_B = 0N$ and T_{0B} is as high as possible.

3.3 Horizontal translation

The horizontal translation manoeuvre refers to a nominal trajectory in which the LuNaDrone will move along the X-axis (see **Errore. L'origine riferimento non è stata trovata.** and Figure 3.1) without changing its altitude. Although this is a simplified manoeuvre (all the assumptions presented in Chapter 3.1 still apply) it could represent, for example, the type of movement that the LuNaDrone will have to perform in order to translate from the point where it is deployed by the rover/lander to the point 2, after which, it will begin its descent inside the lunar pit. In addition to this specific case, this manoeuvre will simply refer to all those cases where, during the flight, the LuNaDrone will move between two waypoints having the same altitude. At present, the Flight Control ConOps has not yet been defined, but we can refer to the one presented in [18] where each waypoint is specified by a position, a translation heading, a dwell time, and a dwell heading, and assume that the LuNaDrone's Flight Control ConOps will follow a similar approach.

In this chapter we will analyse the horizontal translation manoeuvre as follows. Let us suppose that the propulsion system is able to exert three thrust components: one vertical (along the Z-axis and directed in its positive direction), and two horizontal, both directed along the X-axis but opposite to each other as shown in Figure 3.15.

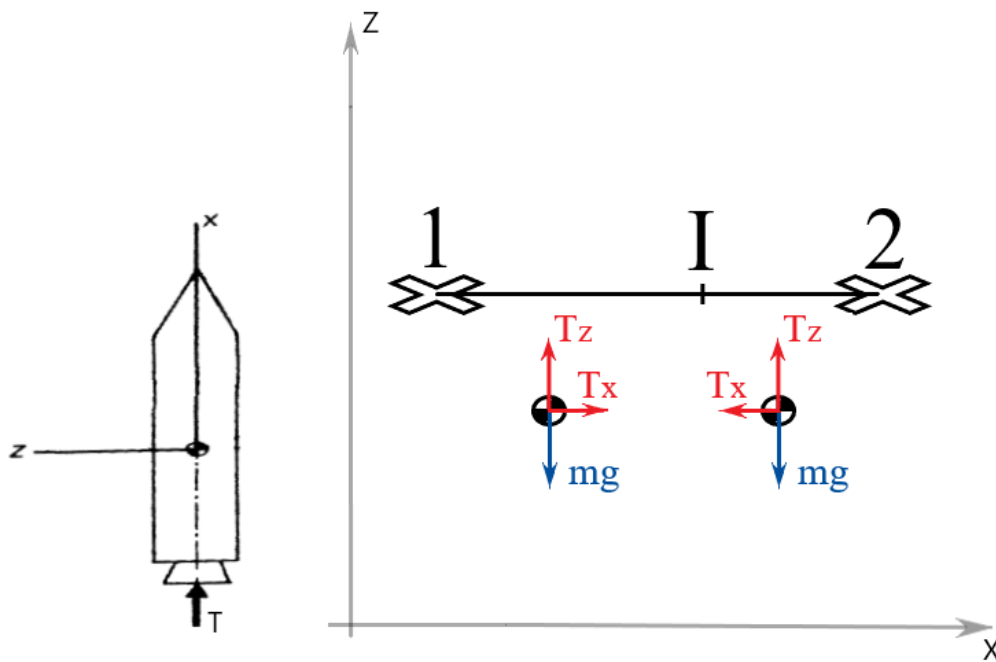


Figure 3.15 – Thrust components in the horizontal translation

It should be noted that at the moment we are not yet making any assumptions about the configuration of the propulsion system, which, we will see later, leads to substantial differences in propellant consumption. Anyway, for the LuNaDrone not to change altitude during this manoeuvre, the absolute value of the vertical thrust component (T_z) must be, instant by instant, equal to the absolute value of the weight of the spacecraft: $m(t)g$. In the models presented in this chapter, this thrust component will be taken into account just for the propellant consumption since, in theory, it should not cause any movement along the Z-axis. The lateral movement of the spacecraft is obviously caused by the T_x thrust components. For the sake of simplicity, we will assume that these components have a constant absolute value, thus $T_x = \pm T_{12}$. However, this does not mean that the acceleration will also be constant because, although the thrust is constant, the spacecraft has a variable mass (due to propellant consumption).

Let us summarise the assumptions and the main characteristics of this manoeuvre.

1. $\varphi = 0^\circ \forall t$ (see Figure 3.2)
2. $|T \cos \alpha| = |T_X| = T_{12} = \text{cost} \quad (V < V_{12_{\max}})$
3. $|T \cos \alpha| = |T_X| = 0 \text{ N} \quad (V \geq V_{12_{\max}})$
4. $|T \sin \alpha| = |T_Z| = |mg|$
5. $V_1 = V_2 = 0 \text{ m/s}$

$t = t_1$

At time t_1 the propulsion system will exert a thrust component T_X equal to T_{12} which will produce a positive horizontal acceleration (according to the positive direction of the X-axis).

$t_1 < t < t_I$

As mentioned before, the thrust program, as far as the horizontal component is concerned, consists in constantly exerting a horizontal thrust equal to T_{12} : $T_X = T_{12}$. If the maximum speed $V_{12_{\max}}$ is reached, the lateral thrust component will cancel ($T_X = 0 \text{ N}$), while the vertical one will continue to be equal to the weight of the spacecraft ($T_Z(t) = m(t)g$). The maximum velocity $V_{12_{\max}}$ can be set either by the performance of the GN&C system, or just to analyse different thrust programs without introducing new parameters. In fact, if it is assumed that during the manoeuvre the maximum velocity is never reached, according to what has been stated so far, the spacecraft would just proceed up to point I , while exerting a constant horizontal thrust ($T_X = T_{12}$). Once the spacecraft reaches point I , the propulsion system will exert a horizontal thrust having the same magnitude as the previous one but directed from point 2 to point 1 ($T_X = -T_{12}$). So, if we want to analyse manoeuvres in which, given T_{12} and the distance between point 1 and point 2, we introduce an intermediate phase, where $T_X = 0$, of increasingly long durations, we just need to progressively lower the value of $V_{12_{\max}}$. In this way, we can analyse different strategies simply by changing the value of $V_{12_{\max}}$ without having to introduce a new parameter.

$t = t_I$

Once the spacecraft has covered a certain distance, reached a certain speed and has a certain instantaneous mass, the propulsion system will exert a horizontal thrust component equal to $-T_{12}$ ($T_X = -T_{12}$), thus starting the braking phase. In order to determine whether the spacecraft has reached point I we can use Equation (3.56). This equation also shows that there is no dependence with the spacecraft mass, position, and velocity-time history but only with their instantaneous values.

$t_I < t < t_2$

The $I-2$ section identifies the deceleration phase. As mentioned above, the lateral thrust component will be constant and equal to $-T_{12}$ ($T_X = -T_{12}$).

$t = t_2$

Once the spacecraft reaches point 2, the model must be able to simulate a stationary hover lasting Δt_{h_2} seconds. Obviously, the most efficient condition will be the one in which $\Delta t_{h_2} = 0 \text{ s}$.

	$t = t_1$	$t_1 < t < t_I$		$t = t_I$	$t_I < t < t_2$	$t = t_2$
$X [m]$	0	$0 < X < X_I$		$X = X_I$	$X_I < X < X_2$	$X = X_2$
$V_X \left[\frac{m}{s} \right]$	0	$0 < V_X < V_{12_{max}}$	$V_X = V_{12_{max}}$	$0 < V_X \leq V_{12_{max}}$	$0 < V_X < V_{12_{max}}$	0
$V_Z \left[\frac{m}{s} \right]$	0	0	0	0	0	0
$a_X \left[\frac{m}{s^2} \right]$	$\frac{T_{12}}{m_1}$	$\frac{T_{12}}{m}$	0	$-\frac{T_{12}}{m}$	$-\frac{T_{12}}{m}$	0
$a_Z \left[\frac{m}{s^2} \right]$	0	0	0	0	0	0
$m [kg]$	m_1	$0 < m < m_1$	$0 < m < m_1$	$0 < m < m_1$	$0 < m < m_1$	$0 < m < m_1$
$T_X [N]$	T_{12}	T_{12}	0	$-T_{12}$	$-T_{12}$	0
$T_Z [N]$	$m_1 g$	mg	mg	mg	mg	mg

Table 3.4 – Summary of horizontal translation manoeuvre

3.3.1 Horizontal translation with auxiliary thrusters – Case 1: $T_X = \text{cost}$, $m = \text{cost}$

There are essentially two ways in which the propulsion system can exert the two thrust components T_X and T_Z . In the first case we use a single thruster with the thrust axis aligned with the longitudinal axis of the spacecraft (as assumed in Chapter 3.1). Therefore, in this case, in order to have a certain T_X component it is necessary to tilt the spacecraft, thus the angle between the x-axis of the vehicle reference frame and the X-axis of the inertial frame is no longer 90° (see the angle θ in Figure 3.1). The other way is to assume that the two thrust components are provided by different thrusters, one aligned with the z-axis and the other with the x-axis of the vehicle reference frame, and assuming that $\theta = 90^\circ$ for the whole manoeuvre. In this chapter we will analyse the latter approach.

Since the propulsion system must exert two horizontal thrust components (both directed along the X-axis but one pointing from point 1 to point 2 and the other from point 2 to point 1) we can assume either to install only one auxiliary thruster and rotate the spacecraft 180° around the x-axis before the deceleration phase, or we can assume to install two auxiliary thrusters, both having the thrust axis aligned with the z-axis of the vehicle reference frame, and hence with the X-axis of the inertial frame, pointing in opposite directions as shown in Figure 3.16.

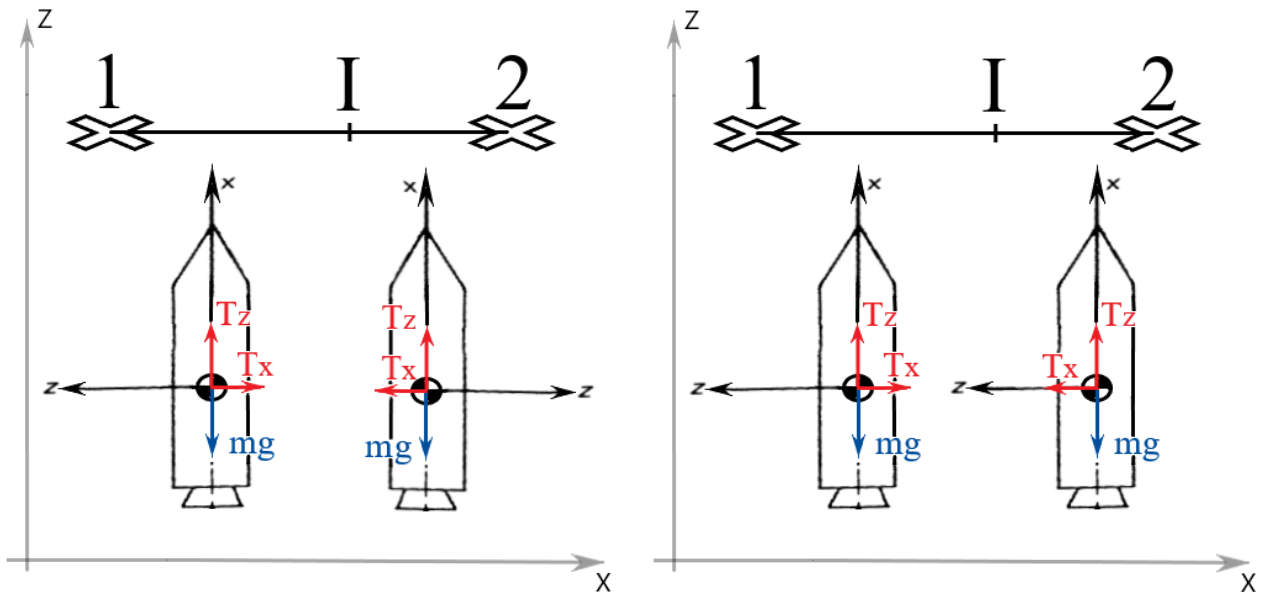


Figure 3.16 – One auxiliary thruster configuration (left), two auxiliary thrusters configuration (right)

It is clear that, once the distance between point 1 and 2 is fixed, the shorter the manoeuvre time and the lower the propellant consumption associated with the vertical thrust T_Z . However, in order to shorten this time it is necessary to accelerate and brake horizontally with the maximum capacity of the spacecraft, thus maximising the propellant consumption associated with T_X . In fact, as Equation 3.40 shows, the propellant consumption associated with T_X is minimal when the absolute value of T_X , and/or the relative firing time, tend to zero. It is evident, however, that by doing so the time of the manoeuvre (t_2) tends to infinity and the propellant consumption associated with T_Z will also tend to infinity.

$$\Delta V_{prop} = \int_{t_1}^{t_2} \frac{T_Z}{m} dt + \int_{t_1}^{t_2} \frac{|T_X|}{m} dt = \int_{t_1}^{t_2} g dt + \int_{t_1}^{t_2} \frac{|T_X|}{m} dt$$

$$\Delta V_{prop} = \overbrace{g(t_2 - t_1)}^{\Delta V_{propT_Z}} + \overbrace{\int_{t_1}^{t_{V_{12max}}} \frac{T_{12}}{m} dt + \int_{t_I}^{t_2} \frac{T_{12}}{m} dt}^{\Delta V_{propT_X}} \quad (3.40)$$

Where $t_{V_{12max}}$ is the time instant in which $V = V_{12max}$ and hence T_X goes from T_{12} to 0.

$$\text{if: } T_{12} \uparrow \text{ and/or } \overbrace{(t_{V_{12max}} - t_1) + (t_2 - t_I)}^{\text{firing time of } T_{12}} \uparrow \quad \overrightarrow{\text{then}} \quad t_2 \downarrow \rightarrow \Delta V_{propT_Z} \downarrow \quad \text{but} \quad \Delta V_{propT_X} \uparrow$$

The greater the T_{12} and/or the relative firing time: $(t_{V_{12max}} - t_1) + (t_2 - t_I)$, the shorter the time t_2 , and therefore the lower will be ΔV_{propT_Z} , but the greater will be ΔV_{propT_X} . Since we have two opposite trends, we need to find a way to determine the minimum consumption condition.

As a first approach we can consider the following assumptions (in addition to those presented in Chapter 3.3):

1. $m = \text{cost}$
2. $V_{12max} = \infty \rightarrow t_{V_{12max}} \equiv t_I$

The first assumption can be considered plausible if the propellant mass consumed during the manoeuvre does not represent an important fraction of the initial mass of the spacecraft. The second one refers to the case in which the acceleration phase is always followed by the deceleration phase without any intermediate phase, during which $T_X = 0$.

Applying these assumptions to Equation 3.40 yields:

$$\Delta V_{prop} = g(t_2 - t_1) + \frac{|T_X|}{m}(t_2 - t_1) = g(t_2 - t_1) + \frac{T_{12}}{m}(t_2 - t_1) \quad (3.41)$$

It is quite obvious that there is a relation between the value of T_{12} and the time $t_2 - t_1$ (it is intuitive that the greater the T_{12} and the lower the $t_2 - t_1$). The same procedure used in Chapter 3 can be used here to demonstrate this relation. The results are:

$$t_I - t_1 = \sqrt{\frac{2d_{12}}{a_{1I} + \frac{a_{1I}^2}{a_{I2}}}} \quad (3.42)$$

$$t_2 - t_1 = \left(\frac{a_{1I}}{a_{I2}} + 1\right) \sqrt{\frac{2d_{12}}{a_{1I} + \frac{a_{1I}^2}{a_{I2}}}} = \left(\frac{a_{1I}}{a_{I2}} + 1\right) (t_I - t_1) \quad (3.43)$$

Where a_{1I} and a_{I2} are the acceleration and deceleration of sections 1-I and I-2 respectively. By substituting $a_{1I} = a_{I2} = |T_X|/m = T_{12}/m$ into Equation 3.43, we find:

$$t_2 - t_1 = 2 \sqrt{\frac{d_{12}}{\frac{|T_X|}{m}}} = 2 \sqrt{\frac{d_{12}}{\frac{T_{12}}{m}}} \quad (3.44)$$

Thus, Equation 3.41 becomes:

$$\Delta V_{prop} = 2g \sqrt{\frac{d_{12}}{\frac{T_{12}}{m}}} + \frac{T_{12}}{m} 2 \sqrt{\frac{d_{12}}{\frac{T_{12}}{m}}} = 2g \sqrt{\frac{d_{12}}{\frac{T_{12}}{m}}} + 2 \sqrt{d_{12}} \sqrt{\frac{T_{12}}{m}} = 2\sqrt{d_{12}} \left(\frac{g}{\sqrt{\frac{T_{12}}{m}}} + \sqrt{\frac{T_{12}}{m}} \right) \quad (3.45)$$

The T_{12} value at which we have the lowest propellant consumption is found by differentiating Equation 3.45 with respect to T_{12}/m , and putting the result equal to zero:

$$\frac{\partial \Delta V_{prop}}{\partial (T_{12}/m)} = \frac{\sqrt{d_{12}} \left(\frac{T_{12}}{m} - g \right)}{\left(\frac{T_{12}}{m} \right)^{3/2}} = 0 \quad \rightarrow \quad \frac{T_{12}}{m} = g \quad (3.46)$$

Actually, in order to determine whether this is a minimum point or not it would be necessary to evaluate the sign of the second derivative of ΔV_{prop} , with respect to T_{12}/m . However, from the following graphs we can clearly see that this is a minimum point, so this operation is not necessary.

In the case presented in this chapter, the optimal condition is reached when the lateral thrust component is equal to the vertical one ($T_x = T_z = mg$). However, this result has been obtained assuming rather strong hypotheses. Therefore, in the next chapter we will analyse a more realistic case in which the mass of the spacecraft varies according to the propellant consumption and we will also consider intermediate phases of varying duration ($t_{V_{12max}} \neq t_I$).

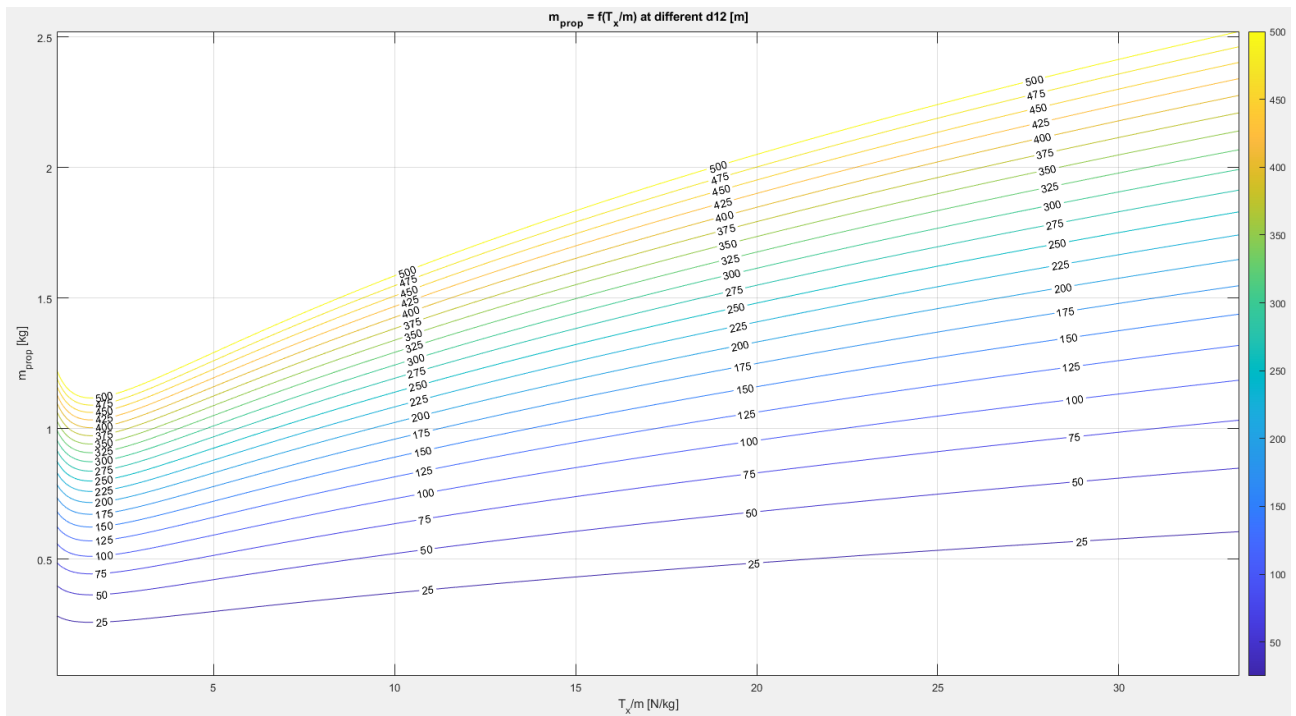


Figure 3.17 – Propellant mass varying T_x/m and d_{12} in the case of $T_x m = \text{cost}$ and $t_{V_{12max}} = t_I$

3.3.2 Horizontal translation with auxiliary thrusters – Case 2: $T_X = \text{cost}$, $m \neq \text{cost}$

In the case presented in this chapter the mass of the spacecraft will vary according to the propellant mass consumed. As we did in the previous chapter, we will assume $T_X = \text{cost}$ while, unlike the previous chapter, we will consider intermediate stages of variable duration ($t_{V_{12\max}} \neq t_I$).

Similar to what we did in Chapter 3.2.5, we need to find a relation that tells us when it is time to start the braking phase ($t = t_I \rightarrow T_X = T_{12}$). In the following equations we will take into account only the dynamics along the X-axis (so, for example, \mathbf{a}_{I2} indicates the acceleration along this axis) and we will analyse only the stretch related to the deceleration phase (I-2).

$$a_{I2}(t) = -\frac{T_{12}}{m} = -\frac{T_{12}}{m_I - \frac{T_{12}}{c}t} = -\frac{c}{\frac{m_I c}{T_{12}} - t} \quad (T_{12}, m_I, c > 0) \quad (3.47)$$

$$V_{I2}(t) = V_I + \int_0^t \left(-\frac{c}{\frac{m_I c}{T_{12}} - t} \right) dt = V_I + c \ln \left(\frac{m_I c}{T_{12}} - t \right) - c \ln \left(\frac{m_I c}{T_{12}} \right) \quad (3.48)$$

where: $0 \leq t \leq t_1 - t_I$

$$\begin{aligned} X_{I2}(t) &= X_I + \int_0^t \left[V_I + c \ln \left(\frac{m_I c}{T_{12}} - t \right) - c \ln \left(\frac{m_I c}{T_{12}} \right) \right] dt = \\ &= X_I + V_I t + c \left[\left(t - \frac{m_I c}{T_{12}} \right) \ln \left(\frac{m_I c}{T_{12}} - t \right) - t \right] - c \ln \left(\frac{m_I c}{T_{12}} \right) t + c \left(\frac{m_I c}{T_{12}} \right) \ln \left(\frac{m_I c}{T_{12}} \right) \end{aligned} \quad (3.49)$$

For the sake of simplicity, in these equations it was considered that $t_I = 0$, therefore when $t = 0 \rightarrow X = X_I$, $V = V_I$ and when $t = t_2 - t_I \rightarrow X = X_2 = d_{12}$, $V = 0$. By substituting these last relations into Equations (3.48) and (3.49) we obtain:

$$0 = V_I + c \ln \left(\frac{m_I c}{T_{12}} - (t_2 - t_I) \right) - c \ln \left(\frac{m_I c}{T_{12}} \right) \quad (3.50)$$

and:

$$\begin{aligned} d_{12} - X_I &= V_I (t_2 - t_I) + c \left[\left((t_2 - t_I) - \frac{m_I c}{T_{12}} \right) \ln \left(\frac{m_I c}{T_{12}} - (t_2 - t_I) \right) - (t_2 - t_I) \right] + \\ &\quad - c \ln \left(\frac{m_I c}{T_{12}} \right) (t_2 - t_I) + c \left(\frac{m_I c}{T_{12}} \right) \ln \left(\frac{m_I c}{T_{12}} \right) \end{aligned} \quad (3.51)$$

From Equation (3.50) we obtain:

$$c \ln \left(\frac{m_I c}{T_{12}} - (t_2 - t_I) \right) = c \ln \left(\frac{m_I c}{T_{12}} \right) - V_I \quad (3.52)$$

Substitution of Equation (3.52) into Equation (3.51) yields:

$$\begin{aligned} d_{12} - X_I &= V_I (t_2 - t_I) + \left[-\frac{m_I c}{T_{12}} + (t_2 - t_I) \right] \left[c \ln \left(\frac{m_I c}{T_{12}} \right) - V_I \right] - c(t_2 - t_I) + \\ &\quad - c \ln \left(\frac{m_I c}{T_{12}} \right) (t_2 - t_I) + c \left(\frac{m_I c}{T_{12}} \right) \ln \left(\frac{m_I c}{T_{12}} \right) \end{aligned} \quad (3.53)$$

$$d_{12} - X_I = V_I (t_2 - t_I) - \frac{m_I c}{T_{12}} c \ln \left(\frac{m_I c}{T_{12}} \right) + \frac{m_I c}{T_{12}} V_I + c \ln \left(\frac{m_I c}{T_{12}} \right) (t_2 - t_I) + \\ - V_I (t_2 - t_I) - c(t_2 - t_I) - c \ln \left(\frac{m_I c}{T_{12}} \right) (t_2 - t_I) + c \left(\frac{m_I c}{T_{12}} \right) \ln \left(\frac{m_I c}{T_{12}} \right) \quad (3.54)$$

$$d_{12} - X_I = \frac{m_I c}{T_{12}} V_I - c(t_2 - t_I) \rightarrow t_2 - t_I = \left[\frac{m_I c}{T_{12}} V_I - (d_{12} - X_I) \right] \frac{1}{c} \quad (3.55)$$

From Equation (3.27) we have that $m_I c / T_{12}$ corresponds to the time instant in which the spacecraft mass goes to zero ($m_p = m_I$). Thus, since we are only interested in physically meaningful results, we know for sure that $t_2 - t_I < \frac{m_I c}{T_{12}}$. During the deceleration phase, the velocity will always be lower than V_I , so if we consider the distance that the spacecraft would ideally cover if it travelled at V_I for a time longer than the actual duration of the braking phase ($\frac{m_I c}{T_{12}} > t_2 - t_I$), will certainly be greater than the actual distance, hence: $\frac{m_I c}{T_{12}} V_I > d_{12} - X_I$, and therefore, as expected, $t_2 - t_I > 0$

By substituting Equation 3.55 into Equation 3.50, we finally obtain the condition to be verified at each integration step of the model in order to determine when the deceleration phase begins (m, V, X are those parameters that vary over time).

$$0 = V + c \ln \left(\frac{mc}{T_{12}} - \left[\frac{mc}{T_{12}} V - (d_{12} - X) \right] \frac{1}{c} \right) - c \ln \left(\frac{mc}{T_{12}} \right) \quad (3.56)$$

Let's now see the main features of the model (developed with MATLAB-Simulink) of the horizontal translation with auxiliary thrusters.

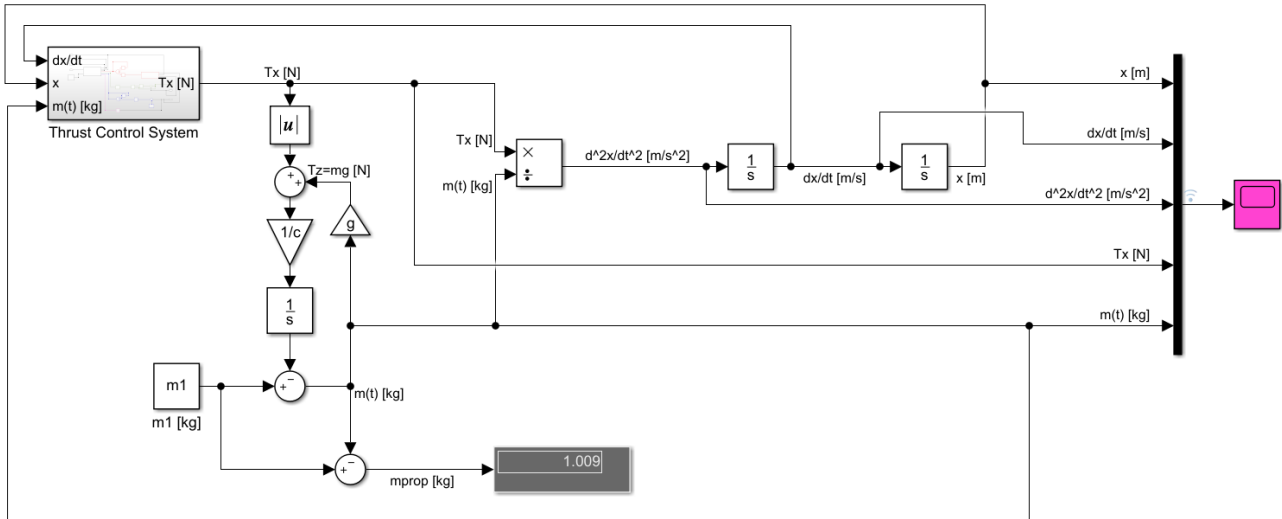


Figure 3.18 – Main system of the horizontal translation model (with auxiliary thrusters)

The main system shown in Figure 3.18 has the task of implementing the following differential and integral equations:

$$\frac{d^2 X}{dt^2} = \frac{T_X(t)}{m(t)} \quad (3.57)$$

$$\frac{dX}{dt} = \int_0^t \frac{d^2X}{dt^2} dt \quad (3.58)$$

$$X = \int_0^t \frac{dX}{dt} dt \quad (3.59)$$

$$m(t) = m_1 - \int_0^t \frac{T_X(t) + T_Z(t)}{c} dt = m_1 - \int_0^t \frac{T_X(t) + m(t)g}{c} dt \quad (3.60)$$

In order to solve these equations it is necessary to know the thrust component T_X which in turn depends on the instantaneous values of mass, velocity and altitude. The "Thrust Control System" has the task of providing the correct T_X by receiving the three above-mentioned values as inputs.

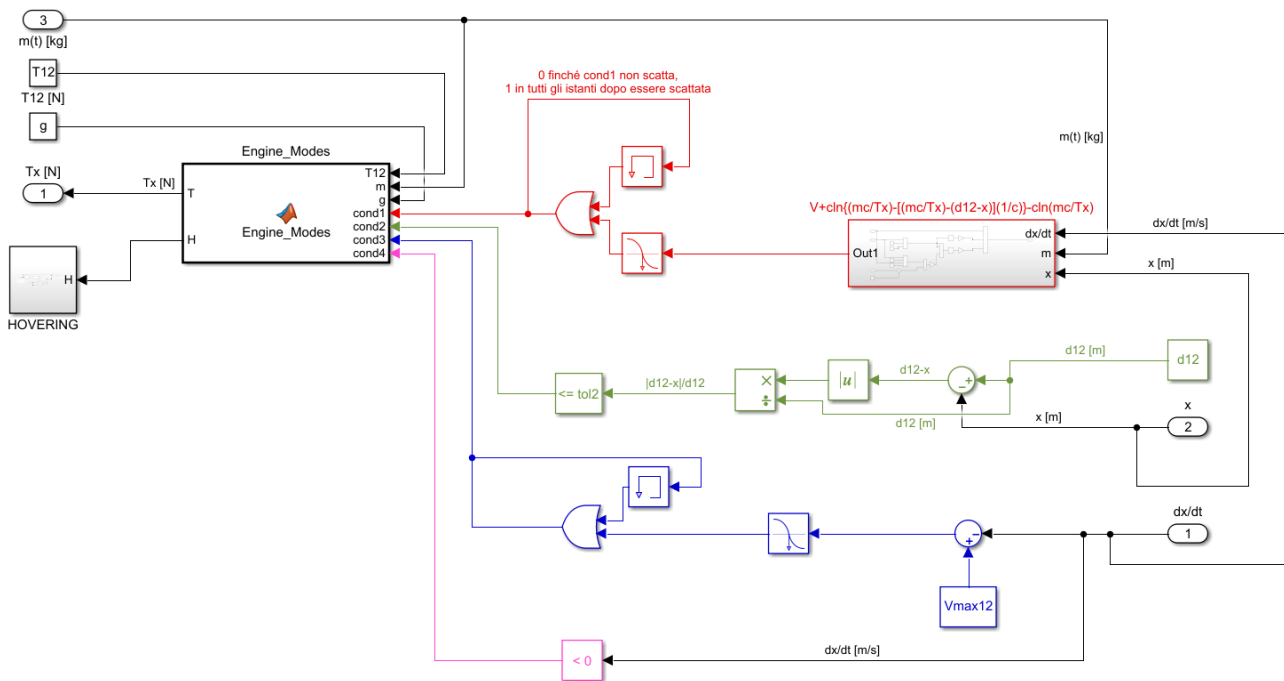


Figure 3.19 – Thrust Control System of the horizontal translation model (with auxiliary thrusters)

cond1

If Equation (3.56) is satisfied, then cond1 goes from 0 to 1 and will remain equal to 1 until the end of the simulation, else, until the equation is not satisfied, cond1 remains equal to 0. This approach was chosen because in this way the condition not only acts as a trigger (the propulsion system will exert a horizontal thrust component equal to $-T_{12}$ when cond1 goes from 0 to 1) but also gives continuous information about the spacecraft phase (if 0: acceleration phase or intermediate phase, if 1: deceleration phase).

cond2

if $\frac{|d_{12}-x|}{d_{12}} \leq tol2$, then cond2 is equal to 1, else it is equal to 0.

Cond2 is not an essential condition for the functioning of this model but is useful to figure out if the spacecraft is close to point 2. If only this condition were used to switch to the hovering mode, the model would have a strong dependence on both the tol2 value and the type of solver and its integration step. In particular, if tol2 is too small with respect to the integration step, once the spacecraft gets close to point 2, instead of switching to the hovering mode, it would slow down until it reverses its motion going back towards point 1. On the contrary,

if $tol2$ is too big, the spacecraft switches to the hovering mode when it is still too far from point 2, thus obtaining results that are not consistent with the input parameters ($d_{12model} < d_{12input}$). Since we're going to perform parametric sweeps, using this condition to switch to the hovering mode would mean that we would have to calibrate both the integration step and $tol2$ for each set of parameters and this would be inconvenient.

cond4

if $V < 0$, then $cond4$ is equal to 1, else, it is equal to 0.

This condition is used to switch to the hovering mode. The X-component of velocity remains greater than or equal to zero during the entire manoeuvre except when the spacecraft reaches point 2. As a matter of fact, due to the braking thrust component $T_X = -T_{12}$, if the start of the deceleration phase takes place with the right timing, the spacecraft will reverse its motion once it reaches point 2. By using this condition, instead of $cond2$, we can reduce the difference between $d_{12model}$ and $d_{12input}$ by simply acting on the integration step and solver type.

cond3

When $V_{12max} - V(t)$ goes from a positive to a negative value, $cond3$ goes from 0 to 1 and will remain 1 until the end of the simulation. This condition is used to limit the maximum horizontal speed by lowering the thrust from T_{12} to 0 during the acceleration phase (1-1).

The logic used in the "Engine_Modes" block is well summarised by the following code.

```
H=0;
if cond1==0 && cond3==0
    T = T12;
elseif cond1==0 && cond3==1
    T = 0;
elseif cond1==1 && cond4==1 && cond2==1
    T = 0;
    H = 1;
elseif cond1==1 && ~(cond2==1 && cond4==1)
    T = -T12;
```

Finally, the "HOVERING" subsystem is basically the same as the one shown in Figure 3.6.

The input parameters used to obtain the results depicted in Figure 3.7 are:

$T_{12} = 10 \text{ N}$	$d_{12} = 100 \text{ m}$	$tol2 = 0.1$
$V_{12max} = 5 \text{ m/s}$	$I_{sp} = 150 \text{ s}$	Solver: ode1(Euler)
$m_1 = 15 \text{ kg}$	$\Delta t_{h_2} = 5 \text{ s}$	$DT = 1 \text{ ms}$

Where DT is the integration step.

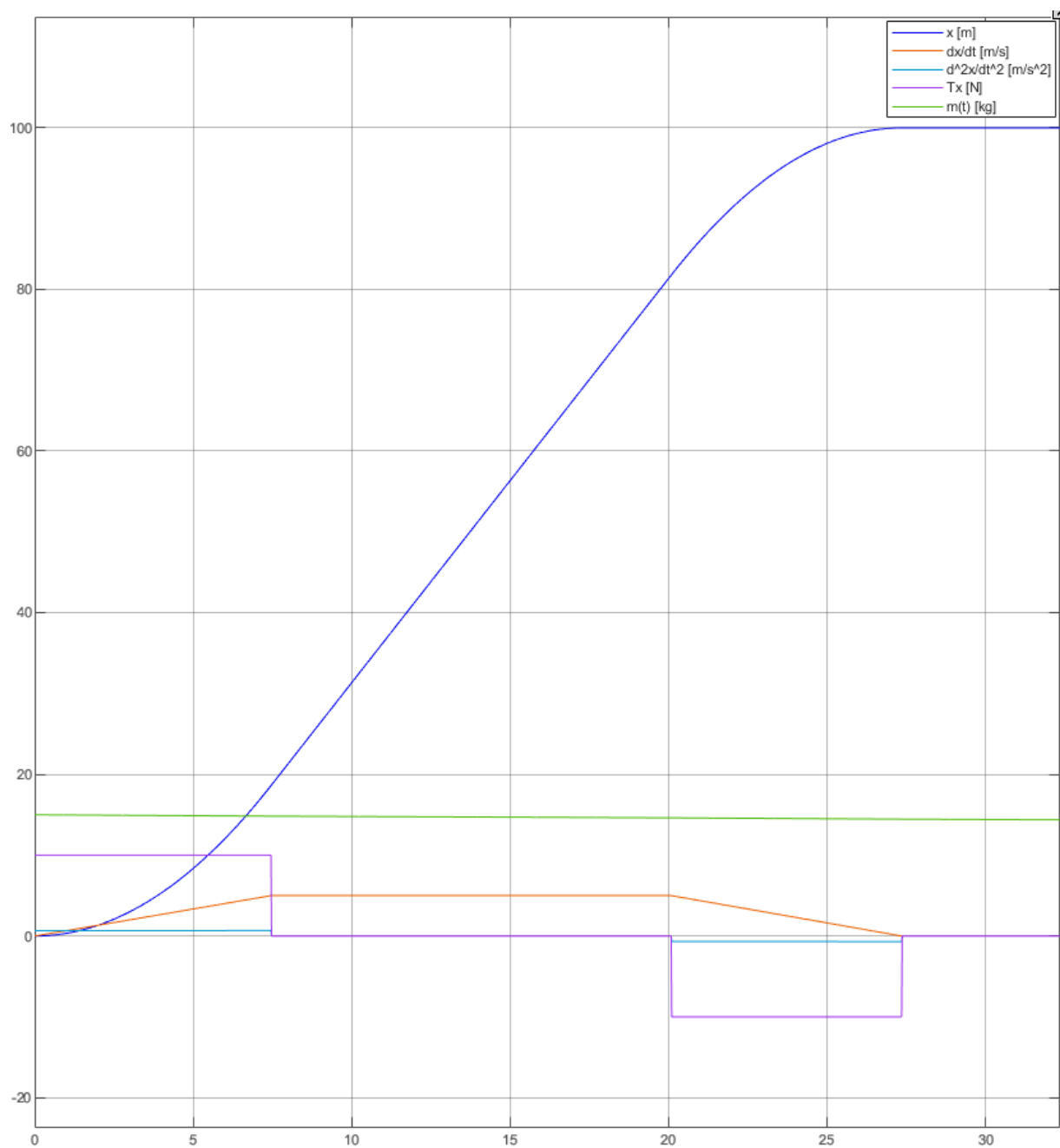


Figure 3.20 – Model output example [horizontal translation model (with auxiliary thrusters)]

In Chapter 3.3.2 it was assumed that the two lateral thrust components ($T_X = \pm T_{12}$) were exerted by auxiliary thrusters (it was also assumed that they had the same I_{sp} as the main thruster). As we mentioned before, if we assume that the spacecraft can tilt its x-axis (see Figure 3.1), the horizontal component of the thrust could be obtained using just the main thruster.

$$\Delta V_{prop} = \int_{t_1}^{t_2} \frac{T}{m} dt = \int_{t_1}^{t_2} \frac{\sqrt{T_X^2 + T_Z^2}}{m} dt \quad (3.61)$$

Since $T_X + T_Z > \sqrt{T_X^2 + T_Z^2}$ it is quite clear that the propellant consumption will be lower with respect to the case with auxiliary thrusters. Furthermore, the results presented in the next chapter will show how the optimal values (which identify the cases of lowest propellant consumption) correspond to lower T_X with respect to the optimum points of the case presented in Chapter 3.3.2. This is an important advantage since the main engine can exert a limited level of thrust.

Page 57 of 154

3.3.4 Horizontal translation – Results and conclusions

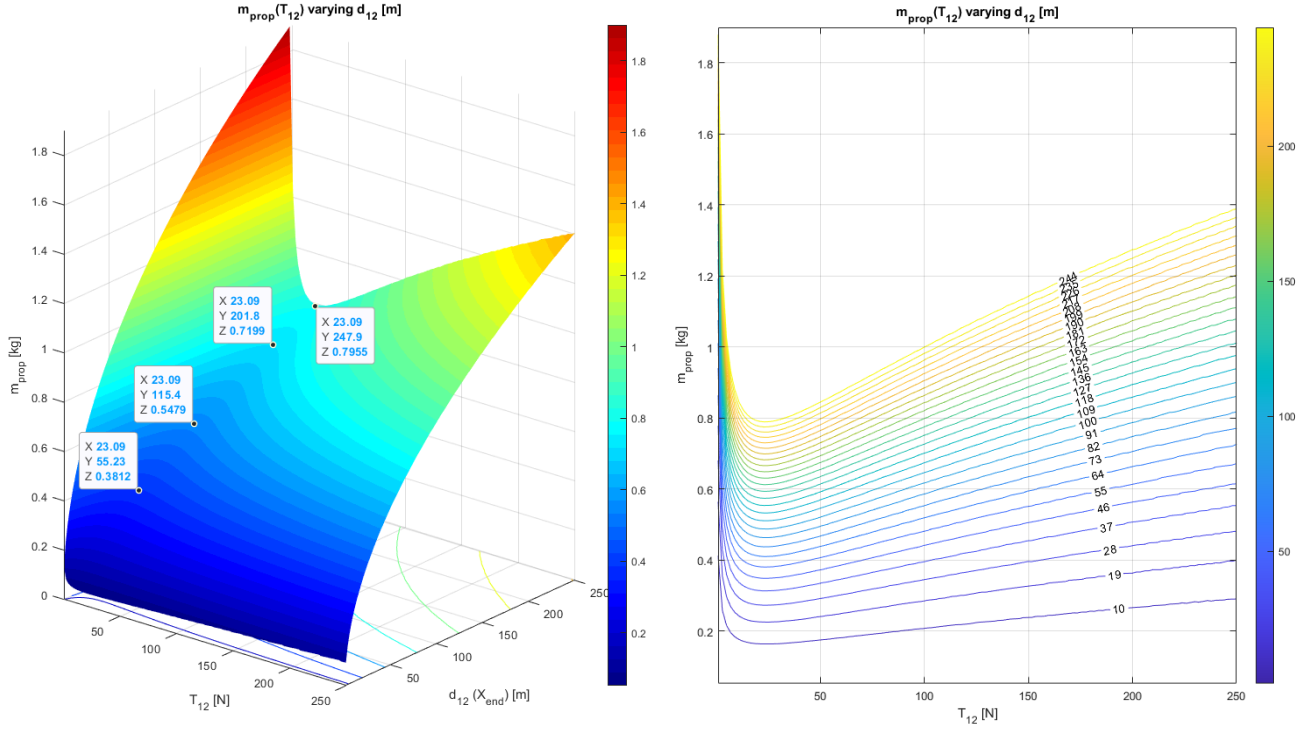


Figure 3.22 – Horiz. transl. (Case 2), assuming $t_I \equiv t_{V_{12max}}$: $m_{prop} = f(T_{12}, d_{12})$

Figure 3.22 shows the propellant mass consumed as a function of T_{12} and d_{12} . In particular, these results refer to the case presented in Chapter 3.3.2 and assuming that there is no intermediate phase ($t_{V_{12max}} \equiv t_I$ or $V_{12max} = \infty$). The results are in line with what was found in Chapter 3.3.1, where a constant mass of the spacecraft was assumed. In particular, the optimal value of T_{12} is approximately equal to the weight of the spacecraft (and hence approximately equal to the vertical thrust component).

However, these results, as mentioned before, do not take into account the possibility of introducing an intermediate phase, in which $T_X = 0$, between the acceleration and deceleration phases. To introduce such a phase, and to analyse cases in which it has different durations, it is sufficient to vary the value of V_{12max} .

The results reported in Chapter 10 Annex 06 clearly show that, in the configuration without auxiliary thrusters, the optimal condition is at $T_{12} \approx 40$ N, regardless of the distance between point 1 and point 2. Assuming, for the sake of simplicity, a constant spacecraft mass, it is quite easy to justify these results.

As described in the previous chapters, the propellant mass is directly related to ΔV_{prop} .

$$\Delta V_{prop} = \int_{t_1}^{t_2} \frac{|T|}{m} dt = \int_{t_1}^{t_2} \frac{\sqrt{T_X^2 + T_Z^2}}{m} dt \quad (3.63)$$

Assuming $m = cost$, and, as in previous chapters, $T_{12} = cost$, the Equation (3.63) becomes:

$$\Delta V_{prop} = \frac{\sqrt{T_{12}^2 + (mg)^2}}{m} \int_{t_1}^{t_{V_{12max}}} dt + g \int_{t_{V_{12max}}}^{t_I} dt + \frac{\sqrt{T_{12}^2 + (mg)^2}}{m} \int_{t_I}^{t_2} dt \quad (3.64)$$

$$\Delta V_{prop} = \frac{\sqrt{T_{12}^2 + (mg)^2}}{m} \left[\left(t_{V_{12max}} - \tilde{t}_1^{=0} \right) + (t_2 - t_l) \right] + g (t_l - t_{V_{12max}}) \quad (3.65)$$

Through simple kinematic equations we can find $t_{V_{12max}}$, $t_2 - t_l$, and $t_l - t_{V_{12max}}$ as a function of the parameters: T_{12} , V_{12max} , d_{12} , m , and g .

$$V_{12max} = \frac{T_{12}}{m} t_{V_{12max}} \rightarrow t_{V_{12max}} = V_{12max} \frac{m}{T_{12}} \quad (3.66)$$

$$0 = V_{12max} - (t_2 - t_l) \frac{T_{12}}{m} \rightarrow t_2 - t_l = V_{12max} \frac{m}{T_{12}} \quad (3.67)$$

$$d_{12} = \frac{1}{2} \frac{T_{12}}{m} t_{V_{12max}}^2 + V_{12max} (t_l - t_{V_{12max}}) + V_{12max} (t_2 - t_l) - \frac{1}{2} \frac{T_{12}}{m} (t_2 - t_l)^2 \quad (3.68)$$

$$d_{12} = V_{12max} (t_l - t_{V_{12max}}) + V_{12max} (t_2 - t_l) \quad (3.69)$$

$$t_l - t_{V_{12max}} = \frac{(d_{12} - V_{12max} (t_2 - t_l))}{V_{12max}} = \frac{d_{12}}{V_{12max}} - V_{12max} \frac{m}{T_{12}} \quad (3.70)$$

The time difference $t_l - t_{V_{12max}}$ is important as it identifies the time frame within which the spacecraft must be able to change its attitude in order to start the braking phase (please note that we are working on the horizontal translation manoeuvre without the auxiliary thrusters).

By substituting the expressions for $t_{V_{12max}}$, $t_2 - t_l$, and $t_l - t_{V_{12max}}$ into the Equation (3.65), we obtain:

$$\Delta V_{prop} = \frac{\sqrt{T_{12}^2 + (mg)^2}}{m} \left[V_{12max} \frac{m}{T_{12}} + V_{12max} \frac{m}{T_{12}} \right] + g \left(\frac{d_{12}}{V_{12max}} - V_{12max} \frac{m}{T_{12}} \right) \quad (3.71)$$

$$\Delta V_{prop} = 2 \frac{\sqrt{T_{12}^2 + (mg)^2}}{T_{12}} V_{12max} + g \frac{d_{12}}{V_{12max}} - g V_{12max} \frac{m}{T_{12}} \quad (3.72)$$

By differentiating Equation (3.72), with respect to T_{12} , and putting this partial derivative equal to zero, we obtain:

$$\frac{\partial \Delta V_{prop}}{\partial T_{12}} = -2 V_{12max} \frac{(mg)^2}{T_{12}^2 \sqrt{T_{12}^2 + (mg)^2}} + \frac{g V_{12max} m}{T_{12}^2} = V_{12max} \left[-2 \frac{(mg)^2}{T_{12}^2 \sqrt{T_{12}^2 + (mg)^2}} + \frac{mg}{T_{12}^2} \right] \quad (3.73)$$

$$\frac{\partial \Delta V_{prop}}{\partial T_{12}} = V_{12max} \frac{-2 (mg)^2 + mg \sqrt{T_{12}^2 + (mg)^2}}{T_{12}^2 \sqrt{T_{12}^2 + (mg)^2}} \quad (3.74)$$

$$\frac{\partial \Delta V_{prop}}{\partial T_{12}} = 0 \rightarrow -2 (mg)^2 + mg \sqrt{T_{12}^2 + (mg)^2} = 0 \quad (3.75)$$

$$\frac{\partial \Delta V_{prop}}{\partial T_{12}} = 0 \rightarrow \sqrt{T_{12}^2 + (mg)^2} = 2mg \rightarrow T_{12}^2 = 4(mg)^2 - (mg)^2 \quad (3.76)$$

$$\frac{\partial \Delta V_{prop}}{\partial T_{12}} = 0 \rightarrow T_{12} = \sqrt{3} mg \quad (3.77)$$

Equation (3.77) indicates that the optimal condition is obtained when $T_{12} = \sqrt{3} mg$. Although this result is valid for the $m = cost$ case, it is still in line with the results (see Chapter 10 Annex 06) of the model presented in Chapter 3.3.3. Similarly to what we did for T_{12} , by differentiating Equation (3.72) with respect to V_{12max} we can find its optimal value which guarantees the lowest ΔV_{prop} and therefore the lowest m_{prop} .

$$\frac{\partial \Delta V_{prop}}{\partial V_{12max}} = 2 \frac{\sqrt{T_{12}^2 + (mg)^2}}{T_{12}} - \frac{mg}{T_{12}} - \frac{gd_{12}}{V_{12max}^2} = \frac{2\sqrt{T_{12}^2 + (mg)^2} - mg}{T_{12}} - \frac{gd_{12}}{V_{12max}^2} \quad (3.78)$$

$$\frac{\partial \Delta V_{prop}}{\partial V_{12max}} = 0 \rightarrow V_{12max}^2 = \frac{gd_{12}T_{12}}{2\sqrt{T_{12}^2 + (mg)^2} - mg} \quad (3.79)$$

$$\frac{\partial \Delta V_{prop}}{\partial V_{12max}} = 0 \text{ and } T_{12} = \sqrt{3} mg \rightarrow V_{12max} = \sqrt{\frac{\sqrt{3}}{3} gd_{12}} \quad (3.80)$$

Figure 3.23 gives $t_2, t_I - t_{V_{12max}}$ and V_{12max} as functions of d_{12} . Please note that these values were obtained assuming a constant spacecraft mass of 15 kg.

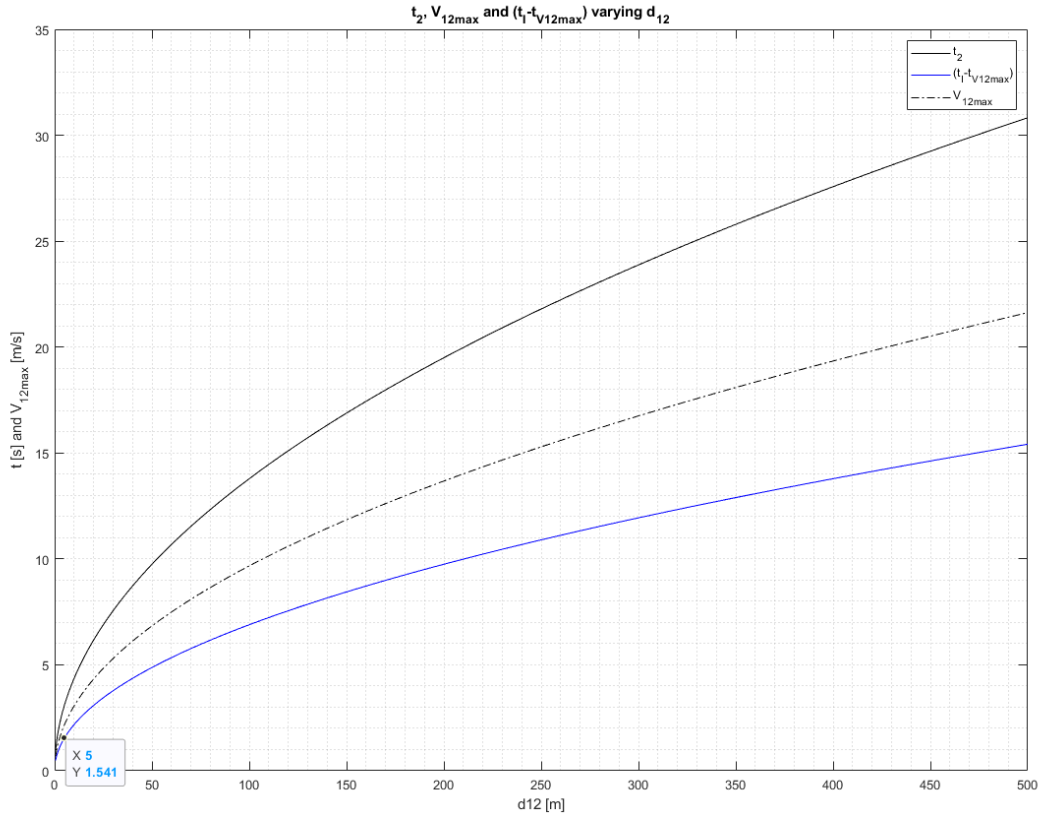


Figure 3.23 –Horiz. transl. w/o auxiliary thrusters, $m=cost$ case

In the real case it may not be possible to reach the optimal condition for several reasons. For instance, the GN&C system may not be able to change the spacecraft attitude in time to start the braking phase; the same system, together with other circumstances, may limit the maximum speed $V_{12_{max}}$ preventing us from reaching the optimal value, etc. For this reason it is necessary to carry out analyses that provide information on how propellant consumption varies according to various parameters (e.g. T_{12} , $V_{12_{max}}$, d_{12} , etc.). The results of these analyses, obtained by means of the models presented in Chapters 3.3.2 and 3.3.3, concerning the case with and without auxiliary thrusters, are reported in Chapter 10 Annex 06.

In conclusion, the configuration without auxiliary thrusters seems to be the most efficient for any set of parameters (T_{12} , $V_{12_{max}}$, d_{12} , m_1). However, this configuration implies the need to tilt the spacecraft by a certain angle, which can be expressed by the following relation:

$$\theta_{opt_{acc}} = \arccos\left(\frac{T_{12}}{\sqrt{T_{12}^2 + T_Z^2}}\right) = \arccos\left(\frac{T_{12}}{\sqrt{T_{12}^2 + (mg)^2}}\right) = \arccos\left(\frac{\sqrt{3}}{2}\right) = 30^\circ \quad (3.81)$$

Although the spacecraft mass varies over time due to propellant consumption, as the optimum T_{12} also varies with the spacecraft mass, the final result is that $\theta_{opt_{acc}}$ will maintain constant and equal to 30° during the acceleration phase, and equal to 120° during the braking phase. Actually, the optimal value of T_{12} , expressed by Equation (3.77), has been obtained assuming $m = cost$, so the real optimum case will not necessarily match this configuration, although it will certainly be close.

The configuration without auxiliary thrusters is therefore the most efficient, from the point of view of propellant consumption, but also requires operating modes that are not necessarily compatible with the other subsystems. Nevertheless, thanks to these quantitative analyses, we have enough data to carry out trade-off analyses involving all the spacecraft subsystems to determine which configuration is actually the most suitable.

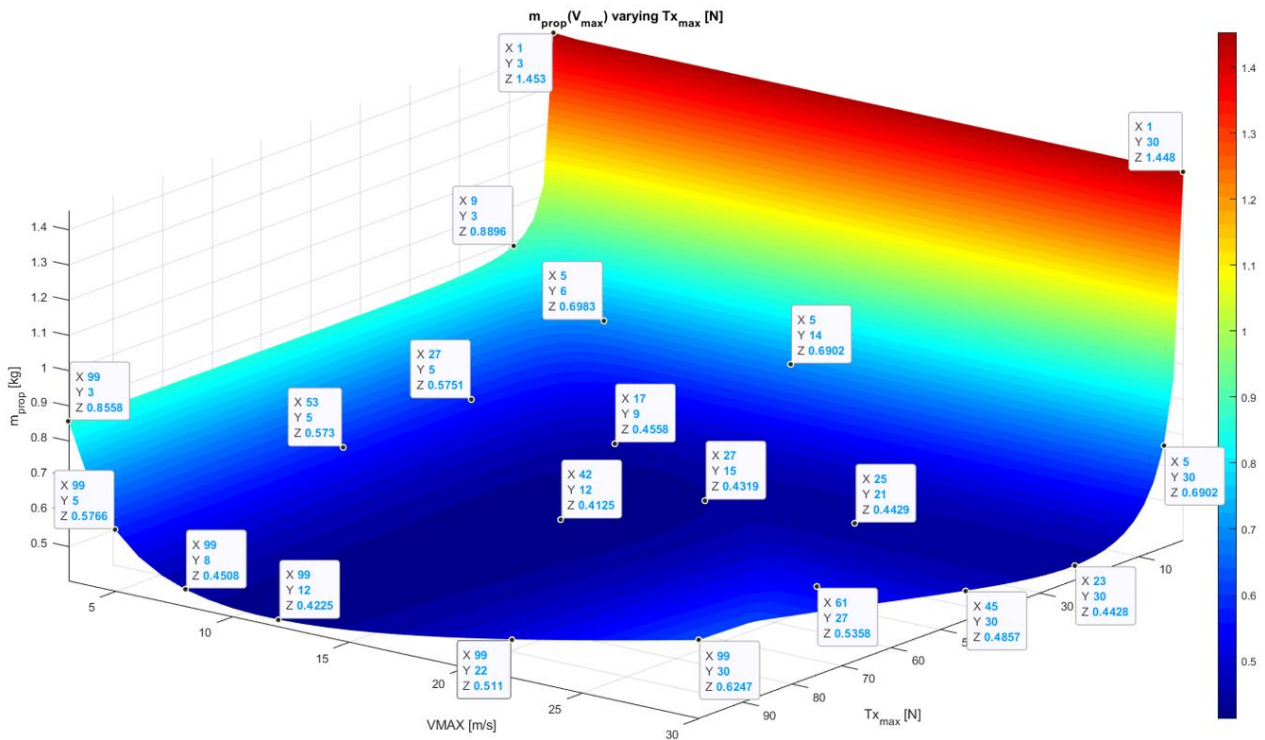


Figure 3.24 – Horizontal translation w/o auxiliary thrusters: $m_1 = 15kg$ $I_{sp} = 150s$ $d_{12} = 150m$

3.4 Vertical Descent

Since the main objective of the mission is to descend through the skylight to photograph the interior of the lunar cave, it is quite clear that one phase of the flight will inevitably involve a vertical descent. Regardless of the flight phase in which this manoeuvre will take place, its main purpose is to reduce the altitude of the spacecraft and to cancel its speed once it reaches a predetermined altitude ($V_2 = V_3 = 0$).

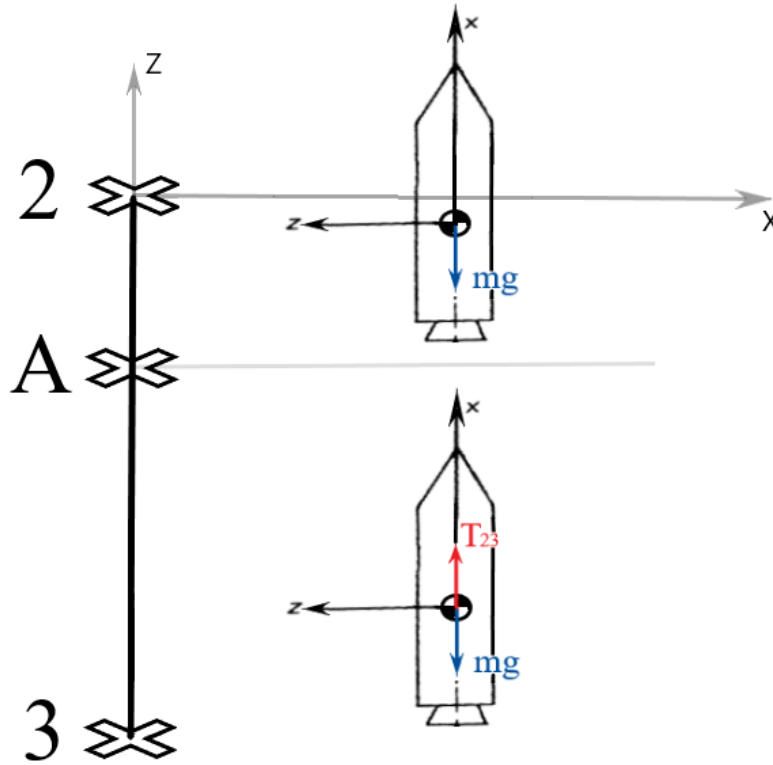


Figure 3.25 – Vertical descent manoeuvre

In the case of the vertical ascent, before we could say that it is never efficient, from the point of view of propellant consumption, to exert a braking thrust, we had to make some analyses. However, in this case we can immediately say that it is never efficient to exert a downward thrust (i.e. towards point 3). In fact, although this would shorten the manoeuvre time, it would also give the spacecraft extra velocity. As a result, the propulsion system will not only have to cancel out the speed generated by gravity, but also the velocity produced by that downward accelerating thrust. Thus, assuming that phase 2-A is essentially a free fall, we can use Equation (3.7) taking into account only the braking phase A-3 (see Figure 3.25):

$$\Delta V_{prop} = \Delta V + g(t_3 - t_A) = V_A + g(t_3 - t_A) = g(t_A - t_2) + g(t_3 - t_A) = g(t_3 - t_2) \quad (3.82)$$

From Equation (3.82) it is clear that, if we want the manoeuvre to consume as low a propellant as possible, we have to shorten the time of the manoeuvre itself. Thus, the propulsion system have to exert its maximum continuous thrust throughout the braking phase; whereas, for phase 2-A, the propulsion system shall not exert any vertical thrust. However, as with the other manoeuvres, there may be, for a variety of reasons, a speed limit which the LuNaDrone should not exceed. Consequently, during the free fall phase, if this speed is reached, the propulsion system must exert a thrust equal to the weight of the spacecraft so as to cancel its acceleration towards the lunar surface. During this phase, exerting a vertical thrust, directed from point 3 to point 2, lower than the weight of the spacecraft would increase the speed beyond the maximum acceptable

value, while exerting a greater thrust than the weight of the spacecraft would unnecessarily increase the time of the manoeuvre, thus increasing gravity losses.

Consequently, taking into account the things we have said so far, the most efficient manoeuvre (depicted in Figure 3.25 as a vertical line between points 2 and 3) will have the following characteristics:

	$t = t_2$	$t_0 < t < t_A$		$t = t_A$	$t_A < t < t_3$	$t = t_3$
$Z [m]$	0	$Z_A < Z < 0$		$Z = Z_A$	$Z_3 < Z < Z_A$	$Z = Z_3$
$\frac{dZ}{dt} \left[\frac{m}{s} \right]$	0	$V_{23_{max}} < V < 0$	$V = V_{23_{max}}$	$V_{23_{max}} \leq V < 0$	$V_{23_{max}} < V < 0$	0
$\frac{d^2Z}{dt^2} \left[\frac{m}{s^2} \right]$	$-g$	$-g$	0	$\frac{T_{23}}{m(t)} - g$	$\frac{T_{23}}{m(t)} - g$	0
$m [kg]$	m_2	$0 < m < m_2$	$0 < m < m_2$	$0 < m < m_2$	$0 < m < m_2$	$0 < m < m_2$
$T [N]$	0	0	$m(t)g$	0	0	$m(t)g$

Table 3.5 – Summary of vertical descent manoeuvre

In agreement with what schematically shown in Table 3.5, let's see the main characteristics of this manoeuvre.

$t = t_2$

At time t_2 the free fall phase begins. The propulsion system does not deliver any thrust and therefore the spacecraft will accelerate vertically, according to the negative direction of the Z-axis, due to gravitational acceleration.

$t_2 < t < t_A$

As mentioned before, the optimal thrust program (for the free fall phase) is simply to deliver no thrust. However, for a variety of reasons (e.g. related to the performance of the GN&C system) the spacecraft may not be allowed to exceed a certain maximum descent velocity: $V_{23_{max}}$. Therefore, if $V = V_{23_{max}}$, the propulsion system will have to constantly exert a thrust equal to the weight of the spacecraft until it reaches point A.

$t = t_A$

Once the spacecraft has reached a certain speed, mass, and altitude, the propulsion will have to start delivering its maximum continuous thrust, so that the deceleration phase can begin. In order to determine whether the spacecraft has reached point A we can use Equation (3.95). This equation also shows that there is no dependence with the altitude, mass and velocity-time history but only with their instantaneous values.

$t_A < t < t_3$

The A-3 section identifies the deceleration phase. As mentioned before, the optimum condition is that the average deceleration is as high as possible. Consequently, during this phase the propulsion system will have to deliver the maximum possible thrust in order to shorten the manoeuvre time, thus reducing gravity losses.

$t = t_3$

Once the spacecraft reaches point 3, the model must be able to simulate a stationary hover lasting Δt_{h_3} seconds. Obviously, the most efficient condition will be the one in which $\Delta t_{h_3} = 0$ s.

As with the other manoeuvres, we need to find the equation that allows us to identify point A.

$$a_{A3}(t) = \frac{T_{23}}{m} - g = \frac{T_{23}}{m_A - \frac{T_{23}}{c}t} - g = \frac{c}{\frac{m_A c}{T_{23}} - t} - g \quad (T_{23}, m_A, c, g > 0) \quad (3.83)$$

$$V_{A3}(t) = V_A + \int_0^t \left(\frac{c}{\frac{m_A c}{T_{23}} - t} - g \right) dt = V_A - c \ln \left(\frac{m_A c}{T_{23}} - t \right) - gt + c \ln \left(\frac{m_A c}{T_{23}} \right) \quad (3.84)$$

where: $[0 \leq t \leq t_3 - t_A]$

$$\begin{aligned} Z_{A3}(t) &= Z_A + \int_0^t \left[V_A - c \ln \left(\frac{m_A c}{T_{23}} - t \right) - gt + c \ln \left(\frac{m_A c}{T_{23}} \right) \right] dt = \\ &= Z_A + V_A t + c \left[\left(\frac{m_A c}{T_{23}} - t \right) \ln \left(\frac{m_A c}{T_{23}} - t \right) + t \right] - \frac{1}{2} g t^2 + c \ln \left(\frac{m_A c}{T_{23}} \right) t - c \left(\frac{m_A c}{T_{23}} \right) \ln \left(\frac{m_A c}{T_{23}} \right) \end{aligned} \quad (3.85)$$

For the sake of simplicity, in these equations it was considered that $t_A = 0$, therefore when $t = 0 \rightarrow Z = Z_A$, $V = V_A$ and when $t = t_3 - t_A \rightarrow Z = Z_3 = h_3$, $V = 0$. By substituting these last relations in equations (3.84) and (3.85), we obtain:

$$0 = V_A - c \ln \left(\frac{m_A c}{T_{23}} - (t_3 - t_A) \right) - g(t_3 - t_A) + c \ln \left(\frac{m_A c}{T_{23}} \right) \quad (3.86)$$

and:

$$\begin{aligned} h_3 - Z_A &= V_A (t_3 - t_A) + c \left[\left(\frac{m_A c}{T_{23}} - (t_3 - t_A) \right) \ln \left(\frac{m_A c}{T_{23}} - (t_3 - t_A) \right) + (t_3 - t_A) \right] - \frac{1}{2} g (t_3 - t_A)^2 + \\ &\quad + c \ln \left(\frac{m_A c}{T_{23}} \right) (t_3 - t_A) - c \left(\frac{m_A c}{T_{23}} \right) \ln \left(\frac{m_A c}{T_{23}} \right) \end{aligned} \quad (3.87)$$

From equation (3.86) we obtain:

$$c \ln \left(\frac{m_A c}{T_{23}} - (t_3 - t_A) \right) = V_A - g(t_3 - t_A) + c \ln \left(\frac{m_A c}{T_{23}} \right) \quad (3.88)$$

Substitution of Equation (3.88) into Equation (3.87) yields:

$$\begin{aligned} h_3 - Z_A &= V_A (t_3 - t_A) + \left[\frac{m_A c}{T_{23}} - (t_3 - t_A) \right] \left[V_A - g(t_3 - t_A) + c \ln \left(\frac{m_A c}{T_{23}} \right) \right] + \\ &\quad + c(t_3 - t_A) - \frac{1}{2} g (t_3 - t_A)^2 + c \ln \left(\frac{m_A c}{T_{23}} \right) (t_3 - t_A) - c \left(\frac{m_A c}{T_{23}} \right) \ln \left(\frac{m_A c}{T_{23}} \right) \end{aligned} \quad (3.89)$$

$$\begin{aligned} h_3 - Z_A &= V_A (t_3 - t_A) - \frac{m_A c}{T_{23}} g (t_3 - t_A) + \frac{m_A c}{T_{23}} c \ln \left(\frac{m_A c}{T_{23}} \right) + \frac{m_A c}{T_{23}} V_A + g (t_3 - t_A)^2 \\ &\quad - c \ln \left(\frac{m_A c}{T_{23}} \right) (t_3 - t_A) + \\ &\quad - V_A (t_3 - t_A) + c(t_3 - t_A) - \frac{1}{2} g (t_3 - t_A)^2 + c \ln \left(\frac{m_A c}{T_{23}} \right) (t_3 - t_A) - c \left(\frac{m_A c}{T_{23}} \right) \ln \left(\frac{m_A c}{T_{23}} \right) \end{aligned} \quad (3.90)$$

$$h_3 - Z_A = -\frac{m_A c}{T_{23}} g(t_3 - t_A) + \frac{m_A c}{T_{23}} V_A + \frac{1}{2} g(t_3 - t_A)^2 + c(t_3 - t_A) \quad (3.91)$$

$$h_3 - Z_A = (t_3 - t_A) \left[c - \frac{m_A c}{T_{23}} g \right] + \frac{1}{2} g(t_3 - t_A)^2 + \frac{m_A c}{T_{23}} V_A \quad (3.92)$$

By setting $t_3 - t_A \equiv x$, we can see Equation (3.92) as a standard quadratic equation.

$$\underbrace{\frac{1}{2} g}_{a} \underbrace{(t_3 - t_A)^2}_{x^2} + \underbrace{\left[c - \frac{m_A c}{T_{23}} g \right]}_b \underbrace{(t_3 - t_A)}_x + \underbrace{Z_A - h_3 + \frac{m_A c}{T_{23}} V_A}_d = 0 \quad \rightarrow \quad x = \frac{-b \pm \sqrt{b^2 - 4ad}}{2a} \quad (3.93)$$

Where:

$$a = \frac{1}{2} g > 0$$

$$b = c - c \frac{m_A c}{T_{23}} > 0$$

$$d = \underbrace{(Z_A - h_3)}_{>0} + \underbrace{\frac{m_A c}{T_{23}} V_A}_{<0} = \underbrace{\frac{m_A c}{T_{23}} V_A}_{|...| > |h_3 - Z_A|} - \underbrace{(h_3 - Z_A)}_{<0} < 0$$

From Equation 3.27 we have that $\frac{m_A c}{T_{23}}$ corresponds to the time instant in which the spacecraft mass goes to zero ($m_p = m_3$). Thus, since we are only interested in physically meaningful results, we know for sure that $t_3 - t_A < \frac{m_A c}{T_{23}}$. During the deceleration phase, the velocity will always be higher than V_A (please note that V_A is negative, according to the positive direction of the Z-axis, and that during the A-3 section the spacecraft velocity will also remain below zero). So, if we consider the distance that the spacecraft would ideally cover if it travelled at V_A for a time longer than the actual duration of the braking phase ($\frac{m_A c}{T_{23}} > t_3 - t_A$), It will certainly be greater than the distance actually travelled by the LuNaDrone, hence: $\left| \frac{m_A c}{T_{23}} V_A \right| > |h_3 - Z_A| \rightarrow \frac{m_A c}{T_{23}} V_A < h_3 - Z_A$.

Thus:

$$x = \frac{-b \pm \sqrt{b^2 - \overbrace{(\dots)}^{>b}}}{2a}$$

Therefore, to have positive values of x , which we remember that it represents the duration of the braking phase ($t_3 - t_A$), the correct result will be:

$$t_3 - t_A = \frac{\frac{m_A g}{T_{23}} c - c + \sqrt{\left(\frac{m_A g}{T_{23}} c - c \right)^2 - 2g \left(\frac{m_A c}{T_{23}} V_A - (h_3 - Z_A) \right)}}{g} \quad (3.94)$$

By substituting this relation into Equation (3.86), we finally obtain the condition to be verified at each integration step of the model in order to determine when the deceleration phase begins (the parameters m, V, Z are those that vary over time).

La condizione da verificare ad ogni passo di integrazione è:

$$0 = V - c \ln \left(\frac{mc}{T_{23}} - \left[\frac{\frac{mc}{T_{23}} g - c + \sqrt{\left(\frac{mc}{T_{23}} g - c \right)^2 - 2g \left(\frac{mc}{T_{23}} V - (h_3 - Z) \right)}}{g} \right] \right) +$$

$$-g \left[\frac{\frac{mc}{T_{23}} g - c + \sqrt{\left(\frac{mc}{T_{23}} g - c \right)^2 - 2g \left(\frac{mc}{T_{23}} V - (h_3 - Z) \right)}}{g} \right] + c \ln \left(\frac{mc}{T_{23}} \right) \quad (3.95)$$

Let's now see the main features of the model (developed with MATLAB-Simulink) of the vertical descent manoeuvre.

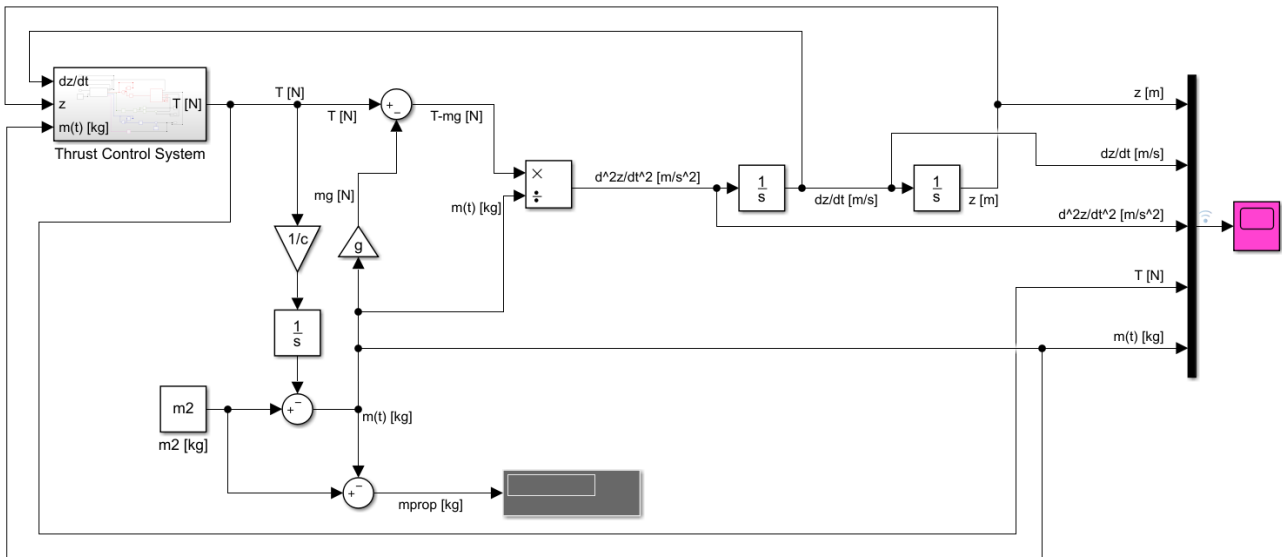


Figure 3.26 – Main system of the vertical descent model

The main system shown in Figure 3.26 has the task of implementing the following differential and integral equations:

$$\frac{d^2Z}{dt^2} = \frac{T(t)}{m(t)} \quad (3.96)$$

$$\frac{dZ}{dt} = \int_0^t \frac{d^2Z}{dt^2} dt \quad (3.97)$$

$$Z = \int_0^t \frac{dZ}{dt} dt \quad (3.98)$$

$$m(t) = m_2 - \int_0^t \frac{T(t)}{c} dt \quad (3.99)$$

In order to solve these equations it is necessary to know T which in turn depends on the instantaneous values of spacecraft mass, velocity and altitude. The "Thrust Control System" has the task of providing the correct T by receiving the 3 above-mentioned values as inputs.

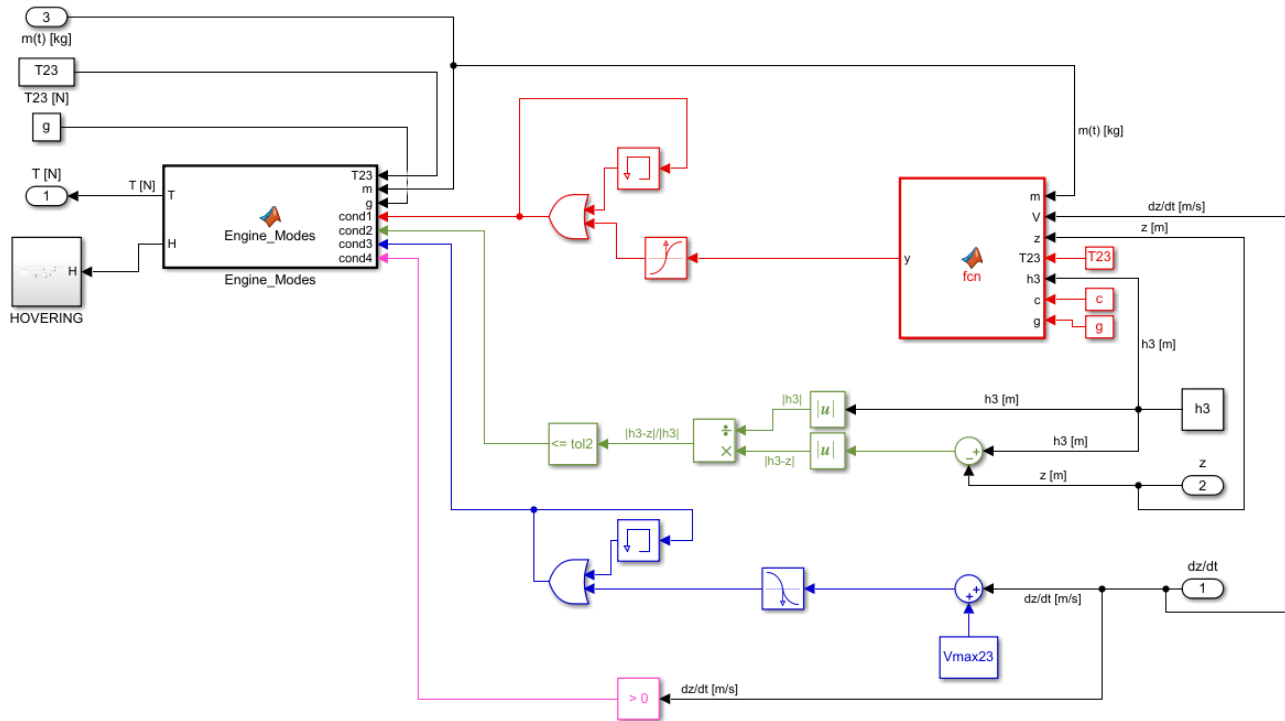


Figure 3.27 – Thrust Control System of the vertical descent model

In the previous chapters the role played by cond1 cond2 cond3 and cond4 has been extensively discussed. Please refer to those chapters for more details.

The logic used in the "Engine_Modes" block is well summarised by the following code.

```
H=0;
if cond1==0 && cond3==0
    T = 0;

elseif cond1==0 && cond3==1
    T = m*g;

elseif cond1==1 && cond4==1 && cond2==1
    T = m*g;
    H = 1;

elseif cond1==1 && ~(cond2==1 && cond4==1)
    T = T23;
```

Finally, the "HOVERING" subsystem is basically the same as the one shown in Figure 3.6.

The input parameters used to obtain the results depicted in Figure 3.28 are:

$T_{23} = 50 \text{ N}$	$h_3 = -100 \text{ m}$	$tol2 = 0.1$
$V_{23_{max}} = 8 \text{ m/s}$	$I_{sp} = 150 \text{ s}$	Solver: ode1(Euler)
$m_2 = 15 \text{ kg}$	$\Delta t_{h_3} = 5 \text{ s}$	$DT = 1 \text{ ms}$

Where DT is the integration step.

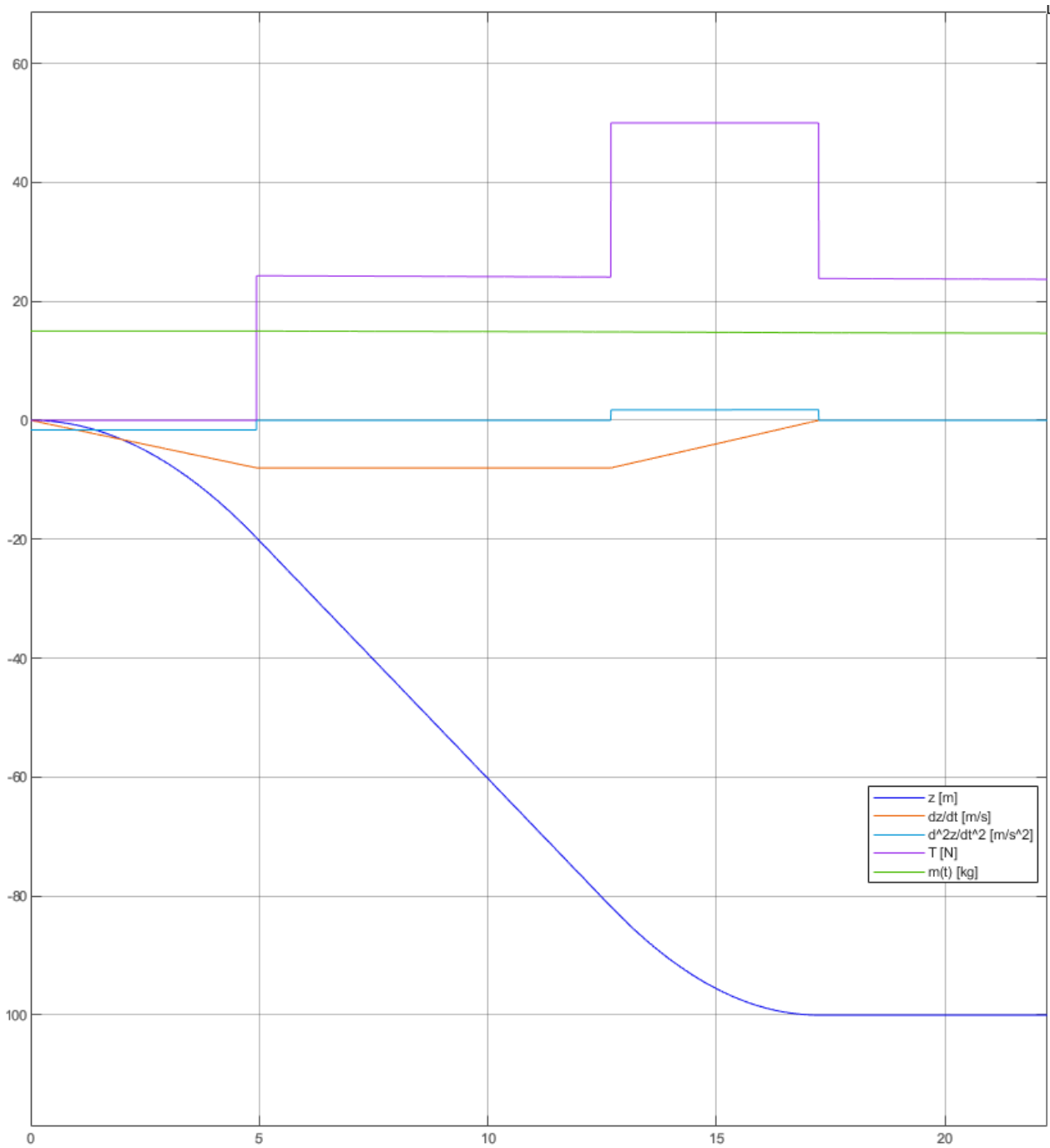


Figure 3.28 – Model output example (Vertical descent model)

3.4.1 Vertical Descent – Results and conclusions

The results reported in the figures below show a similar behaviour to that of the vertical ascent manoeuvre. In particular, the higher the maximum continuous thrust T_{23} and the maximum velocity V_{23max} , the lower the propellant consumption.

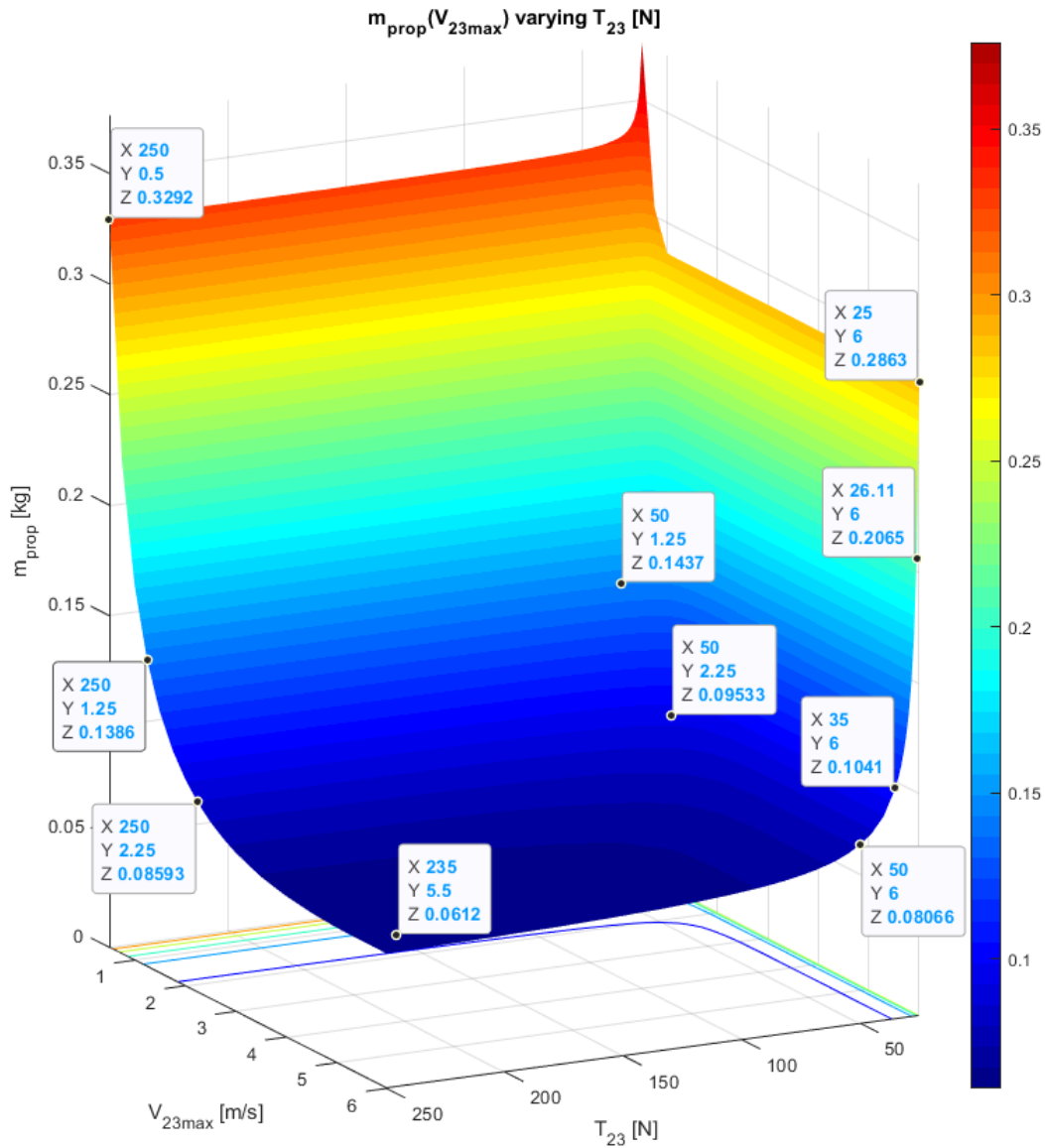


Figure 3.29 – Vertical descent, $m_{prop}(T_{23}, V_{23max}) - d_{12} = 10\text{ m}$

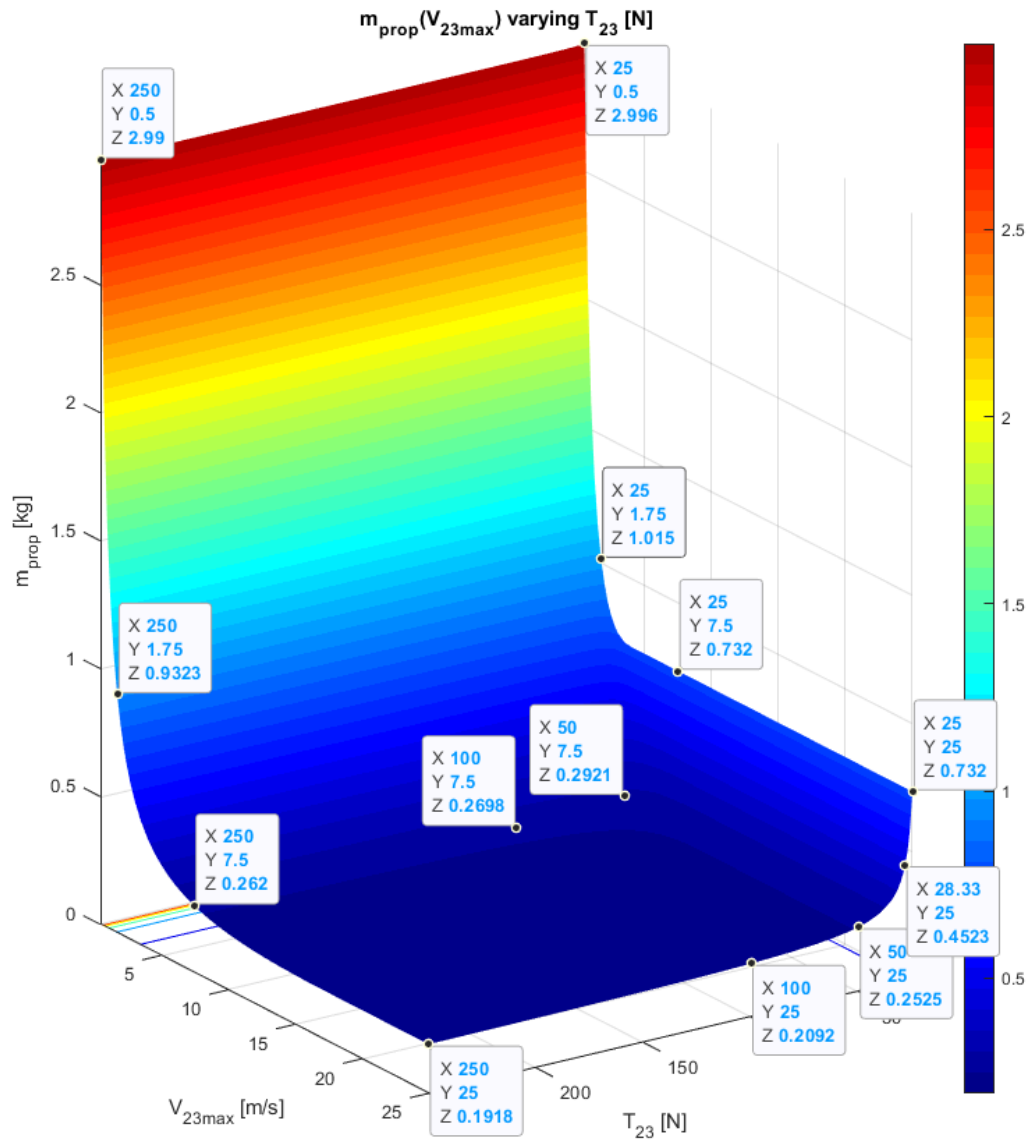


Figure 3.30 – Vertical descent, $m_{prop}(T_{23}, V_{23max}) - d_{12} = 100\text{ m}$

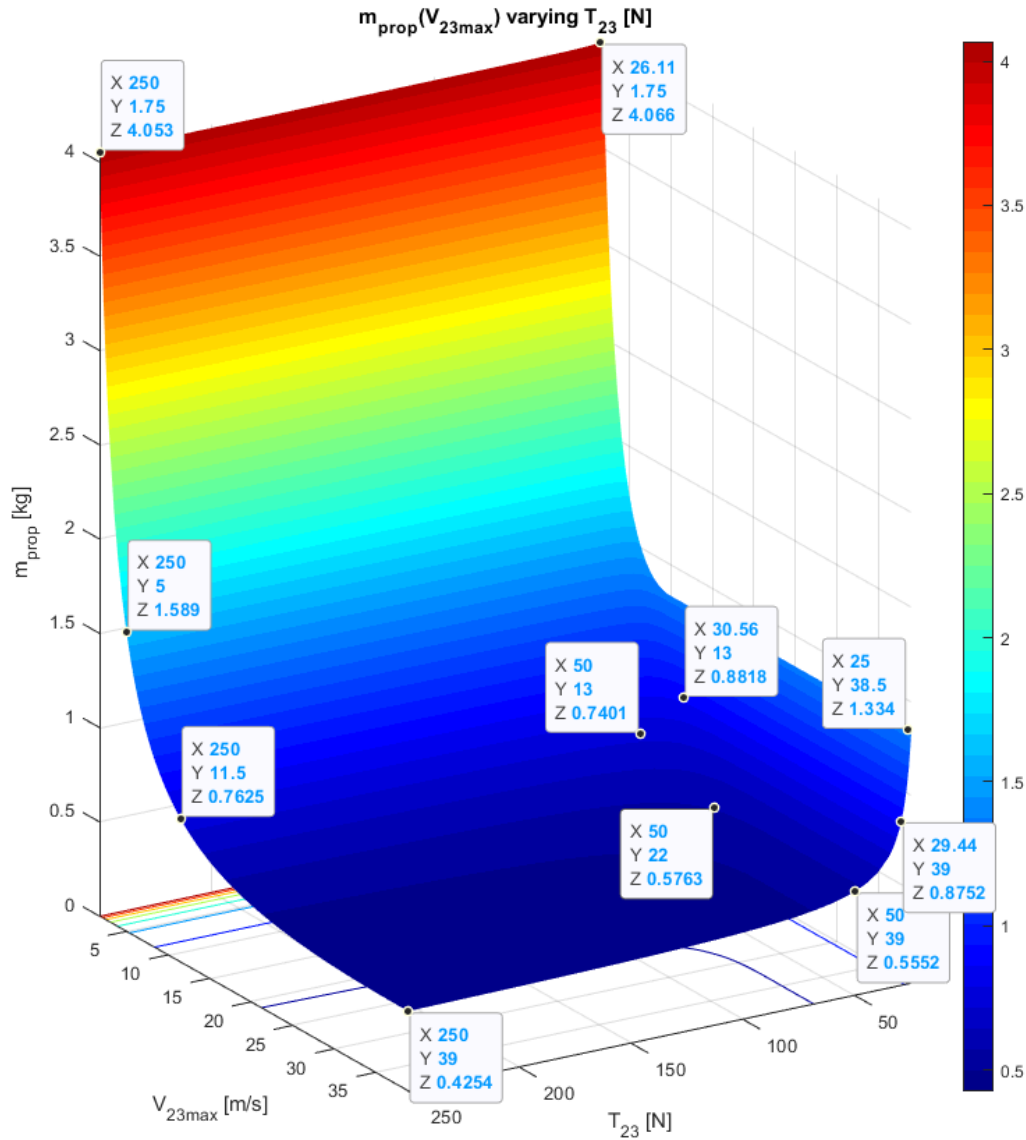


Figure 3.31 – Vertical descent, $m_{prop}(T_{23}, V_{23max}) - d_{12} = 500\text{ m}$

These results refer to a case where the initial mass of the spacecraft is $m_2 = 15\text{ kg}$, the propulsion system has a specific impulse of 150 s and it was assumed that there is no hovering manoeuvre at point 3. Finally, please note that the maximum speed indicated in these figures may not correspond to the actual maximum velocity reached during the manoeuvre. In fact, the same reasoning reported on page 29 also applies here.

3.5 Hovering

At the end of the vertical ascent, horizontal translation and vertical descent manoeuvres; i.e., when the spacecraft reaches the flight waypoints, the LuNaDrone may have to hover for a certain amount of time. This need can be dictated by the GN&C system for navigation purposes, by the need to acquire images of the interior of the lunar pit, but also by other subsystems and mission constraints. Regardless of the reasons why it is necessary to perform this manoeuvre, it is appropriate to determine how the propellant consumption varies with its duration (Δt_h) as this information is crucial for many design choices.

During the hovering manoeuvre, the LuNaDrone will keep its x-axis parallel to the Z-axis (rotations around the x-axis are possible), and will exert a thrust T pointing in the positive direction of the Z-axis and having the same magnitude as the weight of the spacecraft: $|T(t)| = |m(t)g|$. Consequently, Equation (3.3) becomes:

$$\Delta V_{prop} = \int_0^{\Delta t_h} \frac{T}{m} dt = \int_0^{\Delta t_h} \frac{mg}{m} dt = \int_0^{\Delta t_h} g dt = g\Delta t_h \quad (3.100)$$

Thus, the mass of propellant consumed during a hovering manoeuvre lasting Δt_h will be:

$$m_{p_h} = m_0 \left(1 - e^{-\frac{g\Delta t_h}{c}} \right) \quad (3.101)$$

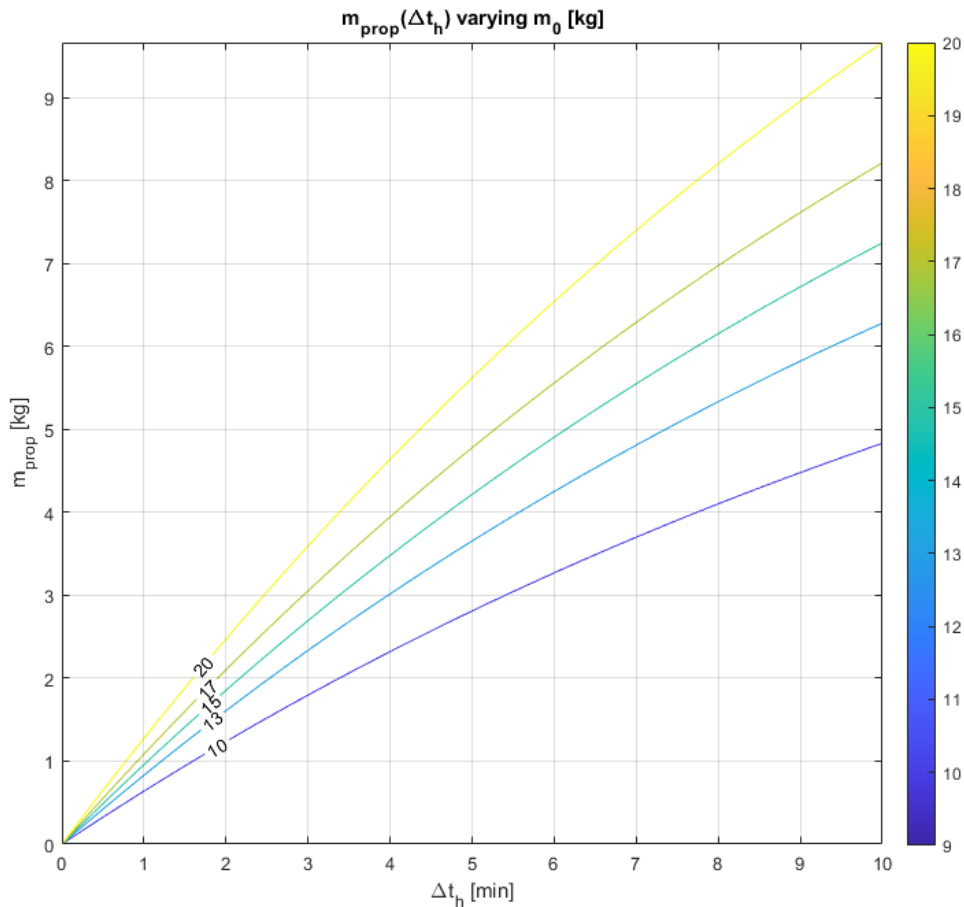


Figure 3.32 –Propellant mass consumed during a hovering manoeuvre (minutes)

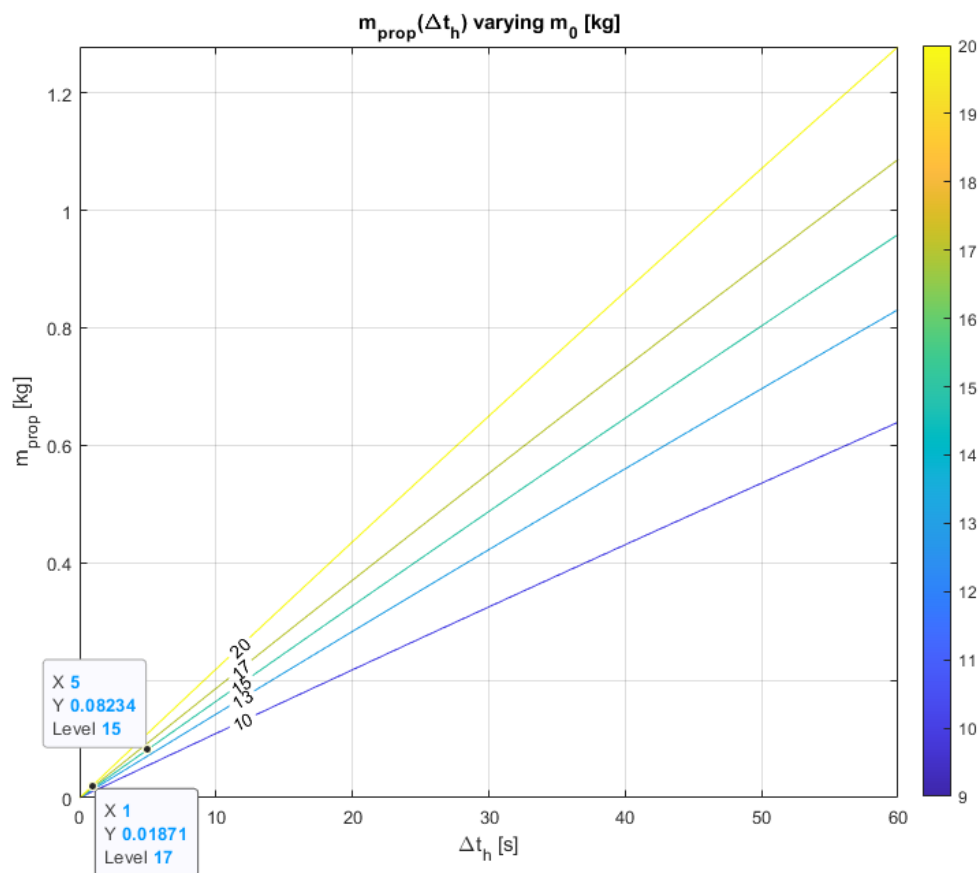


Figure 3.33 – Propellant mass consumed during a hovering manoeuvre (seconds)

The results are quite obvious, the longer the manoeuvre time, the higher the propellant consumption. When evaluating a design choice that requires a hovering manoeuvre, it is advisable to take into account the propellant mass required for that manoeuvre and use this information as one of the criteria used to assess the validity of the design solution.

3.6 Thrust control techniques

In the previous chapters we carried out analyses to evaluate the propellant mass consumed during the manoeuvre in order to determine the optimum combination of parameters (thrust, initial mass, maximum velocity, etc.) that would lead to the lowest propellant consumption. It is important to note, however, that from the system point of view, the optimal trajectory is not always the one that leads to the lowest propellant consumption. There are in fact many other factors that must be taken into account when choosing a trajectory and a certain thrust program. One of these is the way in which you have to control the thrust magnitude in order to perform a certain trajectory.

Considering the type of our propulsion system [16], there are essentially three ways in which we can perform thrust magnitude control (TMC).

- **On/off TMC:** In this case a solenoid shut-off valve is installed in order to control the propellant flow directed to the combustion chamber. This valve has two operating modes: when electrically energised it allow fluid flow, when de-energised it shut off fluid flow. The actuator takes the form of an electromagnet. When energised, a magnetic field builds up which pulls a plunger against the action of a spring (number 8 in Figure 3.34). When de-energised, the plunger is returned to its original position by the spring action.

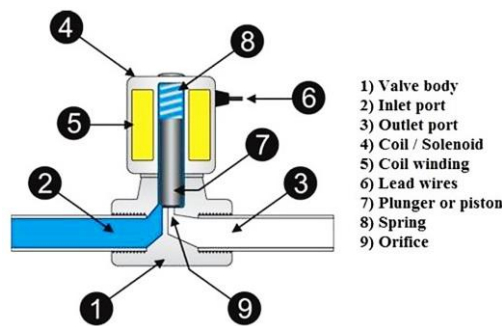


Figure 3.34 – Solenoid shut-off valve

Although the valve is either fully open or fully closed, the thrust, which is obtained when the valve is fully open, is not necessarily always the same but may vary depending on several factors, including the characteristics of the feeding system. In fact, if for example a "Blowdown" system is used, the chamber pressure will decrease as the propellant tank is emptied, causing the thrust to decrease as well (see Equation (3.102)).

$$T = C_F p_c A_t \quad (3.102)$$

Where: p_c is the pressure in the chamber, A_t is the throat area of the nozzle and C_F is the thrust coefficient. Please note that C_F may also vary slightly depending on p_c [19].

- **Step variable thrust:** By installing different flow control valves, it is possible to select different propellant flow rates, and therefore different thrusts, by simply operating the appropriate valve. However, in this way it is not possible to continuously vary the thrust magnitude as you can exert as many discrete thrust values as many valves are installed. Therefore, this solution would inevitably lead to a greater mass, size and complexity than the "On/off TMC" case, without providing complete throttleability of the engine.

- **Throttling:** In this case the propellant flow, and thus the thrust, is directly controlled through valves such as the cavitating venturi valve (also known as adjustable area venturi valve). According to the experience of T4i, using this kind of valve it would be possible to regulate the thrust up to 1/5 of the nominal value. The problem with this valve is that at low flow rates, the construction of certain valve components becomes rather critical due to the small size they must have in order to operate the valve at those low flow rates.

$$T = \dot{m}_p c = \dot{m}_p I_{sp} g_0 \quad (3.103)$$

According to Equation (3.103), if we consider $I_{sp} \approx 150s$ and $T \approx 25 N$, which is the thrust required to perform the hovering manoeuvre in case the spacecraft has a total mass of about 15 kg, the propellant flow rate would be $\dot{m}_p \approx 17 g/s$. With such a low flow rate, taking into account the existing industrial techniques, the construction of the valve itself becomes really difficult as well as extremely expensive. Anyway, according to the advice of T4i, even if it were possible to make a valve suitable for our application, it is expected that such a solution will inevitably lead to a mass of about twice as much as the "On/off TMC" case. The complexity of the system would also increase, and therefore the chance of failures, while the electrical power consumption would be approximately the same.

In conclusion, the most suitable solution seems to be the "On/off TMC" approach. The problem with this solution is that the manoeuvres studied so far all require different levels of thrust, while using an on/off valve would, in theory, provide just one thrust value. A possible solution to this problem could be the use of a bang-bang control.

Let us suppose that the propulsion system is able to provide a certain nominal thrust value: T_{nom} . To obtain lower thrusts it is possible to exploit the PWM technique. In order to do this, we need to act on the t_{on} and t_{off} values, which respectively represent the time interval in which the propulsion system exerts a thrust equal to T_{nom} and the time frame in which it does not exert any thrust. According to the data I received during a private conversation with T4i, the minimum values of these time intervals, for the propulsion system we have selected [16] are about: $t_{on_{min}} = 20 ms$ and $t_{off_{min}} = 20ms$.

Thus:

$$f = \frac{1 s}{t_{on} + t_{off}} \quad [Hz] \quad \rightarrow \quad f_{max} = \frac{1 s}{t_{on_{min}} + t_{off_{min}}} = \frac{1 s}{40 ms} = 25 Hz \quad (3.104)$$

To obtain lower thrusts than the nominal value, it is necessary to act on the duty cycle:

$$DC = \frac{t_{on}}{t_{on} + t_{off}} \quad (3.105)$$

As Equation (3.106) shows, the value of the DC is directly determined by the average thrust we want to obtain.

$$T_{avg} = T_{nom} \cdot DC \quad (3.106)$$

Given the DC, if we want to determine the maximum possible frequency, in order to have the smoothest possible progression of the spacecraft, we can use the following equation:

$$\text{if } DC \leq 0.5 \rightarrow f = \frac{DC}{t_{on_{min}}} \quad \text{if } DC > 0.5 \rightarrow f = \frac{1 - DC}{t_{off_{min}}} \quad (3.107)$$

Let's now see how to implement bang-bang control within the Simulink models developed in previous chapters. As an example we will consider the case of vertical ascent manoeuvre without braking thrust but please note that the same approach can be used for all the other models.

To simulate a bang-bang control, we need to add the “PWM-Thrust” block shown in Figure 3.35.

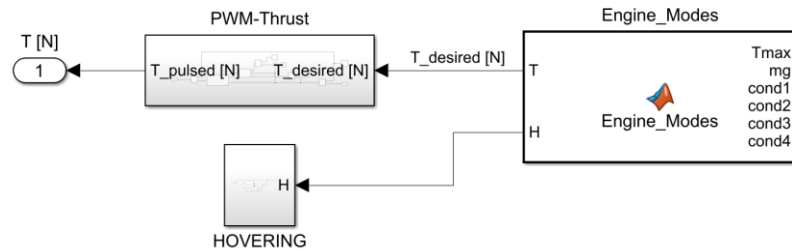


Figure 3.35 – PWM-Thrust block (integration with the main model)

The “T_desired [N]” represents the average thrust we want to obtain and corresponds to the thrust provided by the “Engine_Modes” function block. Its value is compared to “Tmax” which corresponds to the nominal thrust (T_{nom}) of the propulsion system.

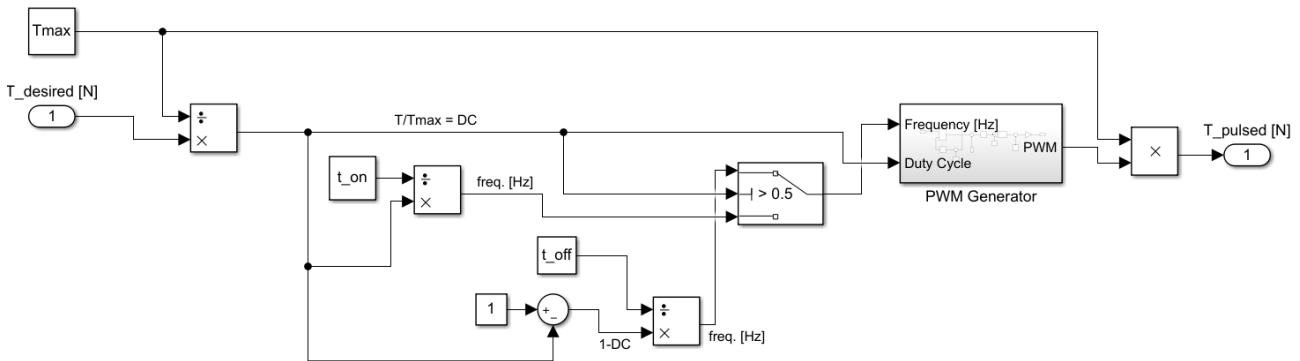


Figure 3.36 – PWM-Thrust subsystem

We then obtain the value of the DC and with it we can calculate the frequency according to the logic expressed by Equation (3.107). These two values will be provided as inputs to the “PWM Generator” block which will generate a square wave with values of 0 and 1 and with the frequency and DC received as inputs.

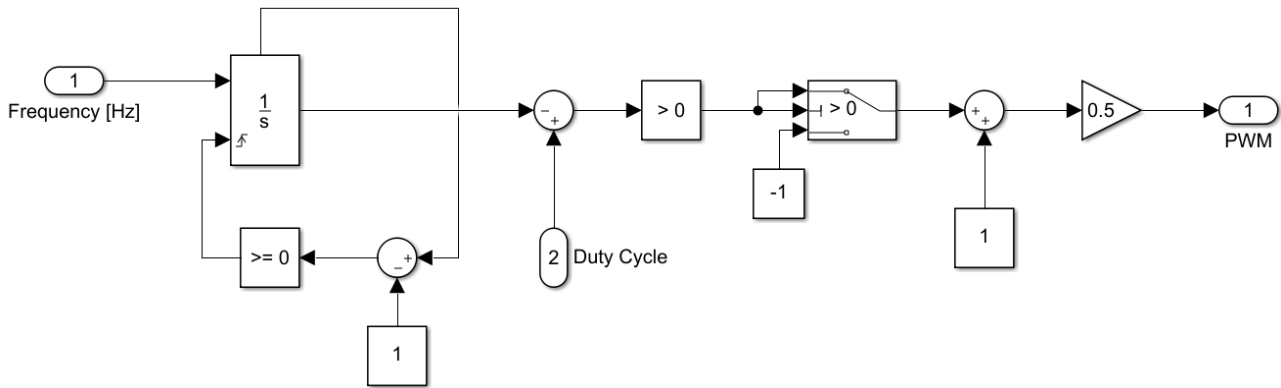


Figure 3.37 – PWM Generator

Finally, this square wave is multiplied by the nominal value of the thrust obtaining a thrust that varies over time as shown in Figure 3.38.

The input parameters used to obtain the results depicted in Figure 3.38 are:

$T_{01} = T_{nom} = 50 \text{ N}$	$h_1 = 100 \text{ m}$	$tol2 = 0.1$
$V_{01_{max}} = 5 \text{ m/s}$	$I_{sp} = 150 \text{ s}$	Solver: ode1(Euler)
$m_0 = 15 \text{ kg}$	$\Delta t_{h_1} = 5 \text{ s}$	$DT = 1 \text{ ms}$

Where DT is the integration step.

Using the values above as input data results in a propellant mass consumed of $m_p = 0.4545 \text{ kg}$; while, considering the same input data, if we use the vertical ascent model without the "PWM-Thrust" block we obtain: $m_p = 0.4553 \text{ kg}$. The difference between these two values is actually due to the fact that the model using the bang-bang control has been developed in such a way that the velocity assumes the trend shown in Figure 3.39. As you can see from this figure the average velocity is about $5,018 \text{ m/s}$ and not 5 m/s as in the case of the model without the "PWM-Thrust" block. As we have seen in Chapter 3.2.2, the higher the maximum velocity, the lower the propellant consumption. This should therefore explain the difference, in terms of m_p , between the two models. In fact, by replacing $V_{01_{max}} = 5,018 \text{ m/s}$ instead of $V_{01_{max}} = 5 \text{ m/s}$, the model without the PWM-Thrust block provide a much closer value: $m_p = 0,4543 \text{ kg}$.

According to the evolution over time of the altitude Z shown in Figure 3.38, the spacecraft seems to be able to maintain a smooth movement even though the thrust is exerted in a pulsed manner. However, it should be remembered that this model is extremely simplified. In fact, in this model, the inertia matrix of the spacecraft, the mechanical characteristics of the structure (e.g. its elasticity), the sloshing of the propellant inside the tank, etc. are not considered.

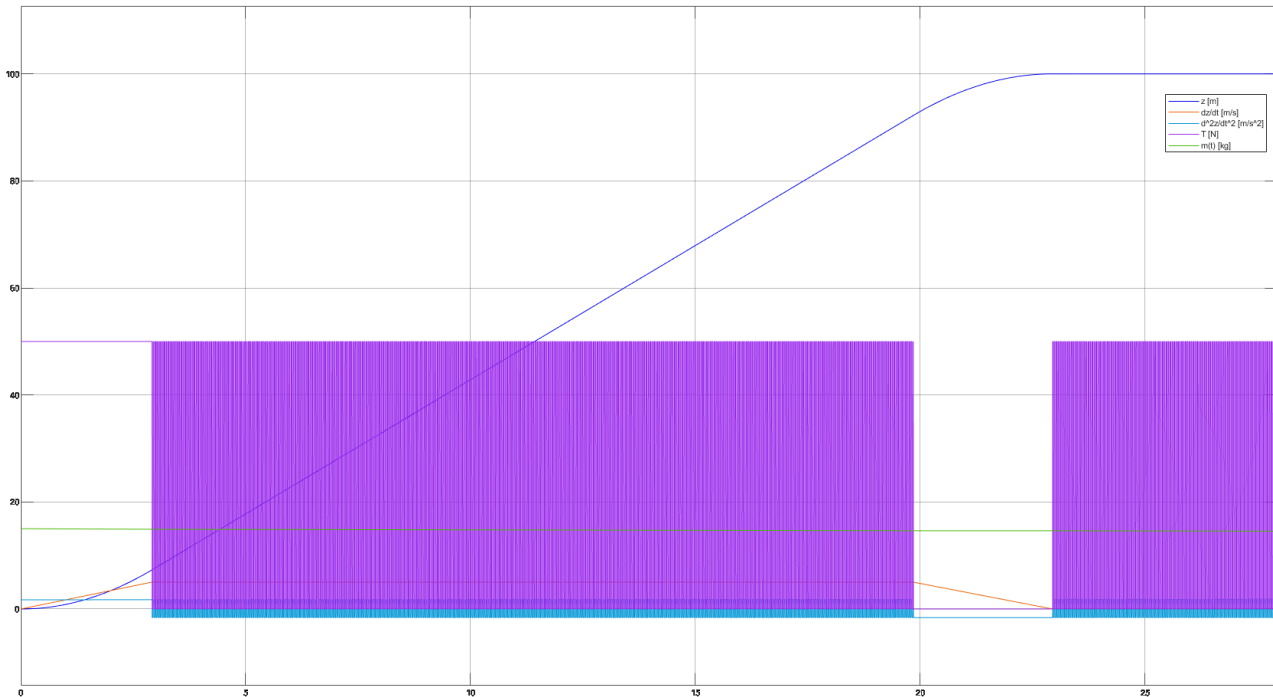


Figure 3.38 – Output example of vertical ascent model with bang-bang control

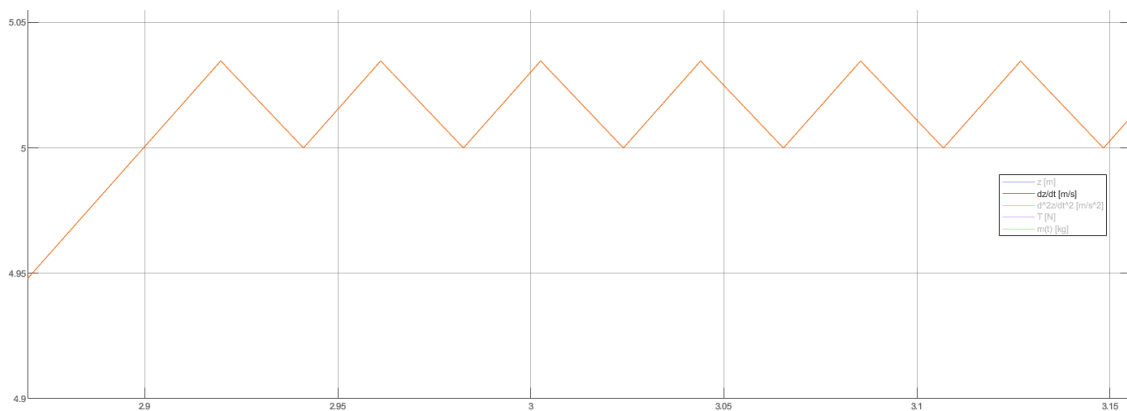


Figure 3.39 – dz/dt as a function of time, zoom of Figure 3.38

In fact, in the model the spacecraft is simply considered as a point object whose mass varies over time due to propellant consumption. It is therefore quite evident that this model is not suitable to ascertain the feasibility of a bang-bang control, it can only determine whether the mass of the spacecraft is high enough to theoretically make it proceed smoothly with a pulsed thrust exerted with a certain frequency, t_{on} and t_{off} . In particular, in an object as small as our spacecraft, a phenomenon like propellant sloshing needs to be handled. However, the treatment of this subject is highly demanding and it varies a lot depending on the type of tanks, bladders and baffles, all of which are not currently defined. In addition to all these aspects, it would be necessary to ensure that the GN&C system is actually capable of handling a bang-bang control with these features and that the components on board the spacecraft are compatible with the vibrations induced by this TMC technique. In conclusion, the current poor definition of the subsystems and characteristics of the spacecraft does not allow the development of a model that could determine the feasibility of a bang-bang control.

3.7 Conclusions and Recommendations

Throughout this chapter we have analysed the vertical ascent, horizontal translation, vertical descent and hovering manoeuvres. For each of them we determined which strategy was the most efficient and highlighted the effects of various parameters on propellant consumption.

As far as the vertical ascent manoeuvre is concerned, we have demonstrated that the most efficient thrust program is to exert the maximum continuous thrust that the propulsion system is able to deliver, during the acceleration phase, and let gravity slow down the spacecraft during the deceleration section. If, for some reason, the LuNaDrone must not exceed a certain maximum velocity, deriving for example from the performance of the GN&C system, the thrust must be limited from the maximum continuous value to a value equal to the weight of the spacecraft. Once the objective of the manoeuvre has been set, i.e. given the altitude to be reached at the end of the manoeuvre, and the characteristics of the spacecraft and propulsion system (total mass and specific impulse) have been fixed, the higher the maximum velocity and maximum continuous thrust, the lower the propellant consumption.

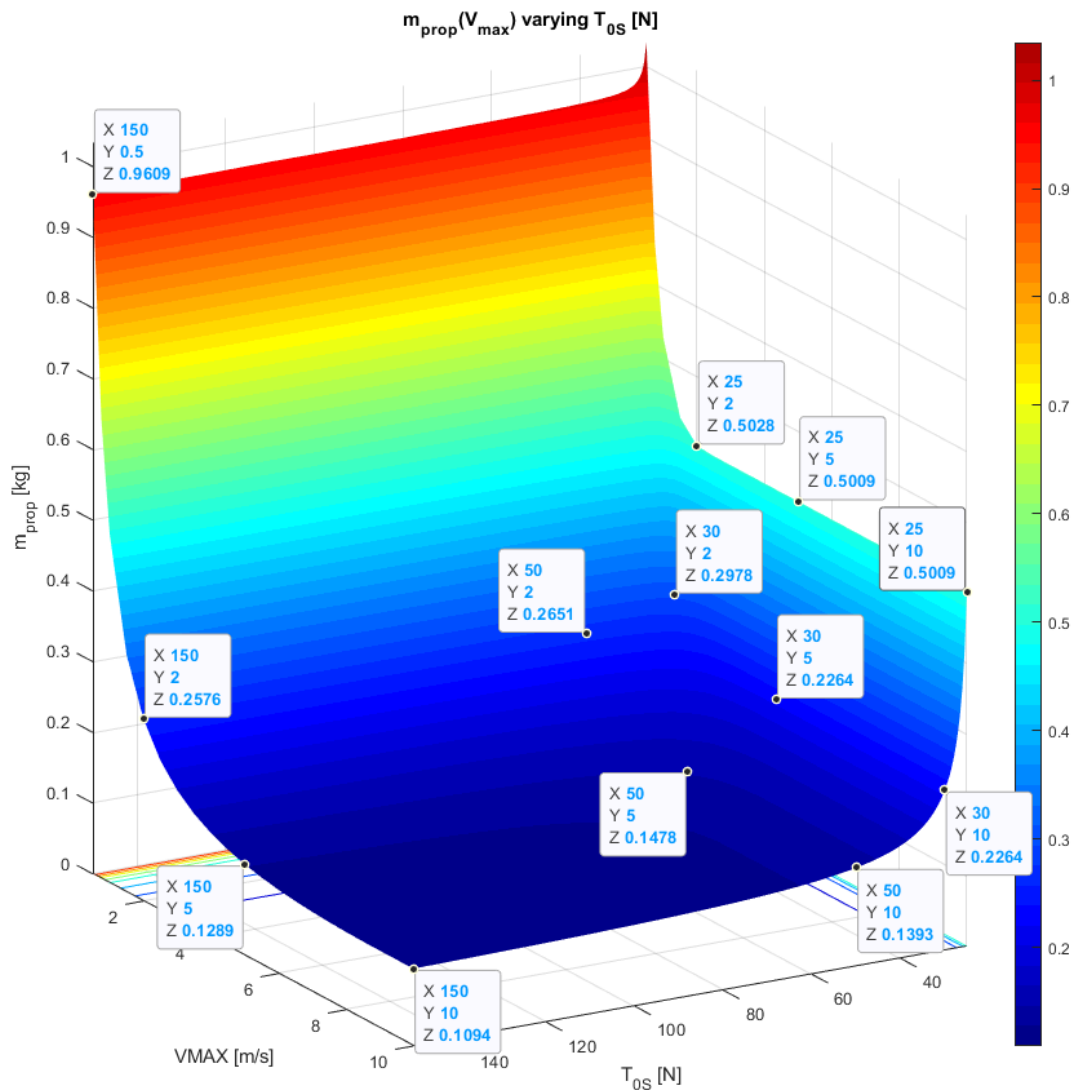


Figure 3.40 – Effect of V_{max} and T_{max} on propellant consumption of the vertical ascent manoeuvre

Figure 3.40 was obtained considering an initial spacecraft mass of 15kg, a specific impulse of 150s (for the reasons discussed on page 28) and an increase in altitude of 30m. Furthermore, as specified in the previous chapters, the initial and final velocities of the spacecraft are both zero. Thanks to these quantitative results, not only do we know that maximum velocity and maximum continuous thrust must be as high as possible, but we can also deduce which parameters make the mission prohibitive if not impossible and, on the contrary, which values, if exceeded, do not lead to substantial propellant savings. In particular, thrusts above 50N do not lead to significant propellant savings, and therefore, increases in engine mass and size, necessary to achieve higher thrusts, may not result to be convenient. Similarly, these analyses show that, at least as far as this manoeuvre is concerned, the navigation system should be able to sustain velocities equal to or greater than approximately 5 m/s. Actually, the navigation system currently under study [17], is capable of guaranteeing vertical and transverse velocities far greater than those expected by the flight profile models.

As far as the horizontal translation manoeuvre is concerned, we have found two relations (valid for the $m = cost$ case) that identify the optimal lateral thrust and the maximum translational velocity that leads to the lowest propellant consumption.

$$T_{12_{opt}} = \sqrt{3}mg \quad (3.108)$$

$$V_{12_{max_{opt}}} = \sqrt{\frac{gd_{12}T_{12}}{2\sqrt{T_{12}^2 + (mg)^2} - mg}} \xrightarrow{T_{12}=\sqrt{3}mg} V_{12_{max_{opt}}} = \sqrt{\frac{\sqrt{3}}{3}gd_{12}} \quad (3.109)$$

The results obtained with the model of this manoeuvre (which also takes into account the variation of the spacecraft mass induced by propellant consumption), have confirmed these theoretical results, as well as providing quantitative data necessary to understand how much the propellant consumption varies when moving away from the optimal condition. Considering a skylight diameter of about 100m and assuming that the rover is able to deploy the LuNaDrone on the lunar surface at a distance of 150m from the edge of the skylight, our spacecraft will have to make a horizontal translation of about 200m. Considering a specific impulse of 150s and an initial mass of 15kg, Figure 3.41 shows the propellant mass needed to perform this manoeuvre varying the maximum velocity and lateral thrust. Please note that in this case the value of “VMAX” is also used to vary the duration of the intermediate phase (for more details see Chapter 3.3).

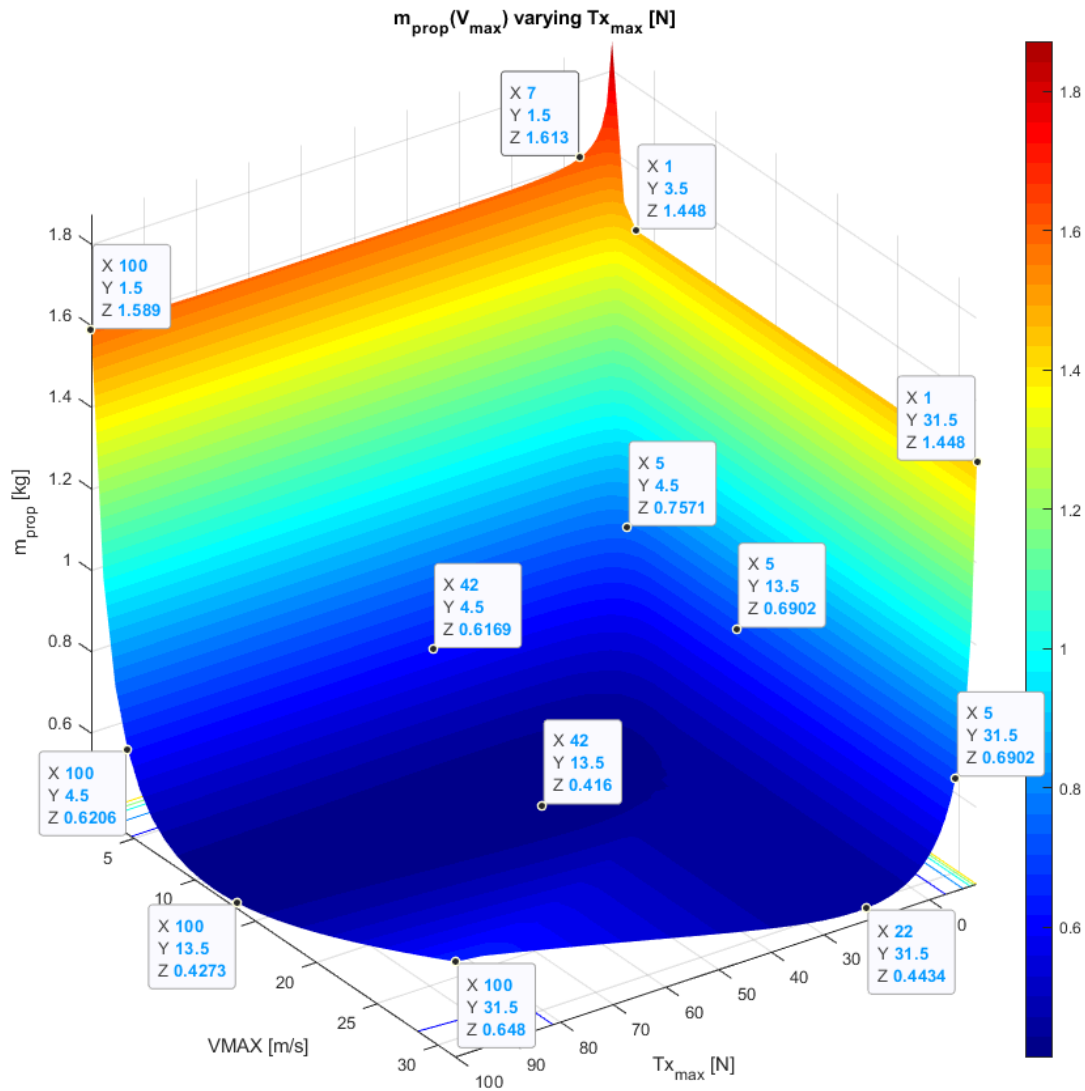


Figure 3.41 – Effect of V_{max} and $T_{x_{max}}$ on prop. consumption of the horiz. translation manoeuvre

With regard to the vertical descent manoeuvre, the same considerations apply as for the vertical ascent. In fact, even in this case, the higher the maximum velocity and maximum continuous thrust, the lower the propellant consumption. According to the previous assumptions, the LuNaDrone hovers, at the beginning of the vertical descent inside the lunar pit, at a height of 30m above the lunar surface. Assuming that the LuNaDrone has to descend by 100m inside the Lunar pit, the change in altitude of this manoeuvre will be a total of 130m. The results in Figure 3.44 refer to the case in which the initial mass of the spacecraft is 15kg and the specific impulse is 150s.

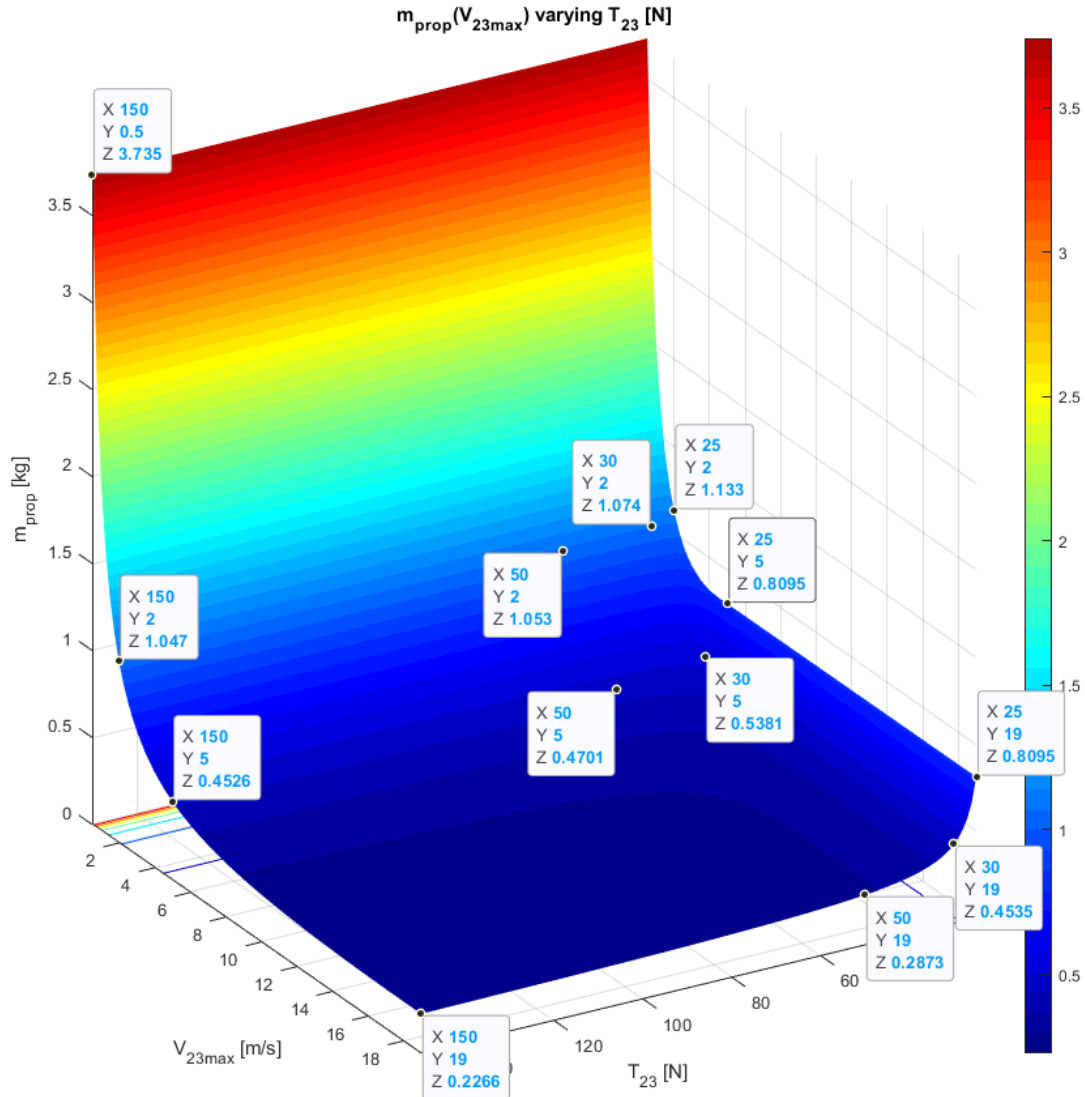


Figure 3.42 – Effect of V_{max} and T_{max} on prop. consumption of the vertical descent manoeuvre

Finally, as far as the hovering manoeuvres are concerned, their results are quite predictable: the longer the manoeuvre time, the greater the propellant consumption (see Figure 3.32).

The optimal trajectory, from a system point of view, does not always correspond to the one that leads to the lowest propellant consumption. In Figure 3.50 we have represented, as a first manoeuvre, a vertical ascent of 30m. The need for such a manoeuvre is dictated by the architecture of the navigation system currently under study [17]. In particular, in order to frame the skylight inside the FOV of the camera, taking into account its orientation inside the spacecraft, it is necessary that the LuNaDrone flies at a certain height which depends on the pitch angle θ and the distance from the centre of the skylight. This navigation system requirement is depicted in Figure 3.43 (in this case it was considered a distance from the centre of the skylight of 200m, a camera FOV of 120° and a camera inclination of 30° with respect to the x-axis of the vehicle reference frame).

From Equation (3.81) we deduced that for the horizontal translation manoeuvre the optimal pitch angle was 30° . However, according to the navigation system requirements, shown in Figure 3.43, if the spacecraft has to maintain that pitch angle during the horizontal translation manoeuvre, or rather, during the acceleration phase of such manoeuvre, it should first perform a vertical ascent of 150m (0-1 section of Figure 3.50).

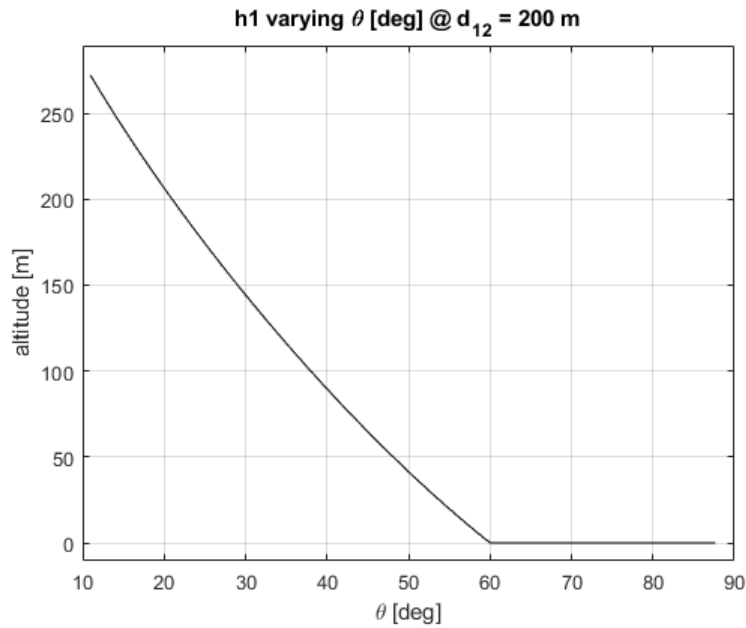


Figure 3.43 – Navigation system requirement

Assuming that the LuNaDrone retraces its forward trajectory back to the rover (in other words, with reference to Figure 3.50, $0 \equiv 7$, $1 \equiv 6$, $5 \equiv 2$ and $4 \equiv 3$), it will also have to perform a vertical descent manoeuvre of 150m (6-7 section) which is added to the vertical descent that the LuNaDrone will have to perform in order to descend inside the lunar pit and assuming it must reach a depth of 100m, the total descent, depicted in Figure 3.50 as a vertical line between points 2 and 3, would be of 250m. In addition to these manoeuvres, there is also the vertical ascent represented in Figure 3.50 by points 4 and 5, whose increase in altitude, assuming $\theta = 30^\circ$, would be 250m as well.

Using the results of the models developed in this chapter, Figure 3.44 shows the propellant mass as a function of the increase in altitude of the four manoeuvres mentioned before: $m_{p_{A_1}} \rightarrow 0-1$ section of Figure 3.50, $m_{p_{D_2}} \rightarrow 6-7$, $m_{p_{D_1}} \rightarrow 2-3$ and $m_{p_{A_2}} \rightarrow 4-5$. Actually $m_{p_{D_1}}$ and $m_{p_{A_2}}$ do not represent the cost of the overall manoeuvre but only the increase in propellant consumption caused by the fact that the spacecraft has to go up/down for a stretch longer than 100m, which corresponds to the indicative value of the depth at which the LuNaDrone must descend inside the lunar cave.

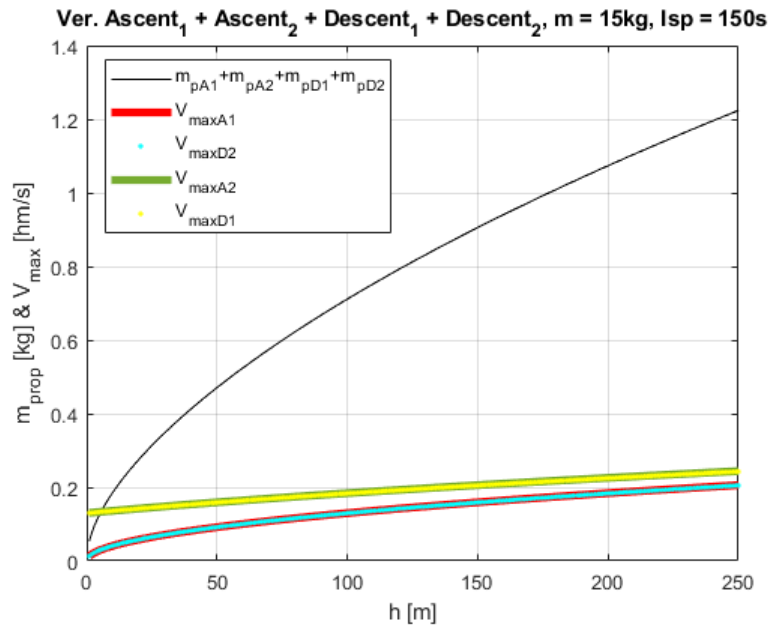


Figure 3.44 – Propellant consumption caused by navigation system requirement

Summing up, in order to make the horizontal translation manoeuvre more efficient, the theta angle must be about 30° , however, this leads to raising the altitude to be reached with the first vertical ascent manoeuvre, which also affects the other three abovementioned manoeuvres, increasing their propellant consumption. Figure 3.45 shows the propellant consumption of the horizontal translation manoeuvre as the horizontal thrust component, T_{12} , varies. For each value of T_{12} , the optimal maximum velocity, expressed by Equation (3.109), was considered. These results refer to a manoeuvre in which the initial mass of the spacecraft is 15kg, the specific impulse is 150s and the distance between the manoeuvre start and end point is 200m. In the configuration without auxiliary thrusters, fixed the value of the vertical thrust (which must be equal to the weight of the spacecraft), varying T_{12} means varying the pitch angle.

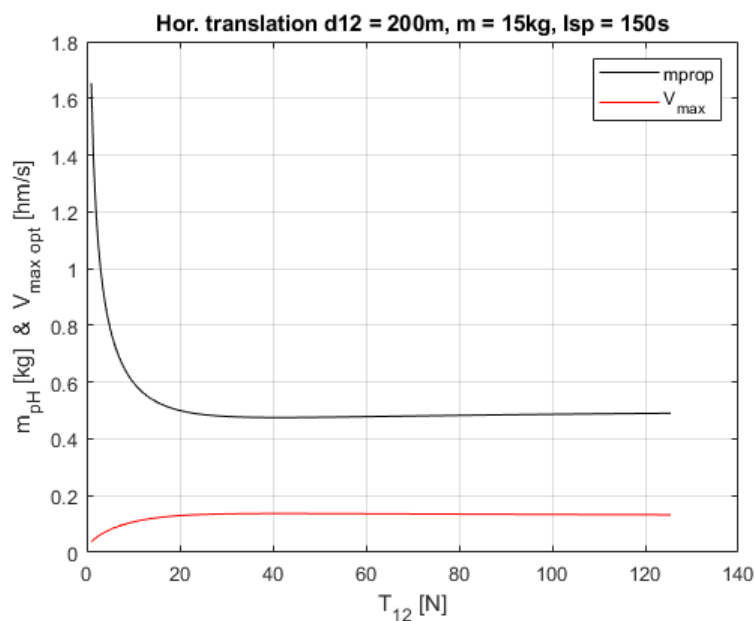


Figure 3.45 – Propellant consumption of the Hor. Translation varying T_{12}

By correlating the pitch angle θ with the horizontal component of the thrust (T_{12}) it is possible to associate the navigation system requirement, expressed in Figure 3.43, with the propellant consumption of the ascent and descent manoeuvres, depicted in Figure 3.44. Finally, we need to correlate the propellant consumption of the horizontal translation manoeuvre with T_{12} (Figure 3.45). In conclusion, as shown in Figure 3.46, it is possible to relate the propellant consumption of all these manoeuvres to T_{12} .

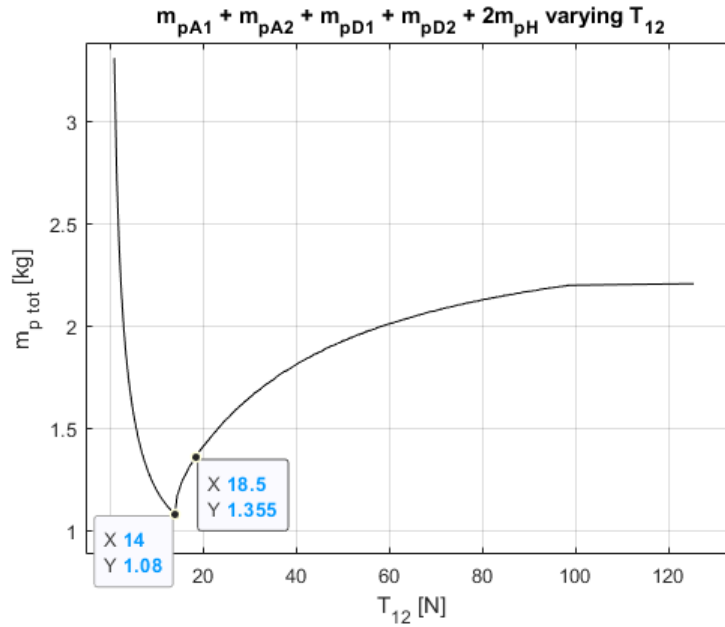


Figure 3.46 – Propellant consumption varying T_{12}

Figure 3.46 shows that the optimal point, from the point of view of propellant consumption, is at $T_{12} = 14N$ which means that during the acceleration phase of the horizontal translation manoeuvre the pitch angle assumes a value of $\theta = 60^\circ$. Therefore, the optimal condition seems to be the one in which the spacecraft theoretically does not perform the first vertical ascent manoeuvre, preventing all the resulting propellant consumption but leading to a slightly less efficient horizontal translation manoeuvre. Nonetheless, other requirements from the navigation system [17] impose a minimum altitude of about 30m. This requirement comes from the need to avoid excessive deformation of the skylight image perceived by the camera and the need to frame it within the camera's FOV once the LuNaDrone hovers above the centre of the skylight. In other words, using the nomenclature used in this chapter, point 1 and point 2 must both have a minimum altitude of 30m relative to the lunar surface. Using the graph in Figure 3.43 we find that this requirement implies a pitch angle of about $\theta \approx 53^\circ$ which in turn implies a T_{12} of about 18.5N.

Although these navigation system requirements are still at a preliminary stage, and may be subject to significant changes, it was nevertheless useful to demonstrate how the models developed in this chapter can actually support the design choices of the spacecraft subsystems. In this regard, it is possible to make another example that concerns the interaction between flight profile simulations and propulsion system performance. Preliminary analysis of the propulsion system revealed a relationship, depicted in Figure 3.47, that relates the mass of the thruster to the thrust magnitude [16].

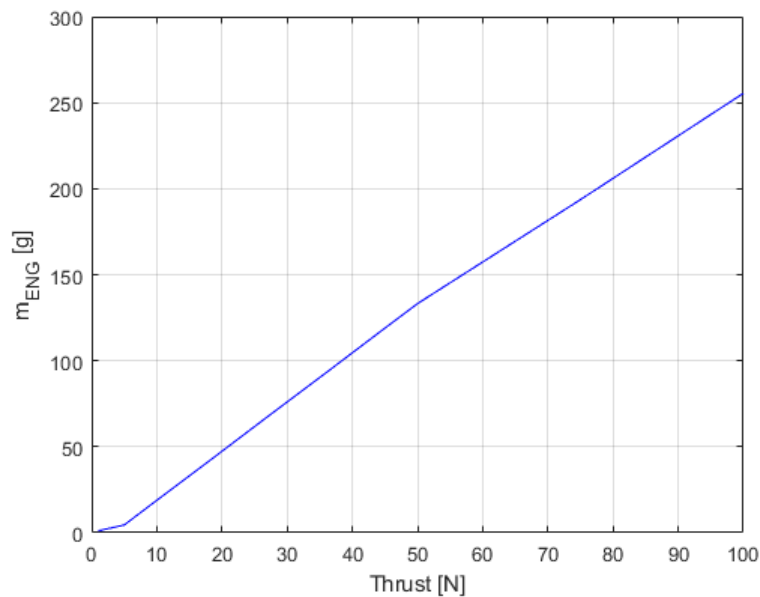


Figure 3.47 – Mass of the thruster as a function of the thrust magnitude

As mentioned before, the greater the maximum continuous thrust that the propulsion system is able to deliver, the lower the propellant consumption of vertical ascent and descent manoeuvres. Once the mission objectives have been set, in particular, once the LuNaDrone's flight profile has been defined, if these manoeuvres require less propellant we can store less of it on board the spacecraft, which in turn leads to the possibility of creating a lighter and more compact propellant feed system. Preliminary analysis of this system (which includes tanks for propellant and pressurising gas, tubes, valves etc.) shows that its mass varies by about 1.5 times the variation of propellant to be stored [16]. Please note that this is still a rather rough estimate and depends a lot on the system architecture and tanks geometry.

Figure 3.48 shows how the propellant consumption of the ascent and descent manoeuvres varies with the changes in altitude and the maximum continuous thrust (for these results no limitations imposed by the maximum velocity were considered). As mentioned before, propellant consumption does not change substantially if the thrust goes from 50N to much higher values, while it suffers significant variations between values just above those required for hovering (e.g. 25N) and slightly higher values (e.g. 30N).

Let us suppose, on the basis of the above considerations, that a 30m and 130m vertical ascent and descent manoeuvres are scheduled in the flight profile. In addition to the propellant consumption of these manoeuvres, we will consider the variation of the propellant feed system mass by multiplying the mass of propellant by 1.5.

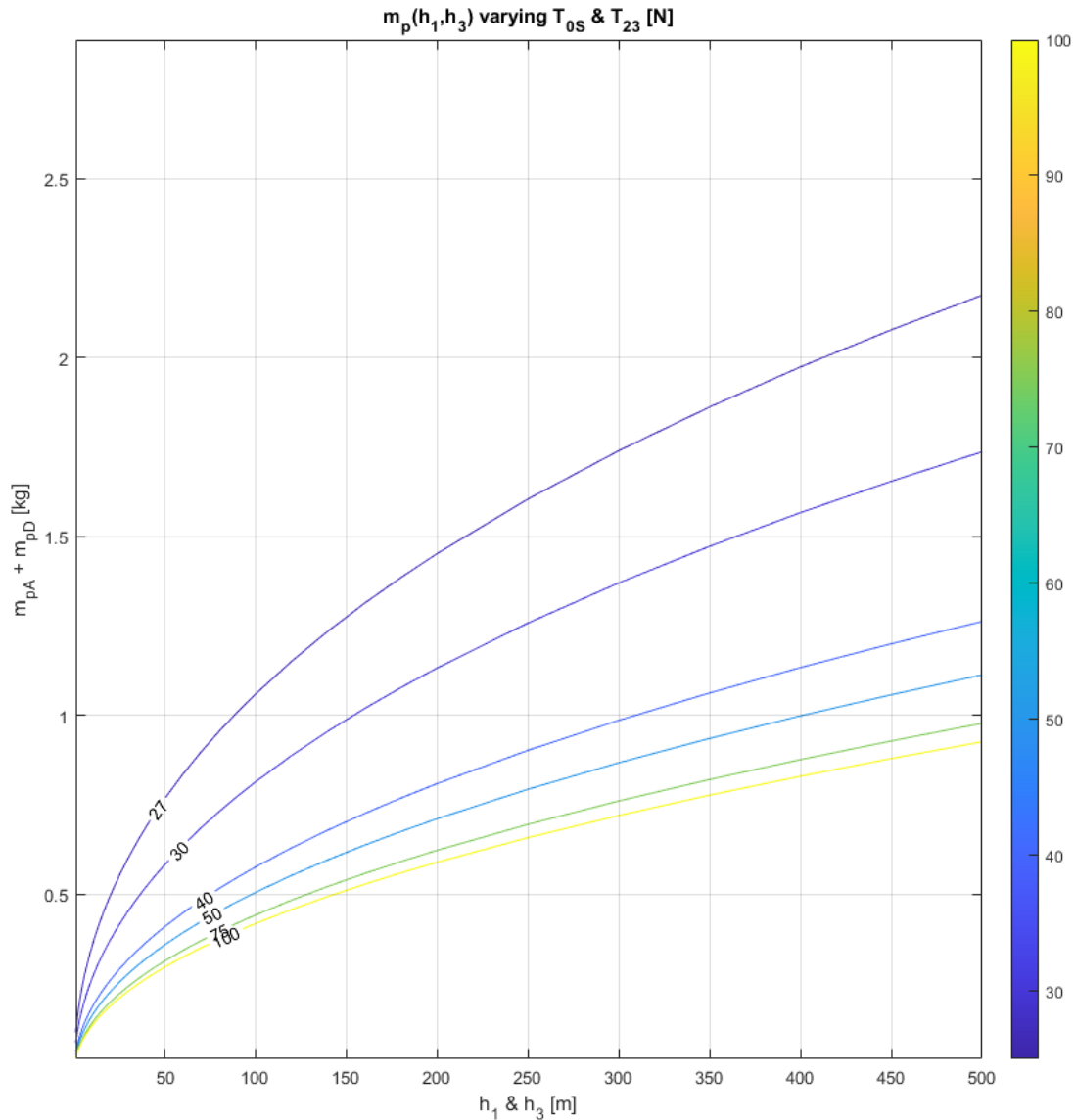


Figure 3.48 – Prop. consumption of ver. ascent and descent manoeuvres ($m_i = 15 \text{ kg}$, $I_{sp} = 150 \text{ s}$)

The total mass of this system does not only depend on the total mass of propellant to be stored as some of its components, such as valves for example, must be installed regardless of the amount of propellant. However, even if we consider, in this particular analysis, also the mass of these additional components and the mass that is dictated by the propellant that is not directly related to the ascent and descent manoeuvres, the effect would simply be to move the curve shown in Figure 3.49 upwards, thus not affecting the position of the optimum point we are interested in.

The $m_p + m_f$ curve represents the mass of propellant required to perform the four vertical ascent and descent manoeuvres plus the increase in mass of the feed system that this propellant causes. The m_{eng} curve shows the relationship between the thruster mass and the thrust magnitude presented in Figure 3.47. Finally, the blue curve is the sum of the two previous curves, which allows us to identify the optimum point that in this case is at 103N.

This curve also shows that for thrusts greater than 50N there are no substantial variations with respect to the optimum point. This aspect is particularly important because the size of the thruster depends directly on the thrust. In particular, the greater the thrust, the more bulky the thruster. Consequently, given the stringent requirements regarding the maximum volume of the LuNaDrone, adopting a solution that is slightly disadvantageous in terms of mass, choosing 50N as the maximum continuous thrust, is largely repaid by the possibility of installing a much more compact thruster on board the spacecraft.

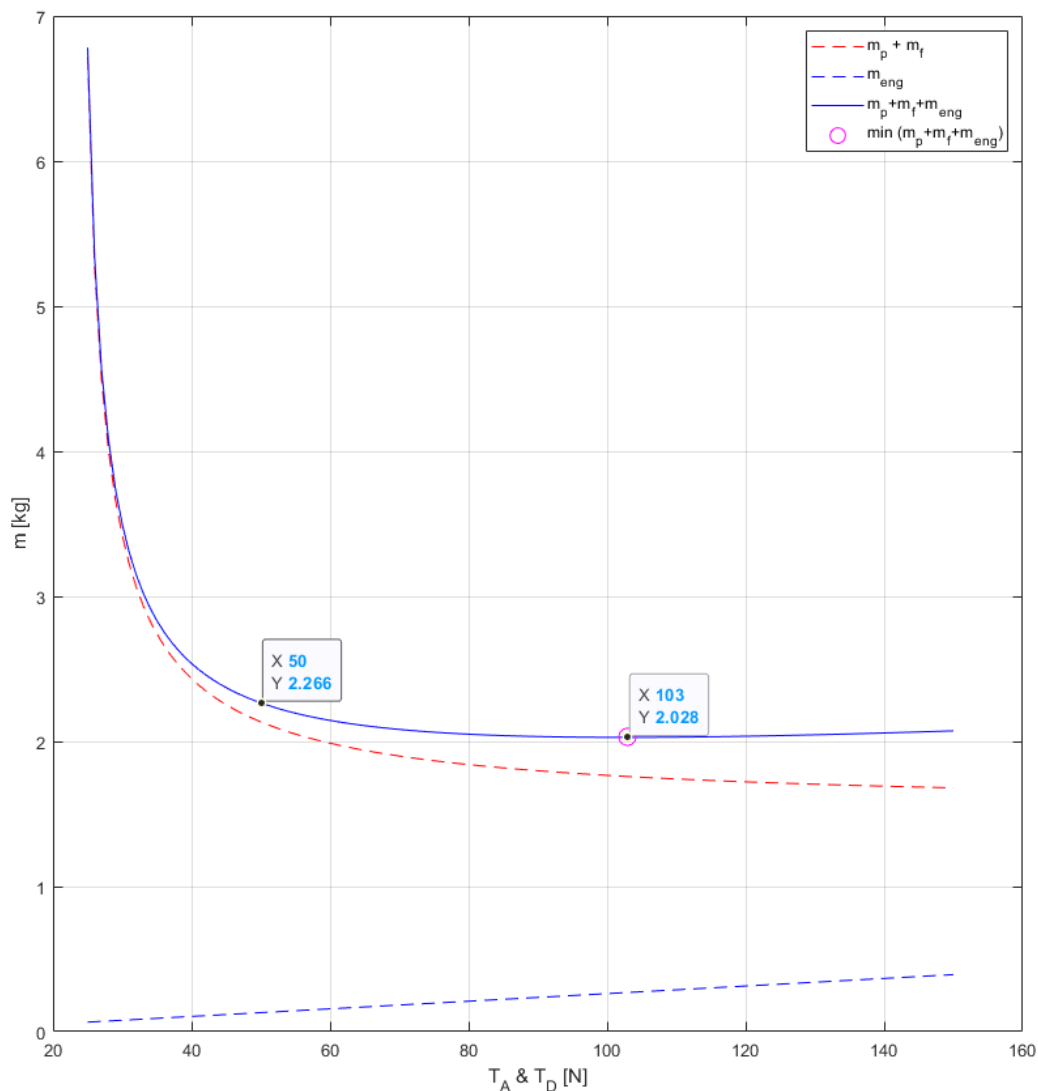


Figure 3.49 – Mass of propellant and propulsion system as a function of thrust

In conclusion, these two examples of interaction between flight profile simulations and navigation and propulsion systems have shown that the models developed in this chapter are able to provide quantitative data that allow us to relate flight performance to the design choices and figures of merits of spacecraft subsystems. As we said at the beginning of Chapter 3 this study has the critical task of assessing the feasibility of the mission. Although the definition of the spacecraft subsystems are still at a very preliminary level, the results on propellant consumption suggest that the mission may be feasible, even though the data we have is not yet sufficient to state this with an acceptable margin of certainty. Also for this reason, in subsequent iterations, new flight profiles should be explored and connections with spacecraft subsystems should be intensified.

Points coordinates	X	Z
0	0 m	0 m
1	0 m	30 m
2	200 m	30 m
3	200 m	-100 m
4	200 m	-100 m
5	200 m	30 m
6	0 m	30 m
7	0 m	0 m

Table 3.6 – Coordinates of the points shown in Figure 3.50 with respect to the inertial reference frame

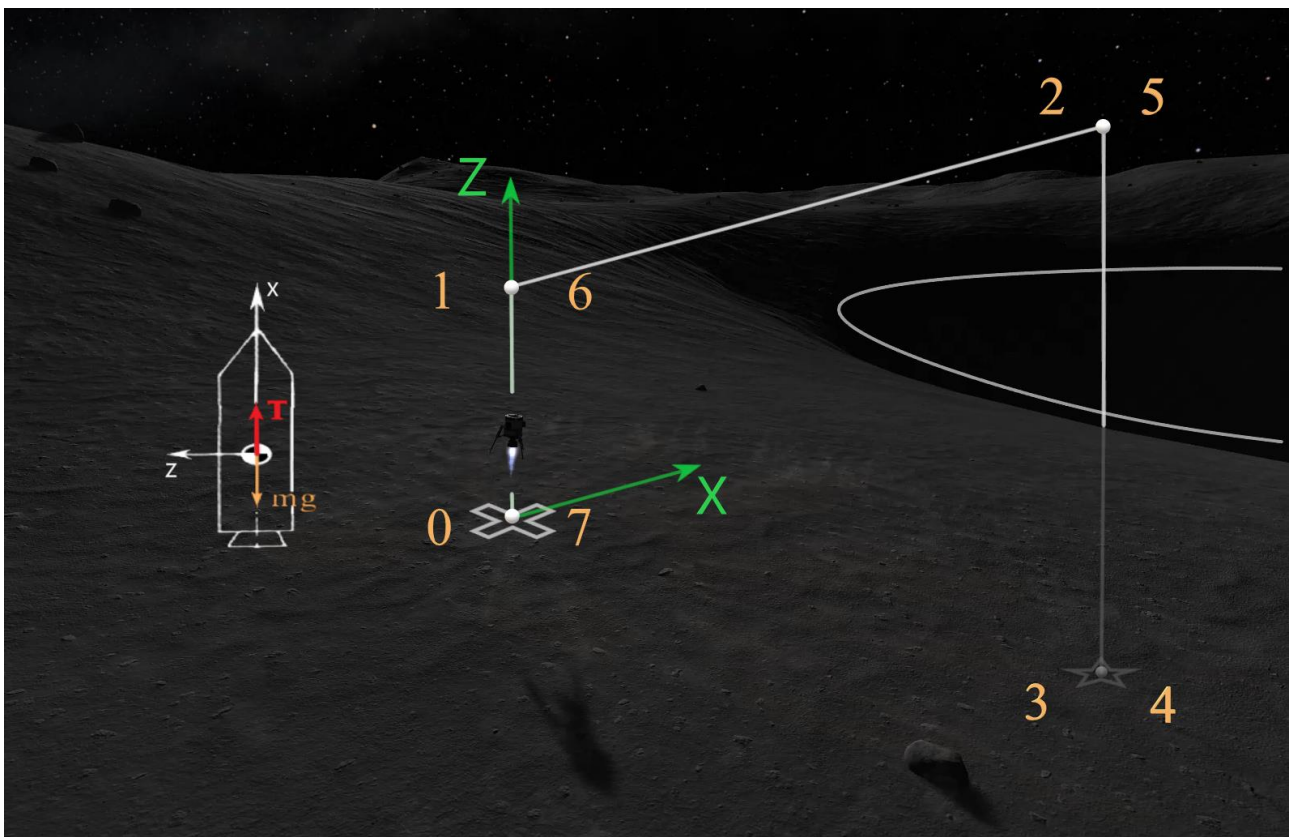
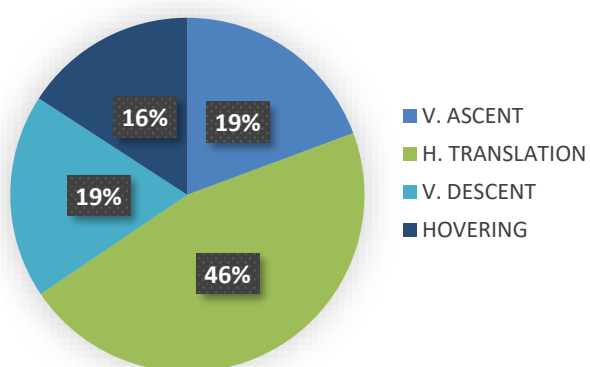


Figure 3.50 – Illustration of the nominal trajectory of the LuNaDrone

OUTWARD					RETURN				
	m_p [kg]	m_p [%]	t [s]	t [%]		m_p [kg]	m_p [%]	t [s]	t [%]
V. ASCENT	0,139	6,8%	8,476	6,9%	V. ASCENT	0,257	12,5%	17,021	13,9%
H. TRANSLATION	0,498	24,3%	25,669	21,0%	H. TRANSLATION	0,449	21,9%	24,817	20,3%
V. DESCENT	0,268	13,0%	17,187	14,1%	V. DESCENT	0,115	5,6%	7,997	6,5%
HOVERING	0,243	11,8%	15,500	12,7%	HOVERING	0,082	4,0%	5,500	4,5%
OUTWARD-TOT	1,148	56,0%	66,832	54,7%	OUTWARD-TOT	0,902	44,0%	55,335	45,3%

Table 3.7 – Propellant masses and manoeuvre times of the flight profile presented in Figure 3.51

Propellant consumption



Manoeuvre time

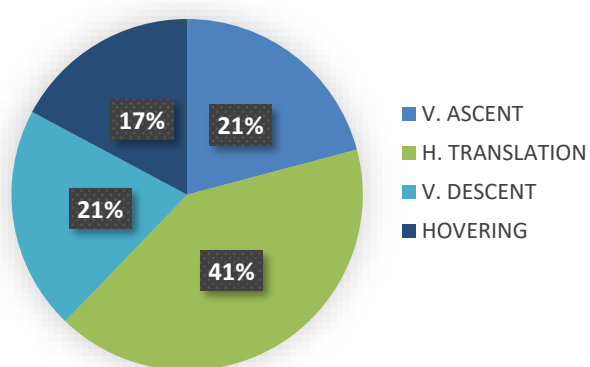


Table 3.8 – Percentages of propellant consumption and manoeuvring time

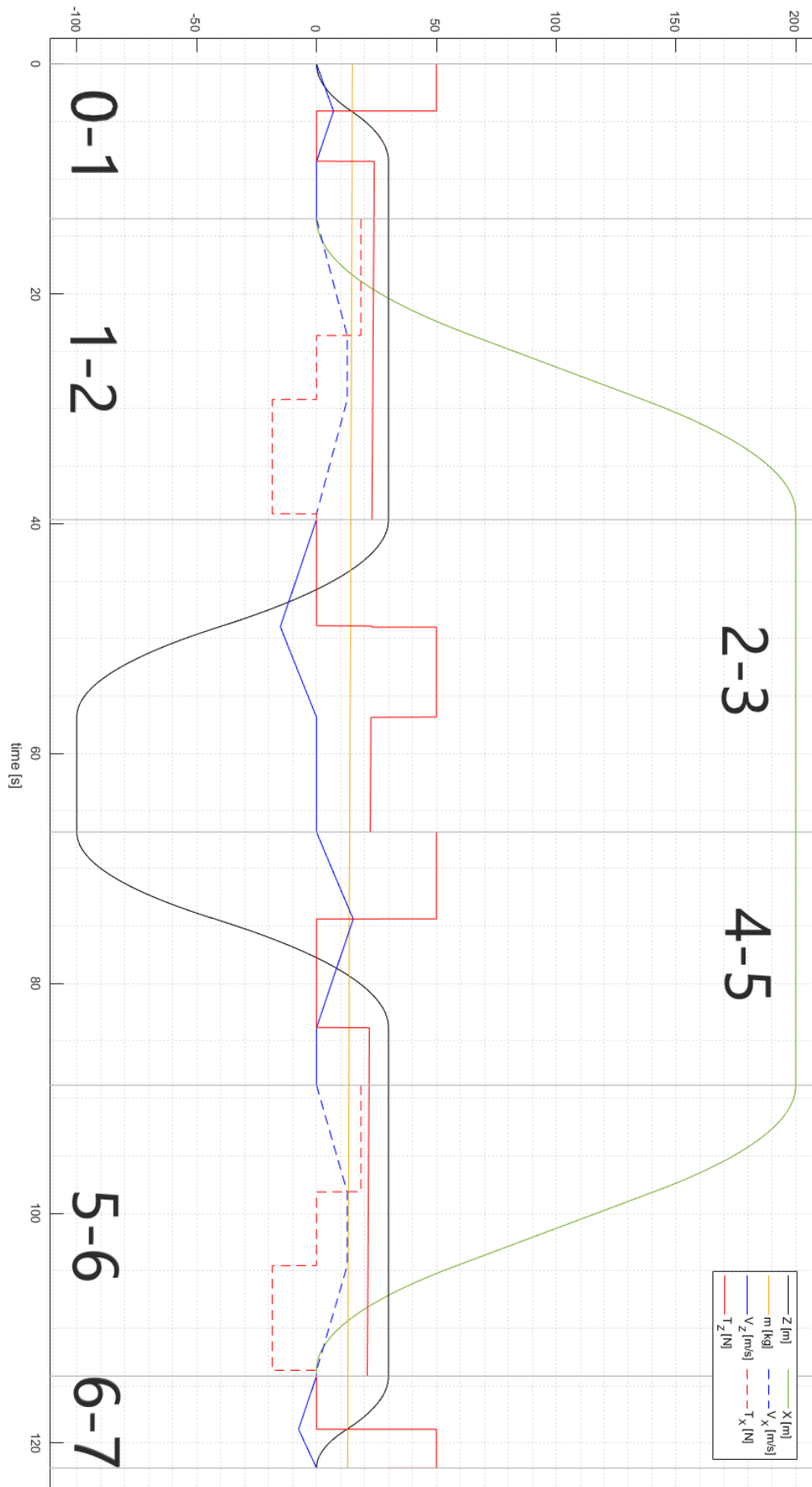


Figure 3.51 – Flight profile simulation of the trajectory depicted in Figure 3.50

4 EPS

4.1 Introduction

The electrical power system (EPS) is designed and configured to perform several key functions: it must be a continuous and reliable source of peak and average electrical power for the life of the mission; it must control, distribute, regulate, and condition the power provided to the various loads; it must be capable of providing data regarding the health and status of its operation; and it must protect itself and its loads from electrical faults anywhere within the spacecraft [20].

In its simplest form, a spacecraft electrical power system consists of four major components, as shown in Figure 4.1. The prime power source will provide energy for conversion into electricity. Conversion into electricity then occurs through a variety of methods, depending on the nature of the prime source and the spacecraft electrical loads. The electricity that is generated will need to be managed, regulated, monitored, and conditioned to match the electrical needs of the spacecraft systems [21].

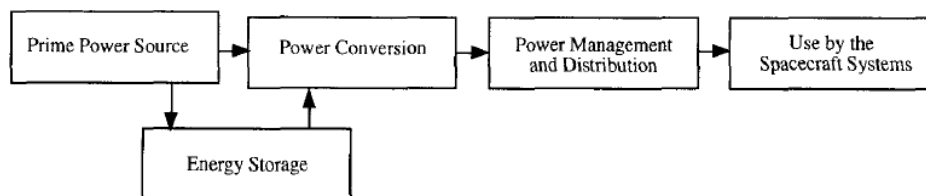


Figure 4.1 – Elements of the Electrical Power System

The choices available as prime power sources in space are limited to three: nuclear, chemical, or solar. As shown in Figure 4.2, the duration of the mission is a key factor in the selection of the prime power source. For short-duration missions, such as ours, chemical systems such as primary batteries or fuel cells, may be the appropriate choice [21].

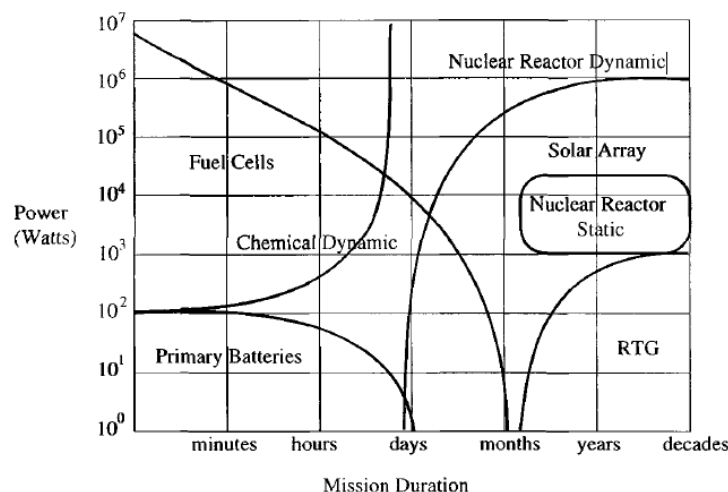


Figure 4.2 – Options for various mission power needs and duration

Although a spacecraft EPS consists of multiple elements and performs different functions, in this thesis we will only discuss about the most suitable prime power sources to be used in our mission. In particular, we will briefly analyse the main three categories of prime power sources: nuclear, chemical and solar; and once identified the most suitable, (which will be the chemical one), a state-of-the-art analysis of the respective energy storage systems will be carried out.

4.2 Prime power sources – Solar Arrays

The majority of present-day spacecraft use a solar array as the primary energy source. The ‘fuel’ in this case is solar radiant energy, which is converted via the photovoltaic effect into electrical energy [22].

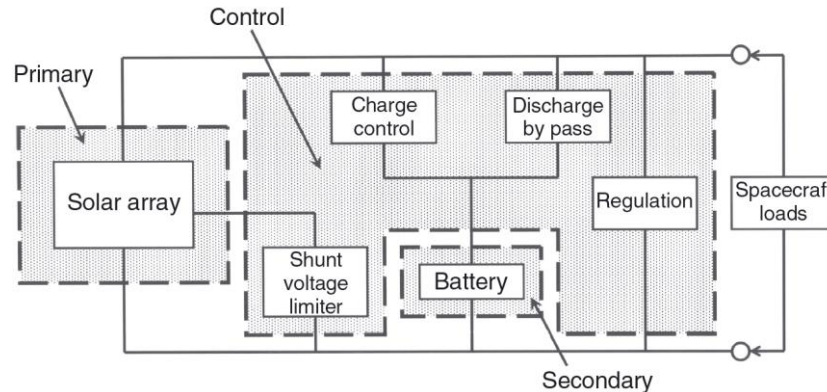


Figure 4.3 – Schematic of typical spacecraft power system block elements [22]

Although the combination of solar arrays and secondary batteries is the most common solution, the use of this technology is not particularly well suited to the concept of operations of our mission. This is due to several reasons including uncertain lighting conditions and the fact that the spacecraft is expected to conduct a single incursion into the lunar pit, in other words, our mission follows a one-shot approach.

Since one of the main mission objectives is to explore and photograph the interior of the lunar pit, it is possible that, even if the lunar surface was initially illuminated by the Sun during the first phases of flight, once entered through the skylight, the spacecraft will operate in a shadowed region and therefore the solar panel would not provide electrical power during this phase. To overcome this issue, one could introduce the mission requirement that the flight should take place when the interior of the lunar pit is illuminated by the sunlight. However, this would make the LuNaDrone's operational capabilities significantly less flexible and introduce a number of other restrictions and problems. For example, due to this requirement, the spacecraft may be required to have the ability to survive on the lunar surface for a long period of time waiting for the right moment to start the flight operations. This in turn would lead to much stricter requirements for certain systems (TCS and EPS for example) and spacecraft components (e.g. radiation tolerance).

In addition to all these issues, it should also be noted that the spacecraft attitude is imposed by the GN&C system for propulsion and navigation needs; thus installing body-mounted solar arrays may not be feasible. Therefore it would be necessary to install sun-tracking solar arrays, hence complicating the system (and therefore the risk of failure) and increasing the mass of the spacecraft. Actually, if the latitude of the mission site allows it, one could think of using body-mounted solar arrays for the sole purpose of recharging secondary batteries and providing the power needed for spacecraft to survive before the flight begins or once the spacecraft has re-emerged from the skylight. However, given the one-shot approach of our mission, such a solution would not be feasible.

Although all these aspects do not refer to any quantitative analysis, it seems rather clear that the choice of solar arrays as prime power source does not offer any advantage than just using secondary or primary batteries (in the case of secondary batteries, the rover/lander could fully recharge them before deploying the LuNaDrone on the Moon surface).

If the features of the mission were to change, and in particular, if multiple explorations of the interior of the lunar pit were planned, then the choice of the solar array as prime power source could be reconsidered. However, until then, this solution does not seem to be particularly promising.

4.3 Prime power sources – Nuclear Systems

From the early days of the space programs, nuclear power has played an important role and will probably continue to do so in the future [21]. Nuclear systems provide a favourable option for missions that require long-duration power in hostile space environments where sunlight for solar power is absent or limited [23].

There are two primary nuclear power technology options: (1) radioisotope power systems (RPSs) utilise the natural decay heat from ^{238}Pu to generate electric power levels up to about 1 kW and (2) fission power systems (FPSs) rely on a sustained fission reaction of ^{235}U and offer the potential to supply electric power from kilowatts to megawatts. Example missions utilising nuclear power include Mars science rovers (e.g., Curiosity, Mars 2020), lunar and Mars surface landers, crewed surface outposts, deep space planetary orbiters, Ocean World science landers, and robotic space probes that utilise nuclear electric propulsion [23].

Before going into details about the operation and performance of these systems, we can consider some of the intrinsic issues of these solutions that lead us to the a priori exclusion of these technologies. Given the maximum size of the LuNaDrone (12 U) the use of FPSs is totally out of the question. There would be many other reasons to exclude this solution, but for reasons of synthesis they will not be reported here.

On the contrary, although a radioisotope power system has not yet been integrated on a small spacecraft, they might be considered for future small spacecraft missions. However this concept would require substantial testing and modified fabrication techniques to facilitate use on smaller platforms [24]. Therefore, even if it becomes feasible to install an RTG in our spacecraft in the future, and assuming that such a solution will provide the best performance compared to all other possible solutions, this technology should still be abandoned as it does not meet the mission prerequisites. In fact, as mentioned before, the study of the solutions and components to be used must take into account, as far as possible, the availability of Italian products and the possibility of carrying out the mission in a reasonable time and cost by universities and SMEs, which is essentially impossible with nuclear systems.

In any case, even if it were possible to make RTGs small enough to be used in our spacecraft, the specific power of these system would be significantly lower than current systems. Analysis shows that radioisotope thermal power system scale poorly to small sizes, due to the cube-square scaling factors: thermal losses scale with surface area, while power generation scales with mass [25]. Taking this into account, we can analyse the advantages and disadvantages of current RTGs.

The advantages of RTGs over other systems include the following [22]:

1. They provide independence of power production from spacecraft orientation and shadowing.
2. They provide independence of distance from the Sun (deep-space missions are possible).
3. They can provide low power levels for long periods of time.
4. They are not susceptible to radiation damage in the Van Allen belts.
5. They are suitable for missions with long eclipse periods, for example, lunar landers.

In our case, advantages 2 and 3 are not particularly useful. In fact, the latter, considering the one-shot approach we intend to adopt, is basically the opposite of what is needed: medium/high power (compared to the small size of the spacecraft) for short periods of time (minutes/hours).

The disadvantages of RTG systems need also be considered, and include [22]:

1. They adversely affect the radiation environment of the satellite whilst in orbit. This will influence the spacecraft configuration significantly.

2. Careful handling procedures are required during satellite integration owing to the radiation hazard posed by the radioactive source.
3. High temperature operation is required for efficient energy conversion. This impacts upon the thermal environment of the vehicle, and again on vehicle configuration.
4. RTGs are a source of interference for plasma diagnostic equipment that may be carried as part of the scientific objectives of the mission.
5. At the political level there has been increasing concern expressed at the inclusion of radioactive material on board a satellite. This is principally of concern because of the potential for such a source to be dispersed in the atmosphere, should there be a launch failure.

These disadvantages, combined with the fact that the advantages listed above are actually rather limited when applied to our mission, are a clear demonstration of the inapplicability of this technology for the LuNaDrone. Add to this the rather limited performance (Table 3) which risks being even lower once the system is scaled to an acceptable size to be implemented in our spacecraft (assuming this is technologically possible).

Name	Power (W)	kg/kW
Cassini (1997 launch)	628	195
Galileo probe/Ulysses (GPHS RTG, late 1980s)	285	195
Nimbus/Viking/Pioneer (SNAP 19, mid 1970s)	35	457
Apollo lunar surface experiment:		
SNAP-27, early 1970s	25	490
SNAP 9A, 1960s	73	261

Table 4.1 – RTG system performance

In conclusion, without further analysis both FPSs and RPSs can be considered as unsuitable for this mission.

4.4 Energy storage systems

Once solar arrays and nuclear systems are excluded, all that remains is the chemical prime power sources, although in this case it would be more correct to call them chemical "energy storage systems".

The specific objective of this section is to assess the capabilities and limitations of state of practice (SOP) energy storage systems in order to evaluate their applicability to our specific mission. Given the technologically demanding nature of our mission, the same analysis will be carried out for advanced energy storage technologies currently under development.

The main energy storage devices used in spacecrafts are primary batteries, rechargeable batteries and capacitors. In addition, fuel cells have been used in several manned space missions but have not yet been used in robotic missions. Nevertheless, this category should not be excluded a priori as their applicability to unmanned missions has been studied for several years.

Before proceeding with the analysis of the available technologies, it should be noted that while making a choice among suitable alternatives to meet the requirements of a spacecraft, the factors to be considered are: 1) reliability, 2) efficiency, 3) life, 4) environmental compatibility, 5) endurance to environmental conditions in space (zero gravity, vibration, shock, acceleration, acoustic noise, etc.), 6) energy densities, 7) storage, 8) heritage, and 9) cost [21].

4.5 Primary Batteries (SOP)

In this chapter we will consider the possibility of using primary batteries as potential candidates for the LuNaDrone's primary energy source. In particular, we are going to consider those primary batteries which have been widely used or are currently used in space missions, in other words: SOP primary batteries.

Our mission is particularly close to the typical application of these devices since primary batteries (single discharge only) are typically used in missions that require a single use of electrical power for a period of a few minutes to several hours. Such missions include planetary probes (Galileo, Deep Impact, and Huygens), sample return capsules (Stardust and Genesis), Mars Landers (MER), and Mars Rovers (Sojourner). Primary batteries that are presently in use in space missions are: silver-zinc (Ag-Zn), lithium-sulfur dioxide (Li-SO₂), and lithium-thionyl chloride (Li-SOCl₂) [26].

4.5.1 Silver-Zinc (Zn-Ag₂O) Batteries

As the Table 4.2 shows, the Zn-Ag₂O cell is not the only zinc anode primary cell to have been used in space applications. However, considering the requirements of our mission, the Silver-Zinc cell appears to be the most suitable (mainly because it offers the highest discharge rate capability and, with the exception of the Zinc-Air cell, the highest value of energy density of the zinc anode cells).

Zinc Anode Primary Cells/ BatteriesZinc - Manganese Dioxide-LeClanche (Zn - MnO_2)Zinc - Manganese Dioxide Alkaline (Zn - MnO_2)Zinc - Mercuric Oxide (Zn - HgO)Zinc - Oxygen (Zn - O_2)Zinc - Silver Oxide ('Silver-Zinc') (Zn - Ag_2O)Lithium Anode-Soluble Cathode Primary Cells/ BatteriesLithium - Sulfur Dioxide (Li - SO_2)Lithium - Thionyl Chloride (Li - SOCl_2)Lithium Anode-Solid Cathode Primary Cells/ BatteriesLithium - Carbon Monofluoride (Li - $(\text{CF})_x$)Lithium - Manganese Dioxide (Li- MnO_2)

Table 4.2 – Primary Cells Used in Shuttle Missions [21]

Name	Cell Designation	Nom. Volt. (V)	OCV (V)	Energy Density (Wh/kg) (Wh/l)		Temp. °C	Comments
LeClanche	Zn // NH_4Cl / ZnCl_2 // MnO_2 / C	1.6	(1.3)	65	100	-5 to 45	Low cost, sloping voltage
Alkaline	Zn // ZnO / KOH // MnO_2 / C	1.6	(1.3)	95	220	-20 to 55	Greater drain rate, sloping voltage
Mercury	Zn // ZnO / KOH // HgO	1.35	(1.3)	105	325	0 to 55	Level voltage
Zinc-Air	Zn // KOH/NaOH // O_2 (Air)	1.5	(1.4)	290	905	0 to 50	Highest available energy of Zn anode cells
Silver-Zinc	Zn // KOH / NaOH // $\text{Ag}_2\text{O}/\text{AgO}$	1.8	(1.6)	200	515	-20 to 55	High drain rate, high cost

Table 4.3 – Zinc Anode Primary Cell Characteristics [21]

In space, Silver-Zinc cells have been used in several important applications: as primary battery in launch vehicles (powering pyro devices and onboard electronics guidance and control systems) [27], to power the tools to repair the Solar Max Mission (SMM) spacecraft [21], and as the electrical power source of the EMU [28]. Most of the primary batteries on Apollo and Skylab were Zinc-Silver Oxide. A 40 Ah, 28 V Ag-Zn battery was used to supply primary power to the Mars Lander for a 30-day mission lasting actually 100 days. As a reserve battery it has been used in some long term missions where the electrolyte is maintained in a bellows leaving the cell dry until activation [21]. This last aspect is particularly important for our mission. In fact, if a hibernation phase was foreseen between launch and operational phases, if the strategy of keeping the cell dry is not used, the self-discharge of the battery would put serious limits on the performance and residual capacity available for the flight phases.

As shown in Table 4.4, the specific energy of a Silver-Zinc cell is 200 Wh/kg and energy density is >500 Wh/l with a very high specific power. The battery parameters are generally 50% of the cell values depending on structure, wiring, connectors and sensors. This system has the highest rate capability compared to other primary battery systems. The major limitations of this battery are short storage life (in the range of 6 months to 1 year) due to dissolution of the active materials, reduced performance at low temperature (70% of capacity at 0°C and 35% at -20°C), limited operating temperature range as for all aqueous systems, and orientation sensitivity. Life is also diminished sharply at elevated temperatures [27].

Type	Cell Parameters and Battery Parameters by Mission Application	Nominal Voltage (a)	Specific Energy, Wh/kg (b)	Energy Density, Wh/l (b)	Specific Power, W/kg (c)	Operating Temp. Range, °C	Capacity Loss % Per Year	Mission Life (yrs)	Manufacturer	Configuration
Ag-Zn	Cell	1.61	200	550	1100	0-55	60	1	Yardney	Prismatic
	Typical Launch Vehicle	28	119	280	120	5 to 40	60	1	Eagle Picher	Manually Activated
Li-SO ₂	Cell	2.9	238	375	680	-40 to 70	<1			Cylindrical
	Galileo Probe Battery	38	91	145	260	-15 to 60	<1	9	Alliant Tech	Three 13 cell batteries
	Genesis Battery	24	142	125	400	-20 to +30	<1	6	SAFT	Two 8 cell batteries
	MER	30	136	390	390	0 to 60	<1	4	SAFT	Five 12 cell batteries
	Stardust	20	192	182	519	-26 to +50	<1	10	SAFT	Two 8 cell batteries
Li-SOCl ₂	Cell	3.2	390	875	140	-30 to -60	<2.5			Cylindrical
	Sojourner	9	245	515	100	-20 to 30	<2.5	4	SAFT	Three 3 cell batteries
	Deep Impact	33	221	380	105	-20 to +30	<2.5	4	SAFT	Three 13 cell batteries
	DS-2	14	128	340	65	-80 to +30	<2.5	4	Yardney	Two 4 cell batteries
	Centaur Launch batteries	30	200	515	85	-20 to +30	<2.5	6	Yardney	One 9 cell batteries
Li-BCX	Cell	3.4	414	930	150	-40 to 70	<2		Wilson GB	Cylindrical
	Astronaut Equipment	6	185	210	115	-40 to +72	<2	3	Wilson GB	2 cell radio batteries
Li-CF _x	Cell	2.6	614	1050	15	-20 to 60	<1		Eagle Picher	Cylindrical DD
	Range Safety battery	39	167	150	15	-20 to 60	<1		Eagle Picher	15 Cell Battery

Table 4.4 – State of Practice of Primary Batteries [27]

Although primary cells can usually be discharged once, this is not wholly true for certain devices including Ag-Zn cells. In this regard, the 2000 Series Increased Capacity Battery for the Extravehicular Mobility Unit is rechargeable for a minimum of 12 charge/discharge cycles over a wet life of 300 days [28]. Hence, this battery, if assembled with adequate separator and design, can be considered a limited use rechargeable cell. Moreover, this particular feature helps to provide the engineers with the information that the batteries can meet the capacity requirements and are acceptable for flight [21]. Therefore, the short storage life, which is one of the major drawbacks of this technology, may be mitigated by the rechargeability of these batteries. In this regard, the lander/rover that takes us close to the skylight may provide the power needed to fully recharge the battery before deploying the LuNaDrone. However, this solution would lead to the installation of the necessary components to recharge the battery, thus increasing complexity, mass and size of the system.

In recent times, Silver-Zinc batteries (and other aqueous alkaline type) have been largely replaced by more energetic lithium-based primary battery systems, e.g., Li-SO₂ and Li-SOCl₂, which have much higher voltage, specific energy, and energy density, exhibit much longer storage life capabilities, and the operational temperature range is much wider than that displayed by aqueous batteries. Nevertheless, the Silver-Zinc batteries are still the best in terms of specific power and do not present the voltage delay anomalies and safety issues affecting lithium systems [26]. Therefore, compared to lithium-based primary battery systems, this technology is not particularly attractive, especially if we consider that Li-BCX batteries have been intensively tested to ensure their safety (to the extent that they have been used for the EMU's helmet lights and cameras). As a result, this system ends up losing one of its few strong points (greater safety than its competitors). Nevertheless, the battery's rechargeability (albeit for a limited number of cycles) and the best specific power remain very interesting features.

4.5.2 Lithium-Sulfur Dioxide (Li-SO₂) Batteries

Lithium anodes and non-aqueous electrolytes cells offer the highest energy densities (Wh/kg, Wh/l), and longest storage life of any electrochemical cell thus far developed. The reason for this is due to the large energy storage capability and lengthy shelf life of lithium itself. However, the same reasons are also the cause of the safety hazards associated with this technology. The majority of safety issues are related to the soluble cathode cells group which includes Li-SO₂ and Li-SOCl₂. In these cells the active material of the cathode is also in contact with the anode, thus providing capability for relatively high discharge rate but also concern for safety.

If subjected to abnormal operations or conditions, the large quantity of energy can be released quickly, resulting in venting or, on rare occasions, explosion [21].

NASA has used Li-SO₂ cells and batteries in planetary probes (Galileo and Cassini), sample return capsules (Genesis and Stardust) and the Mars Exploration Rover (MER) Lander [26].

Technology	Mission	Launch Date	Battery Configuration	Manufacturer	Cell Size, or Model	Capacity (Ah)	Operating Voltage Range	Battery Mass (kg)	Specific Energy (Wh/kg)	Operating Temperature Range (°C)	Calendar Life (Years)
Li-SO ₂	Stardust	2/7/99	4s2p	Saft America, Inc.	LO26SX	14	8V - 12V	1.2	130	- 20° to 40°C	9
Li-SO ₂	Genesis	8/8/01	8s2p	Saft America, Inc.	LO26SX	14	16V - 24V	2.06	150	- 20° to 40°C	5
Li-SO ₂	MER-Rover	6/10/03	12s5p	Saft America, Inc.	LO26SX	34	25V - 34V	7.55	155	0° to 60°C	3.5
Li-SOCl ₂	Deep Impact	1/12/05	9s24p	Saft America, Inc.	LSH20	312	24V - 32V	36.6	250	- 20° to 40°C	4

Table 4.5 – Characteristics of SOP Primary Batteries Used in PSD Missions [29]

Li-SO₂ cells exhibit an open circuit voltage of 3.0 V, a high specific energy of >225Wh/kg) and high energy density of ~375Wh/l. The specific energy and energy density at the battery level depend strongly upon the battery design and construction, and typically varies from 50–80% of the specific energy of the cells.

The Li-SO₂ cell has the highest rate capability (specific power) of SOP lithium primary cells, and can operate with little loss of performance between –40°C and 60°C. When the load is first initiated, this cell exhibits a short delay in reaching the nominal voltage, due to the presence of a passivation layer on the lithium electrode which is broken down with operation. The application of a conditioning discharge prior to use, typically performed using a de-passivation circuit, minimises this problem [26].

4.5.3 Lithium-Thionyl Chloride (Li-SOCl₂) Batteries

Li-SOCl₂ batteries have been used in the past on the Mars Pathfinder Rover-Sojourner (1996), New Millennium Deep Space-2 (1998), with astronaut equipment, and on the Centaur launch vehicles (Air Force). More recently, they have been used on the Deep Impact mission (2005) [26].

Although having lower specific power, Li-SOCl₂ and Li-BCX cells offer higher specific energy (390–410Wh/kg) and energy density (875–925Wh/l) than Li-SO₂ cells. Performance at battery level have varied from 30–60% of cell values in actual applications, depending on design and construction. As in the case of Li-SO₂ cells, Li-SOCl₂ cells are affected by a significant voltage delay, which can nonetheless be easily managed by proper de-passivation circuits. [26].

In some cells (i.e. Li-BCX), bromine chloride (BrCl) is added to the electrolyte to improve safety. This is important as primary lithium batteries can reduce size and weight compared to Ag-Zn batteries, but cannot be used in certain applications until their safety has been proven. In this regard, with the application of adequate safeguards, and after extensive testing, NASA Johnson Space Center (NASA/JSC) approved the use of selected

primary lithium batteries even for specified astronaut equipment. In particular, NASA/JSC has developed safety requirements for all batteries considered for use in astronaut equipment. Several specific cells of the following types have been approved for use in astronaut equipment: alkaline, Ag-Zn, Ni-Cd, Ni-MH, and Li-BCX. In particular, the Li-BCX system has been used in the helmet lights and TV cameras [30].

In addition to the lithium batteries we have discussed so far, there are two other categories that we have not yet considered. The first is a type of developmental cell used in DS-2 Mars Microprobe Battery. In this cell addition of an electrolyte salt, lithium tetrachlorogallate (LiGaCl_4), allowed cell operation down to -80°C [31]. The other category is Li- CF_x batteries. Despite having the highest energy density, they have had limited use in space applications because of their limited rate capability ($\sim 15 \text{ W/kg}$), limited performance at low temperatures and safety concerns [27].

4.6 Advanced Primary Batteries

In case the performance of the SOP primary batteries does not meet our mission requirements, we may consider some of the advanced lithium-primary systems currently under development, which include: Li- CF_x and Li/ CF_x - MnO_2 .

The potential advantages of Li- CF_x batteries are: a) $2\text{--}3\times$ mass and volume savings relative to SOP Li- SO_2 and Li- SOCl_2 batteries, b) wider operating temperature range (-40°C to 60°C), c) minimal voltage delay, and d) improved shelf life characteristics (10-15 years). Existing Li- CF_x batteries have impressive specific energy and energy density, but only at low discharge rates of $\leq C/20$ at room temperature, and display poor performance at low temperatures. The recent improvements with aluminum cans have resulted in impressive performance characteristics: capacity of $>19 \text{ Ah}$ in a D-size cell, specific energy of over 700 Wh/kg and energy density of 1000 Wh/l . Safety characteristics have improved as well with built-in positive temperature coefficient (PTC) current limiting devices [26].

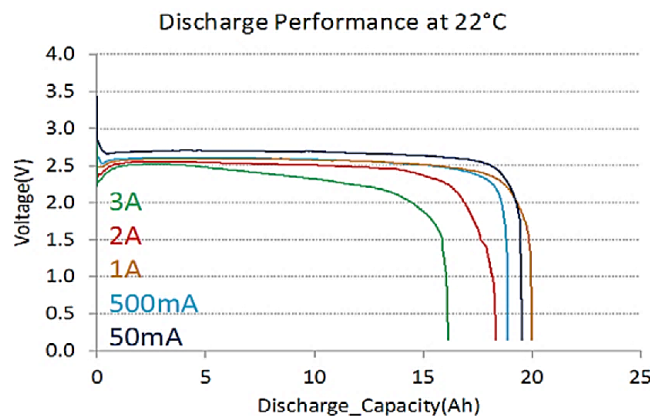


Figure 4.4 – Performance of Li- CF_x D-cell at different discharge currents [26]

A variant of this technology are the Li/ CF_x - MnO_2 cells. Although the latter have a slightly lower specific energy and energy density than Li- CF_x cells, on the other hand they have improved rate capability and safety. Recent improvements observed with lightweight aluminium cans have resulted in impressive performance characteristics: capacity of $>16 \text{ Ah}$ in a D-size cell, corresponding to a specific energy of over 600 Wh/kg and

an energy density of 900 Wh/l. Furthermore, as Figure 4.5 shows, the CFX-MnO₂ hybrid cathode allows operations over a wide range of -40°C to 70°C [26].

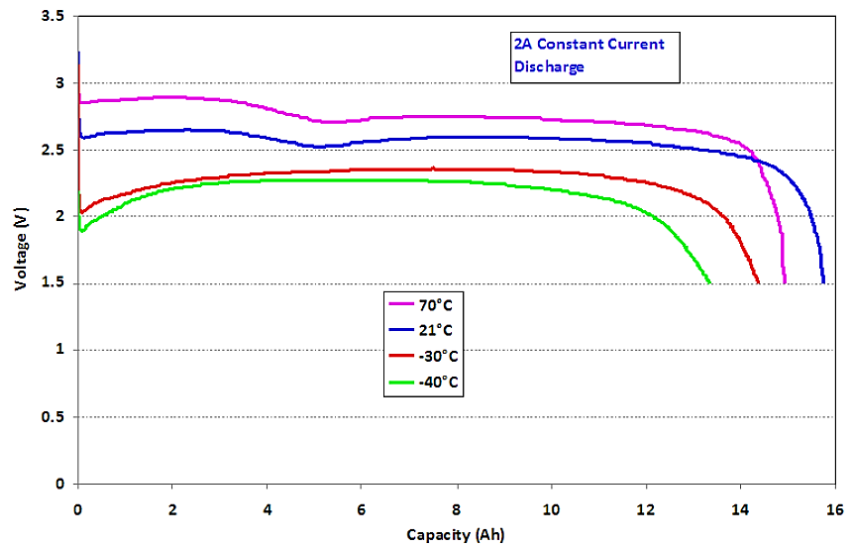


Figure 4.5 – Performance of Li/CFX-MnO₂ D-type cell at different temperatures [26]

The performance we mentioned so far referred to the single cell. As we mentioned before, the same values at battery level are inevitably lower than those associated with the single cell. The estimated battery level performance of the last two technologies (Li-CFx and Li/CF_x-MnO₂), SOP lithium primary batteries and Li-O₂ batteries are shown in Table 4.6.

Battery Level	SOP	Adv. Li-CF _x	Adv. Li-CF _x MnO	Adv. Li-O ₂
Specific Energy (Wh/kg)	150-250	400-500	350-450	500-600
Energy Density (Wh/L)	250-400	600-800	550-600	700-800
Shelf life (Years)	>10	>10	>10	5
Operating Temperature	-40 to +60°C	-30 to +60°C	-40 to +60°C	-20 to +60°C
TRL	9	4	4	3

Table 4.6 – Battery level performance of Lithium Primary Batteries [29]

4.7 Rechargeable batteries (SOP)

Rechargeable batteries (also referred to as secondary batteries) have been used primarily in solar powered missions to provide electrical power during eclipse periods and for load leveling. They have been used in orbital missions (TOPEX, Mars Global Surveyor, and Mars Reconnaissance Observer), Mars landers (Viking and Phoenix), and Mars rovers (Spirit, Opportunity, and Curiosity). Rechargeable batteries used in space missions include: silver-zinc (Ag-Zn), nickel-cadmium (Ni-Cd), nickel-hydrogen (Ni-H₂), and more recently, lithium-ion (Li-ion) [26].

Li-ion batteries offer significant mass and volume advantages compared to the other batteries. The SOP Li-ion batteries have low-specific energies (<100Wh/kg) and low-energy densities (<200Wh/l). Other shortcomings of SOP Li-ion batteries are: a) limited resilience to high temperature exposure (>60°C), b) limited low temperature operational capability (<-30°C), c) poor abuse tolerance (during inadvertent over charge/over discharge and short circuit), and d) incompatibility with standard planetary protection methods. Advanced Li batteries are projected to offer one or more of the following advantages: a) higher specific energy and energy density (2–3× compared to SOP Li-ion batteries, b) long cycle life and calendar life, and c) improved low-temperature performance. The projected specific energies of these advanced rechargeable batteries are: advanced Li-ion (150–200Wh/kg), Li-solid state (250–350 Wh/kg) and lithium-sulfur (250–350 Wh/kg) [26].

Even if we consider the best technology of secondary batteries, i.e. Li-ion cells, their performance (energy density, specific energy, etc.) would still be lower than that of primary batteries. In fact, the present-day mission architecture does not include recharging cycles, therefore, these devices would be used as if they were primary batteries. Once the spacecraft subsystems are defined, and once the power budget has been estimated, it will be possible to carry out more accurate analyses and determine whether it is still convenient to use primary batteries or change the mission architecture so that secondary batteries, which would replace the primary batteries, can be recharged (ensuring better performance at reduced weight and size).

4.8 Capacitors

Capacitors store small amounts of energy per kg compared to batteries, but they can deliver this energy in short high-power pulses. Batteries have a much higher specific energy, but cannot release this energy in short bursts like capacitors.

Capacitors have been used for applications that required repeated high power and short duration pulses (seconds). The Galileo and Cassini missions used capacitors for firing pyros and stepping motorized instrument platforms. New Horizons, with the primary mission to perform a flyby study of the Pluto system and now a Kuiper Belt object, used a capacitor bank in conjunction with a radioisotope thermoelectric generator (RTG) [27].

Supercapacitor cells, whose power capabilities are intermediate between conventional capacitors and batteries, are available in the <1 F to >3000 F range, typically at 2.7 V to 3 V, with a specific energy of 5 Wh/kg and specific power exceeding 1 kW/kg. The capacitors can provide power for extended discharge periods up to a few minutes as opposed to fractions of a second. Furthermore, these cells can operate at temperature <-40°C, and up to 150°C through the use of appropriate cell designs and electrolytes [26].

Primary batteries, which seems to be the most suitable solution, have very good performance in terms of energy density, but limited performance in terms of specific power. For this reason, the use of capacitors or

supercapacitors in a hybrid configuration with primary batteries could be a very interesting solution. However, in order to assess their applicability to our mission, quantitative analyses will be necessary, taking into account the power budget of the mission and the characteristics of the loads of the spacecraft subsystems.

4.9 Fuel Cells

Primary fuel cells have been used in missions that required large amounts of electrical power for periods of many hours to many days, such as human space missions [27]. In particular, fuel cells provided the primary power source for the Shuttle orbiter and they were originally designed as part of the Mercury, Gemini and Apollo US manned missions [22]. Table 4.7 shows how their performance has evolved since the earliest days of manned space flight.

System	Specific power (W/kg)	Operation
Gemini	33	
Apollo	25	
Shuttle	275	2500 h at P_{ave}
SPE technology	110–146	>40 000 h
Alkaline technology	367	>3000 h
Alkaline technology	110	>40 000 h

Note: SPE solid polymer electrolyte.

Table 4.7 – Performance summary of fuel cells for space use [22]

While in the case of batteries specific energy is the main figure of merit, in the case of fuel cells specific power best describes the fuel cell capability. In fact, the capacity of a fuel cell system is increased or decreased simply by the volume of stored fuel and oxidant [21].

A fuel cell converts the chemical energy of an oxidation reaction directly into electrical energy, with minimal thermal changes. In particular, the hydrogen/oxygen fuel cell has been used for space applications, a product of the reaction being water. A schematic diagram of such a cell is shown in Figure 4.6. From a system viewpoint, a major advantage is its flexibility. For example, it provides power during both sunlit and eclipse periods, and the fuel has a high-energy density and thus provides a compact solution compared with a solar array. The evident disadvantage is the need to carry fuel [22].

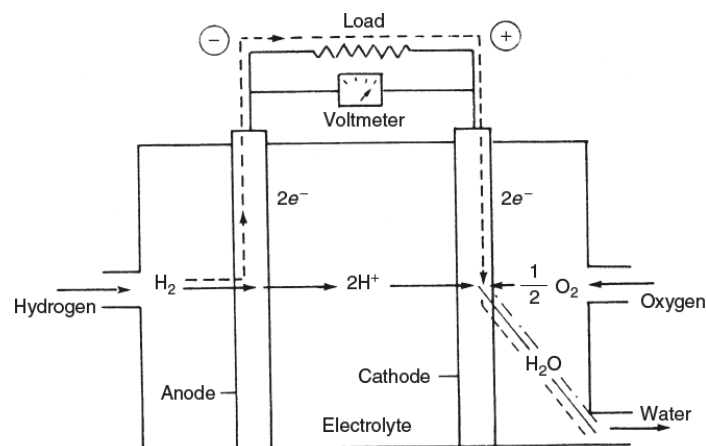


Figure 4.6 – Schematic of a hydrogen/oxygen fuel cell.

Early fuel-cell systems were primarily based upon the technology of solid polymer electrolyte (SPE). For the Gemini series, 1kW was produced at a specific power of 33 W/kg, within a volume of 0.05 m³. The Apollo system, also used for Skylab, was based upon matrix aqueous alkaline technology and achieved a power level of 1.5kW at a specific power of 25 W/kg. Shuttle developments, also based upon the alkaline technology, improved the specific power by an order of magnitude, ~12 kW, 275 W/kg. [22].

So, in summary, the types of fuel cells that have been or are being considered for space use include: Alkaline Electrolyte H₂-O₂ fuel cells (AFC) which operate at 40° - 60°C, Proton Exchange Membrane Electrolyte H₂-O₂ Fuel Cells (PEMFC) which operate at 60°-80°C, and Direct Methanol/O₂, Liquid-Feed Proton Exchange Membrane Fuel Cells (DMLFFC/PEM) operating between 20°C and 90°C. Except for the Biosatellite missions, only the alkaline and PEMFC have been used in space [21].

Anyway, as mentioned before, fuel cells have only been used in missions that required large amounts of electrical power for periods of many hours to many days. This suggests an inherent incompatibility between this technology and our mission. In fact, fuel cells are typically used in those applications where conventional batteries are not suitable because of their much lower specific energy and scalability issues [26]. So in our case we have the opposite problem, if conventional batteries have scalability issues when used in missions that require multi-kilowatts of power for extended periods of up to 10 days (their mass and volume becomes unacceptable), fuel cells, on the contrary, are not suitable to be used in missions like ours which require a few 10s Watts to 100s Watts for duration of fractions of an hour to a few hours. In fact, considering these requirements, SOP fuel cells are not attractive due to miniaturization difficulties and system complexity [26].

Although this is true for SOP fuel cells, it must be said that there are several studies whose aim is to overcome these problems by making fuel cells attractive even for missions like ours. Advanced fuel cell systems under development include: polymer electrolyte membrane (PEM) fuel cells, solid oxide fuel cells, and regenerative fuel cells. Among these systems, H₂-O₂ PEM fuel cells and regenerative fuel cells are the most promising systems in view of their performance advantages and advanced stage of development. In particular, H₂-O₂ PEM fuel cells are projected to provide higher specific energy compared to primary batteries (which at the moment represent the most suitable candidate for our mission). However, fuel cells do not readily scale to small sizes which is a big limitation given the extremely small size of the LuNaDrone. So, even if progress is being made in this direction, small PEM fuel cells could become interesting only for space science missions that require power levels of 100 watts or greater for time periods of 20–30 hours or more [26]. We can therefore conclude that this technology is not currently mature enough to be adopted in our mission.

4.10 Conclusions

As shown in Figure 4.7, the EPS provides, stores, distributes, and controls spacecraft electrical power. Throughout this chapter, we have only discussed about the first two aspects.

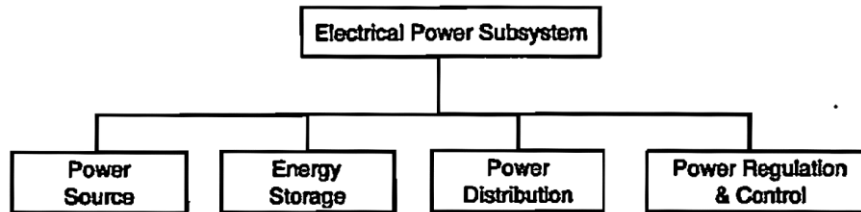


Figure 4.7 – Functional Breakdown for the Spacecraft's Power Subsystem [32]

According to [32] “the most important EPS sizing requirements are the demands for average and peak electrical power and the orbital profile (inclination and altitude)”. Our mission does not include an orbital flight, or rather, it is not expected that during this inevitable phase of the mission the spacecraft will be in an operational mode, as the operational phases of the LuNaDrone will actually take place on the surface of the Moon. Usually, the orbit profile is important to determine the lighting conditions (which in turn are critical for the sizing of solar arrays and secondary batteries). In our case the lighting conditions are dictated by the latitude of the mission site, the date of the LuNaDrone's deployment on the lunar surface and the topographical features of the lunar pit, all of which have not yet been defined. Nevertheless, other factors, such as the short duration of the operational phase of the mission (from tens of minutes up to few hours), have excluded the solar category, of which solar arrays are part, from the possible power sources. For a number of factors specified in Chapter 4.3, nuclear systems have also been excluded, leaving chemical power sources as the only suitable choice. Of this last category we analysed primary batteries, secondary batteries, capacitors and fuel cells. The latter were excluded mainly because fuel cells do not readily scale to small sizes.

As mentioned before, the operational phase of the mission has a very short duration. Moreover, since we have previously excluded the possibility of installing solar arrays, during the flight (which basically coincides with the operational phase) the LuNaDrone will not have the possibility to recharge the secondary batteries. Once re-emerged from the skylight, the spacecraft will start transmitting mission data (photos of the interior of the lunar cave) to the rover/lander and if it does not transmit all of them during this final phase of the flight, it will finish transmitting them once it has landed. Once this is done, the mission will be completed. For this reason, even if in the pre- and post-flight phases you could theoretically use solar arrays to recharge the batteries, or do it directly through the rover/lander, it would be pointless because it is only during the flight phase that the LuNaDrone requires significant levels of electrical power. So in the end, even if we installed secondary batteries, they would still be used as primary batteries (just one discharge) but in this way they would not compete with primary batteries, as they generally have lower performance (e.g. lower specific energy). In conclusion, secondary batteries are not an advantageous solution when compared to primary batteries.

As far as capacitors are concerned, they are mainly useful to provide short-lived power peaks and, if necessary, we can think of using them in a hybrid solution with primary batteries.

Eventually, the most suitable option resulted to be primary batteries. In Chapters 4.5 and 4.6 we have extensively discussed about the characteristics of SOP primary batteries and advanced primary batteries. Table

4.8 summarises the performance of these various cell types considering both space-qualified products and products currently under development for space use.

As mentioned above, one of the main sizing requirements is the average and peak electrical power demand from the individual components of the spacecraft subsystems. Hence, the power budget. Furthermore, in the case of batteries, the operating voltage of these components directly determines the number of cells in series. In order to estimate the power budget, it is also necessary to know the operating modes of the spacecraft (which describe which devices are on, how much electrical power they are requiring and how this demand varies over time) and how long these operating modes will last throughout the mission. Unfortunately, this information is not yet available, except in a rather coarse form. This means that the selection of the most appropriate device (from those listed in Table 4.8) cannot be made until this data is defined.

Type	Cell Parameters and Battery Parameters by Mission Application	Reference	Nominal Voltage	Specific Energy [Wh/kg]	Energy Density [Wh/l]	Specific Power [W/kg]	Operating Temp. Range [°C]	Capacity Loss % Per Year	Mission Life (yrs)	Manufacturer	Configuration
Zn-Ag2O	Cell	[24] p. 28	1,61	200	550	1100	0° to 55°	60	1	Yardney	Prismatic
	Cell	[18] p. 187	1,6	200	515	-	-20° to 50°	-	-	-	-
	Cell	[18]	1,6	120	500	-	-	-	-	-	-
	Typical Launch Vehicle	[24] p.28	28	119	280	120	5° to 40°	60	1	Eagle Picher	Manually Activated
	ICB for EMU	[34]	-	100	200	-	-	-	1	-	-
	ICB for EMU - 2000 Series	[25]	16,8	67	152	10	-	-	300 days	-	11 cells in series
Li-SO2	Cell	[18]	3	280	440	-	-55° to 60°	-	-	-	Cylindrical
	Cell	[24]	2,9	238	375	680	-40° to 70°	<1	-	-	Cylindrical
	Cell (LO26SX)	[30]	2,8	255	400	-	-60° to 70°	<3	-	SAFT	D- size spiral cell
	Cell (LO26XSC)	[35] [36]	2,8	303	473	-	-60° to 71°	<3	-	SAFT	D- size spiral cell
	Galileo Probe Battery	[24]	38	91	145	260	-15° to 60°	<1	9	Alliant Tech	Three 13 cell batteries
	Genesis	[23]	16-24	150	-	-	-20° to 40°	-	6	SAFT	8s2p
	Genesis	[24]	24	142	125	400	-20° to 30°	<1	6	SAFT	Two 8 cell batteries
	MER	[23]	25-34	155	-	-	0° to 60°	-	3,5	SAFT	12s5p
	MER	[24]	30	136	390	390	0° to 60°	<1	4	SAFT	Five 12 cell batteries
	Stardust	[23]	8 - 12	130	-	-	-20° to 40°	-	5	SAFT	4s2p
	Stardust	[23]	20	192	182	519	-26° to 50°	<1	10	SAFT	Two 8 cell batteries
Li-SOCl2	Cell	[18]	3,6	600	900	-	-40° to 60°	-	-	-	Cylindrical
	Cell	[24]	3,2	390	875	140	-30° to 60°	<2,5	-	-	Cylindrical
	Cell (LSH20)	[33] [36]	3,6	468	892	79	-60° to 85°	<3	-	SAFT	D- size spiral cell
	Sojourner	[24]	9	245	515	100	-20° to 30°	<2,5	4	SAFT	Three 3 cell batteries
	Deep Impact	[23]	24 - 32	250	-	-	-20° to 40°	-	6	SAFT	9s24p
	Deep Impact	[24]	33	221	380	105	-20° to 30°	<2,5	4	SAFT	Three 13 cell batteries
	DS-2	[24] [28]	6 - 14	128	340	65	-80° to 30°	<2,5	4	Yardney	Two 4 cell batteries
	Atlas Centaur Launch batteries	[24]	30	200	515	85	-20° to 30°	<2,5	6	Yardney	One 9 cell batteries
	Philae Lander	[31] [32]	29,36	475	-	79	0° to 60°	-	-	SAFT	8s4p
Li-BCx	Cell	[18]	3,5	430	960	-	-40° to 60°	-	-	-	Cylindrical
	Cell	[24]	3,4	414	930	150	-40° to 70°	<2	-	Wilson GB	Cylindrical
	Astronaut Equipment	[24]	6	185	210	115	-40° to 72°	<2	3	Wilson GB	2 cell radio batteries
Li-CFx	Cell	[24]	2,6	614	1050	15	-20° to 60°	<1	-	Eagle Picher	Cylindrical DD
	Cell	[36] [41]	3	357	565	-	-40° to 85°	-	-	Panasonic	C
	Range Safety battery	[24]	39	167	150	15	-20° to 60°	<1	-	Eagle Picher	15 Cell Battery
Adv. Li-CFx	Cell	[23]	2,6	700	1000	74	-40° to 60°	-	10 - 15	-	D-Cell Alluminum Can
	Cell	[36] [42]	2,6	716	1001	-	-20° to 90°	<2	>10	Rayovac	D-Cell Alluminum Can
	Battery level	[26]	-	400 - 500	600 - 800	-	-30° to 60°	-	>10	-	-
Li-FeS2	Cell	[36] [37]	1,5	350	656	-	-40° to 60°	-	20	Energyizer	AA
Li-MnO2	Cell	[36] [38]	3	275	603	-	-40° to 72°	-	10	Ultralife	D
Li/CFx-MnO2	Cell	[36] [39]	2,6	464	734	-	-40° to 60°	-	-	EaglePicher	D
	Cell	[36] [40]	3	425	874	-	-30° to 55°	-	15	Ultralife	D

Table 4.8 – Summary of primary cells for space applications

Please note that for certain figures of merit, such as specific energy, it must always be specified at which operating temperature, and at which discharge current, it has been evaluated. Figure 4.8 shows an example of how the same data (referred to specific energy) varies according to the operating temperature and discharge current.

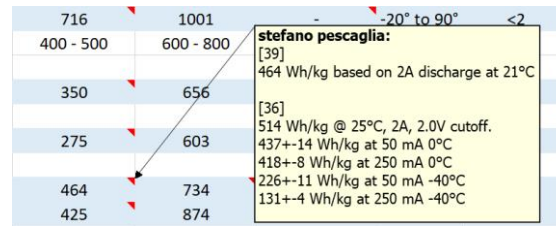


Figure 4.8 – Specific energy at varying discharge current and operating temperature

	Size [dm ³]	Mass [kg]	Power [W]	Voltage [V]
LiDAR XY	0.68	0.925	10	18
LiDAR Z	0.65	0.51	7	16
IMU	0.45	0.84	15	15.5
CAMERA	0.36	0.34	4.2	12
LED	0.008	0.06	80	34
OBC	0.13	0.15	1.3	16
Total	2.28	2.82	117.5	-

Table 4.9 – Technical characteristics of the navigation system components

From the technical characteristics of the components that make up the current navigation system [17] the most suitable nominal voltage, for the main power bus of the spacecraft, seems to be 18V. The only component that exceeds this voltage is the LED. This device, which is used to illuminate the area to be photographed by the camera, will operate for a rather short time. For this reason, if the maximum continuous current of the battery is not high enough to power the LED, the maximum pulse current is likely to be sufficiently high for this purpose. If this is not the case, we can think of installing capacitors, which are added to the voltage lift circuit necessary to raise the bus voltage to the operating voltage of the LED, which would provide the necessary electrical power to supply the LED during its short-time use.

In addition to the components listed in Table 4.9, we should also consider all the loads, which have not yet been defined, of the propulsion system, communication system and all the other spacecraft subsystems. Moreover, as mentioned before, it will be necessary to evaluate the operating modes and the duration of the various mission phases. In conclusion, after identifying the most suitable energy storage system category, i.e. primary lithium/silver-zinc batteries, we still do not have enough data to determine which device, belonging to this class, is the most suitable for our mission.

As a first iteration, we can reasonably consider a battery made up of 6 primary lithium D-type cells connected in series. The voltage produced by this battery should be high enough to meet the operating voltage requirements of the components of the various spacecraft systems. According to the values shown in Table 4.8, and considering the short duration of the operational phase of the mission, it is likely that the sizing requirement will be the maximum power that the battery can provide, rather than the energy it contains. For this reason, in the subsequent iterations, it will be necessary to carefully analyse Silver-Zinc primary cells, which in terms of power capabilities outperforms lithium based primary cells, or, if compatible with the mission's power budget, the use of rate-optimized lithium primary cells as the one reported in Figure 4.9.



Specifications

Part Number	LCF-136
Weight	29.5 g (0.07 lb)
Continuous Current/Power ¹	refer to tables on page 2
Maximum Pulse Current	20A for 20 sec
Voltage Range, Nominal	3.3-1.5V, 2.65V
Operating Temperature	-40 to +60°C (-40 to +140°F)
Transportation	UN 3090 Class 9

Figure 4.9 – Li/CFx-MnO₂ Primary Electrochemistry Rate-Optimized, High Energy Pouch Cell [33]

5 Annex 01 - Analysis of vertical ascent without braking thrust

Model: Tratto01h1V10.slx

Solver: Euler (ode1)

$DT: 1 \text{ ms}$

$m_0 = 15 \text{ kg}$

$I_{sp} = 150 \text{ s}$

$g = 1.62 \text{ m/s}^2$

$\Delta t_{h_1} = 0.5 \text{ ms}$

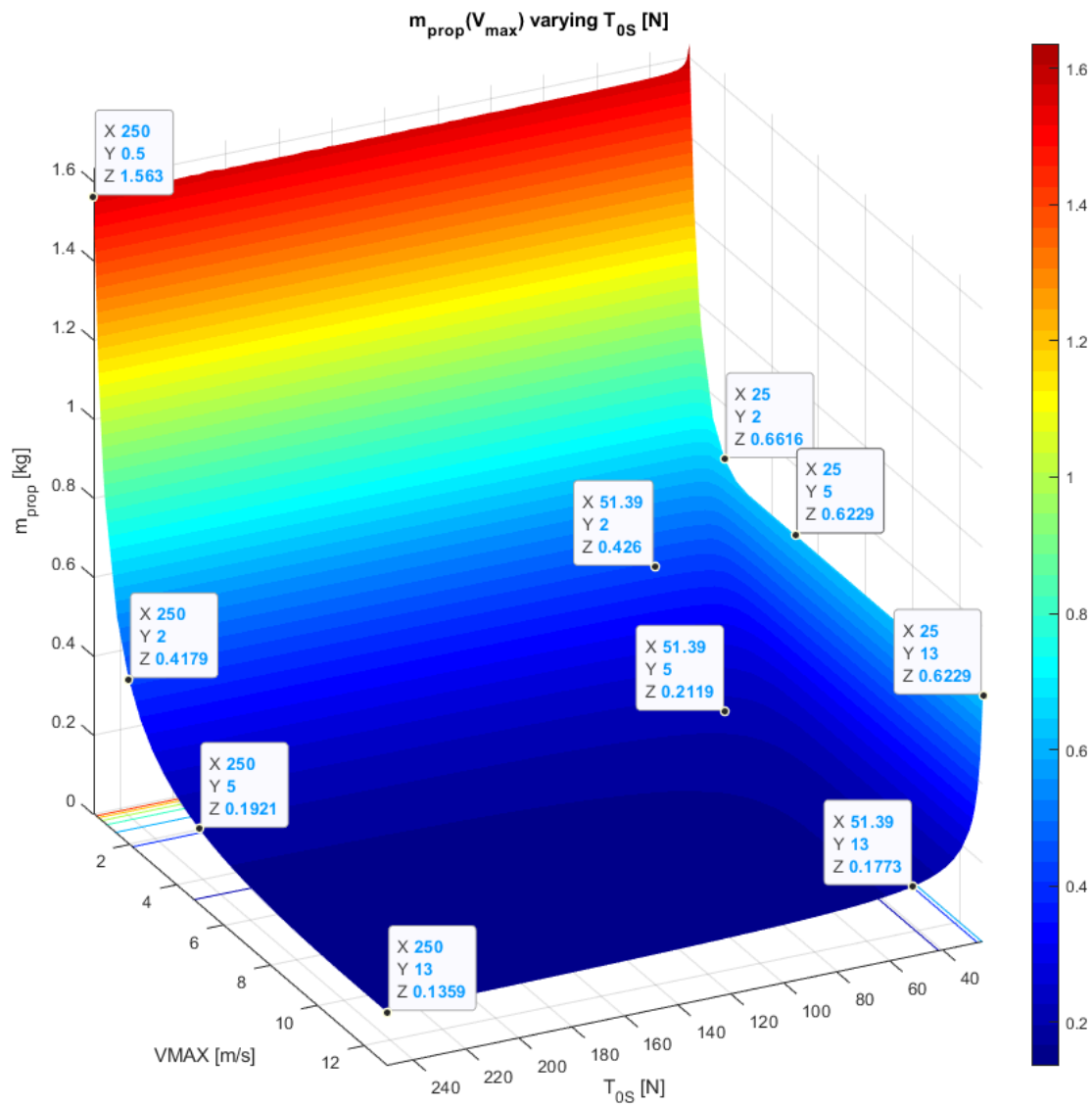


Figure 5.1 – $h_1 = 50 \text{ m}$, $I_{sp} = 150 \text{ s}$, $m_0 = 15 \text{ kg}$

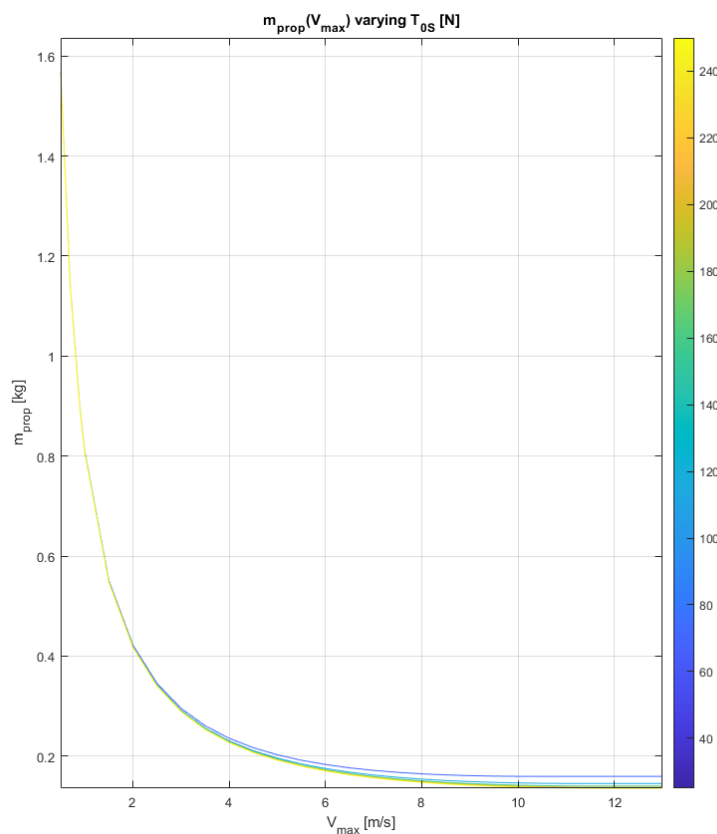


Figure 5.2 – $h_1 = 50 \text{ m}$, $I_{sp} = 150 \text{ s}$, $m_0 = 15 \text{ kg}$

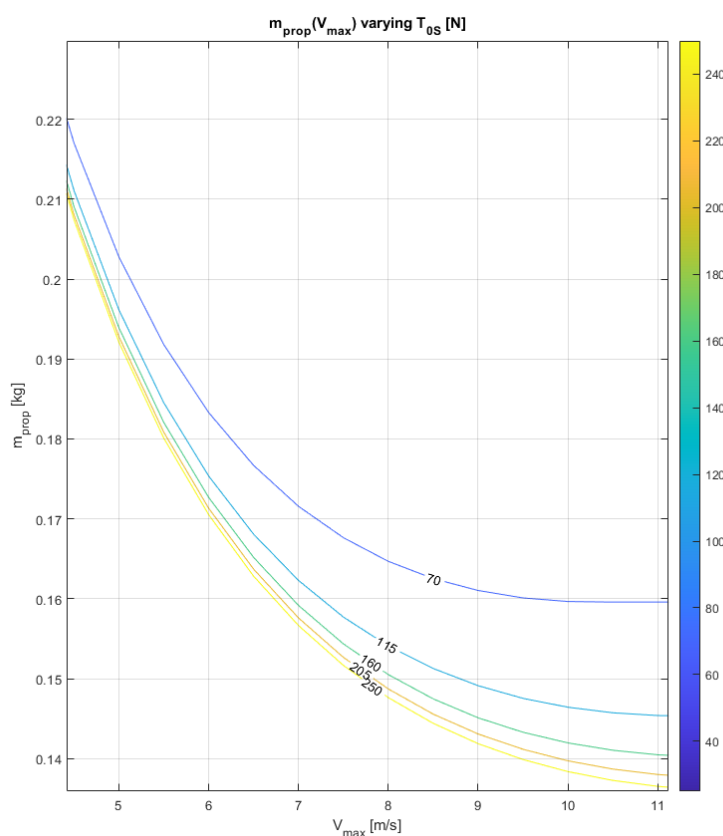


Figure 5.3 – $h_1 = 50 \text{ m}$, $I_{sp} = 150 \text{ s}$, $m_0 = 15 \text{ kg}$

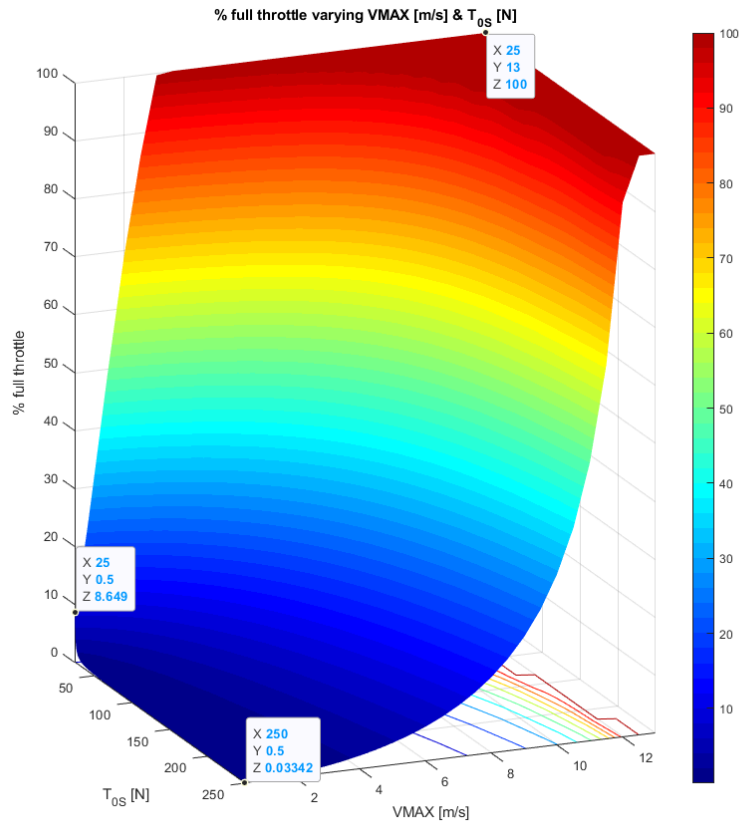


Figure 5.4 – $h_1 = 50 \text{ m}$, $I_{sp} = 150 \text{ s}$, $m_0 = 15 \text{ kg}$

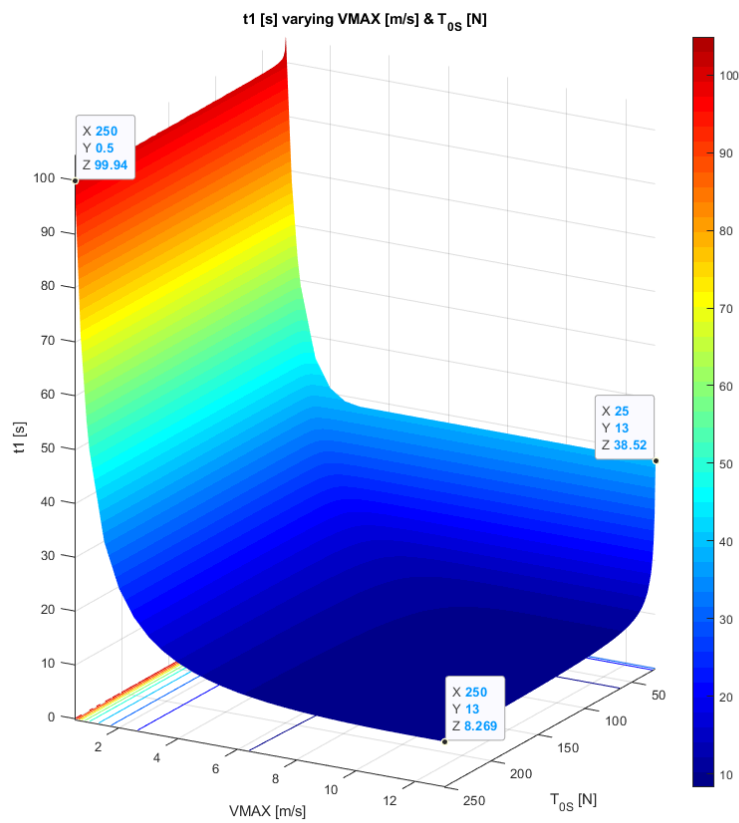


Figure 5.5 – $h_1 = 50 \text{ m}$, $I_{sp} = 150 \text{ s}$, $m_0 = 15 \text{ kg}$

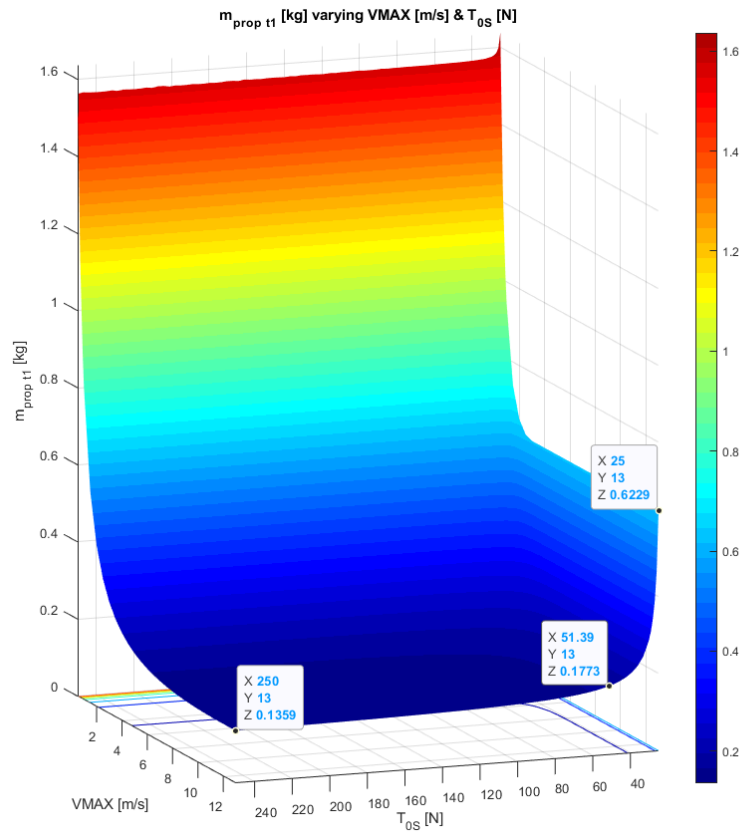


Figure 5.6 – $h_1 = 50$ m, $I_{sp} = 150$ s, $m_0 = 15$ kg

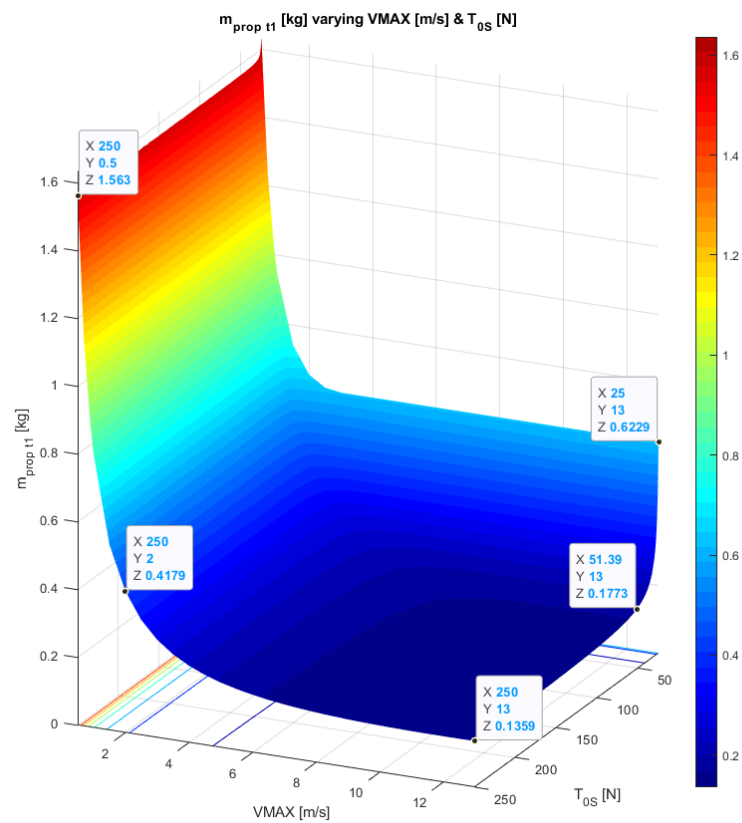


Figure 5.7 – $h_1 = 50$ m, $I_{sp} = 150$ s, $m_0 = 15$ kg

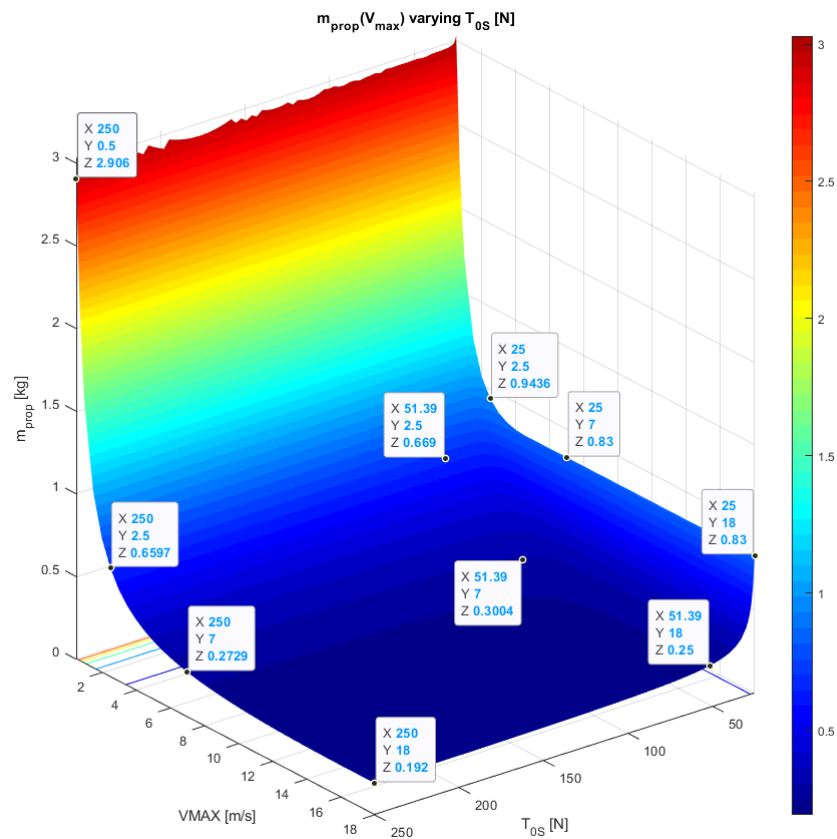


Figure 5.8 – $h_1 = 100$ m, $I_{sp} = 150$ s, $m_0 = 15$ kg

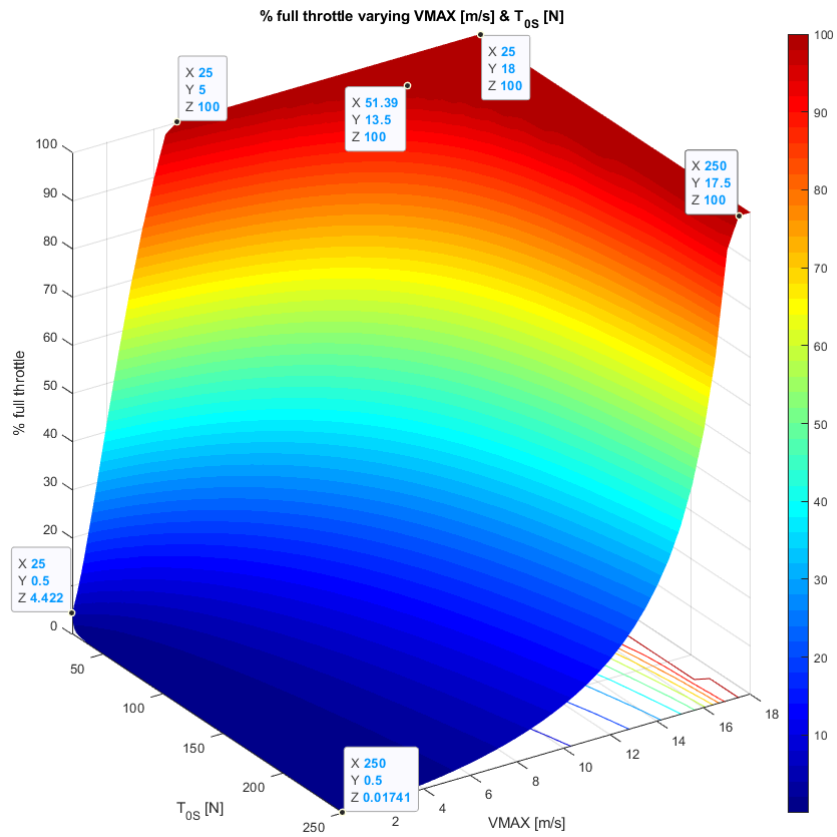


Figure 5.9 – $h_1 = 100 \text{ m}$, $I_{sp} = 150 \text{ s}$, $m_0 = 15 \text{ kg}$

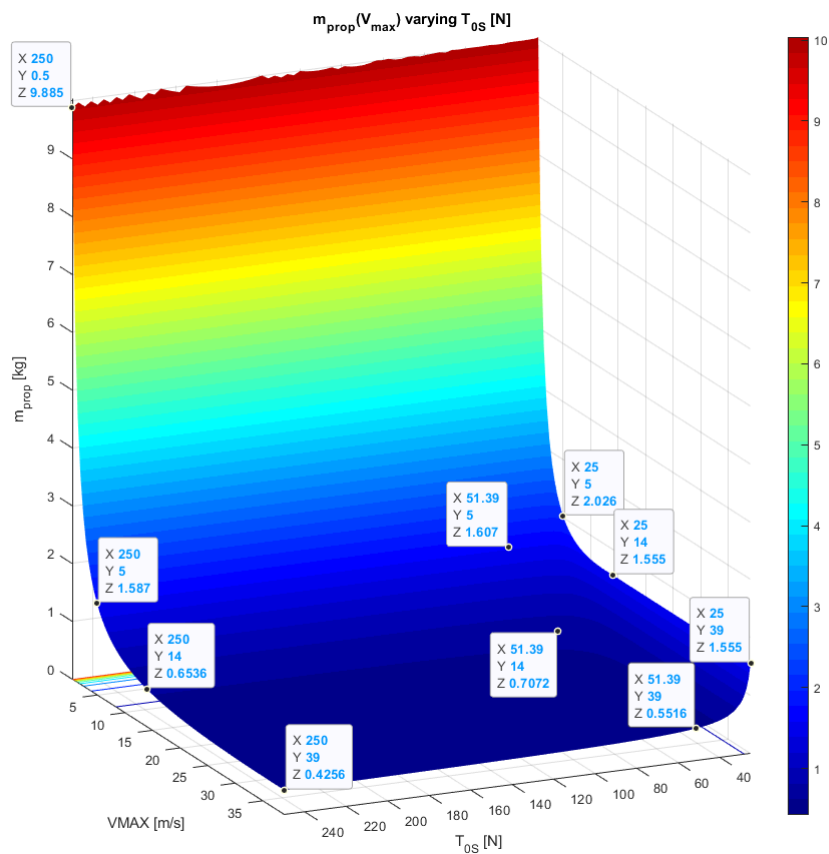


Figure 5.10 – $h_1 = 500 \text{ m}$, $I_{sp} = 150 \text{ s}$, $m_0 = 15 \text{ kg}$

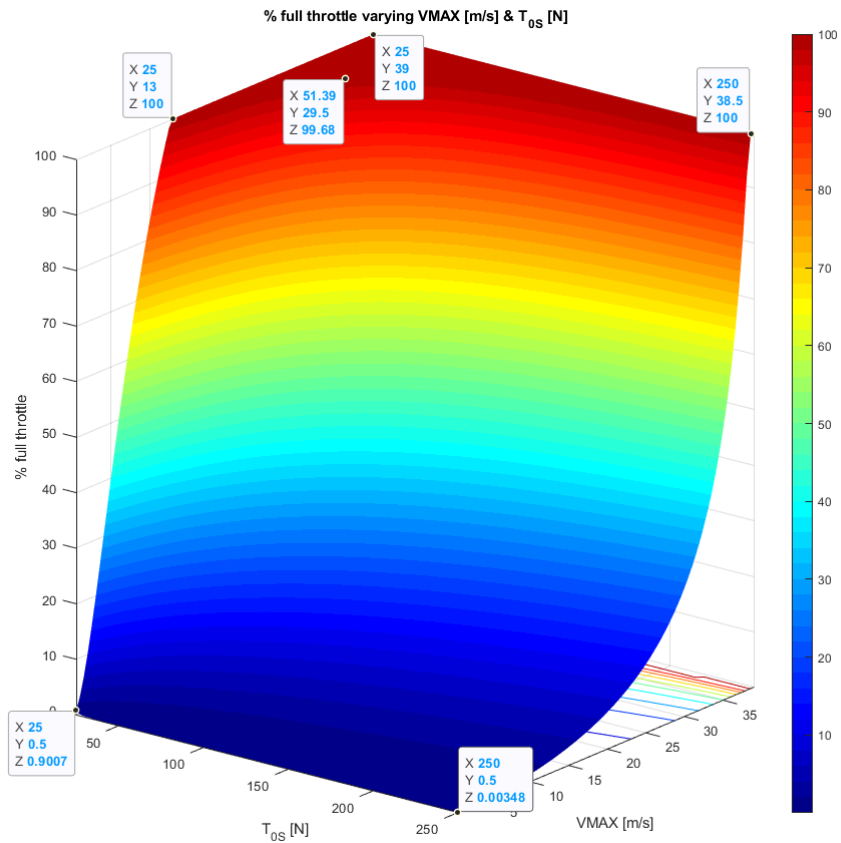


Figure 5.11 – $h_1 = 500 \text{ m}$, $I_{sp} = 150 \text{ s}$, $m_0 = 15 \text{ kg}$

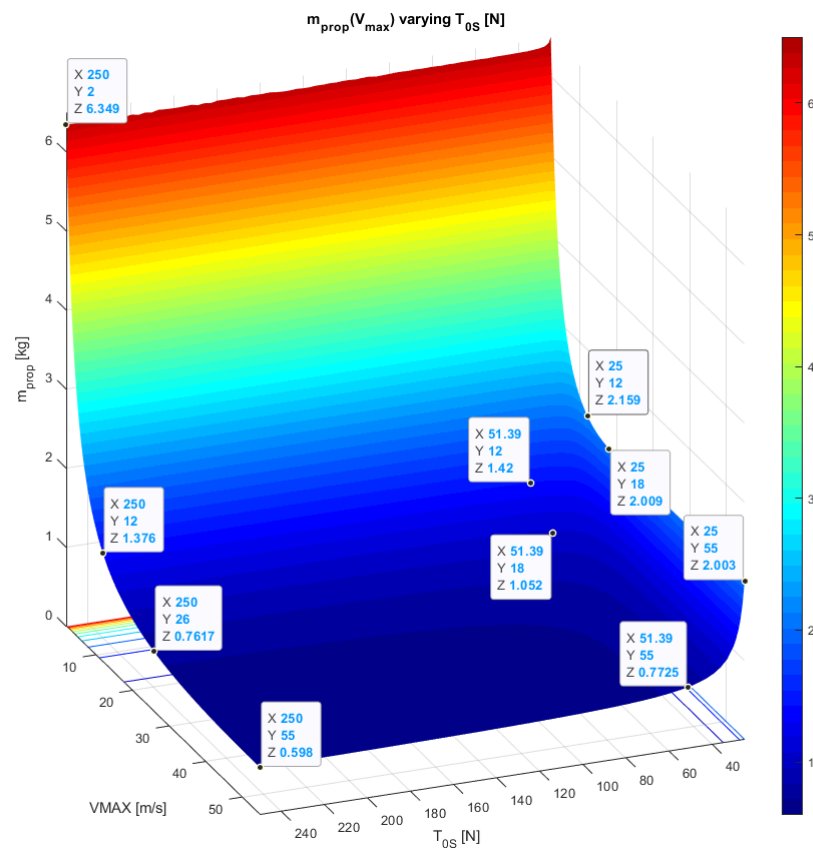


Figure 5.12 – $h_1 = 1000 \text{ m}$, $I_{sp} = 150 \text{ s}$, $m_0 = 15 \text{ kg}$

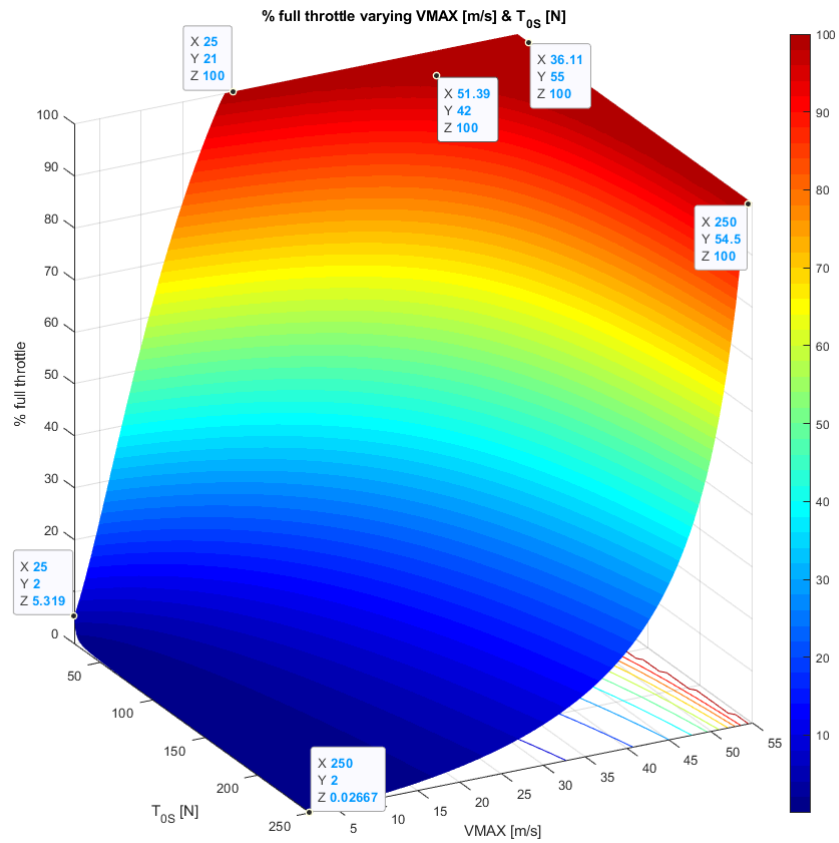


Figure 5.13 – $h_1 = 1000 \text{ m}$, $I_{sp} = 150 \text{ s}$, $m_0 = 15 \text{ kg}$

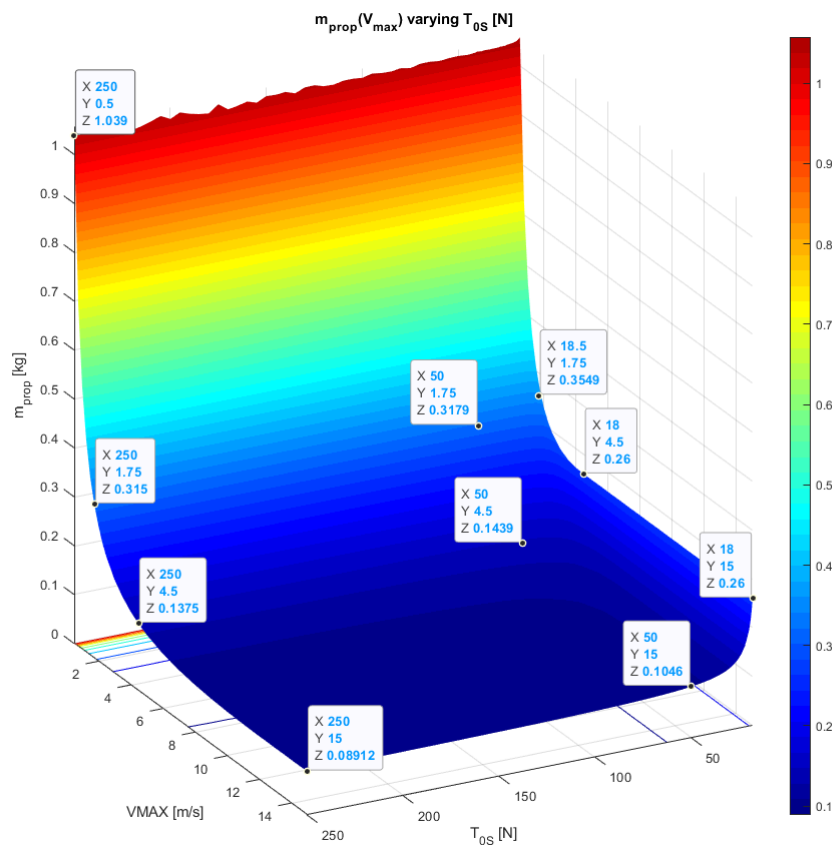


Figure 5.14 – $h_1 = 50 \text{ m}$, $I_{sp} = 150 \text{ s}$, $m_0 = 10 \text{ kg}$

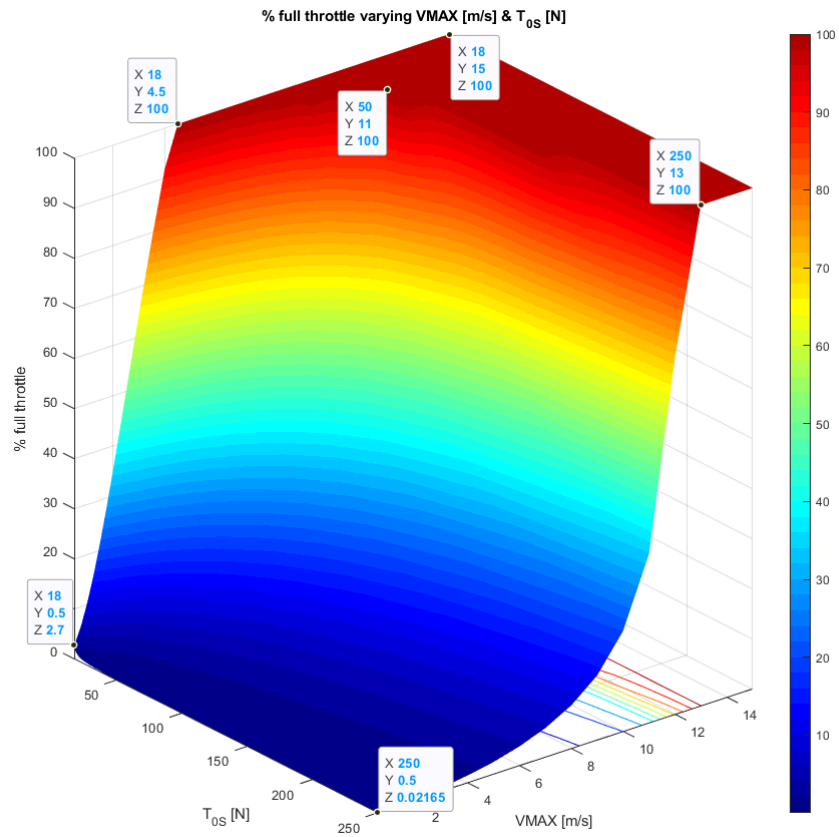


Figure 5.15 – $h_1 = 50 \text{ m}$, $I_{sp} = 150 \text{ s}$, $m_0 = 10 \text{ kg}$

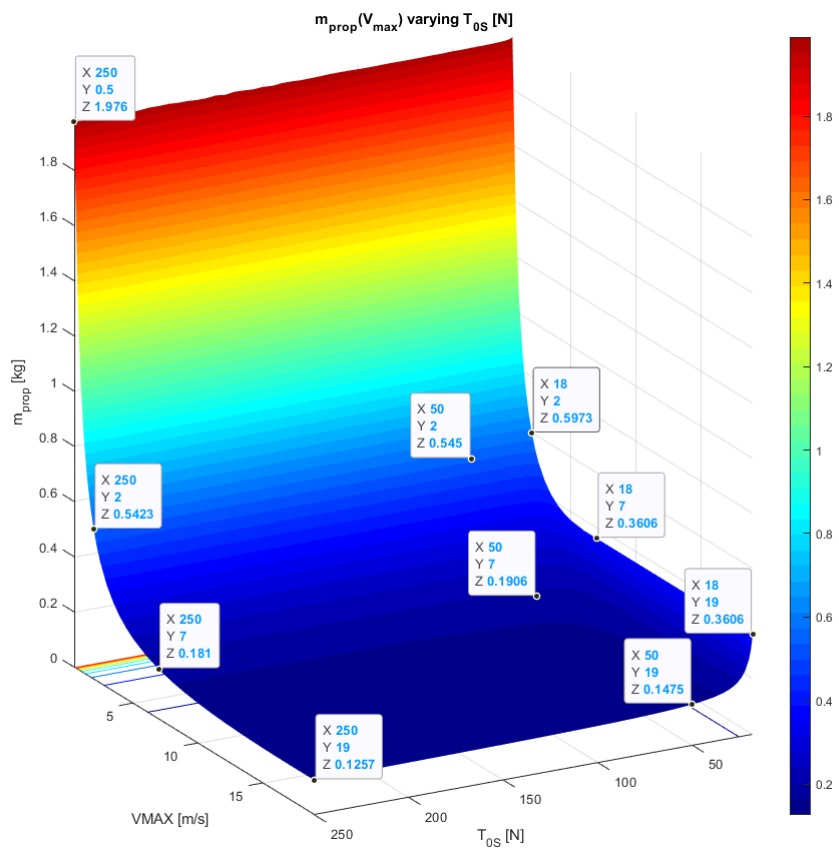


Figure 5.16 – $h_1 = 100 \text{ m}$, $I_{sp} = 150 \text{ s}$, $m_0 = 10 \text{ kg}$

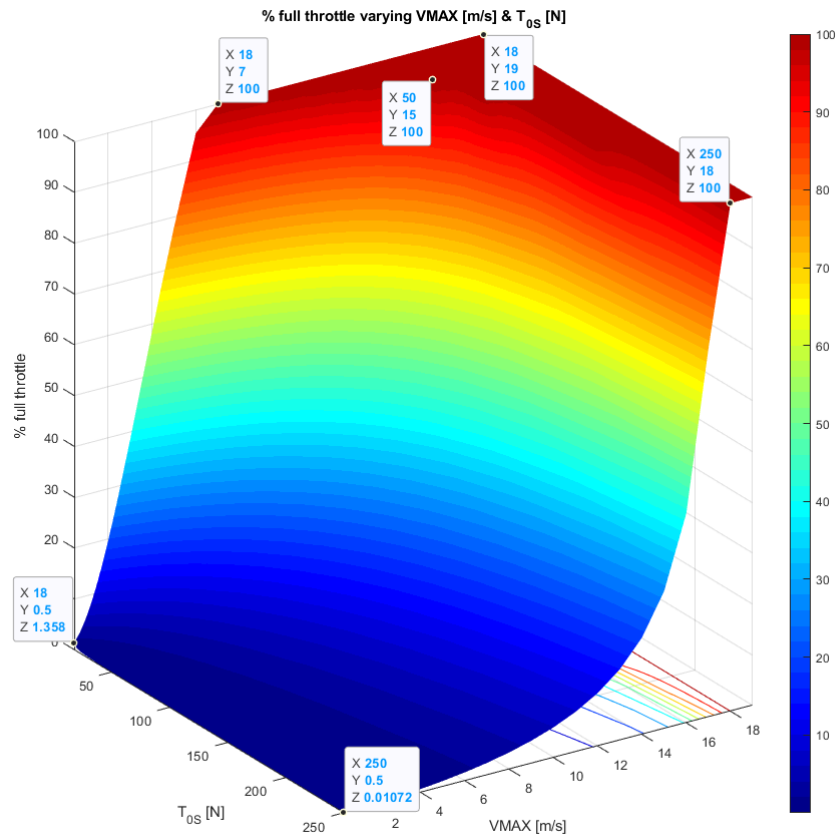


Figure 5.17 – $h_1 = 100 \text{ m}$, $I_{sp} = 150 \text{ s}$, $m_0 = 10 \text{ kg}$

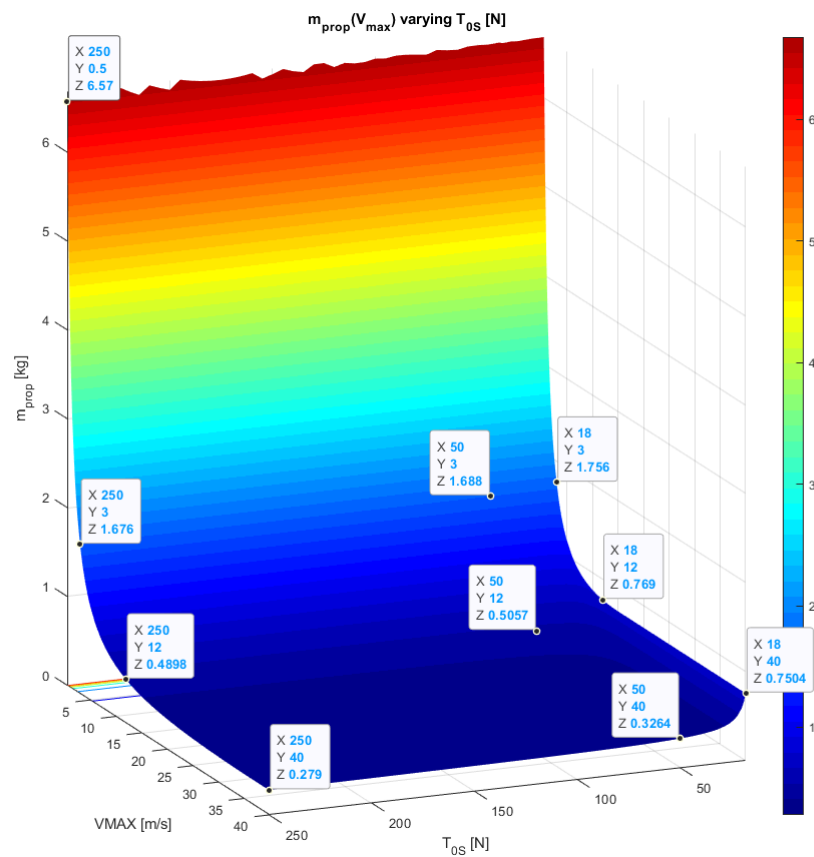


Figure 5.18 – $h_1 = 500 \text{ m}$, $I_{sp} = 150 \text{ s}$, $m_0 = 10 \text{ kg}$

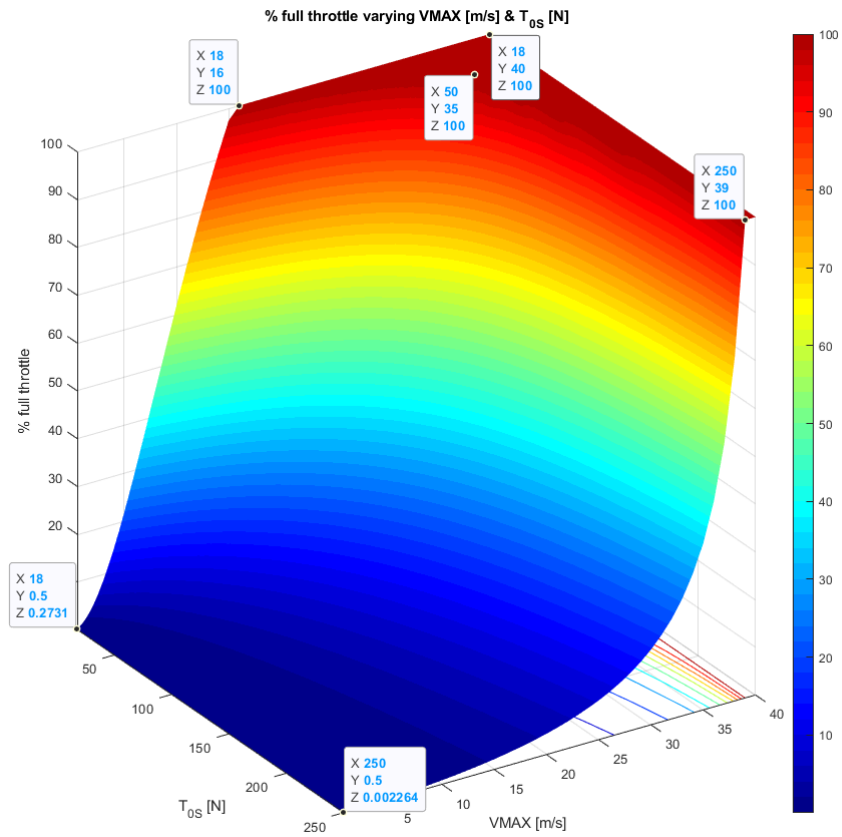


Figure 5.19 – $h_1 = 500 \text{ m}$, $I_{sp} = 150 \text{ s}$, $m_0 = 10 \text{ kg}$

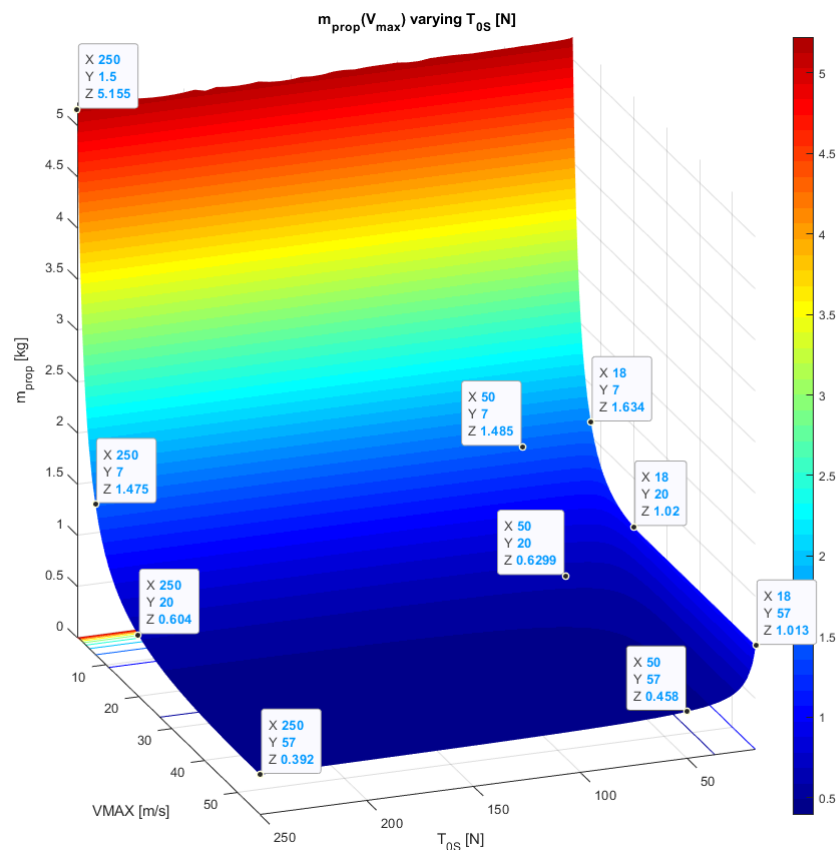


Figure 5.20 – $h_1 = 1000 \text{ m}$, $I_{sp} = 150 \text{ s}$, $m_0 = 10 \text{ kg}$

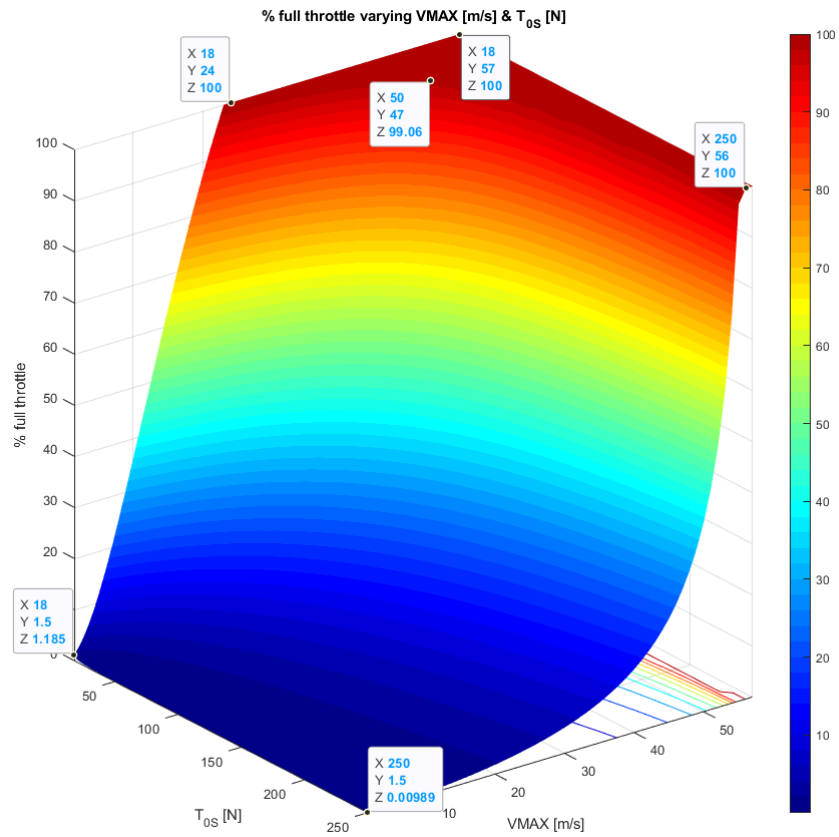


Figure 5.21 – $h_1 = 1000 \text{ m}$, $I_{sp} = 150 \text{ s}$, $m_0 = 10 \text{ kg}$

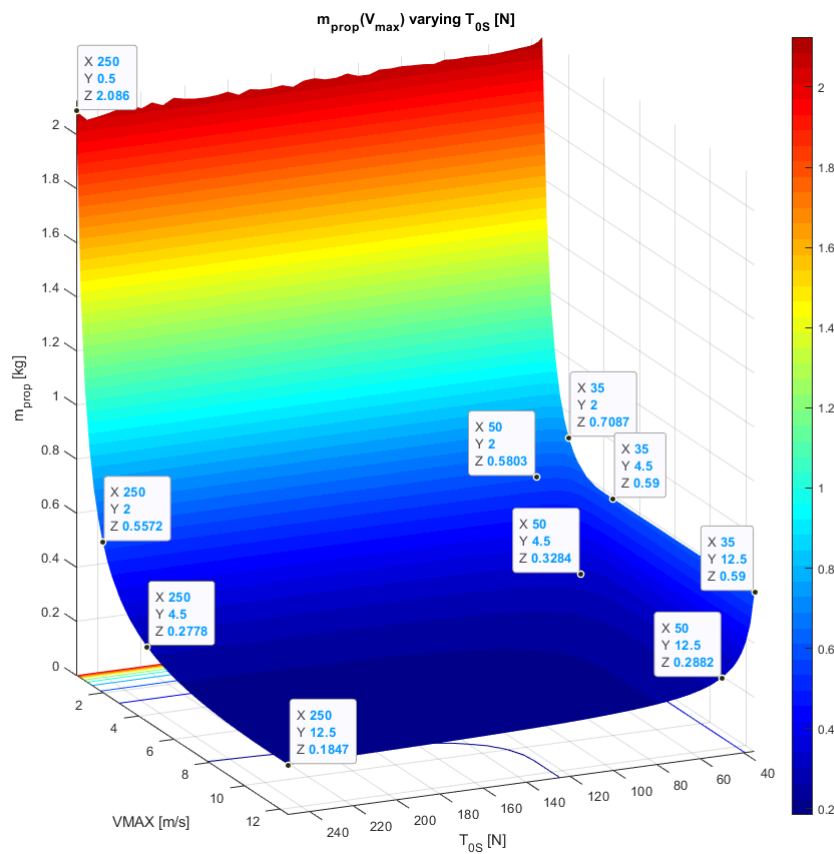


Figure 5.22 – $h_1 = 50 \text{ m}$, $I_{sp} = 150 \text{ s}$, $m_0 = 20 \text{ kg}$

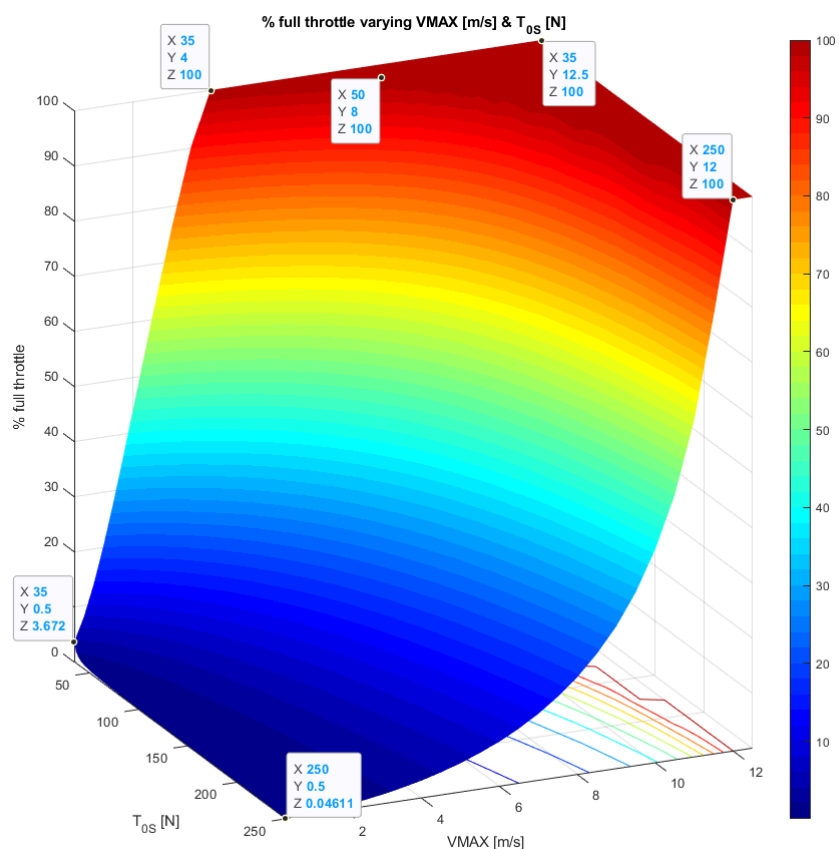


Figure 5.23 – $h_1 = 50 \text{ m}$, $I_{sp} = 150 \text{ s}$, $m_0 = 20 \text{ kg}$

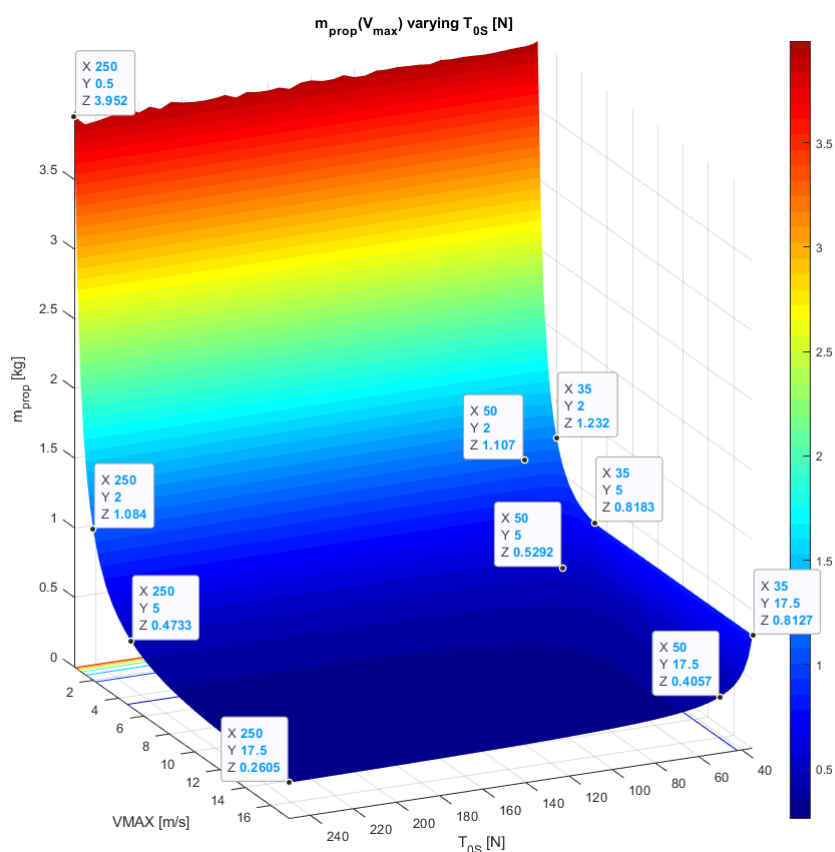


Figure 5.24 – $h_1 = 100 \text{ m}$, $I_{sp} = 150 \text{ s}$, $m_0 = 20 \text{ kg}$

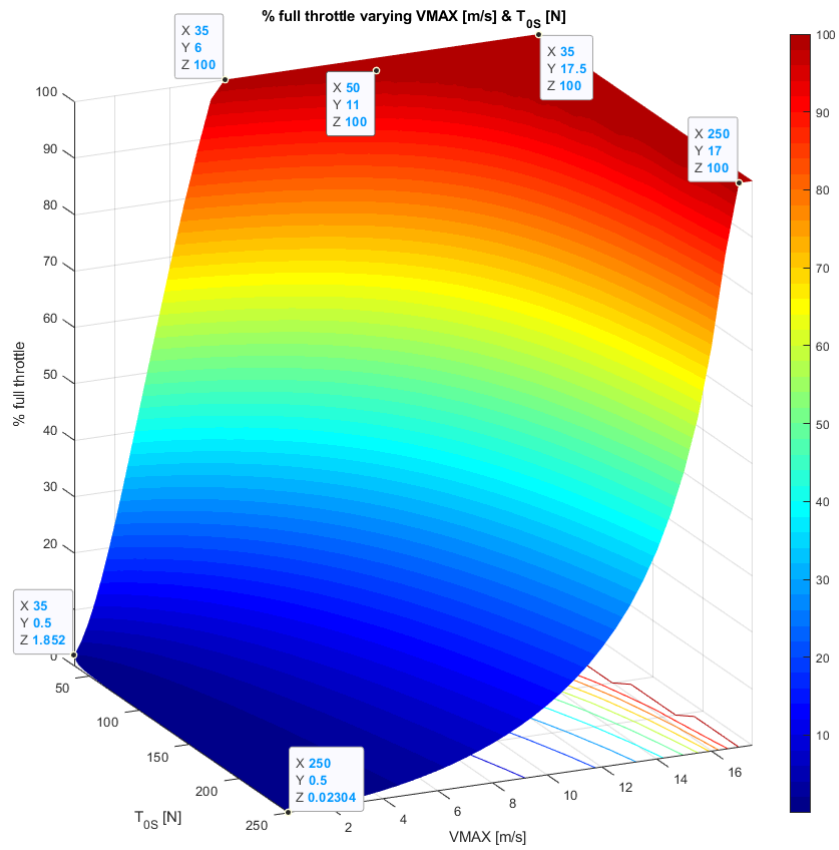


Figure 5.25 – $h_1 = 100 \text{ m}$, $I_{sp} = 150 \text{ s}$, $m_0 = 20 \text{ kg}$

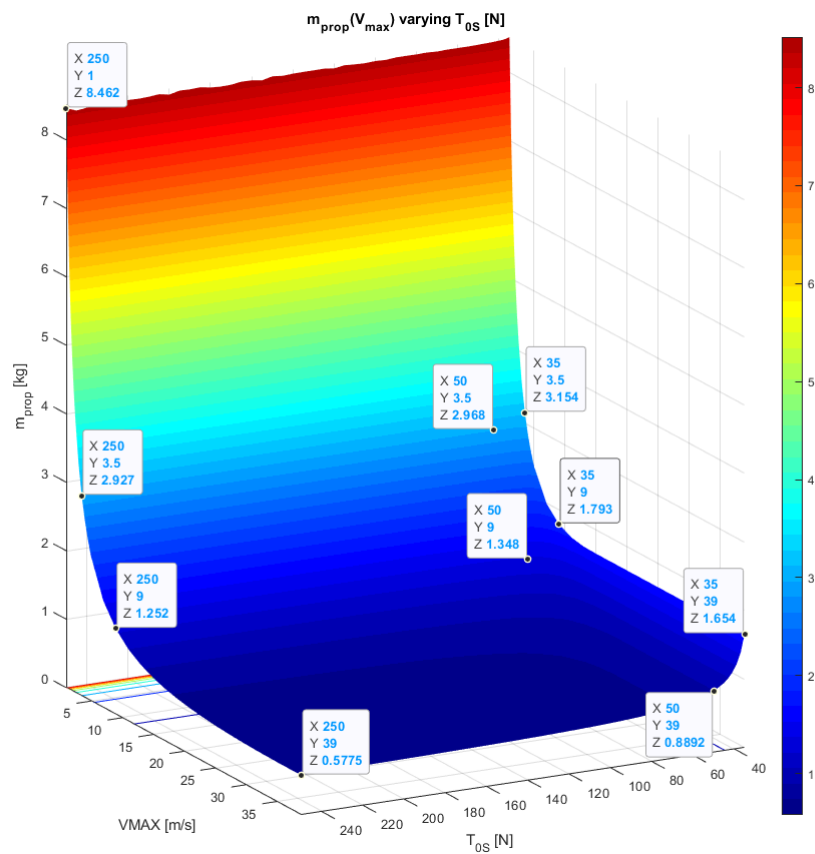


Figure 5.26 – $h_1 = 500 \text{ m}$, $I_{sp} = 150 \text{ s}$, $m_0 = 20 \text{ kg}$

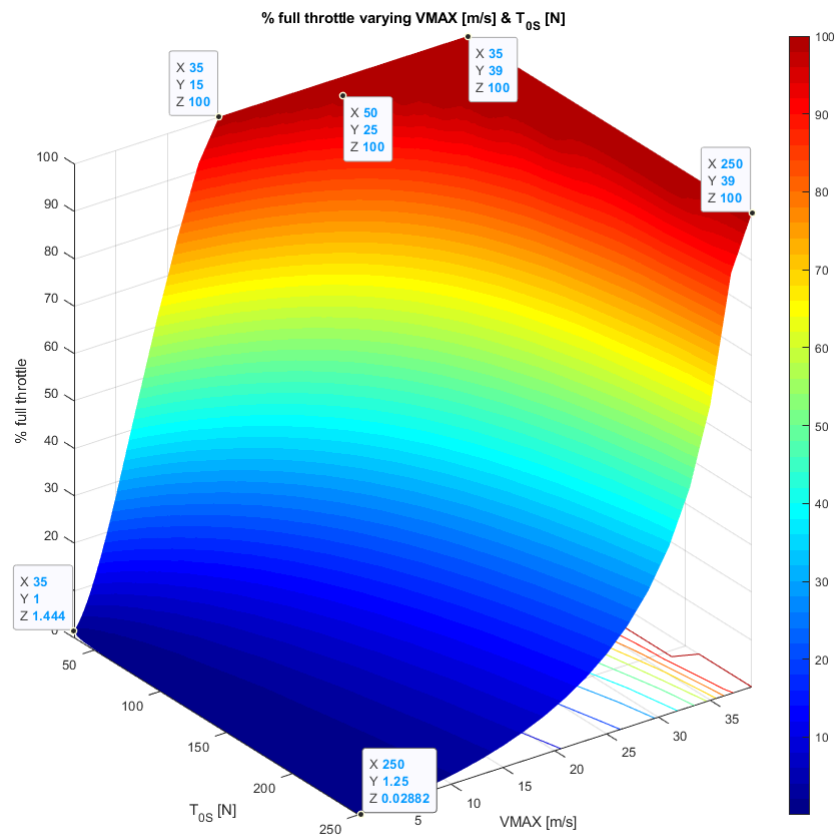


Figure 5.27 – $h_1 = 500 \text{ m}$, $I_{sp} = 150 \text{ s}$, $m_0 = 20 \text{ kg}$

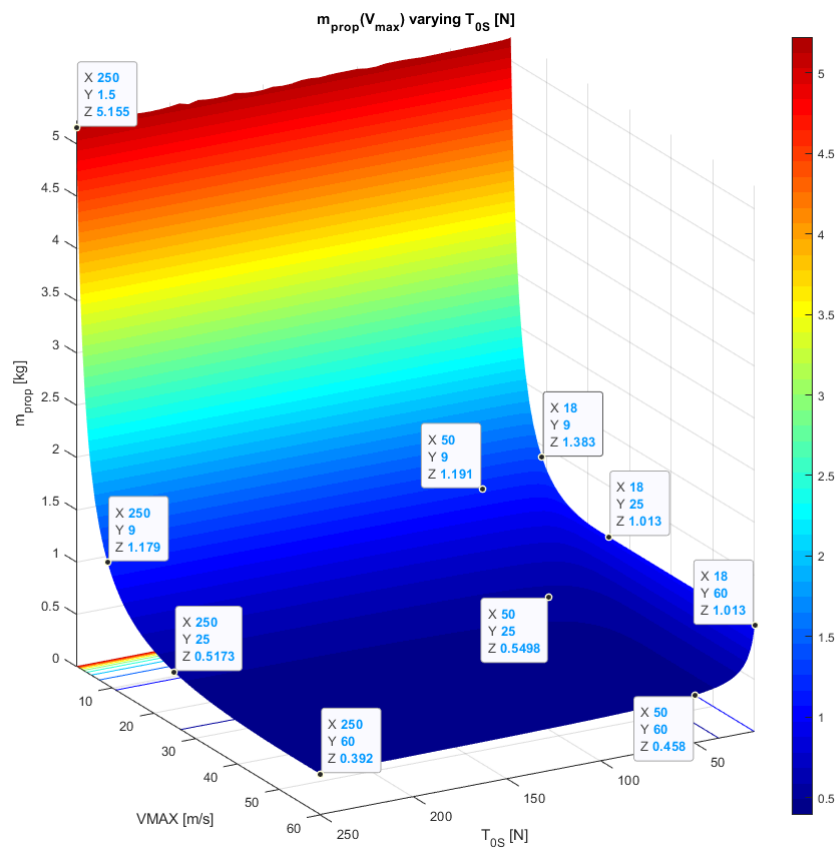


Figure 5.28 – $h_1 = 1000 \text{ m}$, $I_{sp} = 150 \text{ s}$, $m_0 = 20 \text{ kg}$

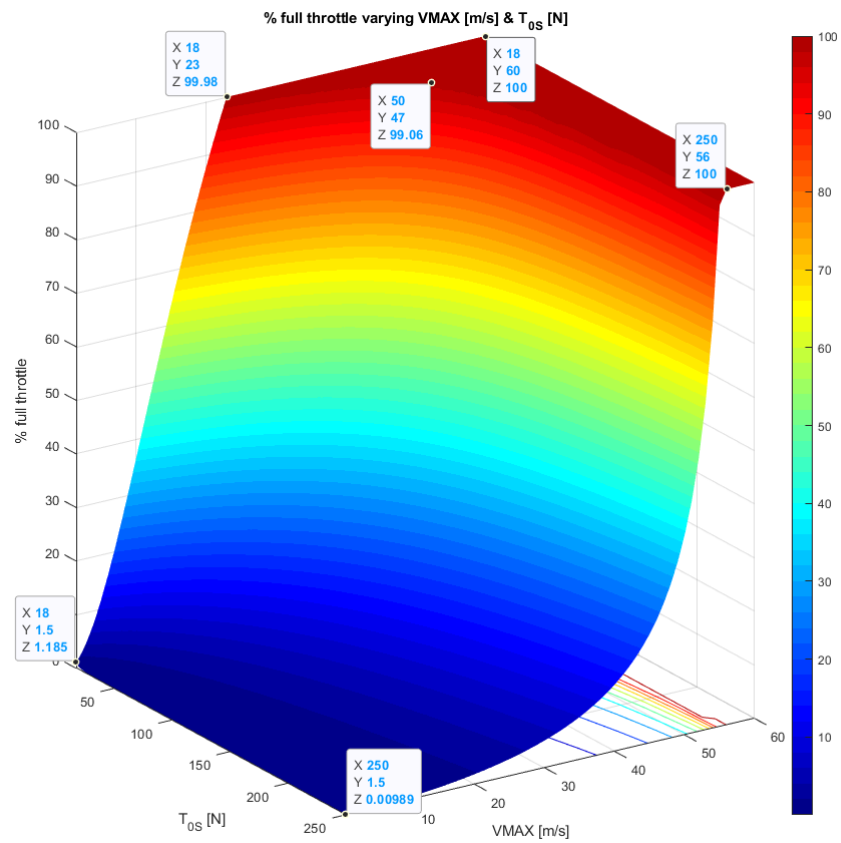


Figure 5.29 – $h_1 = 1000 \text{ m}$, $I_{sp} = 150 \text{ s}$, $m_0 = 20 \text{ kg}$

6 Annex 02 – Vertical ascent ($T_B \neq 0$, $m \approx \text{cost}$) parametric sweep of m_0

Model ($m \approx \text{cost}$) \rightarrow Tratto01_ValutazioniV2.m

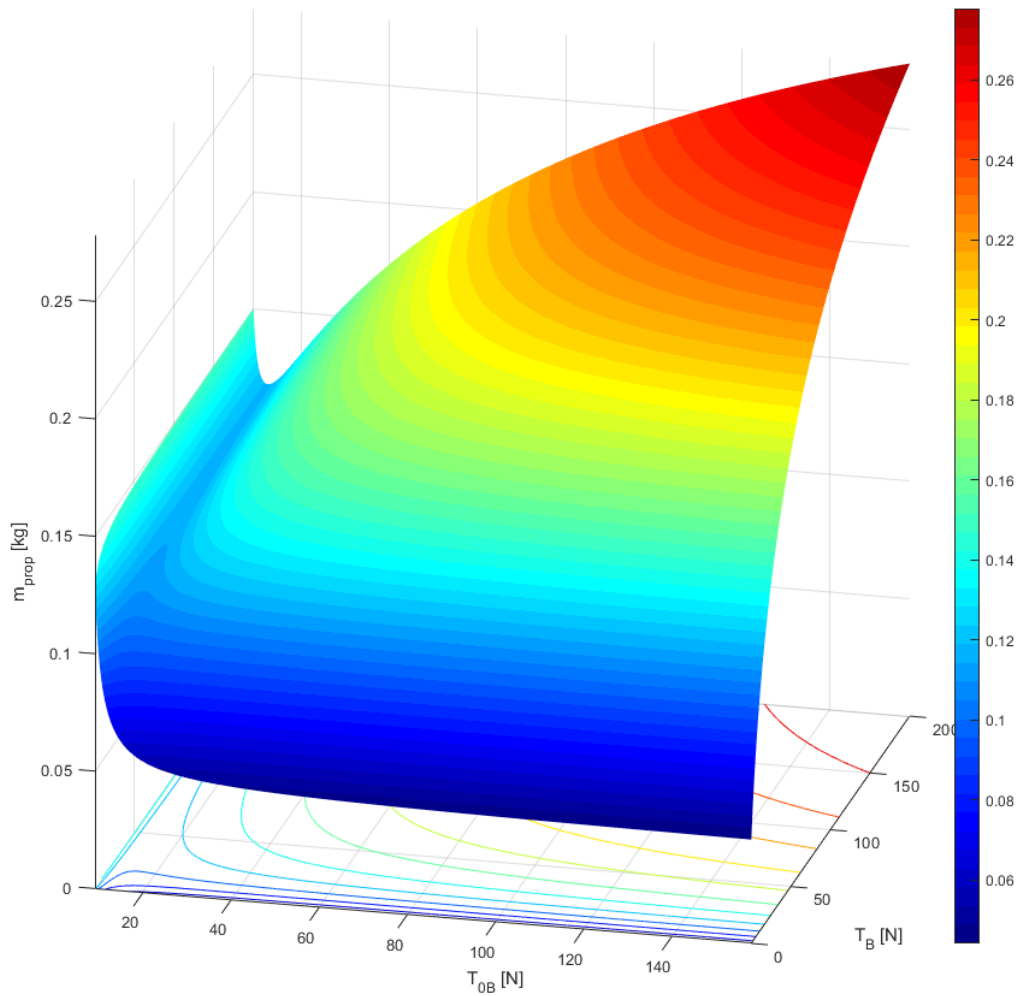


Figure 6.1 – $h_1 = 50 \text{ m}$, $I_{sp} = 150 \text{ s}$, $m_0 = 5 \text{ kg}$

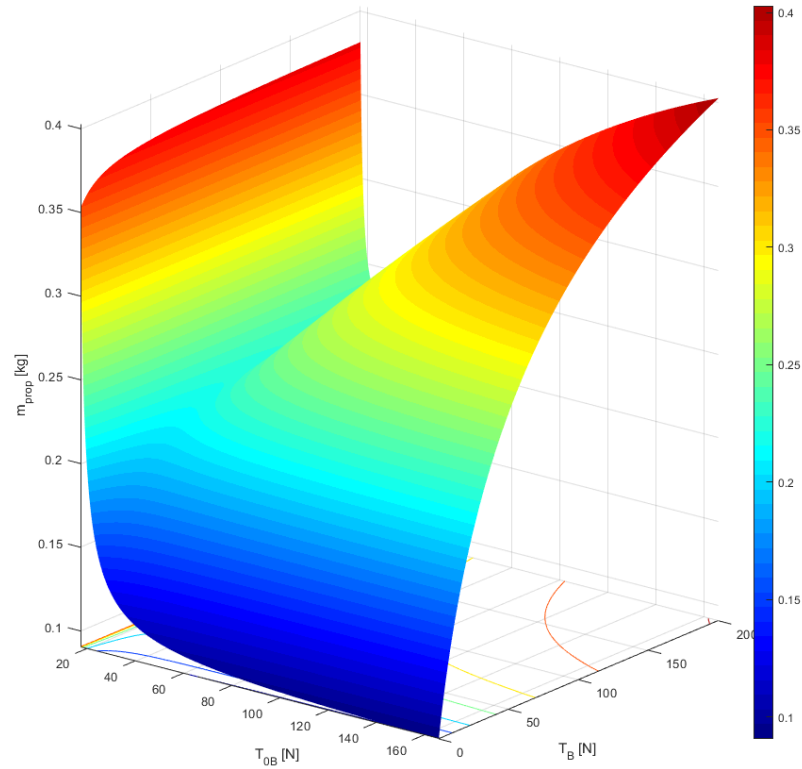


Figure 6.2 – $h_1 = 50 \text{ m}$, $I_{sp} = 150 \text{ s}$, $m_0 = 10 \text{ kg}$

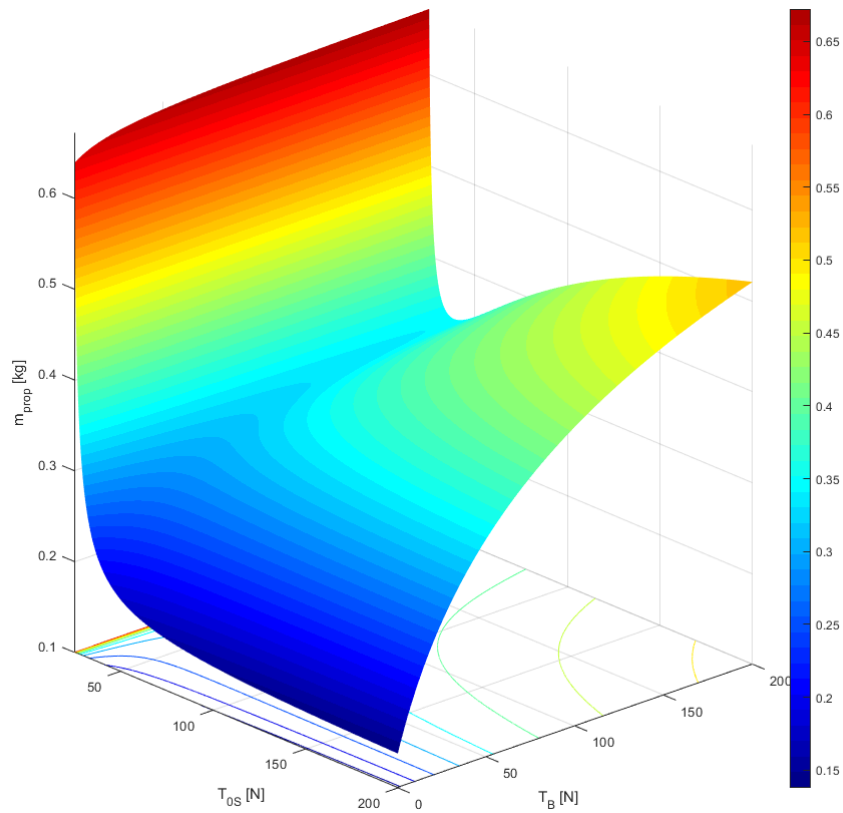


Figure 6.3 – $h_1 = 50 \text{ m}$, $I_{sp} = 150 \text{ s}$, $m_0 = 15 \text{ kg}$

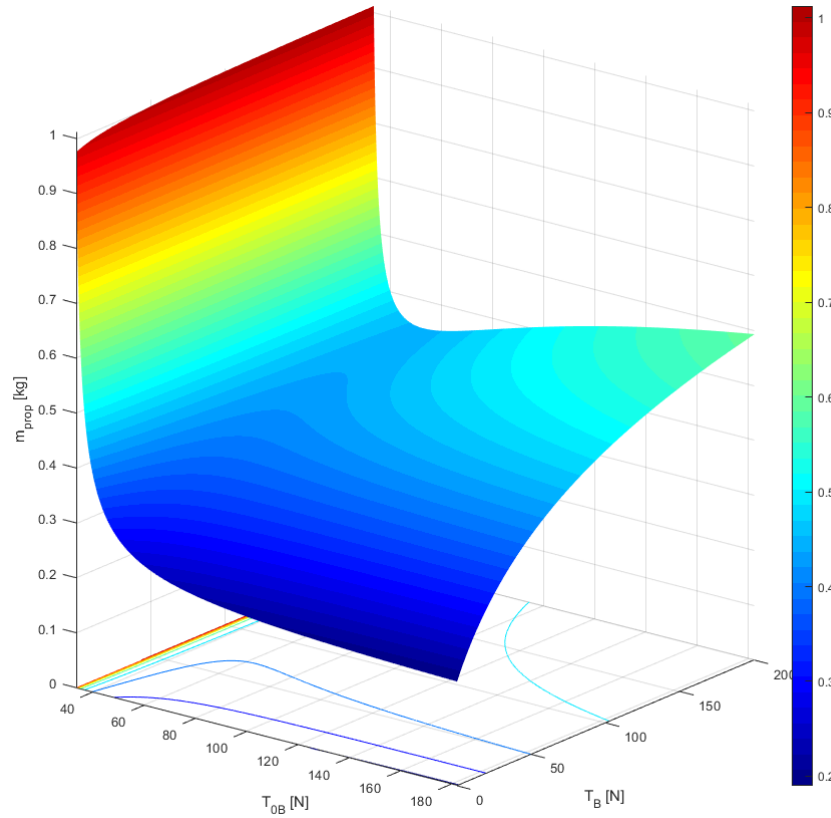


Figure 6.4 – $h_1 = 50$ m, $I_{sp} = 150$ s, $m_0 = 20$ kg

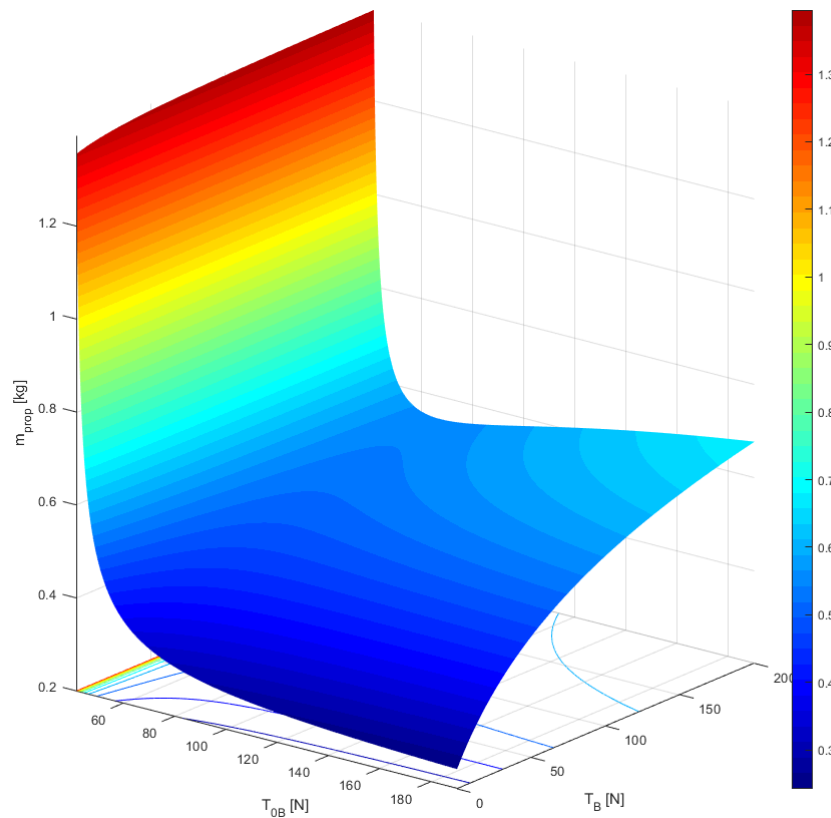


Figure 6.5 – $h_1 = 50$ m, $I_{sp} = 150$ s, $m_0 = 25$ kg

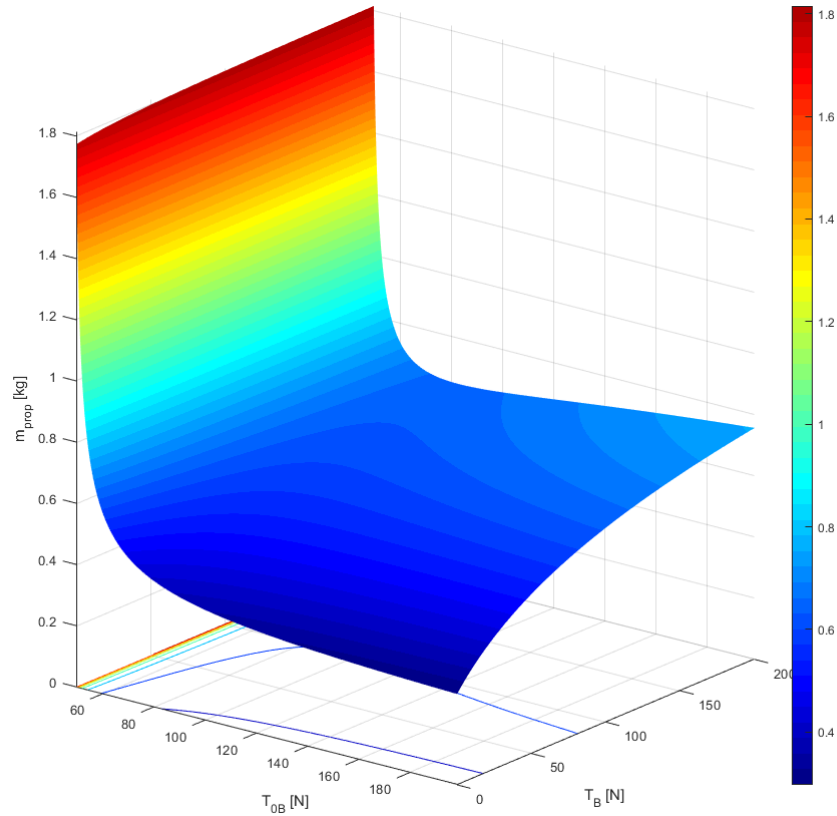


Figure 6.6 – $h_1 = 50$ m, $I_{sp} = 150$ s, $m_0 = 30$ kg

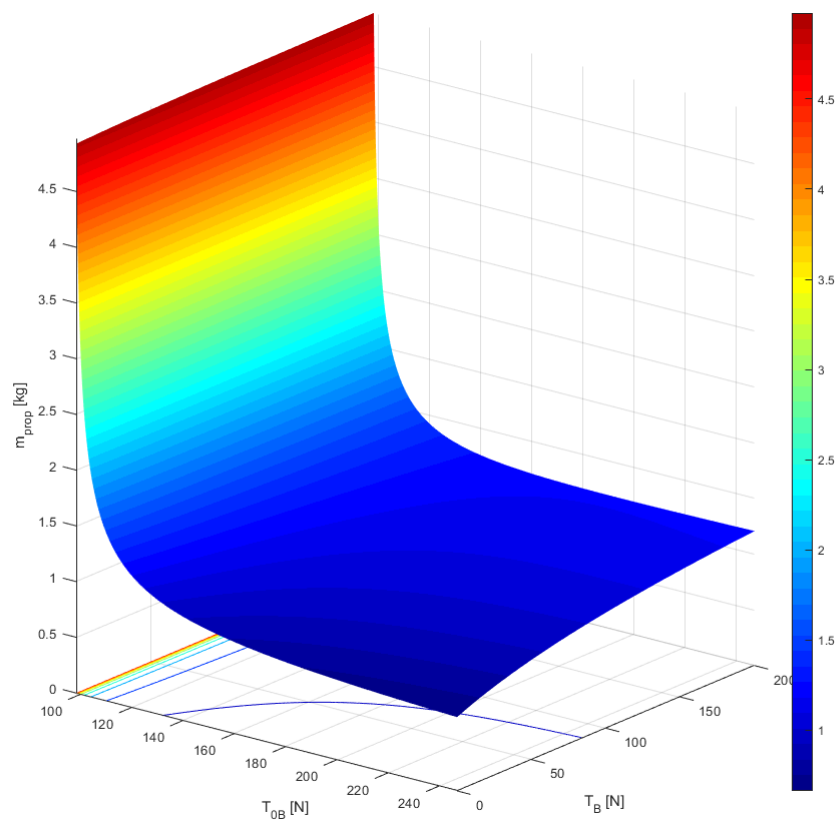


Figure 6.7 – $h_1 = 50$ m, $I_{sp} = 150$ s, $m_0 = 60$ kg

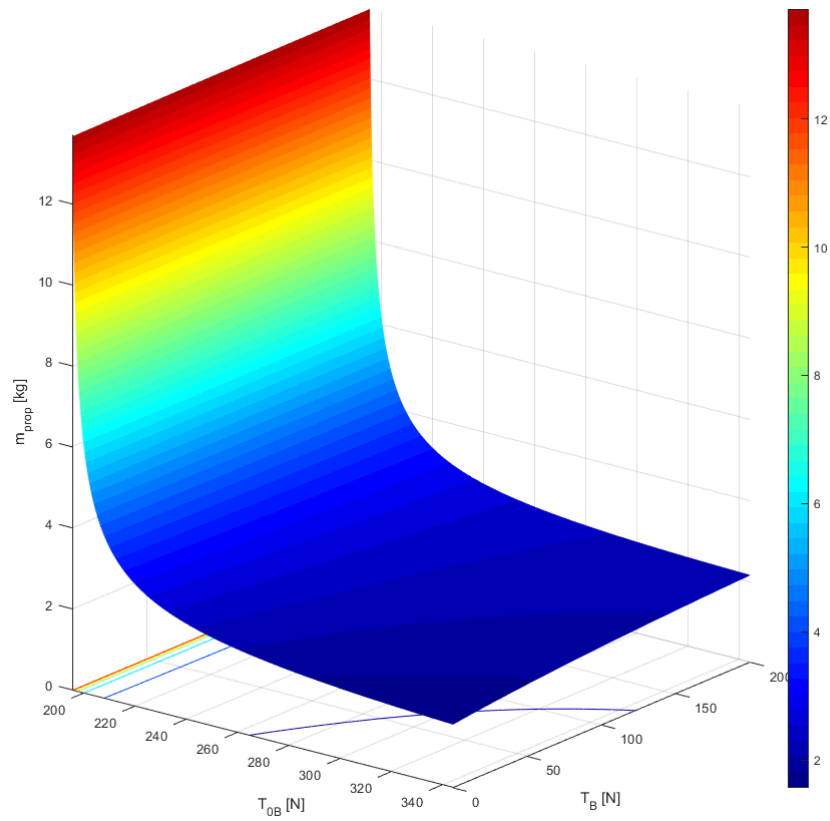


Figure 6.8 – $h_1 = 50 \text{ m}$, $I_{sp} = 150 \text{ s}$, $m_0 = 120 \text{ kg}$

7 Annex 03 – Vertical ascent ($T_B \neq 0$, $m \approx \text{cost}$) parametric sweep of h_1

Model ($m \approx \text{cost}$) \rightarrow Tratto01_ValutazioniV2.m

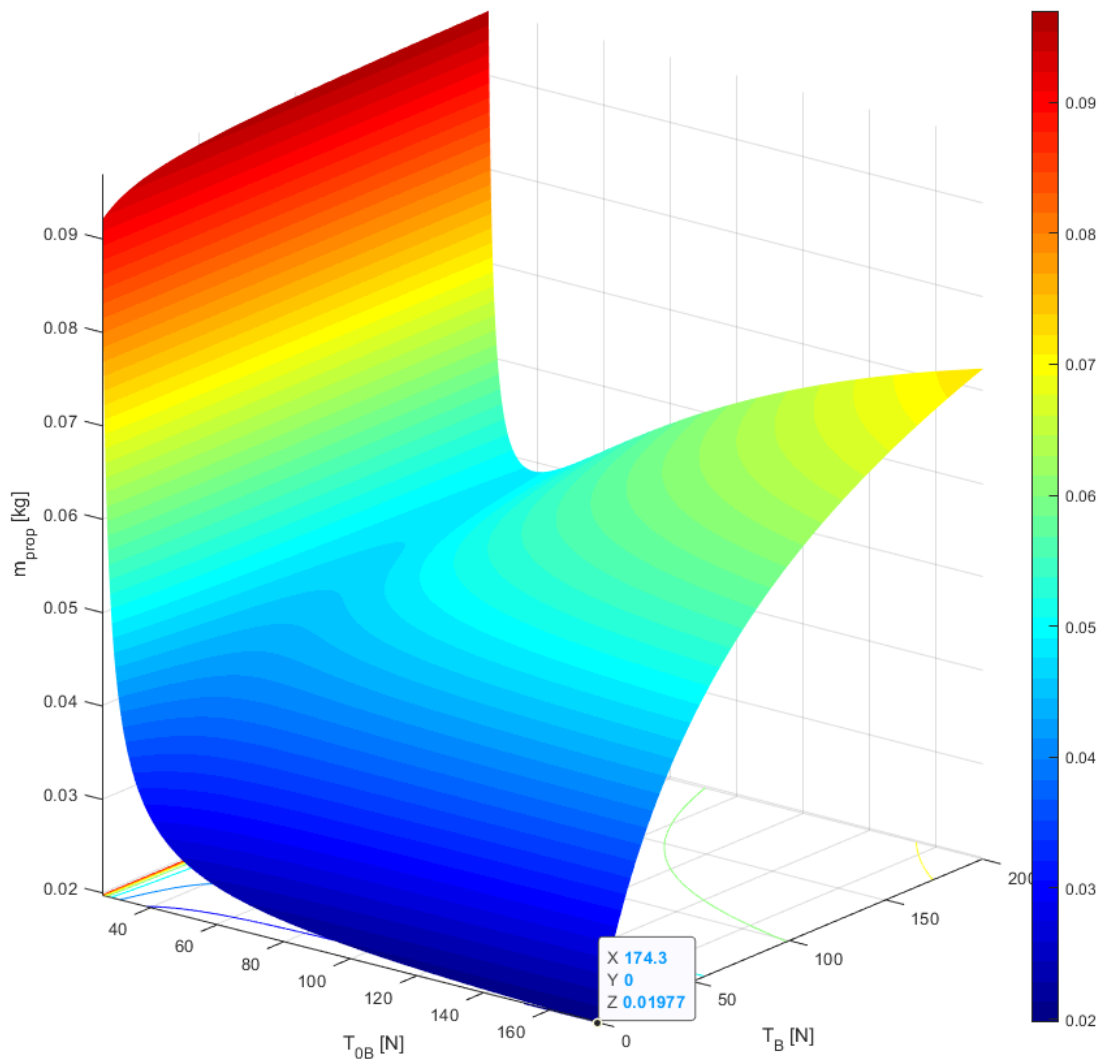


Figure 7.1 – $h_1 = 1 \text{ m}$, $I_{sp} = 150 \text{ s}$, $m_0 = 15 \text{ kg}$

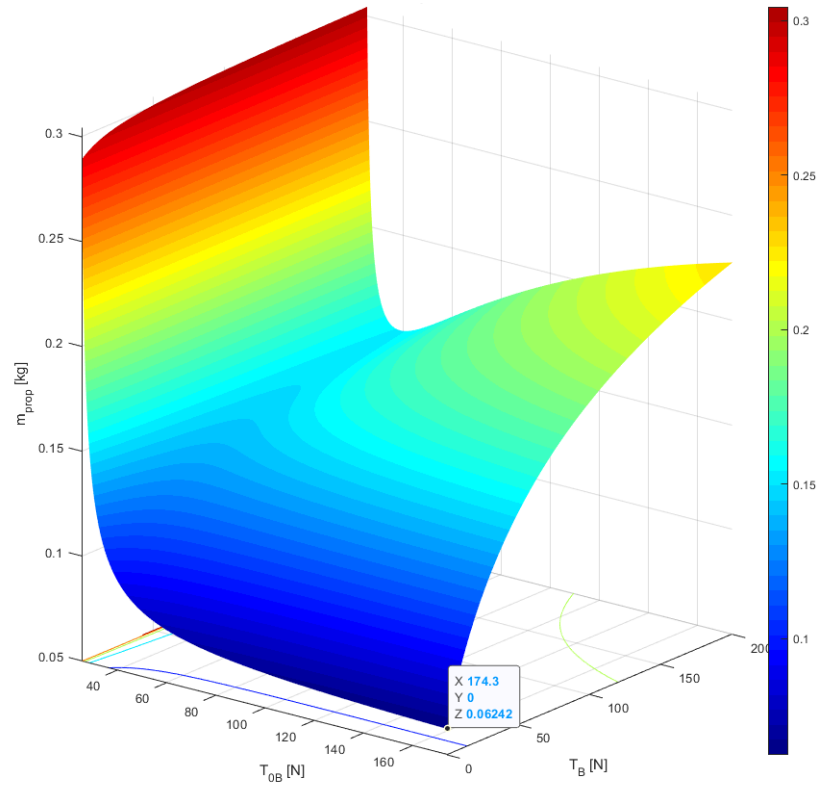


Figure 7.2 – $h_1 = 10$ m, $I_{sp} = 150$ s, $m_0 = 15$ kg

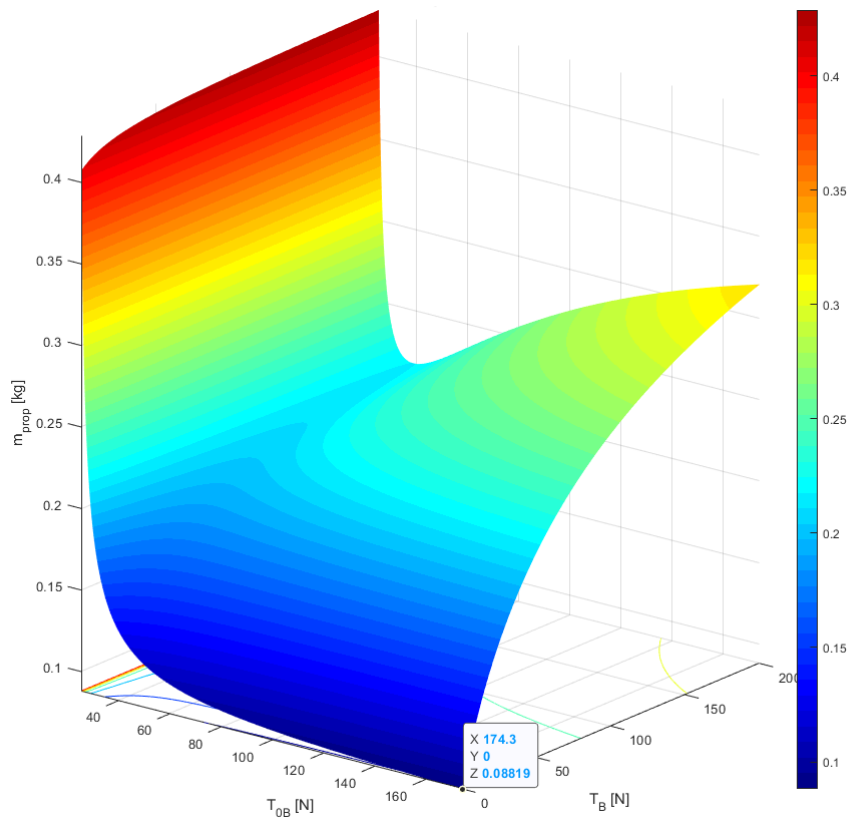


Figure 7.3 – $h_1 = 20$ m, $I_{sp} = 150$ s, $m_0 = 15$ kg

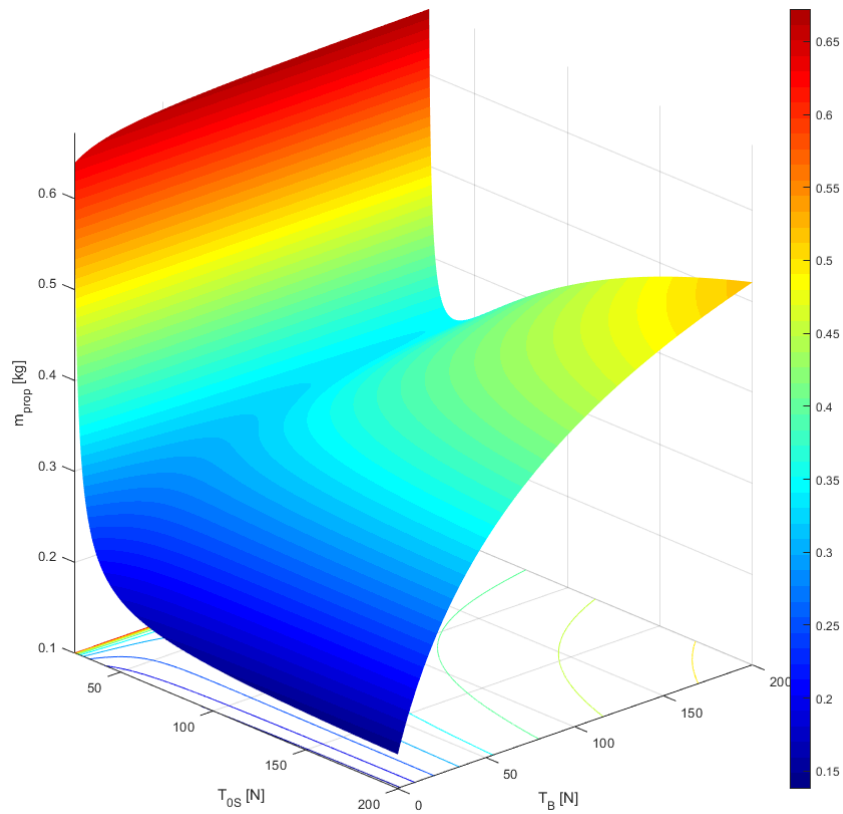


Figure 7.4 – $h_1 = 50$ m, $I_{sp} = 150$ s, $m_0 = 15$ kg

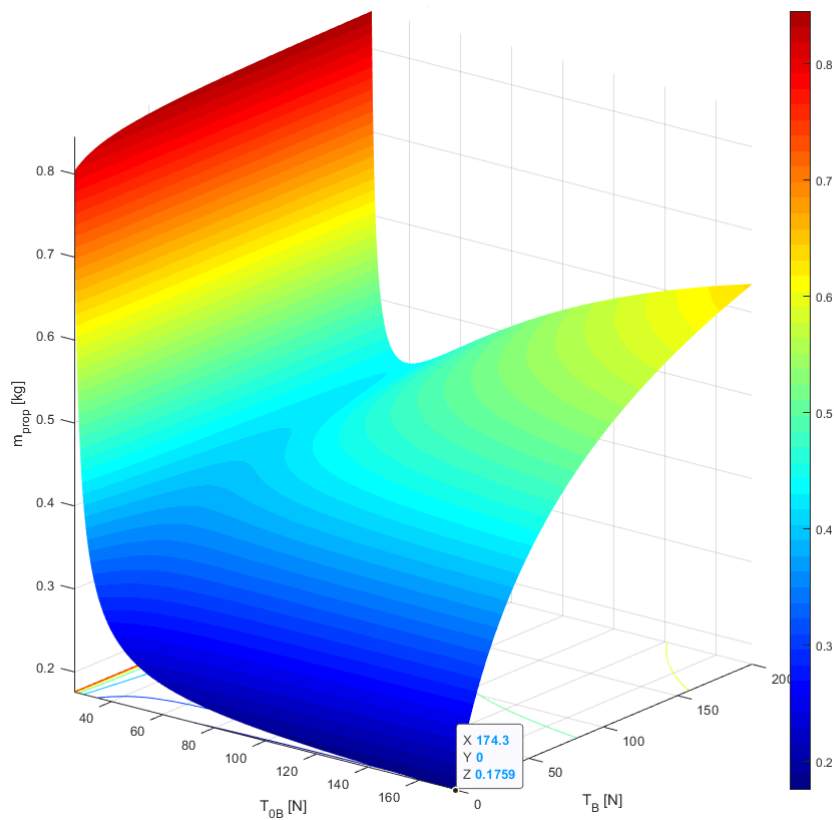


Figure 7.5 – $h_1 = 80$ m, $I_{sp} = 150$ s, $m_0 = 15$ kg

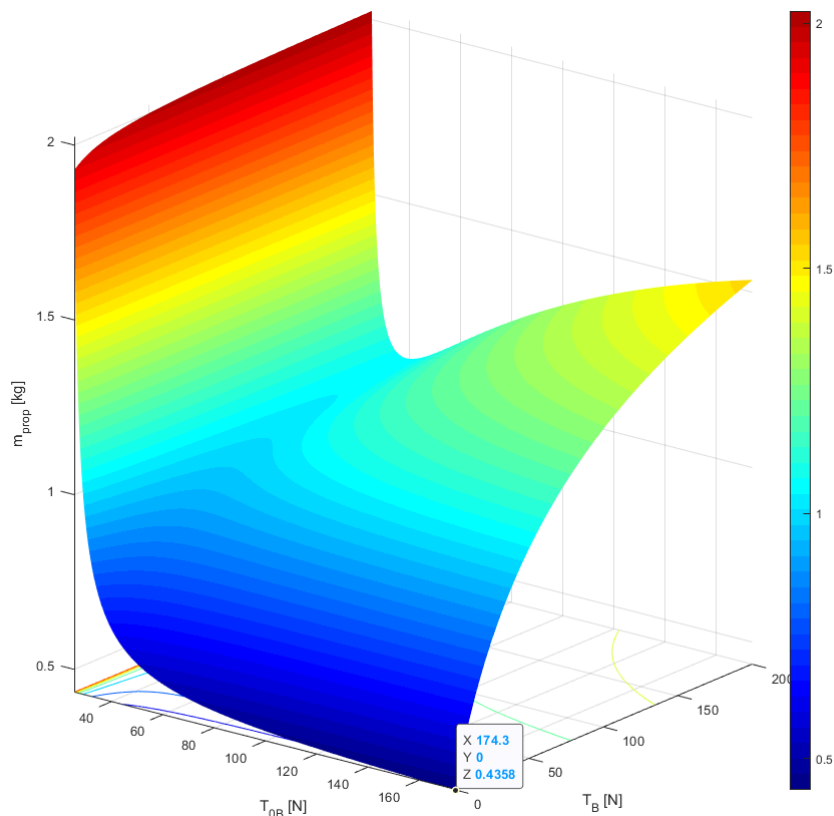


Figure 7.6 – $h_1 = 500$ m, $I_{sp} = 150$ s, $m_0 = 15$ kg

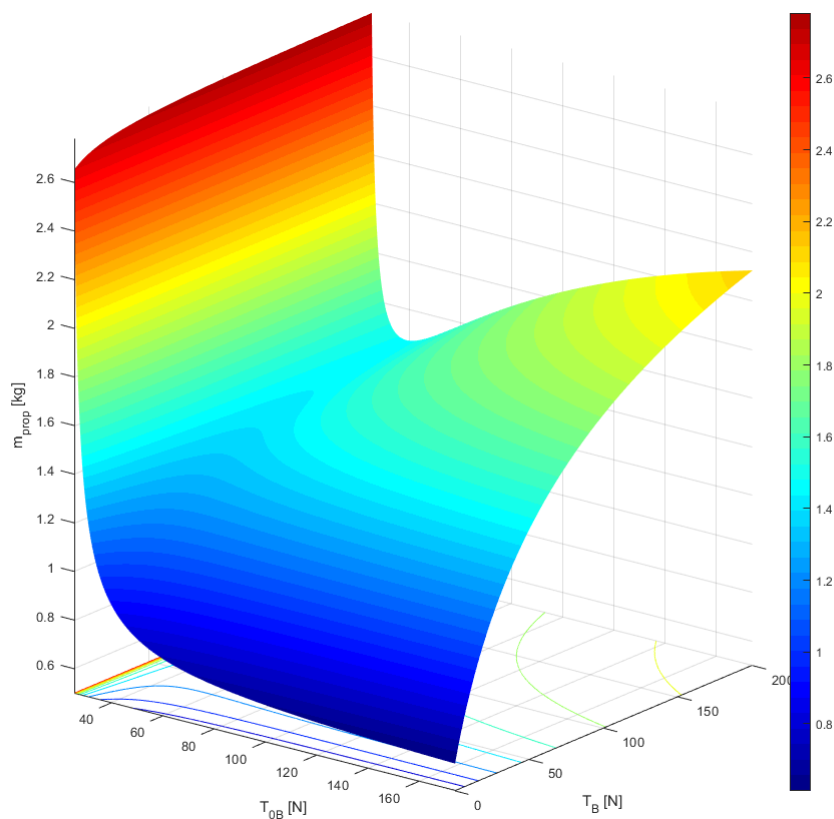


Figure 7.7 – $h_1 = 1000$ m, $I_{sp} = 150$ s, $m_0 = 15$ kg

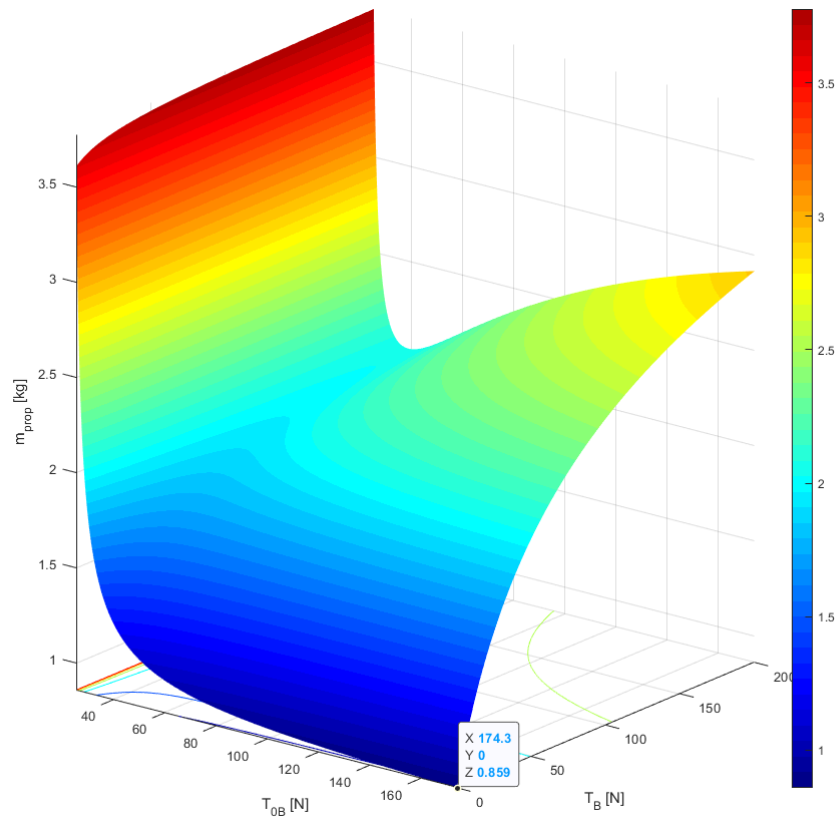


Figure 7.8 – $h_1 = 2000\text{ m}$, $I_{sp} = 150\text{ s}$, $m_0 = 15\text{ kg}$

8 Annex 04 – Vertical ascent ($T_B \neq 0$, $m \approx \text{cost}$) parametric sweep of I_{sp}

Model ($m \approx \text{cost}$) \rightarrow Tratto01_ValutazioniV2.m

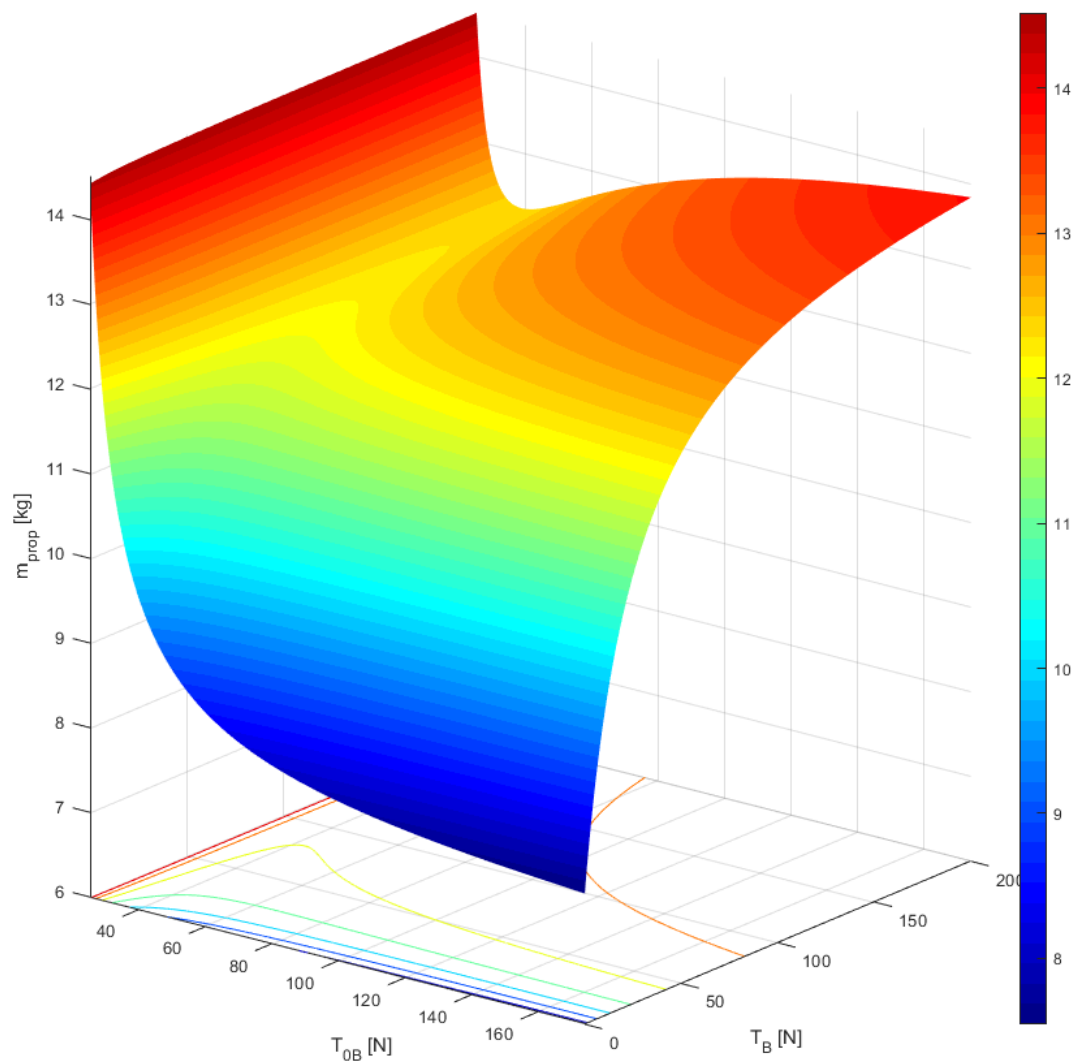


Figure 8.1 – $h_1 = 50 \text{ m}$, $I_{sp} = 2 \text{ s}$, $m_0 = 15 \text{ kg}$

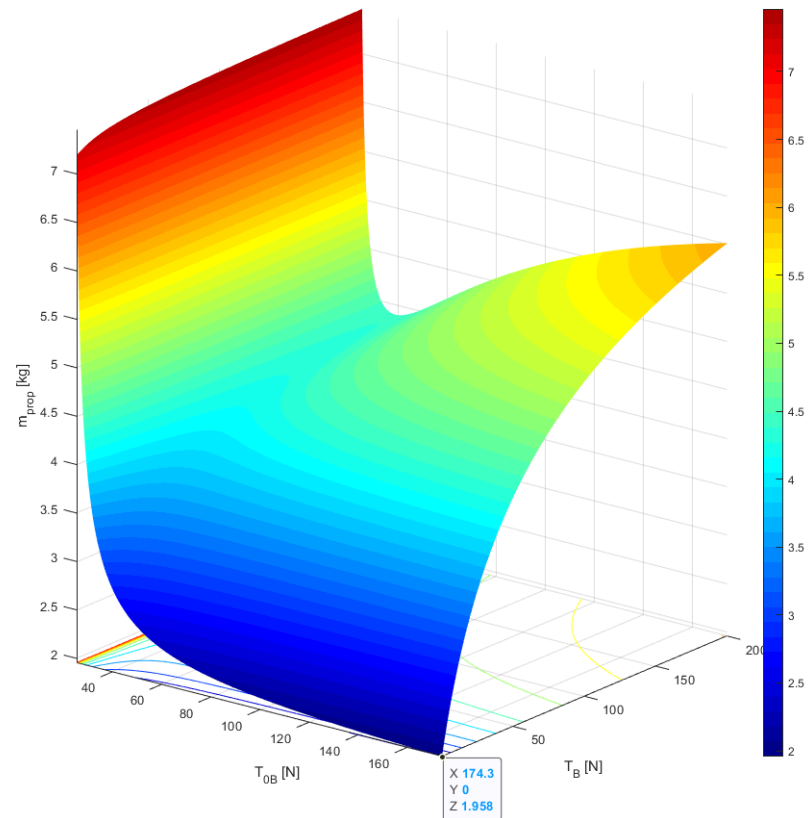


Figure 8.2 – $h_1 = 50$ m, $I_{sp} = 10$ s, $m_0 = 15$ kg

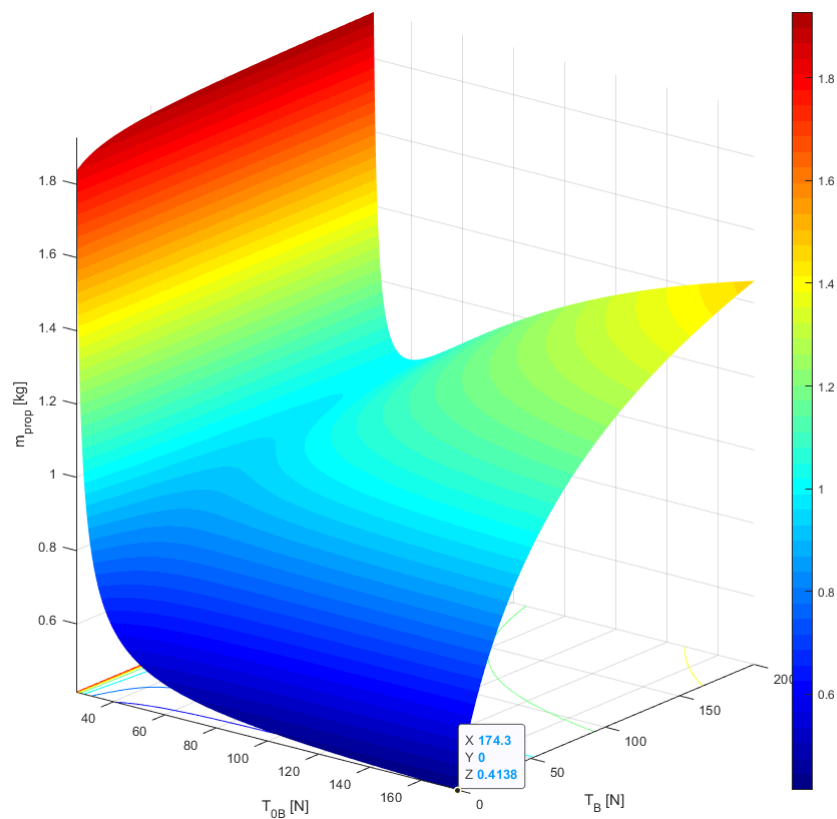


Figure 8.3 – $h_1 = 50$ m, $I_{sp} = 50$ s, $m_0 = 15$ kg

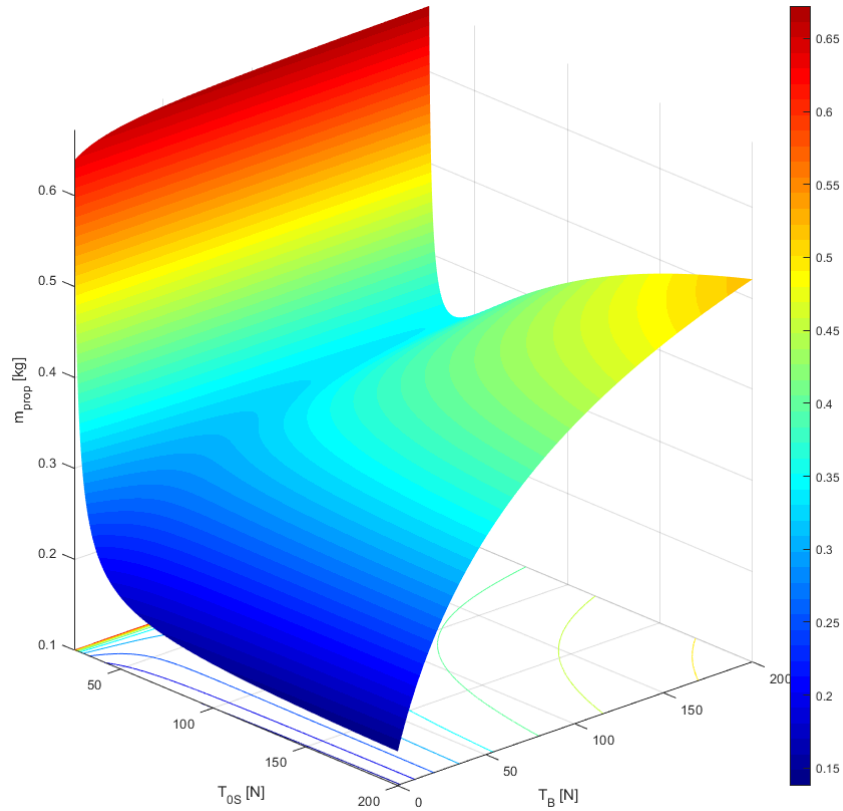


Figure 8.4 – $h_1 = 50$ m, $I_{sp} = 250$ s, $m_0 = 15$ kg

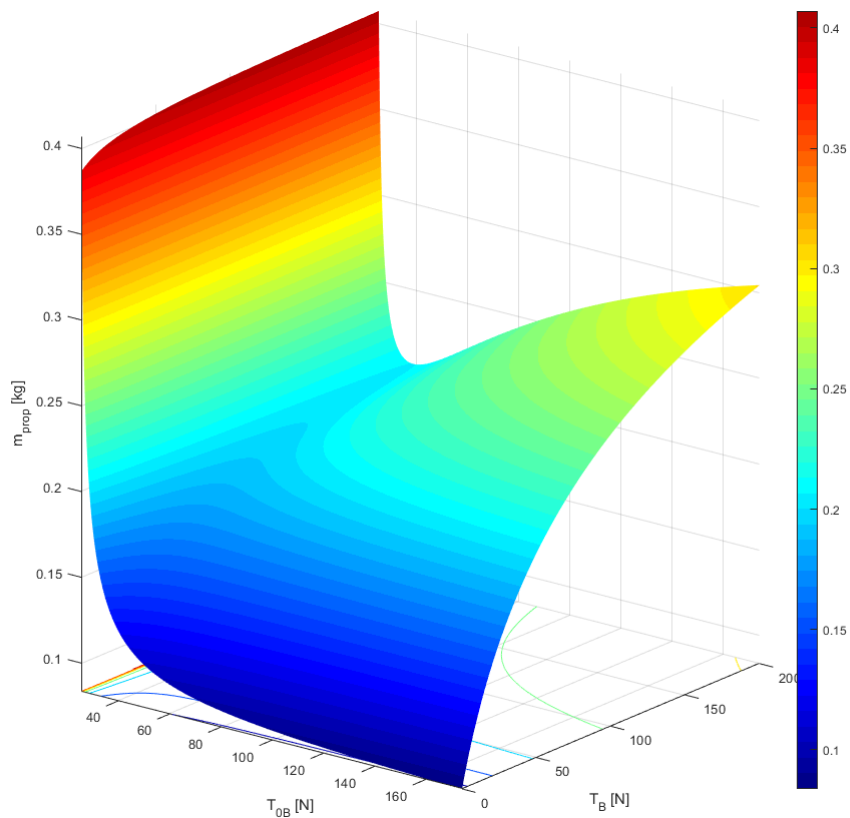


Figure 8.5 – $h_1 = 50$ m, $I_{sp} = 150$ s, $m_0 = 15$ kg

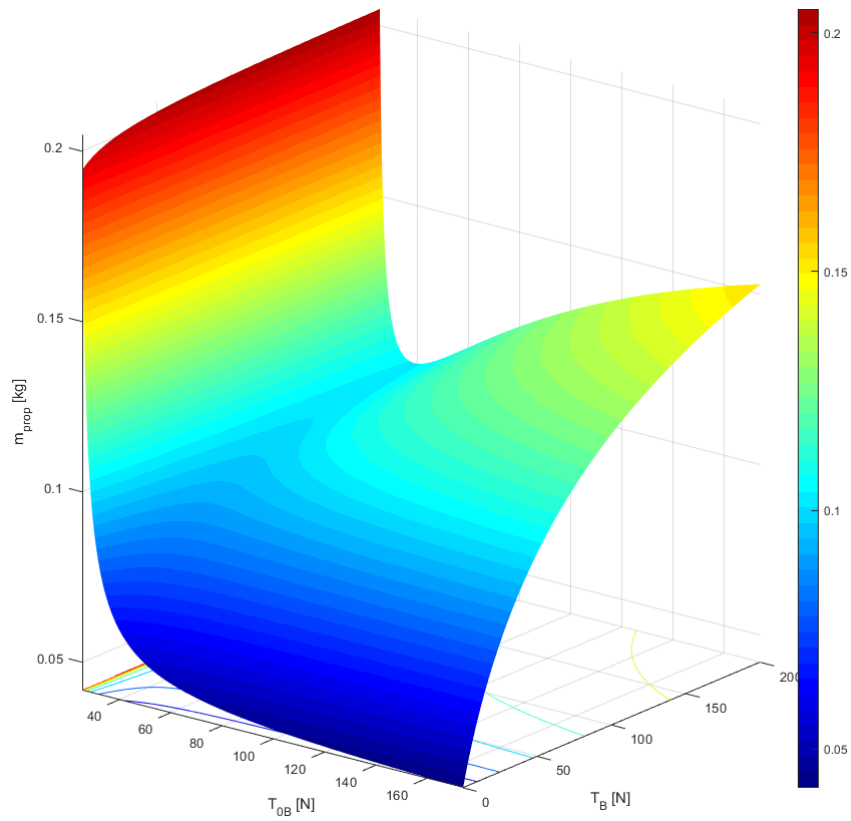


Figure 8.6 – $h_1 = 50 \text{ m}$, $I_{sp} = 500 \text{ s}$, $m_0 = 15 \text{ kg}$

9 Annex 05 – Vertical ascent, comparison between Case 1 and Case 2

Model: $m \neq cost \rightarrow$ Tratto01ConFreno.slx || $m = cost \rightarrow$ Tratto01_Confronti.m

Solver: Euler (ode1)

$DT: 1 \text{ ms}$

$m_0 = 15 \text{ kg}$ or $m_0 = 5 \text{ kg}$

$I_{sp} = 150 \text{ s}$ or $I_{sp} = 10 \text{ s}$

$h_1 = 100 \text{ m}$

$g = 1.62 \text{ m/s}^2$

$t_{h_1} = 1 \text{ ms}$

With $m_0 = 15 \text{ kg}$ and $I_{sp} = 150 \text{ s}$

"·": $T_{0B} = [25 \ 30 \ 40 \ 50] \text{ N}$ $T_B = [0 \ 1 \ 3 \ 5 \ 10 \ 20 \ 30 \ 40 \ 50 \ 60] \text{ N}$ $m \neq cost \rightarrow$ Tratto01ConFreno.slx

"·": $T_{0B} = [25 \ 30 \ 40 \ 50] \text{ N}$ $T_B = [0 \ 1 \ 3 \ 5 \ 10 \ 20 \ 30 \ 40 \ 50 \ 60] \text{ N}$ $m = cost \rightarrow$ Tratto01_Confronti.m

With $m_0 = 5 \text{ kg}$ and $I_{sp} = 10 \text{ s}$

"·": $T_{0B} = [8.5 \ 12 \ 20 \ 30 \ 40 \ 50] \text{ N}$ $T_B = [0 \ 1 \ 3 \ 5 \ 10 \ 20 \ 30 \ 40 \ 50 \ 60] \text{ N}$ $m \neq cost \rightarrow$ Tratto01ConFreno.slx

"·": $T_{0B} = [8.5 \ 12 \ 20 \ 30 \ 40 \ 50] \text{ N}$ $T_B = [0 \ 1 \ 3 \ 5 \ 10 \ 20 \ 30 \ 40 \ 50 \ 60] \text{ N}$ $m = cost \rightarrow$ Tratto01_Confronti.m

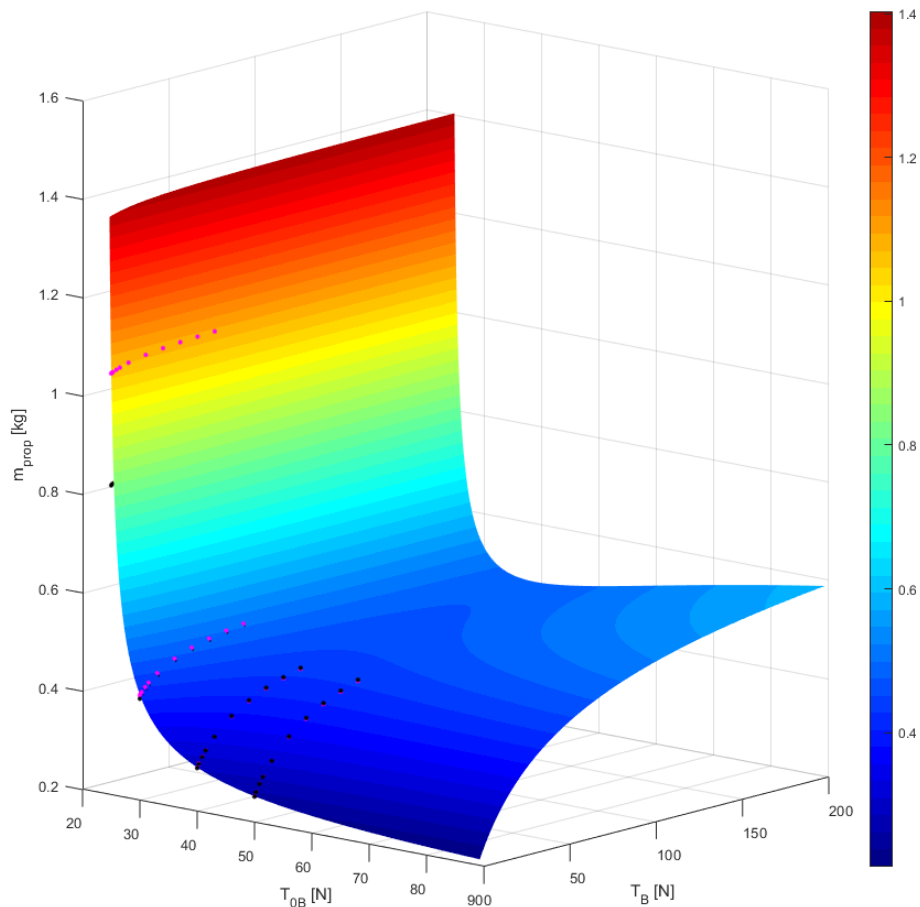


Figure 9.1 – $h_1 = 100 \text{ m}$, $I_{sp} = 150 \text{ s}$, $m_0 = 15 \text{ kg}$ || black · $m \neq cost$ || mag · $m = cost$

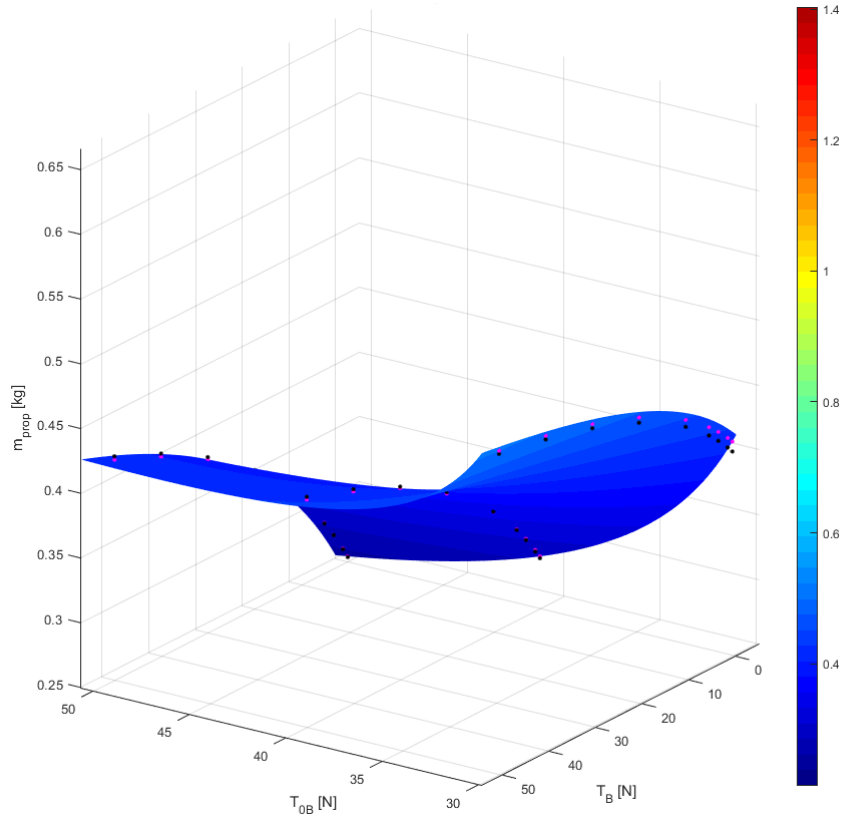


Figure 9.2 – $h_1 = 100$ m, $I_{sp} = 150$ s, $m_0 = 15$ kg || black · $m \neq cost$ || mag. · $m = cost$

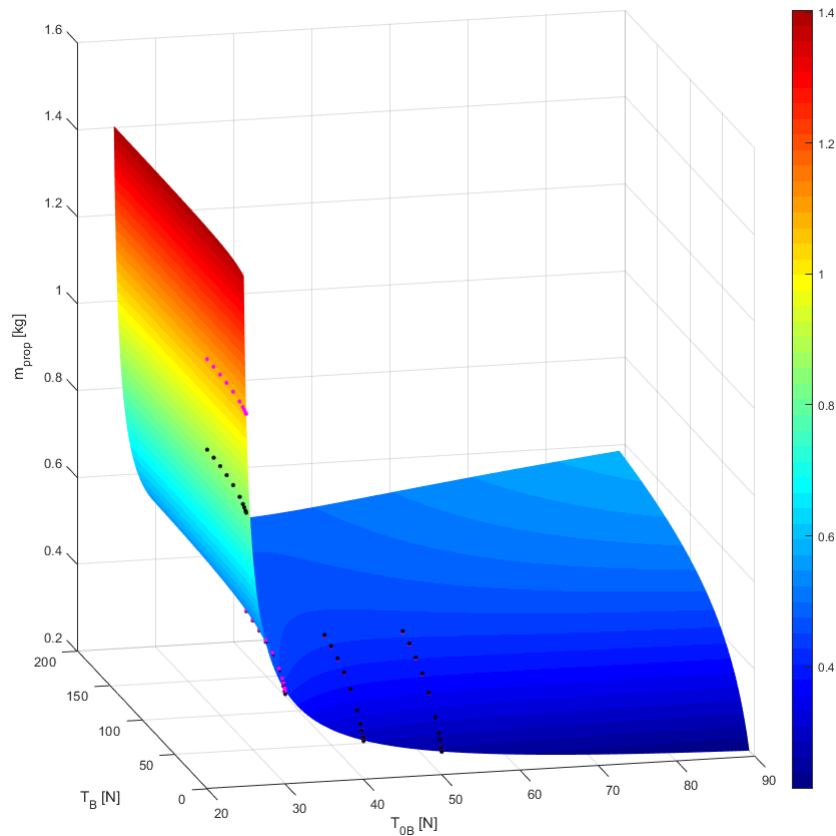


Figure 9.3 – $h_1 = 100$ m, $I_{sp} = 150$ s, $m_0 = 15$ kg || black · $m \neq cost$ || mag. · $m = cost$

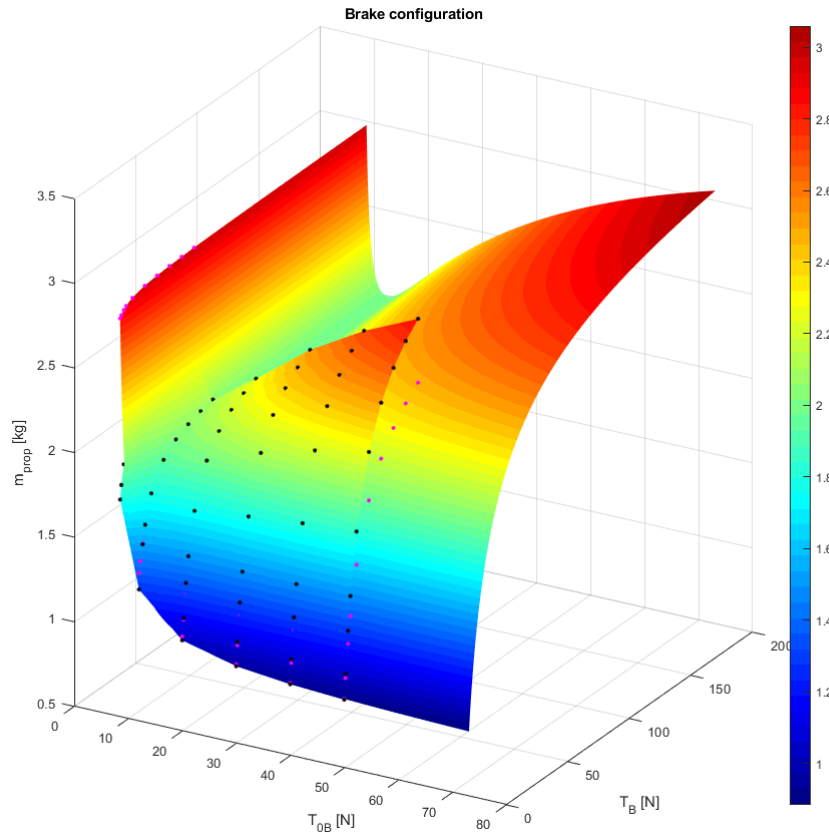


Figure 9.4 – $h_1 = 100$ m, $I_{sp} = 10$ s, $m_0 = 5$ kg || black · $m \neq cost$ || mag · $m = cost$

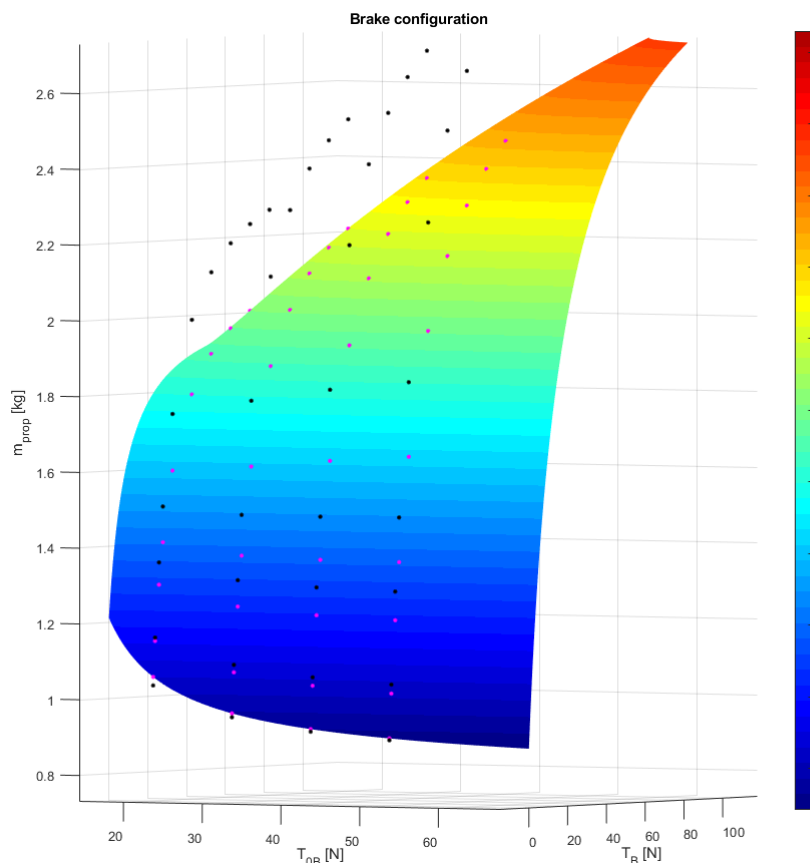


Figure 9.5 – $h_1 = 100$ m, $I_{sp} = 10$ s, $m_0 = 5$ kg || black · $m \neq cost$ || mag · $m = cost$

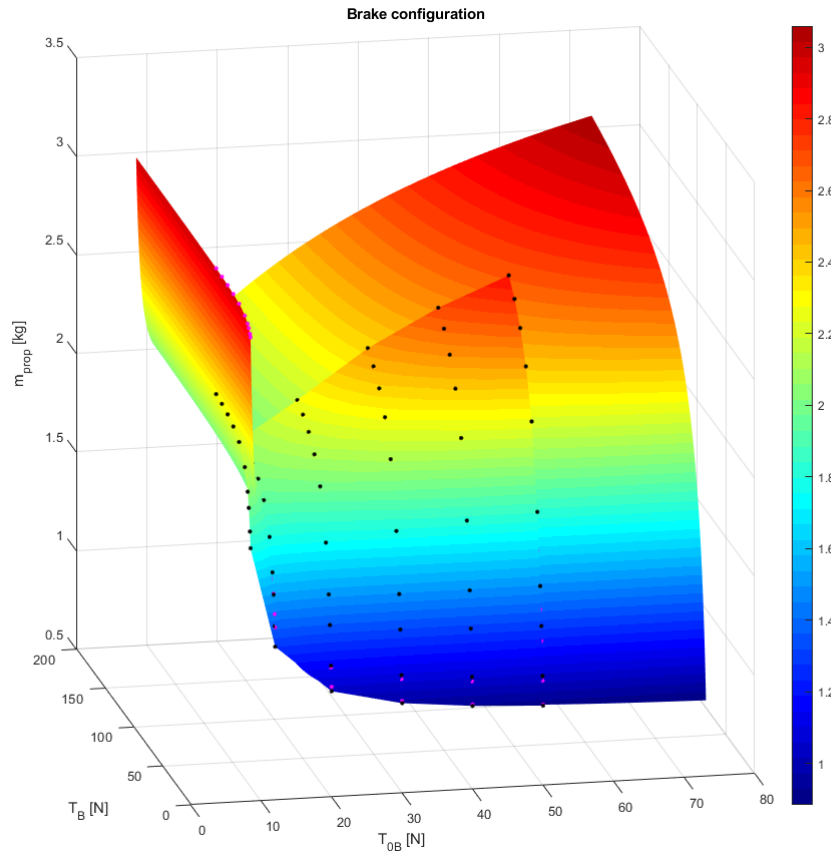


Figure 9.6 – $h_1 = 100$ m, $I_{sp} = 10$ s, $m_0 = 5$ kg || black · $m \neq cost$ || mag · $m = cost$

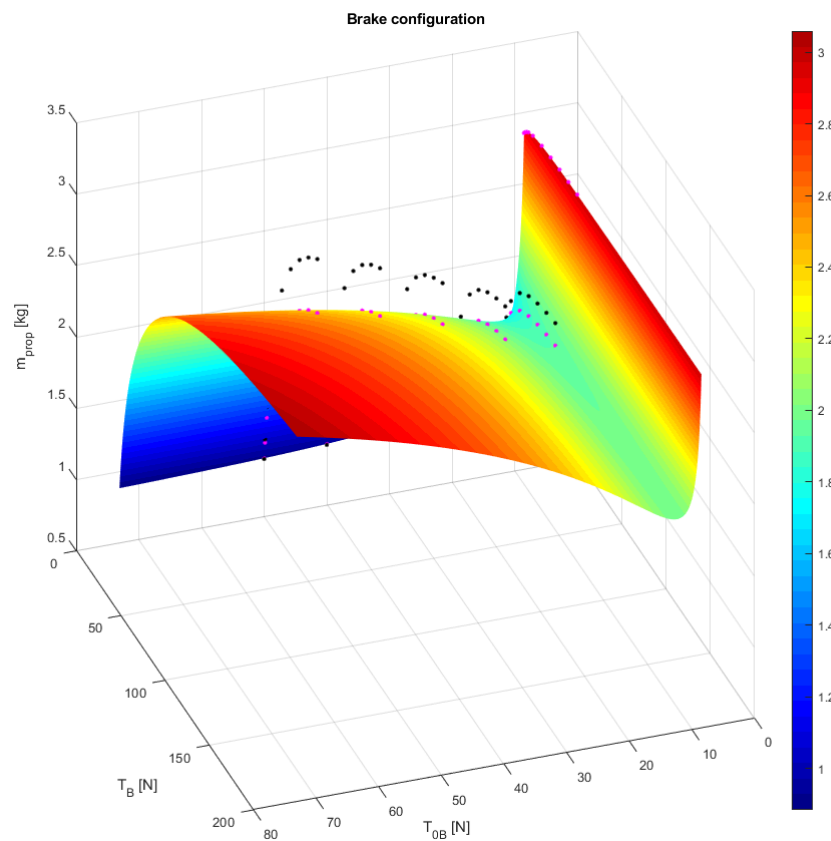


Figure 9.7 – $h_1 = 100$ m, $I_{sp} = 10$ s, $m_0 = 5$ kg || black · $m \neq cost$ || mag · $m = cost$

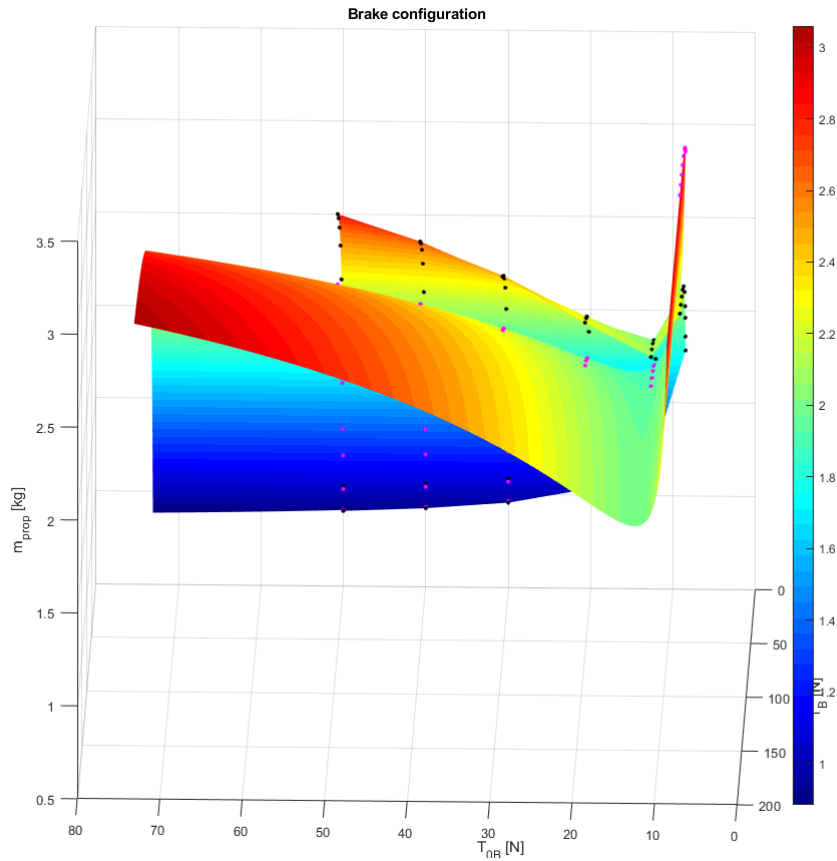


Figure 9.8 – $h_1 = 100 \text{ m}$, $I_{sp} = 10 \text{ s}$, $m_0 = 5 \text{ kg}$ || black · $m \neq \text{cost}$ || mag. · $m = \text{cost}$

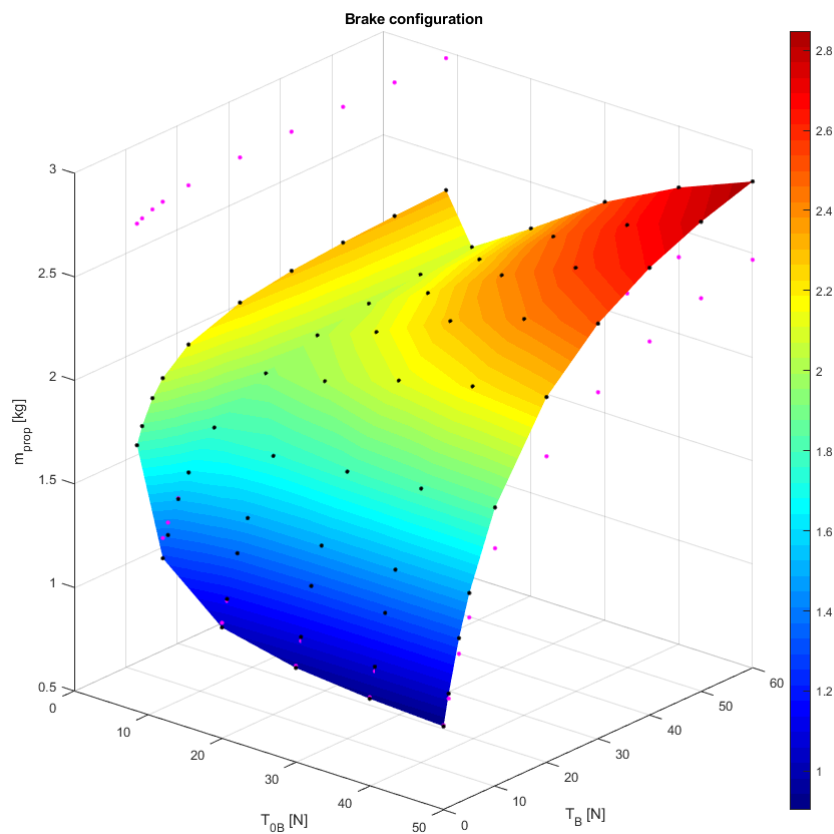


Figure 9.9 – $h_1 = 100 \text{ m}$, $I_{sp} = 10 \text{ s}$, $m_0 = 1 \text{ kg}$ || black · $m \neq \text{cost}$ || mag. · $m = \text{cost}$

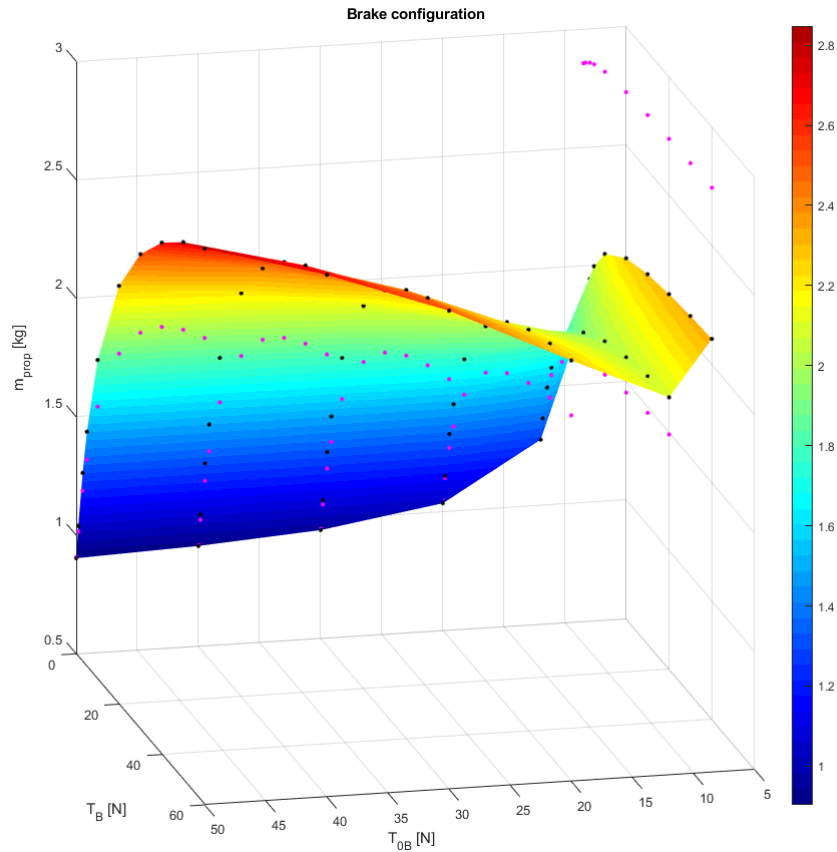


Figure 9.10 – $h_1 = 100$ m, $I_{sp} = 10$ s, $m_0 = 5$ kg || black · $m \neq cost$ || mag · $m = cost$

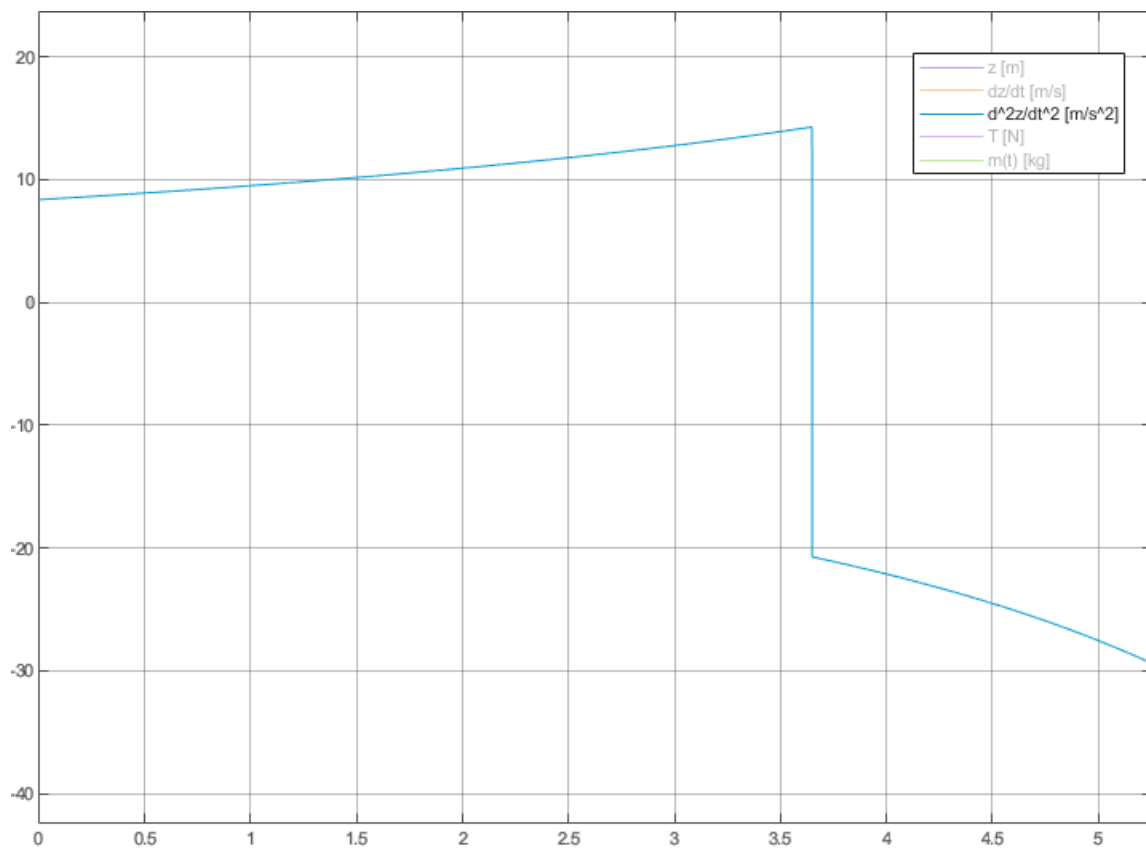


Figure 9.11 – y-axis: z x-axis: t $T_{0B} = 50$ N, $T_B = 60$ N, $m_0 = 5$ kg, $I_{sp} = 10$ s, $h_1 = 100$ m

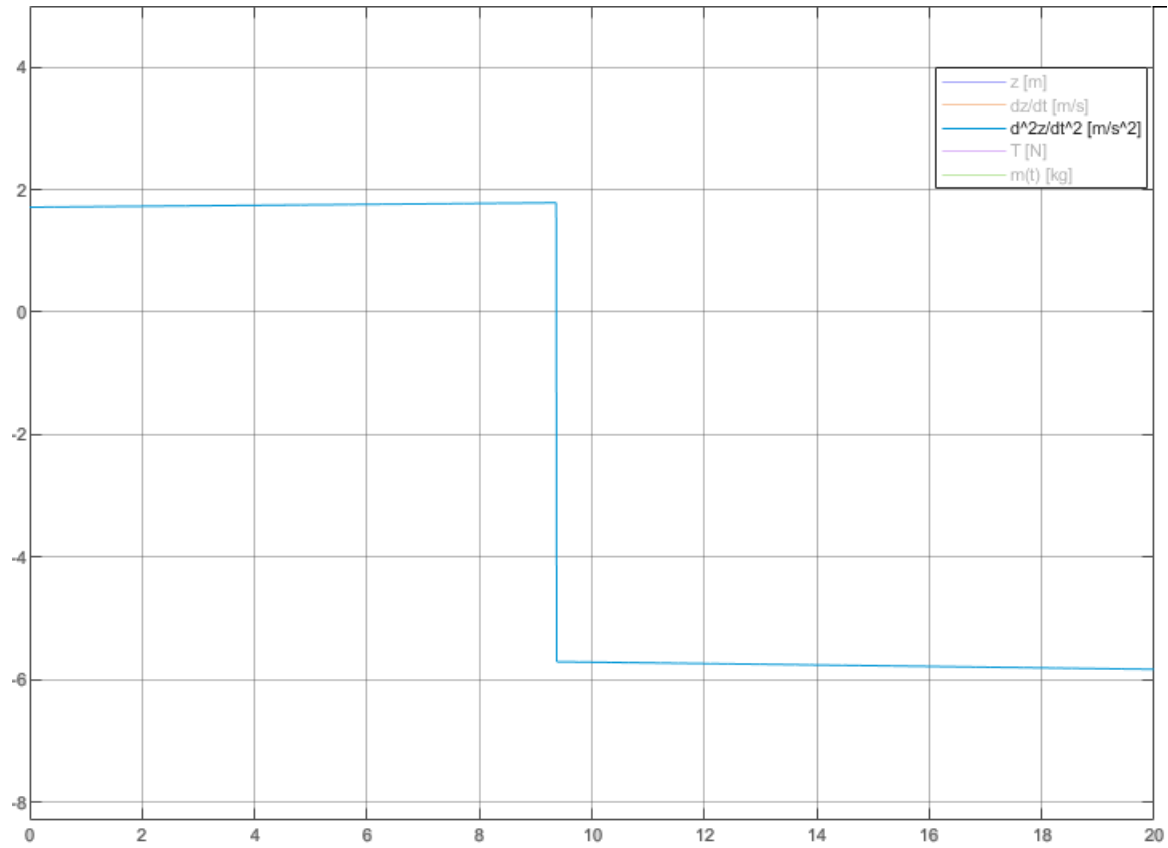


Figure 9.12 – y-axis: a x-axis: t $T_{0B} = 50N$, $T_B = 60N$, $m_0 = 15kg$, $I_{sp} = 150s$, $h_1 = 100m$

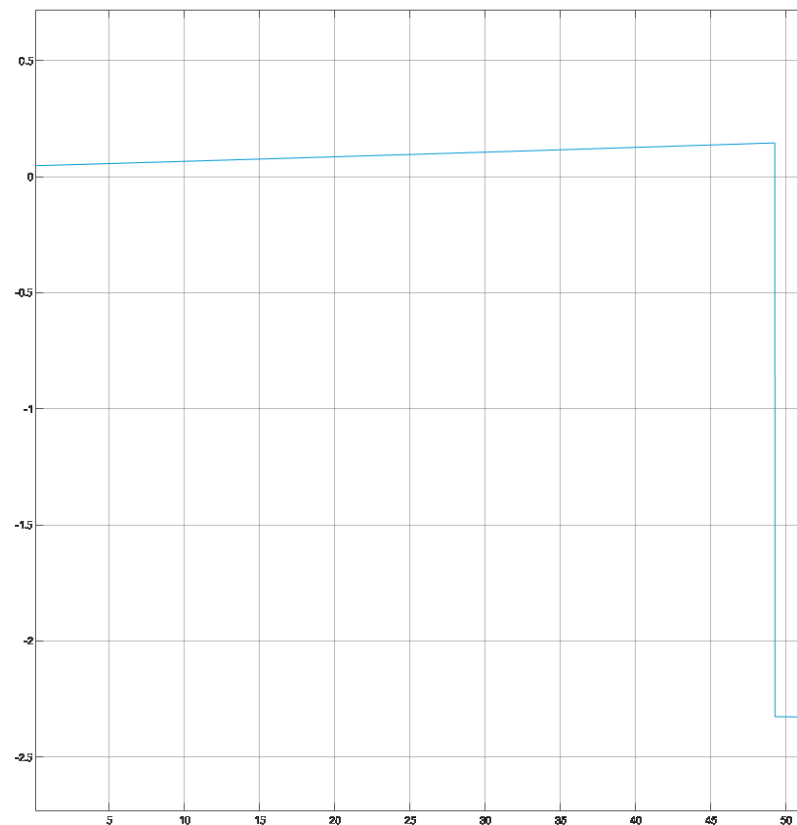


Figure 9.13 – y-axis: a x-axis: t $T_{0B} = 25N$, $T_B = 10N$, $m_0 = 15kg$, $I_{sp} = 150s$, $h_1 = 100m$

10 Annex 06 – Horizontal translation

Modes: w. Auxiliary Thrusters → Chapter 3.3.2 || w/o. Auxiliary Thrusters → Chapter 3.3.3

Solver: Euler (ode1)

$DT: 1 \text{ ms}$

$m_1 = 15 \text{ kg}$

$I_{sp} = 150 \text{ s}$ (also for auxiliary thrusters)

$g = 1.62 \text{ m/s}^2$

$\Delta t_{h_2} = 1 \text{ ms}$

Figure legend

Δ : with auxiliary thrusters (w A.T.)

\star : without auxiliary thrusters (w/o A.T.)

\bullet : Minimum consumption point, case w A.T.

\bullet : Minimum consumption point, case w/o A.T.

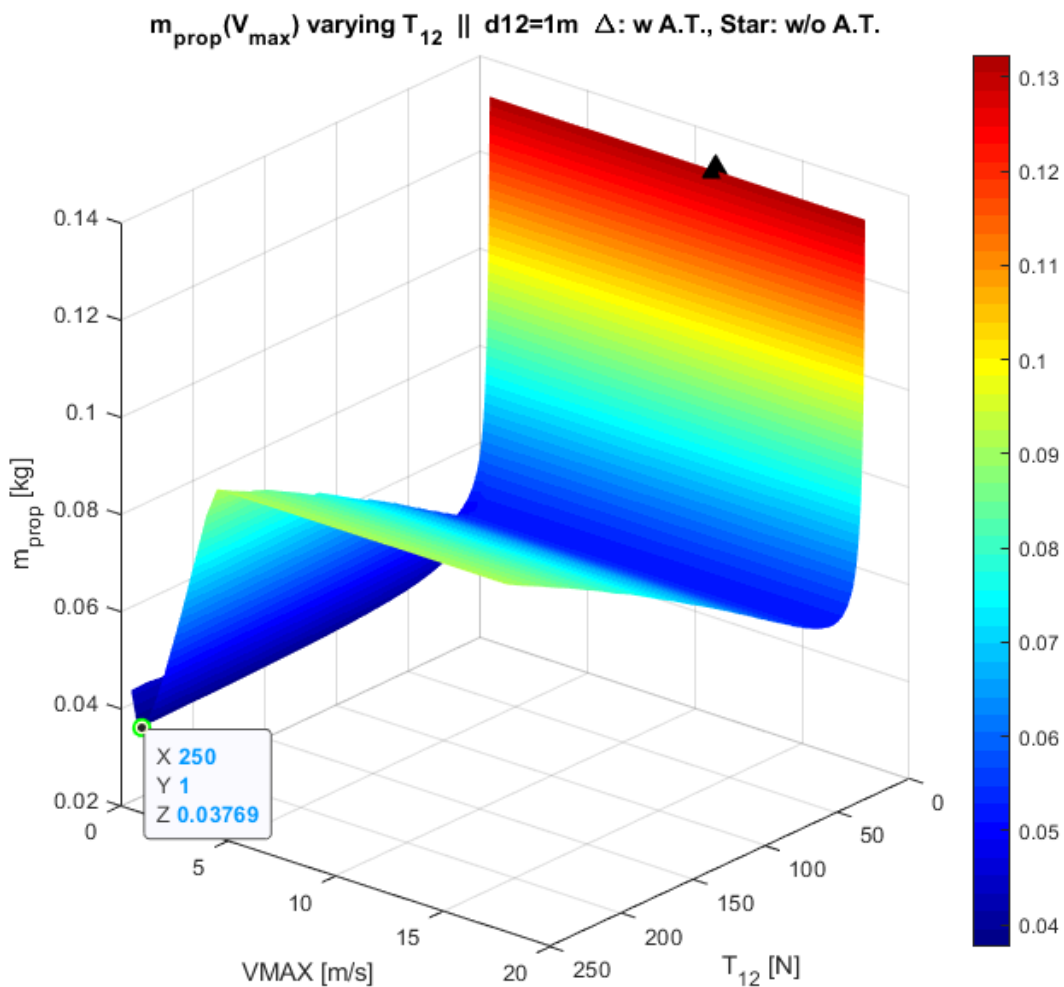


Figure 10.1 – Horizontal translation: $m_{prop} = f(T_{12}, V_{12_{max}})$ with $d_{12} = 1\text{m}$

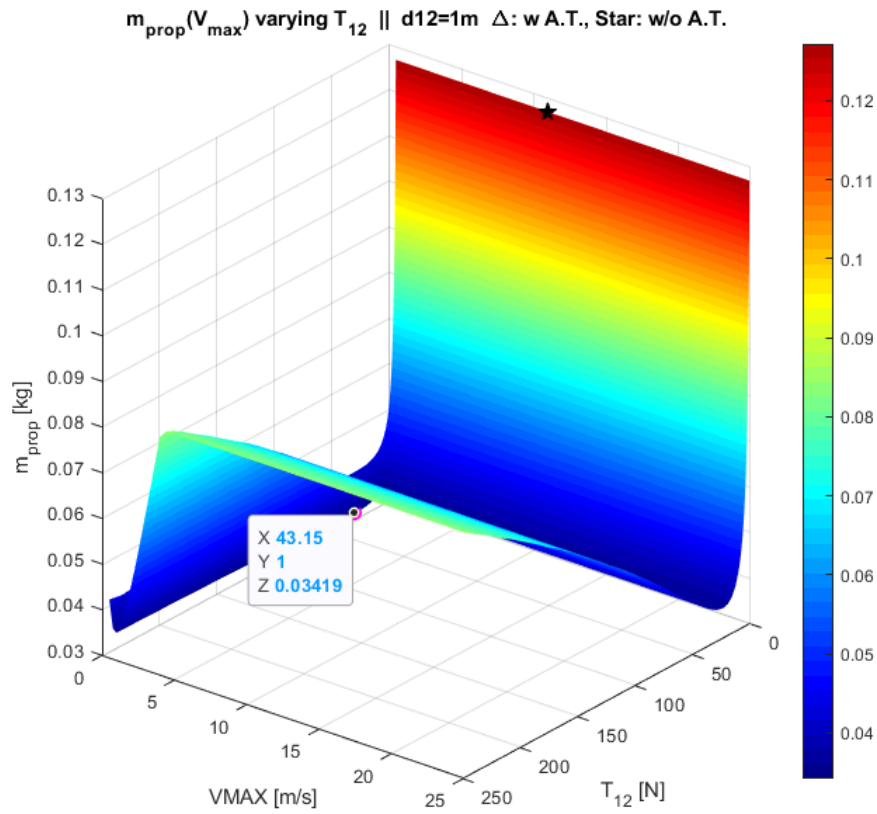


Figure 10.2 – Horizontal translation: $m_{prop} = f(T_{12}, V_{12_{max}})$ with $d_{12} = 1m$

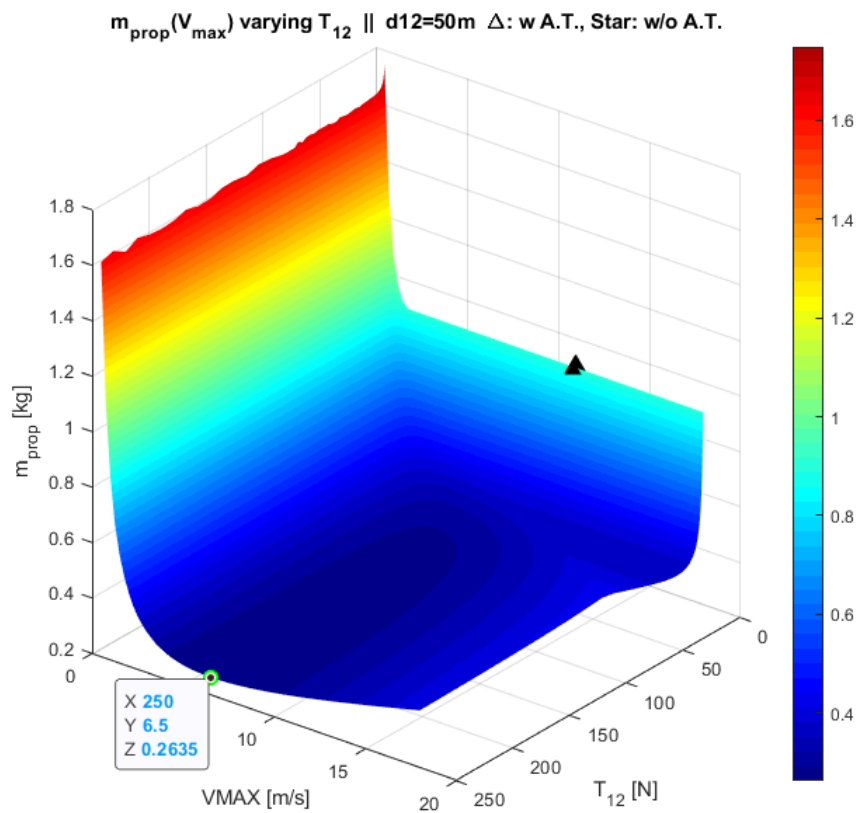


Figure 10.3 – Horizontal translation: $m_{prop} = f(T_{12}, V_{12_{max}})$ with $d_{12} = 50m$

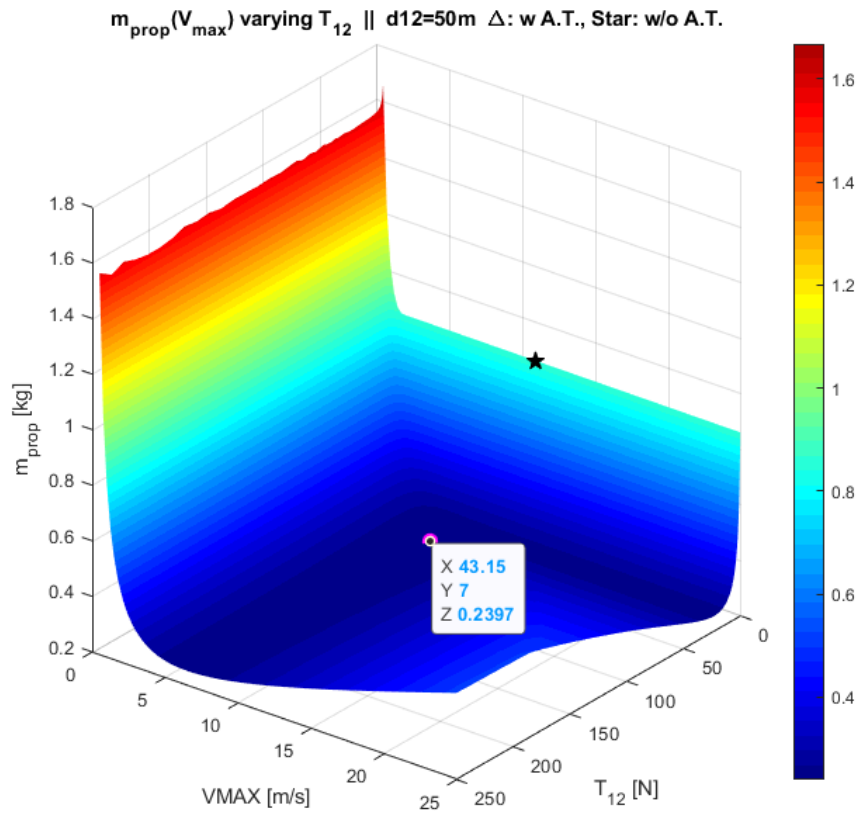


Figure 10.4 – Horizontal translation: $m_{prop} = f(T_{12}, V_{12_{max}})$ with $d_{12} = 50m$

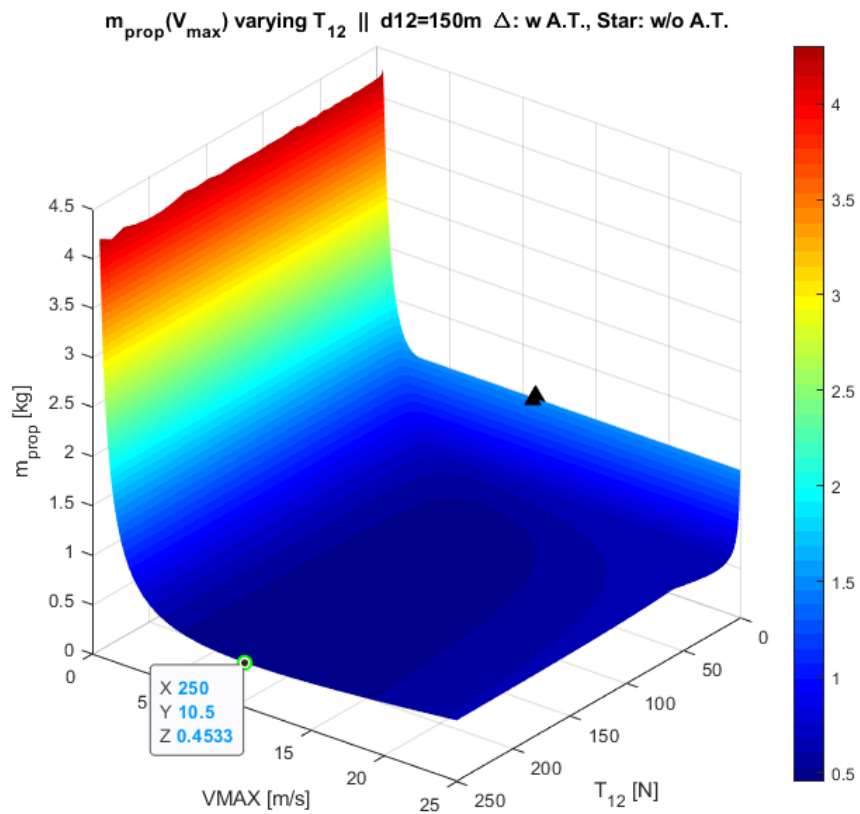


Figure 10.5 – Horizontal translation: $m_{prop} = f(T_{12}, V_{12_{max}})$ with $d_{12} = 150m$

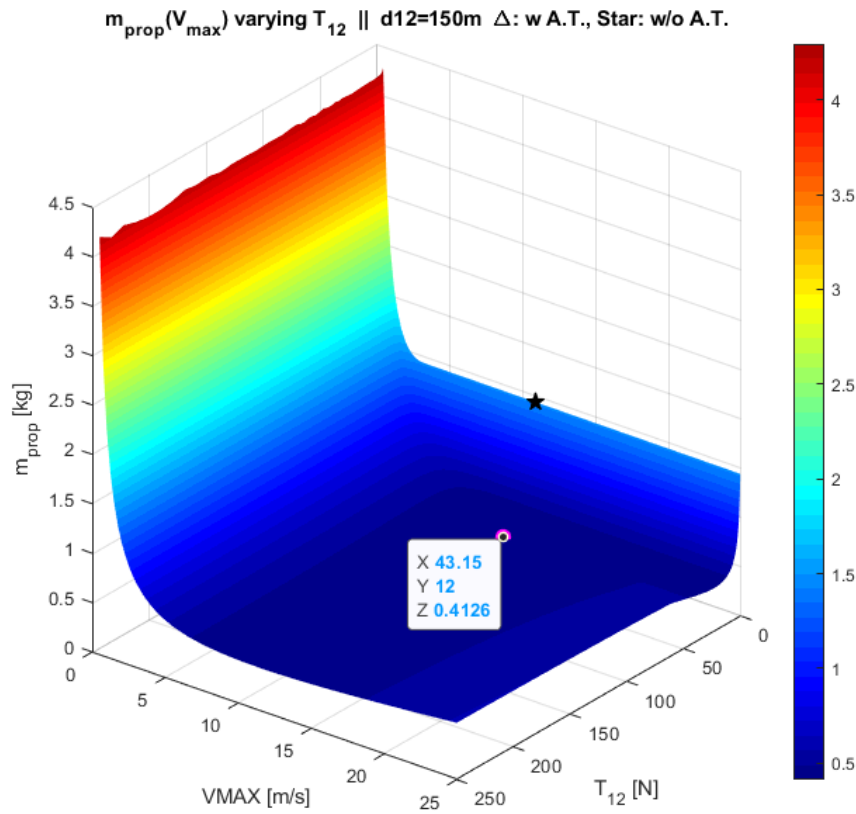


Figure 10.6 – Horizontal translation: $m_{prop} = f(T_{12}, V_{12_{max}})$ with $d_{12} = 150m$

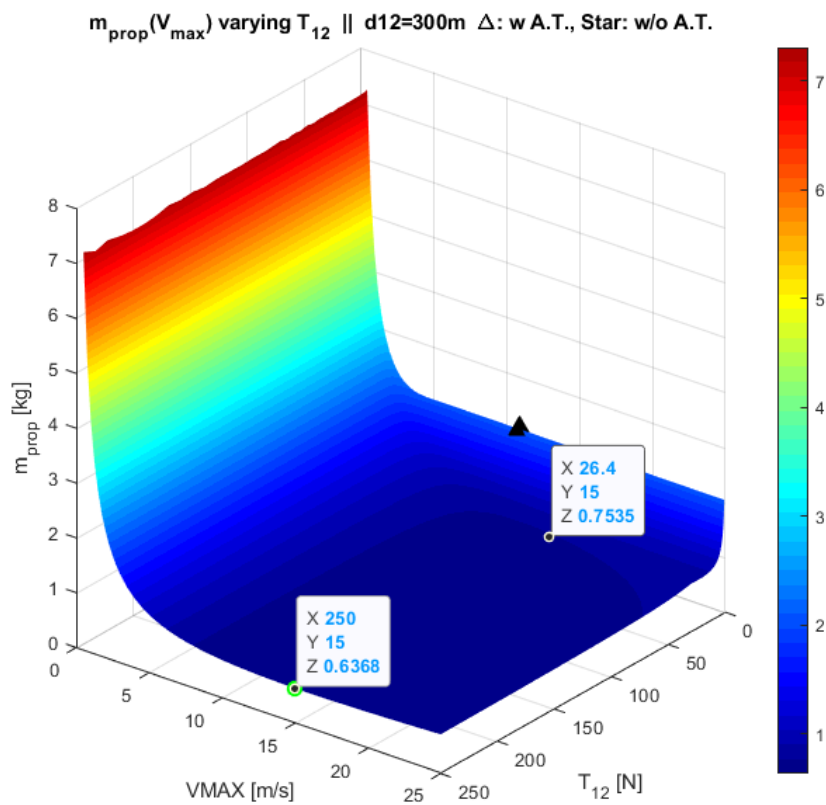


Figure 10.7 – Horizontal translation: $m_{prop} = f(T_{12}, V_{12_{max}})$ with $d_{12} = 300m$

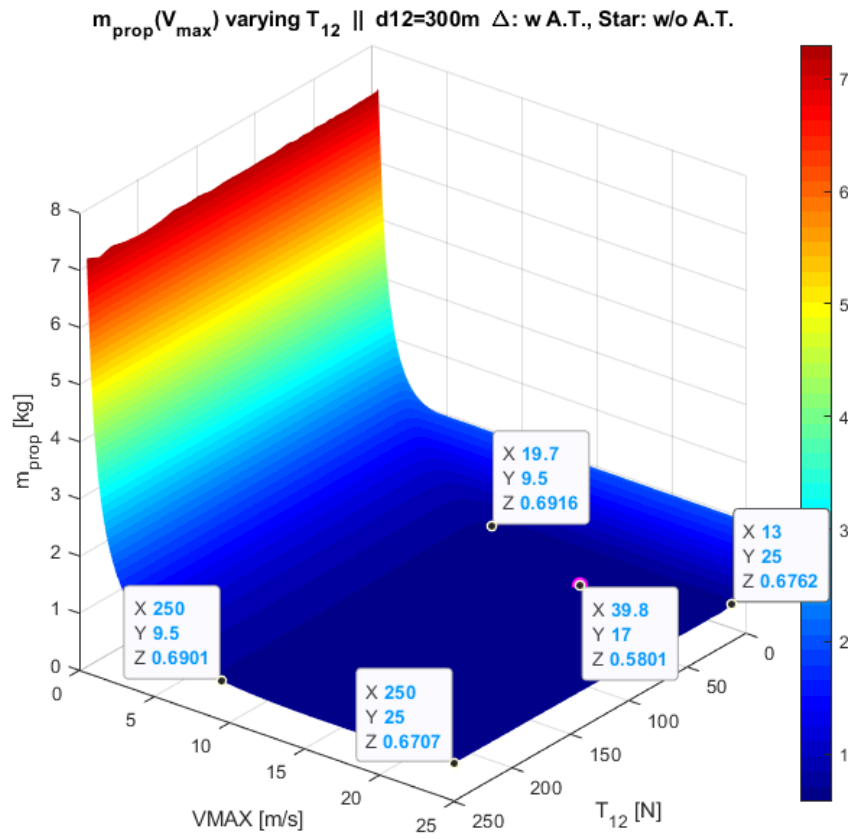


Figure 10.8 – Horizontal translation: $m_{prop} = f(T_{12}, V_{12_{max}})$ with $d_{12} = 300m$

11 References

- [1] R. Greeley, «Lava Tubes and Channels at Lunar Marius Hills,» [Online]. Available: <https://ntrs.nasa.gov/archive/nasa/casi.ntrs.nasa.gov/19710008532.pdf>.
- [2] J. Universities, «Mission Concepts of Unprecedented Zipangu Underworld of the Moon Exploration».
- [3] H. e. al., «Possible lunar lava tube skylight observed by SELENE cameras».
- [4] «Photojournal JPL,» [Online]. Available: <https://photojournal.jpl.nasa.gov/catalog/PIA12954>.
- [5] NASA. [Online]. Available: <https://www.nasa.gov/content/goddard/lunar-pits-could-shelter-astronauts-reveal-details-of-how-man-in-the-moon-formed>.
- [6] L. Chappaz, «Evidence of large empty lava tubes».
- [7] A. Arya, «Detection of potential site for future human habitability on the Moon using Chandrayaan-1 data,» 2011.
- [8] O. B. Samuel W. Ximenes and J. O. Elliott, «Defining a Mission architecture and Technologies for Lunar Lava Tube Reconnaissance,» 2012.
- [9] M. Robinson, «Annual Meeting of the Lunar Exploration Analysis Group, ARNE - SUBLUNAREAN EXPLORER,» 2014.
- [10] NASA, 17 July 2014. [Online]. Available: <https://www.nasa.gov/content/goddard/lunar-pits-could-shelter-astronauts-reveal-details-of-how-man-in-the-moon-formed>.
- [11] W. Whittaker, «Technologies Enabling Exploration of Skylights, Lava Tubes and Caves,» in *NASA Innovative Advanced Concepts (NIAC) Phase I*, 2011.
- [12] U. Today. [Online]. Available: <https://www.universetoday.com/tag/lunar-lava-tubes/>.
- [13] Haruyam, et. al , «Exploration of Lunar Holes, Possible Skylights of Underlying Lava Tubes, by Smart Lander for Investigating Moon (SLIM),» in *Trans. JSASS Aerospace Tech. Japan Vol. 10, No. ists28, pp. Pk_7-Pk_10, 2012*, 2011.
- [14] NASA. [Online]. Available: <https://www.nasa.gov/content/commercial-lunar-payload-services-overview>.
- [15] iSpace. [Online]. Available: <https://ispace-inc.com/project/>.
- [16] G. Podestà, «Lunar Nano Drone for a mission of exploration of lava tubes on the Moon: Propulsion System,» 2020.
- [17] G. Latiro, «Lunar Nano Drone for a mission of exploration of lava tubes on the Moon: Navigation System,» 2020.
- [18] F. G. Håvard and e. al., «Flight Control System for NASA's Mars Helicopter,» *AIAA 2019-1289*, 2019.
- [19] J. W. Cornelisse, H. F. Schoyer and K. F. Wakker, *Rocket Propulsion and Spaceflight Dynamics*, London: Pitman, 1979.
- [20] J. McDermott, Power, in *Space Mission Analysis and Design (Second Edition)*, Microcosm, Inc., Torrance, California, and Kluwer Academic Publishers, Dordrecht, 1992.
- [21] A. Hyder, R. Wiley, G. Halpert, D. Flood and S. Sabripour, *Spacecraft Power Technologies*, Imperial College Press, 2003.
- [22] P. Fortescue, G. Swinerd and J. Stark, *Spacecraft Systems Engineering*, Wiley, 2011.
- [23] L. S. Mason, «Comparison of Energy Conversion Technologies for Space Nuclear Power Systems,» *NASA/TM—2019-219935 AIAA—2018-4977*, December 2019.

- [24] NASA/TP—2018–220027, «State of the Art, Small Spacecraft Technology,» Ames Research Center, Moffett Field, California, 2018.
- [25] G. A. Landis, «Power Systems for Miniature Interstellar Flyby Probe,» NASA John Glenn Research Center, 21000 Brookpark Road, Cleveland OH 44017, U.S.A., 2019.
- [26] NASA, «Energy Storage Technologies for Future Planetary Science Missions - JPL D-101146,» 2017.
- [27] NASA, Energy Storage Technology for Future Space Science Missions JPL D-30268, November 2004.
- [28] NASA, EXTRAVEHICULAR MOBILITY UNIT (EMU) LSS/SSA DATA BOOK, UTC Aerospace Systems, September, 2017.
- [29] R. Surampudi, «Advanced Energy Storage Technologies for Future NASA Planetary Science Mission Concepts,» February 23, 2018.
- [30] G. Halpert, H. Frank and S. Surampudi, “Batteries and Fuel Cells in Space,” The Electrochemical Society Interface, 1999.
- [31] NASA, «DS-2 Mars Microprobe Battery, Document ID: 19990032328,» in *The 1998 NASA Aerospace Battery Workshop*, February 1, 1999.
- [32] J. W. Larson e J. R. Wertz, Space Mission Analysis and Design, El Segund, California: Microcosm Press, 2005.
- [33] EAGLEPICHER , «LCF136-1019 Datasheet,» 2019.
- [34] SAFT, «Primary lithium batteries LO26SX (Doc. N° 31033-2-1005),» October, 2005.
- [35] C. Cénac-Morthé, et al., “ROSETTA LANDER BATTERIES EXPERIENCE DURING ALL OPERATION PHASES,” 2016.
- [36] M. Maibaum, «Rosetta Lander User Manual (RO-DLR-UM-3100),» 2003.
- [37] SAFT, «Primary lithium battery LSH20 (Doc. No 31015-2-1006),» October, 2006.
- [38] NASA, «Power Subsystem for Extravehicular Activities,» in *Exploration Extravehicular Activity Conference*, Clear Lake Hilton, 2005.
- [39] SAFT , «Primary lithium batteries LO26SXC (Doc. No 31047-2-0604),» June, 2004.
- [40] Krause, F.C., et al., «High Specific Energy Lithium Primary Batteries as Power Sources,» *Journal of The Electrochemical Society*, 165 (10) A2312-A2320 (2018), 2018.
- [41] Energizer, «Product Datasheet: Energizer L91 (Form No. L91GL1218)».
- [42] Ultralife, «UHR-CR34610 Technical Datasheet,» 2016.
- [43] EAGLEPICHER, «Datasheet LCF133S-0319 Li/CFx-MnO₂ Hybrid,» 2019.
- [44] Ultralife, «UHR-XR34610 Technical Datasheet,» 2014.
- [45] Panasonic, «Datasheet BRC LITHIUM POLY-CARBONMONOFLUORIDE,» 2015.
- [46] B. Bushong, «Rayovac D Sized CFx Battery Technology,» 2016.
- [47] SAFT, «Saft lithium batteries, Selector guide (Document N° 54083-2-0320),» March, 2020.